



University of Kentucky
UKnowledge

Theses and Dissertations--Physics and
Astronomy

Physics and Astronomy


2022

Extraction of Deep Inelastic Cross Sections Using a 10.4 GeV Electron Beam and a Polarized Helium-3 Target

Murchhana Roy

University of Kentucky, murchhana2013@gmail.com

Author ORCID Identifier:

 <https://orcid.org/0000-0002-0318-7080>

Digital Object Identifier: <https://doi.org/10.13023/etd.2022.147>

[Right click to open a feedback form in a new tab to let us know how this document benefits you.](#)

Recommended Citation

Roy, Murchhana, "Extraction of Deep Inelastic Cross Sections Using a 10.4 GeV Electron Beam and a Polarized Helium-3 Target" (2022). *Theses and Dissertations--Physics and Astronomy*. 94.
https://uknowledge.uky.edu/physastron_etds/94

This Doctoral Dissertation is brought to you for free and open access by the Physics and Astronomy at UKnowledge. It has been accepted for inclusion in Theses and Dissertations--Physics and Astronomy by an authorized administrator of UKnowledge. For more information, please contact UKnowledge@lsv.uky.edu.

STUDENT AGREEMENT:

I represent that my thesis or dissertation and abstract are my original work. Proper attribution has been given to all outside sources. I understand that I am solely responsible for obtaining any needed copyright permissions. I have obtained needed written permission statement(s) from the owner(s) of each third-party copyrighted matter to be included in my work, allowing electronic distribution (if such use is not permitted by the fair use doctrine) which will be submitted to UKnowledge as Additional File.

I hereby grant to The University of Kentucky and its agents the irrevocable, non-exclusive, and royalty-free license to archive and make accessible my work in whole or in part in all forms of media, now or hereafter known. I agree that the document mentioned above may be made available immediately for worldwide access unless an embargo applies.

I retain all other ownership rights to the copyright of my work. I also retain the right to use in future works (such as articles or books) all or part of my work. I understand that I am free to register the copyright to my work.

REVIEW, APPROVAL AND ACCEPTANCE

The document mentioned above has been reviewed and accepted by the student's advisor, on behalf of the advisory committee, and by the Director of Graduate Studies (DGS), on behalf of the program; we verify that this is the final, approved version of the student's thesis including all changes required by the advisory committee. The undersigned agree to abide by the statements above.

Murchhana Roy, Student

Dr. Wolfgang Korsch, Major Professor

Dr. Christopher Crawford, Director of Graduate Studies

Extraction of Deep Inelastic Cross Sections Using a 10.4 GeV Electron Beam and a
Polarized Helium-3 Target

DISSERTATION

A dissertation submitted in partial
fulfillment of the requirements for
the degree of Doctor of Philosophy
in the College of Arts and Sciences
at the University of Kentucky

By
Murchhana Roy
Lexington, Kentucky

Director: Dr. Wolfgang Korsch, Professor of Physics
Lexington, Kentucky
2022

Copyright© Murchhana Roy 2022

ABSTRACT OF DISSERTATION

Extraction of Deep Inelastic Cross Sections Using a 10.4 GeV Electron Beam and a Polarized Helium-3 Target

Experiment E12-06-121 at Jefferson Lab aims to do a precision measurement of the neutron spin structure function g_2 using inclusive inelastic scattering of electrons over a large kinematic range of x and Q^2 . The third moment of the linear combination of the spin structure functions g_1 and g_2 , d_2 , is one of the cleanest higher twist observables and contains information on quark-gluon correlations. It is connected to the “color polarizability or “color Lorentz force” of the nucleon. The experimental data taking was successfully conducted in Hall C using a longitudinally polarized electron beam with 10.4 GeV energy, and a polarized ^3He gas target. The combination of the Super High Momentum Spectrometer (SHMS) and the High Momentum Spectrometer (HMS) allowed us to run the experiment for three constant Q^2 values (3.0, 4.3, and 5.6 GeV^2/c^2) over a wide range of x ($0.20 < x < 0.95$) for the first time. To extract the neutron spin structure functions, precision determination of the unpolarized cross-sections and double spin asymmetries are required. The analysis of the deep inelastic scattering data and the results from the first measurements of unpolarized ^3He cross-sections are reported in this work. The extracted cross-sections will be combined with the electron asymmetry results (ongoing work) to obtain the g_2 and d_2 of ^3He . Finally, nuclear correction to the ^3He results will have to be applied to extract g_2 and d_2 for the neutrons.

KEYWORDS: DIS, neutron, g_2^n , d_2^n , compass, cross-section, polarized ^3He

Murchhana Roy

May 15, 2022

Extraction of Deep Inelastic Cross Sections Using a 10.4 GeV Electron Beam and a
Polarized Helium-3 Target

By
Murchhana Roy

Dr. Wolfgang Korsch

Director of Dissertation

Dr. Christopher Crawford

Director of Graduate Studies

May 15, 2022

Date

To my beloved parents and Alind

ACKNOWLEDGMENTS

I would like to express my sincere gratitude to my advisor Dr. Wolfgang Korsch, for his support and guidance in my Ph.D. study. His immense knowledge and experience provided me with invaluable help both in my academic endeavors as well as in shaping my professional career. I will always be grateful to him for giving me this opportunity and always motivating me to achieve my goals.

I would also like to thank Dr. Brad Sawatzky and Dr. Jian-Ping Chen at the Jefferson Lab, Dr. Todd Averett at the College of William and Mary, Dr. Xiaochao Zheng at the University of Virginia and the other collaborators for helping and mentoring me during the experimental data taking and the data analysis following that. I could not have completed my Ph.D. without the help and support of William Henry, Arun Tadepalli, Junhao Chen, Mingyu Chen, and Melanie Cardona. I would like to thank them for not only making the experiment successful but also making the long challenging days and the owl shifts at Hall C counting house fun and memorable. I would also like to thank the engineering team, technical staff and survey group at Jefferson Lab for all the support needed during the experiment.

I am very grateful to my committee members Dr. Susan Gardner, Dr. Brad Plaster and Dr. Lee Johnson for dedicating their valuable time and energy to serve on my advisory committee. I would like to specially thank Dr. Gardner for guiding me on my very first project at the University of Kentucky which gave me insight into the workings of graduate research. I would also like to thank Dr. Chris Crawford for his help and support in every step of graduate school.

I would like to thank my colleagues at the University of Kentucky for providing insights and help in my research efforts. Special thanks to Josh and Mark for sharing their valuable experience and knowledge of experimental nuclear physics and helping

me in all possible ways. I would like to acknowledge Suman, Ashoke and Bruce for their help and support. Special shoutout to my fellow graduate students Ritwika, Nikhil, Ashish and Michelle who made my stay at Lexington very enjoyable, specially with late night discussion sessions and potluck dinners.

Lastly I would like to thank my parents, Dr. Mrityunjoy Roy and Mrs. Chhanda Roy for their unconditional love, supporting my academic ambitions, and sending me to the USA to pursue my Ph.D. in nuclear physics. I would like to thank Alind for tolerating my endless tantrums, listening to my presentations for hours, and providing me with the endless supply of late night coffee and delicious snacks to help me complete my dissertation.

This study was supported by the U.S. Department of Energy Office of Nuclear Physics under Contract No. DEFG02-99ER41101 from 2017 to 2022 and the Max Steckler Fellowship in 2017.

TABLE OF CONTENTS

Acknowledgments	iii
Table of Contents	v
List of Figures	viii
List of Tables	xv
Chapter 1 Introduction	1
Chapter 2 Electron Scattering	2
2.1 Scattering Formalism	6
2.2 The Unpolarized Structure Functions	9
2.3 The Polarized Structure Functions	11
2.4 The Electron Asymmetries	13
2.5 Bjorken Scaling in One-Photon Exchange DIS	13
2.6 Scaling Violation	14
2.7 The Structure Functions in the Naive Parton Model	15
Chapter 3 The Neutron Spin Structure Function g_2 and the Quark-Gluon Correlations	18
3.1 g_2 , d_2 and Higher twist Effects	18
3.2 Theoretical Predictions and Existing Results	23
3.2.1 d_2^n Models	23
3.2.2 Previous d_2^n Measurements	24
Chapter 4 The Experimental Overview	27
4.1 Goal of the Experiment	28
4.2 The Experimental Setup	29
4.2.1 The Polarized Electron Beam	29
4.2.2 The Polarized Helium-3 Target	31
4.2.3 Spectrometers and Detectors	32
4.3 Kinematic Coverage	36
4.4 The Coordinate Systems	37
Chapter 5 Electron Beamline Instrumentation and Polarimetry	39
5.1 Electron Beam Position Monitors	39
5.2 Electron Beam Current Monitors and Accumulated Charge	40
5.3 Electron Beam Energy Measurement	40
5.4 Electron Beam Polarization Measurement	41
5.4.1 Moller Polarimeter Setup	44

5.4.2	Hall C Spin Dance	47
5.4.3	Moller Measurement Results	48
Chapter 6	The Polarized Helium-3 Target System	50
6.1	Target Cell	50
6.2	The Holding Magnetic Field	55
6.3	The Target Optics	56
6.4	The Target Oven and the Heating System	59
6.5	Polarizing The Target	60
6.6	Target Polarimetries	63
6.7	The Target Ladder	71
6.8	The Target Enclosure	72
6.9	The Target Polarization Direction Measurement	72
6.9.1	The Target Holding Magnetic Field Mapping	72
6.9.2	The Horizontal Compass	74
6.9.3	Compass Mirror Alignment	75
6.9.4	Compass Measurements in Hall C	76
6.9.5	Survey Data Analysis and Results	82
6.9.6	Sources of Systematic Uncertainties	86
6.9.7	Studies Done to Investigate the Differences in the March and September Data	88
Chapter 7	Experimental Data Analysis	92
7.1	Data Acquisition	94
7.2	Reference Time Cuts	94
7.3	Detector Analysis	98
7.4	Particle Identification Studies	109
7.4.1	Cherenkov efficiency and pion rejection factor:	109
7.4.2	Calorimeter efficiency and pion rejection factor:	112
7.4.3	Background Estimation	116
7.4.4	Live time	119
7.4.5	Trigger Efficiencies	119
7.4.6	Tracking Efficiency	120
7.4.7	Spectrometer Acceptance	120
7.5	Cross-section Extraction	126
7.5.1	Background Correction to Obtain σ_{rad}	128
7.5.2	Radiative Correction	129
7.5.3	Bin Centering Correction	134
7.5.4	Systematic Uncertainties	140
Chapter 8	Summary	145
Appendix A:	Compass Measurement Results	146
Appendix B:	F1F2IN09 and F1F2IN21 Models	149

Appendix C: Inputs of the rc-externals Code	150
Appendix D: Beam Current Monitors during Data Collection	152
Appendix E: Tabulated Unpolarized Cross Sections	154
Bibliography	157
Vita	162

LIST OF FIGURES

2.1	First order diagram for lepton-hadron scattering.	2
2.2	The cross section (arbitrary units) spectrum for the electron scattering from a nuclear target. The different peaks for the elastic, quasi-elastic, resonance regions are shown in the $Q^2 - \nu$ plane. In case of a nucleon target, only the elastic peak occurs for $W = M_n$ before the resonances.[10]	5
2.3	Kinematically allowed region for Deep Inelastic Scattering (shown by shaded region). The maximum value of Q^2 is bound by fixed x values [11]. . . .	7
2.4	Electron scattering plane and relevant angles.	12
2.5	Examples of higher order radiative processes that contribute with the dominating one-photon exchange process in DIS.	14
2.6	Q^2 evolution of $F_2^p(x, Q^2)$ at different x that shows scaling violation. [15]	15
2.7	Electron scattering from an individual parton in the Naive Parton Model.	16
3.1	The helicity exchange in virtual Compton scattering by twist-2 and twist-3 processes. g_2 is the combination of these two processes.	19
3.2	The induced color electric and magnetic field when the nucleon is transversely polarized and hit by the virtual photon.	21
3.3	The theoretical predictions, previous experimental measurements of neutron and proton d_2 with Q^2 . The projections of d_2^n at three constant Q^2 values for the experiment E12-06-121 are also shown.	22
3.4	The projection of $x^2 g_2^n$ over the whole x region. The three sets of colored points (vertically offset from each other) represent the constant $Q^2=3, 4.3, 5.6 \text{ GeV}^2/c^2$ where the d_2^n will be evaluated.	25
4.1	The aerial view of the Thomas Jefferson Accelerator Facility.	27
4.2	CEBAF after 12 GeV upgrade [64].	28
4.3	Experimental setup in Hall C.	29
4.4	The source of the electron beam with high polarization	30
4.5	The diagram of the injector optics system and the helicity feedback system to compensate charge asymmetry.[68]	30
4.6	The components of the polarized ^3He ground states.	31
4.7	The layout of the target system in Hall C.	32
4.8	The CAD drawing of the SHMS showing the HB, quadrupoles, dipole and the detector hut [76].	35
4.9	The kinematic coverage of HMS and SHMS for the experiment E12-06-121. The large momentum acceptance of SHMS is shown in the right part of the plot and the left part shows the HMS kinematic coverage.	36
4.10	The different coordinate systems used in the experiment E12-06-121. . .	37
5.1	The view of the Hall C beamline looking from the entrance to the hall towards the target region [76].	39

5.2	The schematic of the beam current monitor system located in Hall C. . .	40
5.3	The analyzing powers (a_{xx} , a_{yy} , a_{zz}) as a function of scattering angle in the center of mass frame (θ_{CM}) in Moller scattering [84].	42
5.4	(a) The layout of the target, quadrupoles, collimators, and the detectors are shown. (b) The iron targets with different thicknesses were placed in a target ladder which could be remotely moved horizontally into the beam. For the purpose of the experiment E12-06-121, only the 4 μm thick target was used. (c) Target saturation using $\sim 3\text{-}4$ T magnetic field, the polarization was out-of-plane. (d) The movable collimators in the beamline are shown. [76].	43
5.5	The results of the Monte-Carlo simulation of collimator scan for 10 μm thick target and 1 μA electron beam current.	45
5.6	The results of the Monte-Carlo simulation of collimator scan and, the real collimator scans performed in Hall C before the experiment E12-06-121. .	46
5.7	The Moller detector package consisting of the hodoscope, collimator, the lead glass counter and the photomultiplier tube [85].	47
5.8	The results of the Hall C spin dance. Electron beam polarization was measured for four different Wien angle settings. The maximum polarization was obtained for the Wien angle of -32.24° [86].	47
5.9	The Moller measurement results from that performed during the E12-06-110 and the E12-06-121 experiments.	48
6.1	The ^3He gas target cell and the dimensions of its different chambers. . .	51
6.2	The locations where the target cell wall thickness was measured using the ultrasonic gauge (not to scale).	52
6.3	The target magnetic field system.	56
6.4	(a) The laser transport from the laser room to Hall C via optical fibers. (b) The top and bottom mirror orientations reflect the laser beam towards the pumping chamber for the longitudinal and transverse directions. . . .	57
6.5	The longitudinal and transverse optics setup in Hall C.	58
6.6	The target oven control system. The instruments inside the dashed box were located far away from the target region and the rest were located on top of the target cell.	59
6.7	The splitting of the energy levels of ^{85}Rb in presence of the external magnetic field [72].	61
6.8	The demonstration of the spin exchange polarization transfer from the alkali atoms to the ^3He nuclei. [15]	62
6.9	The oscillating voltage induced in the pick up coils as a result of NMR spin flip and a typical NMR up-sweep and down-sweep signal peaks are shown.	65
6.10	^3He polarizarion measurement results from all NMR measurement performed during experiment E12-06-121.	66
6.11	The EPR AFP signal for the target cell Tommy with target polarization direction 270° w.r.t. the electron beamline.	69
6.12	An example PNMR FID signal after the RF pulse ends.	70

6.13	The target polarization measurement results from all the PNMR measurements during the experiment E12-06-121.	70
6.14	The target ladder with different targets mounted on it. From top to bottom: The ^3He cell, carbon foils, and the reference cell can be seen in the picture.	71
6.15	The magnetic field mapping device used in experiment E12-06-121.	73
6.16	Design of the horizontal compass.	74
6.17	Compass mirror alignment in the target lab.	76
6.18	Straight line fits to the compass mirror alignment data for A_1^n experiment (October, 2019).	77
6.19	Straight line fit to the compass mirror alignment data for d_2^n experiment (March, 2020).	77
6.20	Straight line fit to the compass mirror alignment data for d_2^n experiment (September, 2020).	78
6.21	The compass measurement setup in Hall C.	80
6.22	The magnetic field direction measurement procedures in Hall C.	81
6.23	Determining the transverse magnetic field direction.	82
6.24	Determining the longitudinal magnetic field direction.	83
6.25	The magnetic field direction measurement results for the A_1^n experiment. All angles were calculated w.r.t. +Z direction in absolute Hall C coordinate system. The results from one of the d_2^n kinematic settings (SHMS at 18° , 5.6 GeV/C) were added to this plot because of the similar Helmholtz coil orientation in Hall C.	87
6.26	The magnetic field direction measurement results for the d_2^n experiment (March, 2020). All angles were calculated w.r.t. +Z direction in absolute Hall C coordinate system.	88
6.27	The magnetic field direction measurement results for the d_2^n experiment (September, 2020). All angles were calculated w.r.t. +Z direction in absolute Hall C coordinate system.	89
6.28	Comparison of March and September compass measurement results.	90
6.29	Magnetic field direction if the compass was placed in the wrong location.	91
6.30	Check for consistent offset in compass locations to match the March and September results.	91
7.1	The experimental data analysis flowchart that is being followed to extract g_2^n and d_2^n	92
7.2	The HMS and SHMS detector stacks showing the order of the particle tracking and particle identification (PID) detectors [88].	93
7.3	The hcana multiplicity leaf of HMS 1-pass elastic run 2608 and the corresponding reference time variable with the three multiplicity cuts.	96
7.4	The determination of HMS (a, b, c) and SHMS (d, e, f) reference time cuts, the determined cuts are shown by a red dashed line in each plot.	97
7.5	The β distribution plots after HMS and SHMS hodoscope calibration. The blue and red plots are the uncalibrated and the calibrated β distributions respectively. (Plots generated by M. Chen)	98

7.6	The drift time and drift distance distribution plots for the SHMS first drift chamber wire plane U. The analysis was done using a SHMS defocussed run 9644. (Plots generated by J. Chen.)	99
7.7	The electron read out of Cherenkov PMTs when one photoelectron is extracted from the photocathode.	101
7.8	The detector time window cuts for the HMS CER and the SHMS NGCER. The precalculated goodAdcTdcDiffTime (red) with multiplicity==1 overlapped with the calculated time difference (magenta) with multiplicity==1.	102
7.9	The calibration of HMS gas Cherenkov for PMT1.	103
7.10	The calibration of HMS gas Cherenkov for PMT2.	104
7.11	The SHMS Cherenkov calibration for all four PMTs for run 11538 (13° , -2.1286 GeV/c). The x-axis has unit pC and the inverse of the fit parameter p_2 was the calibration constant.	105
7.12	The determination of the total energy cut from the 2D histogram of total energy in calorimeter and the energy in shower.	105
7.13	The average number of photo electron distributions in the NGCER mirror plane is shown that was used to determine the mirror plane cuts. This was calculated by dividing the PMT good pulse integral weighted events in X-Y by pure event distribution in mirror X-Y.	106
7.14	Representative plots of SHMS calorimeter calibration. By minimizing the ΔP , the calibration constants to transform ADC pulse integral to energy deposition was determined and the calibrated E_{DEP}/P histogram was centered at 1. (Plots generated by M. Cardona.)	107
7.15	The energy dependence of the HMS and SHMS calorimeter resolution. (Plots generated by M. Cardona.)	108
7.16	The calorimeter cuts to separate electron and pion samples in HMS run 4101 (20° , -4.0 GeV/c). The nominal acceptance cuts used: $-8 < H.gtr.dp < 8$ (momentum acceptance), $abs(H.gtr.th) < 0.1$ (out-of-plane angle), $abs(H.gtr.ph) < 0.06$ (in-plane angle) and, $abs(H.react.z) < 22$ (target z cut). (Plots generated by M. Cardona.)	110
7.17	The Cherenkov npe distribution of electrons and pions for HMS run 4101 (20° , -4.0 GeV/c). The nominal acceptance cuts used: $-8 < H.gtr.dp < 8$ (momentum acceptance), $abs(H.gtr.th) < 0.1$ (out-of-plane angle), $abs(H.gtr.ph) < 0.06$ (in-plane angle) and, $abs(H.react.z) < 22$ (target z cut). (Plots generated by M. Cardona.)	111
7.18	Determining npe cut position for optimal ε_{cheren} and PRF_{cheren} . (Plot generated by M. Cardona.)	111
7.19	Determining npe cut position to distinguish between electron and pion sample for SHMS run 11445 (Kin-Z: 18° , -5.6 GeV/c). (Plot generated by M. Cardona)	112
7.20	The calorimeter energy distribution of electrons and pions for SHMS run 11445 (Kin-Z: 18° , -5.6 GeV/c). The nominal acceptance cuts used: $-10 < H.gtr.dp < 22$ (momentum acceptance), $abs(H.gtr.th) < 0.05$ (out-of-plane angle), $abs(H.gtr.ph) < 0.07$ (in-plane angle) and, $abs(H.react.z) < 22$ (target z cut). (Plot generated by M. Cardona.)	113

7.21	SHMS calorimeter efficiency plot with different calorimeter shower energy cuts. A shower energy cut > 0 was applied to ensure selection of good electrons (Plot generated by M. Cardona.)	113
7.22	Determining calorimeter preshower energy cut for optimum efficiency and pion rejection factor for SHMS run 11445 (Kin-Z: 18° , -5.6 GeV/c). (Plot generated by M. Cardona.)	114
7.23	Pion contamination in good electron sample for SHMS run 11445 (Kin-Z: 18° , -5.6 GeV/c). The nominal acceptance cuts used: $-10 < H.gtr.dp < 22$, $abs(H.gtr.th) < 0.05$, $abs(H.gtr.ph) < 0.07$ and, $abs(H.react.z) < 22$, the PID cut used: preshower $E/P > 0.05$, preshower $E/P > 0$, $npeSum > 11$ for electrons and preshower $E/P > 0.05$, $npeSum < 0.1$ for pions.(Plot generated by M. Cardona.)	115
7.24	The ratio of positrons to the total number of triggers for SHMS positive polarity run 11090. The top left plot shows where the SHMS NGCER very restrictive PID cut ($npe > 11$) was applied, the bottom left and right plots show the calorimeter PID cut ($E/P > 0.8$) position. The number of positrons that passed the PID cuts was calculated.	116
7.25	The ratio of positrons to the total number of triggers for SHMS negative polarity run 11085. The top left plot shows where the SHMS NGCER very restrictive PID cut ($npe > 11$) was applied, the bottom left and right plots show the calorimeter PID cut ($E/P > 0.8$) position. The number of electrons that passed the PID cuts was calculated.	117
7.26	The ratio of positrons to electrons from E12-10-002 experimental data analysis. This data was also compared with the P. Bosted model that shows that the e^+/e^- ratio decreases with higher momentum and smaller spectrometer angle [87].	118
7.27	The computer live times for good SHMS and HMS runs.	119
7.28	Comparison of data (magenta) and simulated yield (black) in z, delta, yp and xp for HMS run 4233 (Kin-C: 20° , -4.0 GeV/c). The upstream window (blue), downstream window (red), ^3He target (green) and the nitrogen gas (yellow) between the beam window and cell upstream window were simulated separately and everything was combined to get the combined simulated yield histogram (black).	122
7.29	The acceptance function is generated in $E' - \theta$ space for HMS Kin-A. The x-axis is the energy of the scattered electron (E') and the y axis is the deviation of scattering angle from the spectrometer's central momentum ($\theta - \theta_0$).	123
7.30	The acceptance function is generated in $E' - \theta$ space for SHMS Kin-Z. The x axis is the energy of the scattered electron (E') and the y axis is the deviation of scattering angle from the spectrometer central momentum ($\theta - \theta_0$).	124
7.31	The one dimensional delta acceptances for different sets of rectangular xp and yp cuts.	125
7.32	The acceptance corrected raw cross-section for HMS Kin-C.	127

7.33	The nitrogen dilution cross-section for HMS Kin-C. (a) Nitrogen cross-section extracted from reference cell data, (b) The nitrogen dilution correction to the raw cross-section.	128
7.34	The measured acceptance corrected radiative cross-section after background subtraction for HMS Kin-C.	129
7.35	Different internal radiative processes that contribute to the inclusive electron scattering [90].	130
7.36	The processes contributing to the measured scattering cross section in experiment E12-06-121 [90].	131
7.37	The elastic and quasi-elastic tail contributions calculated using rc-externals code binned in $E' - \theta$ for HMS Kin-C.	132
7.38	The extracted Born cross-section for HMS Kin-C.	133
7.39	The scattering angle dependence of the measured radiated and Born cross-sections for each E' bin. The error bars are statistical only.	133
7.40	The θ bin centering corrections on Born cross-sections for each E' bin. The error bars are statistical only.	134
7.41	The average of θ bin centered Born cross-sections for each E' bin. The error bars are statistical only.	135
7.42	The average of θ bin centered radiative cross-sections for each E' bin. The error bars are statistical only.	135
7.43	The θ bin centering corrected radiative and Born cross-sections binned in E' for HMS kinematic settings.	136
7.44	The θ bin centering corrected radiative and Born cross-sections binned in E' for SHMS kinematic settings.	137
7.45	The extracted Born cross-sections for HMS kinematic settings. The statistical error on each data point is shown by bars and the systematic errors are shown by gray band. The prediction from the F1F2IN21 model is shown by the blue line on the same plot.	138
7.46	The extracted Born cross-sections for SHMS kinematic settings. The statistical error on each data point is shown by bars and the systematic errors are shown by gray band. The prediction from the F1F2IN21 model is shown by the blue line on the same plot.	139
7.47	The comparison of data yield (magenta) with F1F2IN09 (blue) and F1F2IN21 (green) cross-section models for smaller (HMS Kin-A, 13.5°) and larger (HMS Kin-C, 20°) spectrometer angles.	141
7.48	The Born and Radiative cross-section from F1F2IN21 model as a function of E' for fixed scattering angle, $\theta=13.5^\circ$	142
7.49	The Born and Radiative cross-section weighted yield for HMS Kin-A.	143
7.50	The acceptance uncertainty estimation from variation of scale factors with z , δ , xp and, yp acceptance cuts.	143
1	The target geometry update in rc-externals source code for polarized ^3He target.	150
2	The target input file in rc-externals code that specifies the thickness of all pre target and post target materials.	150

3	The BCM1 and BCM2 gain vs. calibration runs. The yellow bands correspond to $\pm 0.5\%$. This plot was generated by Dave Mack.	152
4	The beam currents with calibration runs taken during the experiment E12-06-121. The yellow bands correspond to $\pm 0.5\%$. This plot was generated by Dave Mack.	152
5	The ratio of BCM1 and BCM2 currents during the data collection period. The runs before 3660 were taken in March, 2020 before the COVID shut down. The ratio changed significantly after the experiment resumed in August, 2020	153

LIST OF TABLES

2.1	List of kinematic variables for electron scattering.	3
3.1	The spin, dimension, and twist of quark and gluon operators.	19
4.1	List of important CEBAF parameters and their respective values.	28
4.2	List of HMS and SHMS design parameters.	33
4.3	The list of HMS and SHMS production kinematic settings.	37
4.4	The definition of the accelerator coordinate system.	38
4.5	The definition of the Hall C coordinate system.	38
4.6	The definition of the spectrometer (HMS and SHMS) coordinate system.	38
4.7	The definition of the target coordinate system.	38
5.1	The systematic uncertainties contributing to the electron beam polarization measurements.	49
6.1	The target chamber window thickness measurement results, volumes of the three chambers and the fill density measurement results for the cells Briana, Tommy, and Austin.	52
6.2	The target cell wall thickness measurement results using the ultrasonic thickness gauge for the target cell Briana.	53
6.3	The target chamber wall thickness measurement results using the ultrasonic thickness gauge for the cells Tommy and Austin.	54
6.4	The temperature corrected ^3He densities in the target chamber of the cells Brianna, Tommy, and Austin.	55
6.5	The characteristics of the main Helmholtz coils.	56
6.6	Systematic uncertainties from the compass mirror alignment.	78
6.7	Helmholtz coil and correction coil settings used during compass measurements for A_1^n kinematic settings with the Helmholtz coils at 45° w.r.t. electron beam direction.	78
6.8	Helmholtz coil and correction coil settings used during compass measurements in March, 2020 for d_2^n kinematic settings with the Helmholtz coils at 0° w.r.t. electron beam direction.	79
6.9	Helmholtz coil and correction coil settings used during compass measurements for d_2^n kinematic setting with the Helmholtz coils at 45° w.r.t. electron beam direction.	79
6.10	Definition of target polarization directions in Hall C.	79
6.11	Helmholtz coil and correction coil settings used during compass measurements in September, 2020 for d_2^n kinematic settings with the Helmholtz coils at 0° w.r.t. electron beam direction.	85
6.12	Helmholtz coil and correction coil settings used during d_2^n production run with the Helmholtz coils at 0° w.r.t. electron beam direction.	86

7.1	The list of HMS and SHMS reference times associated with the detectors.	94
7.2	The list of HMS and SHMS reference time variables in the hcana leaf. . .	95
7.3	The list of final HMS and SHMS reference time cuts.	96
7.4	The list of HMS and SHMS Cherenkov detector variables used in determining the time window cuts.	100
7.5	The list of Cherenkov and calorimeter particle identification results. . . .	115
7.6	The list normalization and correction factors to the HMS yields for Kin-C.	127
7.7	The list of radiation lengths of different materials present in the electron beam path.	131
7.8	List of systematic uncertainty contributions in DIS cross-section extraction.	144
1	The uncertainties in the magnetic field direction measurements for the d_2^n kinematic settings (March, 2020) with Helmholtz coil at 0° w.r.t. beamline	146
2	The uncertainties in the magnetic field direction measurements (October, 2019) with Helmholtz coil at 45° w.r.t. beamline	147
3	The uncertainties in the magnetic field direction measurements for the d_2^n kinematic settings (September, 2020) with Helmholtz coil at 0° w.r.t. beamline	148
4	Extracted radiative cross-section results binned in E' with the corresponding statistical and systematic errors for HMS ($\theta = 13.5^\circ$).	154
5	Extracted radiative cross-section results binned in E' with the corresponding statistical and systematic errors for HMS ($\theta = 20.0^\circ$).	154
6	Extracted Born cross-section results binned in E' with the corresponding statistical and systematic errors for HMS ($\theta = 13.5^\circ$).	154
7	Extracted Born cross-section results binned in E' with the corresponding statistical and systematic errors for HMS ($\theta = 20.0^\circ$).	155
8	Extracted radiative cross-section results binned in E' with the corresponding statistical and systematic errors for SHMS ($\theta = 11.0^\circ$).	155
9	Extracted radiative cross-section results binned in E' with the corresponding statistical and systematic errors for SHMS ($\theta = 18.0^\circ$).	155
10	Extracted Born cross-section results binned in E' with the corresponding statistical and systematic errors for SHMS ($\theta = 11.0^\circ$).	156
11	Extracted Born cross-section results binned in E' with the corresponding statistical and systematic errors for SHMS ($\theta = 18.0^\circ$).	156

Chapter 1 Introduction

The quark model, independently proposed in 1964 by the two physicists Murray Gell-Mann and George Zweig was a classification scheme of hadrons in terms of their constituent valence quarks. Following that in 1968, a series of electron-proton scattering experiments performed by the MIT-SLAC collaboration at the Stanford Linear Accelerator Center (SLAC) revealed that the nucleons have an inner structure. Up until 1980's, the understanding of the nucleon spin was that it is equally distributed among its valence quarks. But, the spin structure of the nucleons became a theoretical crisis after an experiment carried out by the European Muon Collaboration (EMC) in 1987. Contrary to the expectation that the quark spin constitutes 75% of the spin of the nucleon, the experiment revealed that they contributed a small fraction ($\sim 12\%$) of the total spin. This crisis has since resulted in multiple theoretical and experimental research endeavors to crack one of the unsolved problems of physics, popularly known as the “proton spin puzzle”. The current understanding of the nucleon spin is that the total spin is distributed among valence quarks, sea quarks, their orbital angular momenta, and gluons.

Experiment E12-06-121 in Hall C at the Jefferson lab aims to explore the neutron spin structure over a wide kinematic range with very high precision data. Due to the non-perturbative nature of strong interactions, it is extremely difficult to make absolute predictions using the existing theory (Quantum Chromodynamics or QCD) on how the spin is decomposed in all the components. To experimentally investigate the nucleon spin structure, deep inelastic scattering (DIS) is used where the high-energy electrons are scattered inelastically from the nucleons by transferring a virtual photon with momentum Q . In DIS the electrons are scattered elastically from the quarks inside the nucleon by carrying a fraction x of the nucleon momentum, and it provides a measurement of the nucleon structure functions. Two structure functions g_1 and g_2 encode information on the momentum structure and spin structure of the nucleon respectively. This simple two-particle (electron-quark) scattering process is expected to break down at lower energies and momentum transfers because of the quark-gluon correlation. It is yet unknown at which point the correlation process starts. The third moment of the linear combination of g_1 and g_2 , denoted by d_2 , is a clean probe to the quark-gluon correlation.

The experiment aims to do a precision determination of g_2 and d_2 of neutrons which will give insight into the unanswered questions of physics, “How does the quark spin contribute to the overall spin of the nucleon?” and “At what energy does the quark-gluon correlation process start?”

Chapter 2 Electron Scattering

Electron scattering experiments are used to probe the internal structure of atomic nuclei. The binding force of the nucleons within the target are strong compared to the electromagnetic interactions of the electrons with the target and the negligible weak interactions between small masses. This allows the interaction of the electrons with the hadrons to be treated as a single photon exchange process in the simplest picture. Exclusive electron scattering allows us to investigate a single specific physics process by the measurements of the energy and momenta of all the final products. On the other hand, in inclusive electron scattering, only the scattered electron is detected, and it provides information on a collection of processes. The dominant one-photon exchange in the inclusive measurements makes the study of nucleon structure possible with moderate corrections. The kinematics of the inclusive scattering is described in the following.

As shown in Fig. 2.1 the incoming electron with mass m , four-momentum $k = (E, \vec{k})$ and spin four-vector s is scattered from the target nucleus (or nucleon) with mass M , four-momentum $p = (\epsilon, \vec{p})$ and spin four-vector S by exchanging a virtual photon with four-momentum $q = (\nu, \vec{q})$. The scattered electron has four-momentum $k' = (E, \vec{k}')$, spin four-vector s' and the target has final four-momentum $p' = (\epsilon', \vec{p}')$, spin four-vector S' . For a fixed target, the initial four-momenta of the target in the laboratory frame is $p = (M, \vec{0})$. The invariant, $Q^2 \equiv -q^2$ is the spatial resolution of the probe to the nuclear structure. The invariant mass of the unknown target system X after scattering is W with $W^2 \equiv (q + p)^2$, and it describes the final hadronic state. Another invariant, x is known as Bjorken scaling variable, and it is defined as the fraction of nucleon momentum carried by the constituent, struck quark in the infinite

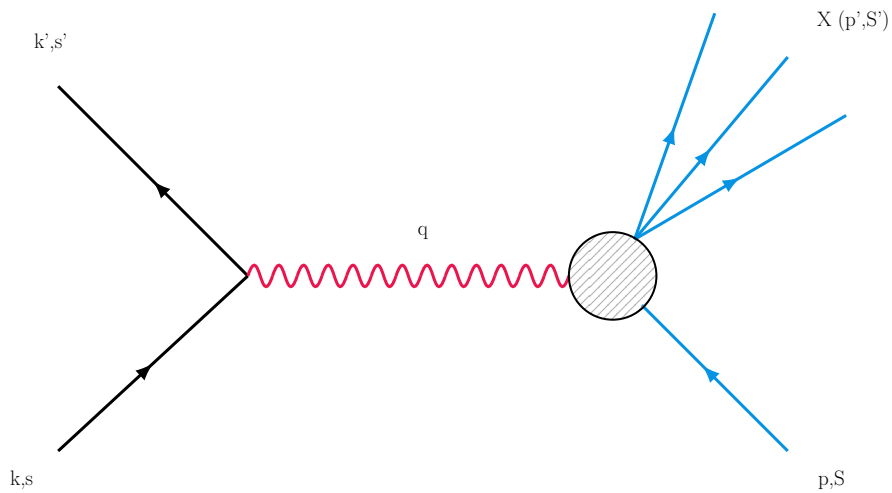


Figure 2.1: First order diagram for lepton-hadron scattering.

momentum frame (nucleon momentum infinite in the direction of \vec{q}) at large Q^2 . The kinematic factors and the relativistic invariants of electron scattering are listed in Table. 2.1.

Table 2.1: List of kinematic variables for electron scattering.

Kinematic Variable	Expression (Lab Frame)	Expression (Invariant)	Definition
k	(E, \vec{k})		four-momentum of incident electron
k'	(E, \vec{k}')		four-momentum of scattered electron
p	$(M, \vec{0})$		four-momentum of initial fixed target
p'	(ϵ', \vec{p}')		four-momentum of scattered target
θ			electron scattering angle
q	$k - k'$		four-momentum transfer
ν	$E - E'$		energy transfer
Q^2	$4EE' \sin^2(\frac{\theta}{2})$	$-q^2$	virtuality of exchanged photon
W^2	$M^2 + 2M\nu - Q^2$	$M^2 + p \cdot q + q^2$	invariant mass of target after scattering
x	$\frac{Q^2}{2M\nu}$	$\frac{Q^2}{2p \cdot q}$	Bjorken variable
y	$\frac{\nu}{E}$	$\frac{q \cdot p}{k \cdot p}$	fraction of electron energy loss
X			unknown final hadronic state

Depending on the momentum (Q) and energy transfer (ν) by the virtual photon, compared to the same of the incident particle, the electron scattering can be classified in the following way.

- **Elastic scattering:** The elastic scattering happens at very low Q^2 , ν and $W^2 = M^2$. The electron scatters from the target nucleus elastically by leaving the nucleus intact. The nucleons inside the target share the momentum transfer and the spatial resolution is very low to probe the structure of the nucleus. The invariant mass is given by $W^2 \equiv M^2 + 2M\nu - Q^2$ with very low Q^2 and ν , where M is the mass of the target nucleus.
- **Quasi-elastic scattering:** The quasi-elastic scattering occurs at $\nu >$ nuclear binding energy, and $W^2 = M_n^2$. The electron scatters from the target nucleus

with energy transfer greater than the nuclear binding energy. The nucleons obey the Fermi gas model where they behave as quasi-free fermions in a constant potential well. Several calculations of quasielastic scattering were done using the Fermi gas model by Moniz [1], the harmonic oscillator shell model by de Forest [2], the square well shell model by Donnelly [3] and the Woods-Saxon shell model by Klawansky [4] [5]. However, for large momentum and energy transfers the Fermi gas model is applied as it agreed very well with the experiments.[7] In this case the electron elastically scatters from the nucleon with mass M_n and momenta of 55-250 MeV/c due to the “Fermi motion” inside the target. The invariant mass is given by $W^2 \equiv M_n^2 + 2M_n\nu - Q^2$ with energy loss of electron, $\nu = \frac{Q^2}{2M_n}$.

- **Nucleon resonances:** The nucleon resonances happen when Q^2 and ν increases to give $W^2 = M_{n^*}^2$. When the electron scatters from the nucleon, the nucleon gets excited to the state called the “nucleon resonance” by absorbing the virtual photon. In this case, the internal structure of the nucleon is explored and the invariant mass is given by $W^2 = M_{n^*}^2$ where M_{n^*} is the mass of the nucleon resonance. The resonances occur in the region $1.2 < W < 2.0$ GeV/c². The first resonance, $\Delta(1232)$ has mass, $M_\Delta = 1232$ MeV/c², total spin, $J = \frac{3}{2}$ and it consists of three quarks with their spins aligned in the same direction. Higher resonances occur beyond $W > 1.4$ GeV/c² with overlapping tails.
- **Deep inelastic scattering (DIS):** The deep inelastic scattering occurs at very large Q^2 , ν , and $W^2 > 2.0$ (GeV/c)². The electron scatters from an asymptotically free quark (or antiquark) inside the nucleon. At very high Q^2 and ν , the nucleon is viewed as a collection of partons and this region is known as the Deep inelastic region. In this region,

$$W^2 \geq M_n^2 \Rightarrow M_n^2 + 2p \cdot q + q^2 \geq M_n^2 \quad (2.1)$$

$$\Rightarrow M_n^2 + 2p \cdot q - Q^2 \geq M_n^2 \quad (2.2)$$

$$\Rightarrow \frac{Q^2}{2p \cdot q} \leq 1. \quad (2.3)$$

The Bjorken variable x is defined as,

$$x = \frac{Q^2}{2p \cdot q}. \quad (2.4)$$

For a fixed (at rest) nucleon target,

$$x = \frac{Q^2}{2M_n\nu}. \quad (2.5)$$

Since $Q^2, \nu \geq 0$, using Eq. 2.1, Eq. 2.4 and, Eq. 2.4 we have,

$$0 \leq x \leq 1 \quad (2.6)$$

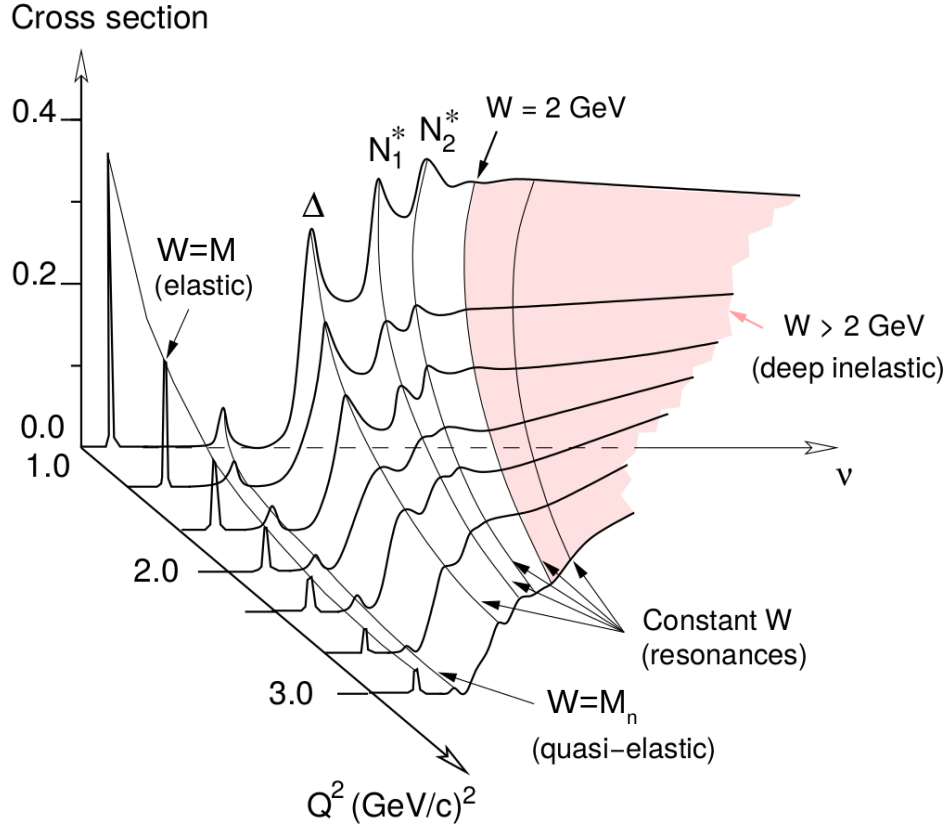


Figure 2.2: The cross section (arbitrary units) spectrum for the electron scattering from a nuclear target. The different peaks for the elastic, quasi-elastic, resonance regions are shown in the $Q^2 - \nu$ plane. In case of a nucleon target, only the elastic peak occurs for $W = M_n$ before the resonances.[10]

The scattering cross section is a measure of probability of interaction between the incident electron and the target nucleon. The differential cross section is defined as the rate of scattered particles in solid angle $d\Omega$ in the direction (θ, ϕ) divided by the incident flux. The incident flux Φ_{in} is the number of incident electrons per unit area dA per unit time dt on the target. The total cross section is calculated by integrating the differential cross section $(\frac{d\sigma}{d\Omega})$ over the solid angle.

$$\frac{d\sigma}{d\Omega}(\theta, \phi) = \frac{N}{\Phi_{in}} \quad (2.7)$$

$$\sigma = \int \frac{d\sigma}{d\Omega} d\Omega \quad (2.8)$$

$$= \int_0^{2\pi} d\phi \int_0^\pi \frac{d\sigma}{d\Omega}(\theta, \phi) \sin(\theta) d\theta. \quad (2.9)$$

In Fig. 2.2 the cross section spectrum for all four electron scattering regions is shown in arbitrary units. The deep inelastic scattering formalism will be described in details in Section 2.1 as our experiment was performed in the DIS region.

2.1 Scattering Formalism

In scattering experiments in which the double differential cross section is measured, the cross section is extracted as a function of three independent variables- the energy, E' of the scattered electron and the electron scattering angle, Ω (θ, ϕ). However, for many cases the cross section is independent of the azimuthal angle ϕ which implies, $\frac{d^2\sigma}{d\Omega dE'}$ is a function of (E', θ) only. The allowed kinematic region for DIS is shown in Fig. 2.3 by the shaded region and it requires,

$$0 \leq x \leq 1 \quad (2.10)$$

$$0 \leq \theta \leq \pi \quad (2.11)$$

$$0 \leq \nu \leq E. \quad (2.12)$$

In the Fig. 2.3, the constant x lines are straight lines passing through the origin because it is given by,

$$\begin{aligned} x &= \frac{Q^2}{2M_n\nu} \\ &= \frac{Q^2}{2M_nE} \\ &= \frac{\nu}{E}. \end{aligned}$$

The constant θ lines are straight lines intersecting the $\frac{\nu}{E}$ axis at 1 and the $\frac{Q^2}{2M_nE}$ axis at $\frac{E}{M_n}(1 - \cos \theta)$ because,

$$Q^2 = 2EE'(1 - \cos \theta) \Rightarrow \frac{Q^2}{2M_nE} = \frac{E'}{M_n}(1 - \cos \theta) \quad (2.13)$$

$$= \frac{1}{M_n}(E - \nu)(1 - \cos \theta) \quad (2.14)$$

$$= \left(1 - \frac{\nu}{E}\right) \left[\frac{E}{M_n}(1 - \cos \theta)\right]. \quad (2.15)$$

We also see that, for a fixed electron beam energy (E) and fixed x , the maximum value of Q^2 for DIS is determined by the intersection of the fixed x line and $\theta=\pi$ line which is,

$$Q_{max}^2 = 2M_nEx \left(\frac{2E}{2E + M_nx}\right). \quad (2.16)$$

The scattering amplitude for the scattering shown in Fig. 2.1 is written as,

$$i\mathcal{M} = (-ie)^2 \left(\frac{-ig_{\mu\nu}}{q^2}\right) \langle k', s' | j^\mu(0) | k, s \rangle \langle p', S' | J_\mu(0) | p, S \rangle. \quad (2.17)$$

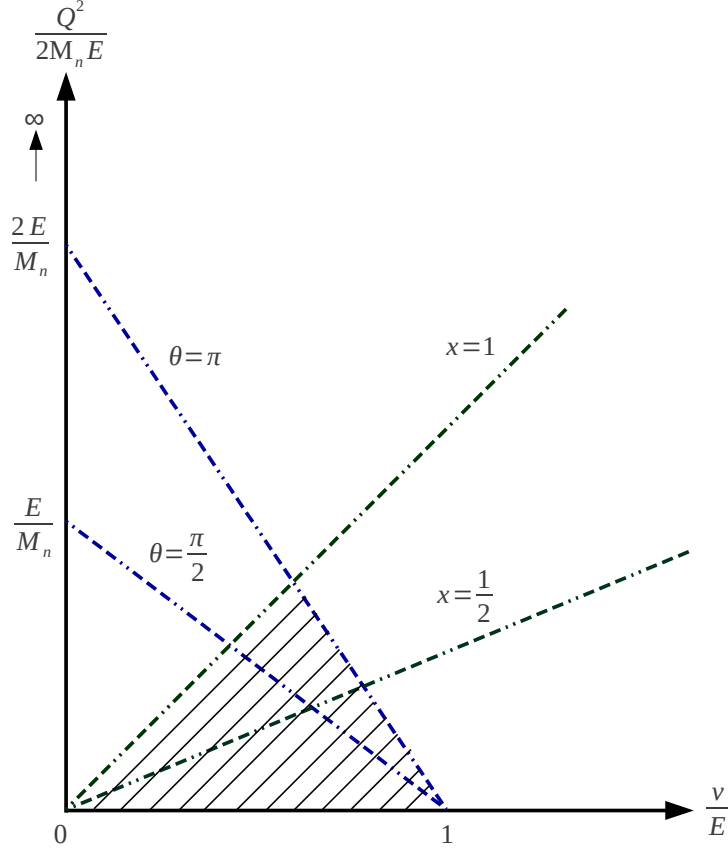


Figure 2.3: Kinematically allowed region for Deep Inelastic Scattering (shown by shaded region). The maximum value of Q^2 is bound by fixed x values [11].

where j^μ and J_μ are the leptonic and hadronic electromagnetic currents respectively [8][9][10]. In case of inclusive scattering, the polarization of the final lepton and hadron states are not measured. Summing over the final polarization states, the differential cross-section in the laboratory frame is written as,

$$\begin{aligned}
 d\sigma &= \sum_X \int \frac{d^3k'}{(2\pi)^3 2E'} (2\pi)^4 \delta^4(k + p - k' - p') \frac{|\mathcal{M}|^2}{4M_n E} \\
 &= \sum_X \int \frac{d^3k'}{(2\pi)^3 (2E')(4M_n E)} (2\pi)^4 \delta^4(k + p - k' - p') \frac{e^4}{q^4} \\
 &\quad \langle p, S | J^\mu(0) | p' \rangle \langle p, S | J^\nu(0) | p' \rangle^* \langle k, s | j_\mu(0) | k' \rangle \langle k, s | j_\nu(0) | k' \rangle^* . \quad (2.18)
 \end{aligned}$$

The leptonic and hadronic currents are hermitian,

$$\langle p, S | J^\nu(0) | p' \rangle^\dagger = \langle p' | J^\nu(0) | p, S \rangle \quad (2.19)$$

$$\langle k, s | j^\nu(0) | k' \rangle^\dagger = \langle k' | j^\nu(0) | k, s \rangle . \quad (2.20)$$

Using Eq. 2.18 and Eq. 2.19, the differential cross-section can be written as,

$$d\sigma = \sum_X \int \frac{d^3k'}{(2\pi)^3(2E')(4M_n E)} (2\pi)^4 \delta^4(k + p - k' - p') \frac{e^4}{q^4} \langle p, S | J^\mu(0) | p' \rangle \langle p' | J^\nu(0) | p, S \rangle \langle k, s | j_\mu(0) | k' \rangle \langle k' | j_\nu(0) | k, s \rangle. \quad (2.21)$$

Conventionally the leptonic ($l_{\mu\nu}$) and the hadronic tensors ($W_{\mu\nu}$) are defined as the following,

$$l^{\mu\nu} = \sum_{s'} \langle k' | j^\nu(0) | k, s \rangle \langle k, s | j^\mu(0) | k' \rangle \quad (2.22)$$

$$W^{\mu\nu}(p, q) = \frac{1}{4\pi} \int d^4x e^{iq \cdot x} \langle p, S' | [J^\mu(x), J^\nu(0)] | p, S \rangle. \quad (2.23)$$

By inserting a complete set of states $\sum_X |X\rangle\langle X|$ in Eq. 2.23 we get,

$$W^{\mu\nu}(p, q) = \frac{1}{4\pi} \sum_X \int d^4x e^{iq \cdot x} [\langle p, S' | J^\mu(x) | X \rangle \langle X | J^\nu(0) | p, S \rangle - \langle p, S' | J^\nu(0) | X \rangle \langle X | J^\mu(x) | p, S \rangle]. \quad (2.24)$$

Using translation invariance in Eq. 2.24,

$$W^{\mu\nu}(p, q) = \frac{1}{4\pi} \sum_X [(2\pi)^4 \delta^4(q + p - p') \langle p, S' | J^\mu(0) | X \rangle \langle X | J^\nu(0) | p, S \rangle - (2\pi)^4 \delta^4(q + p' - p) \langle p, S' | J^\nu(0) | X \rangle \langle X | J^\mu(0) | p, S \rangle]. \quad (2.25)$$

The second delta function in Eq. 2.25 becomes zero because $p_X^0 > p^0$ and $q^0 > 0$ and the expression of $W^{\mu\nu}$ becomes the hadronic current part of Eq. 2.21. So, in the laboratory frame, the differential cross section for detecting the scattered electron in a solid angle $d\omega$ with the energy between E' and $E' + dE'$ is given by,

$$\frac{d^2\sigma}{d\Omega dE'} = \frac{\alpha^2}{2M_n q^4} \frac{E'}{E} l_{\mu\nu} W^{\mu\nu}, \quad (2.26)$$

where α is the fine structure constant.

The leptons are pointlike fermions and the leptonic tensor $l_{\mu\nu}$ is computed as,[11]

$$l_{\mu\nu} = \sum_{s'} [\bar{u}(k', s') \gamma_\mu u(k, s)]^* [\bar{u}(k', s') \gamma_\nu u(k, s)] \quad (2.27)$$

$$\simeq 2(k_\mu k'_\nu + k_\nu k'_\mu - g_{\mu\nu} k \cdot k' - i\epsilon_{\mu\nu\alpha\beta} q^\alpha s^\beta) \quad (2.28)$$

$$= 2l_{\mu\nu}^{(S)} + 2il_{\mu\nu}^{(A)}, \quad (2.29)$$

where the spin independent part (symmetric in μ, ν) is $l_{\mu\nu}^{(S)} = k_\mu k'_\nu + k_\nu k'_\mu - g_{\mu\nu} k \cdot k'$ and the spin dependent part (antisymmetric in μ, ν) is $l_{\mu\nu}^{(A)} = \epsilon_{\mu\nu\alpha\beta} q^\alpha s^\beta$. For unpolarized electron scattering, averaging over the initial spin state s , we have $l_{\mu\nu} = 2l_{\mu\nu}^{(S)}$.

On the other hand, the hadronic tensor cannot be computed trivially and it is defined similar to the leptonic tensor as,

$$W_{\mu\nu}(q; p, S) = W_{\mu\nu}^{(S)}(q; p) + iW_{\mu\nu}^{(A)}(q; p, S), \quad (2.30)$$

where the two terms in the Eq. 2.30 are,

$$\begin{aligned} \frac{1}{2M_n} W_{\mu\nu}^{(S)}(q; p) = & \left(-g_{\mu\nu} + \frac{q_\mu q_\nu}{q^2} \right) W_1(p \cdot q, q^2) \\ & + \left[\left(p_\mu - \frac{p \cdot q}{q^2} q_\mu \right) \left(p_\nu - \frac{p \cdot q}{q^2} q_\nu \right) \right] \frac{W_2(p \cdot q, q^2)}{M_n^2} \end{aligned} \quad (2.31)$$

$$\begin{aligned} \frac{1}{2M_n} W_{\mu\nu}^{(A)}(q; p, S) = & \epsilon_{\mu\nu\alpha\beta} q^\alpha M_n S^\beta G_1(p \cdot q, q^2) \\ & + \epsilon_{\mu\nu\alpha\beta} q^\alpha [(p \cdot q) S^\beta - (S \cdot q) p^\beta] \frac{G_2(p \cdot q, q^2)}{M_n}. \end{aligned} \quad (2.32)$$

This is the most general expression for the hadronic tensor satisfying the following constraints.[11]

- Strong interactions are parity invariant, and this implies that $W_{\mu\nu}$ should be invariant under parity transformation.
- $W_{\mu\nu}$ should be invariant under time reversal.
- The hadronic current conservation, $\delta_\mu J^\mu(x) = 0$ implies,

$$q_\mu W^{\mu\nu}(p, q, S) = q_\nu W^{\mu\nu}(p, q, S) = 0.$$

For a spin- $\frac{1}{2}$ target, $W_{\mu\nu}^{(S)}(q; p)$ and $W_{\mu\nu}^{(A)}(q; p, S)$ are the spin-independent, symmetric and spin-dependent, antisymmetric parts of $W_{\mu\nu}$, respectively. W_1 , W_2 are called the spin averaged or unpolarized structure functions that provide information about the momentum structure of the nucleon. G_1 , G_2 are known as spin dependent or polarized structure functions which contain information about the spin structure of the nucleon. These four structure functions effectively parametrize the unknown hadronic structure.

2.2 The Unpolarized Structure Functions

The differential cross-section in the Eq. 2.26 can be written in terms of measurable quantities as following,

$$\frac{d^2\sigma}{d\Omega dE'} = \frac{\alpha^2}{2M_n q^4} \frac{E'}{E} \left(2l_{\mu\nu}^{(s)} W^{\mu\nu(s)} - 2l_{\mu\nu}^{(A)} W^{\mu\nu(A)} \right). \quad (2.33)$$

If both the electron and the target nucleon are unpolarized, the cross-section in Eq. 2.33 has to be averaged over the initial spin states (s, S) and the unpolarized cross-section is obtained.

$$\frac{d^2\sigma^{unpol}}{d\Omega dE'} = \frac{\alpha^2}{2M_n q^4} \frac{E'}{E} 2l_{\mu\nu}^{(s)} W^{\mu\nu(s)}. \quad (2.34)$$

When unpolarized relativistic electrons scatter from an infinitely heavy, point-like, spin- $\frac{1}{2}$ target, the cross-section is called the Mott cross-section. In this case the electron mass and target recoil are neglected. Using Feynman's rules, the Mott cross section is obtained as the following,

$$d\sigma^{Mott} = \frac{1}{v_{rel}} \frac{2\pi}{E} |\mathcal{M}|^2 \frac{1}{(2\pi)^3} k E d\Omega \quad (2.35)$$

$$= \frac{2\pi}{E} \left[\frac{4\pi e^2}{4E^2 \sin^2(\frac{\theta}{2})} \bar{u}(k') \gamma_\mu u(k) \right]^2 \frac{1}{(2\pi)^3} k E d\Omega. \quad (2.36)$$

Where, $v_{rel} = \frac{k}{E} \approx 1$. Finally,

$$\frac{d\sigma^{Mott}}{d\Omega} = \frac{\alpha^2 \cos^2 \frac{\theta}{2}}{4E^2 \sin^4 \frac{\theta}{2}}. \quad (2.37)$$

In our case, the target is not point-like and it has internal structure. Using Eq. 2.34, Eq. 2.37 and, Eq. 2.31, the unpolarized cross-section is factorized as,

$$\frac{d^2\sigma^{Unpol}}{d\Omega dE'} = \frac{d\sigma^{Mott}}{d\Omega} \left[W_2(p, q, q^2) + 2W_1(p, q, q^2) \tan^2 \frac{\theta}{2} \right]. \quad (2.38)$$

Where the first Mott cross-section term describes the point-like target and the second part containing the structure functions W_1 and W_2 characterizes the internal nucleon structure. The structure functions W_1 and W_2 are functions of the energy (ν) and momentum (Q^2) transferred by the virtual photon. They are commonly redefined as,

$$F_1(x, Q^2) = M_n W_1(\nu, Q^2) \quad (2.39)$$

$$F_2(x, Q^2) = \nu W_2(\nu, Q^2). \quad (2.40)$$

The unpolarized cross-section in Eq. 2.38 can be expressed in terms of the structure functions F_1 and F_2 as,

$$\frac{d^2\sigma^{Unpol}}{d\Omega dE'} = \frac{d\sigma^{Mott}}{d\Omega} \left[\frac{1}{\nu} F_2(x, Q^2) + \frac{2}{M_n} F_1(x, Q^2) \tan^2 \frac{\theta}{2} \right]. \quad (2.41)$$

For a nuclear target with mass number A , F_1 and F_2 are the structure functions over the nucleus. There is another definition of structure function per nucleon as, $F'_1 = F_1/A$ and $F'_2 = F_2/A$. In my dissertation, I will be using the first definition of the unpolarized structure functions.

2.3 The Polarized Structure Functions

When both the incident electron and the target nucleon are polarized, the polarized cross-section is expressed as the difference of cross-sections with opposite target spins (the target spin is \vec{S} or $-\vec{S}$ in arbitrary direction) with fixed electron spin direction or, as the difference of cross-sections with opposite electron spins with fixed target spin direction. In the polarized case, the Eq. 2.33 with opposite target spins results in the following equation.

$$\sum_{s'} \left[\frac{d^2\sigma}{d\Omega dE'}(k, s, p, S; k', s') - \frac{d^2\sigma}{d\Omega dE'}(k, s, p, -S; k', s') \right] = \frac{2\alpha^2}{M_n q^4} \frac{E'}{E} l_{\mu\nu}^{(A)} W^{\mu\nu(A)}. \quad (2.42)$$

The Eq. 2.42 can be rewritten using Eq. 2.32 as the following.

$$\begin{aligned} \frac{d^2\sigma_{s,S}}{d\Omega dE'} - \frac{d^2\sigma_{s,-S}}{d\Omega dE'} = \frac{8m\alpha^2 E'}{q^4 E} & \left[\left\{ (q \cdot S)(q \cdot s) + Q^2(s \cdot S) \right\} M_n G_1(p \cdot q, Q^2) \right. \\ & \left. + \left\{ Q^2(s \cdot S)(p \cdot q) - (q \cdot S)(p \cdot s) \right\} \frac{G_2(p \cdot q, Q^2)}{M_n} \right]. \end{aligned} \quad (2.43)$$

Similar to the unpolarized structure functions, the spin structure functions G_1 and G_2 are also functions of the energy (ν) and momentum (Q^2) transfer by the virtual photon and they access the antisymmetric part of the hadronic tensor. They are most commonly expressed as,

$$g_1(x, Q^2) = M_n^2 \nu G_1(\nu, Q^2) \quad (2.44)$$

$$g_2(x, Q^2) = M_n \nu^2 G_2(\nu, Q^2). \quad (2.45)$$

To access the polarized cross-section in our experiment, the electrons were always polarized in the longitudinal direction i.e. the spin of the electrons were either parallel or antiparallel to their momentum and they were scattered from the polarized nucleons at rest in the laboratory frame. If the electrons are transversely polarized ($\hat{s} \perp \hat{k}$, $\hat{s} \cdot \hat{k} = 0$), the \vec{s} does not change as it is perpendicular to the direction of boost. So, there is no factor of $\frac{E}{m}$ that can cancel the factor $\frac{m}{E}$ in the expression of the cross-section difference in Eq. 2.43. In the high energy limit, $\frac{m}{E} \rightarrow 0$, which results in a zero cross-section difference. For longitudinally polarized electron, the spin four-vector is defined as,

$$s_{\rightarrow}^{\mu} = -s_{\leftarrow}^{\mu}. \quad (2.46)$$

The spin four-vector of the target nucleon at rest is defined as,

$$S^{\mu} = (0, \vec{S}). \quad (2.47)$$

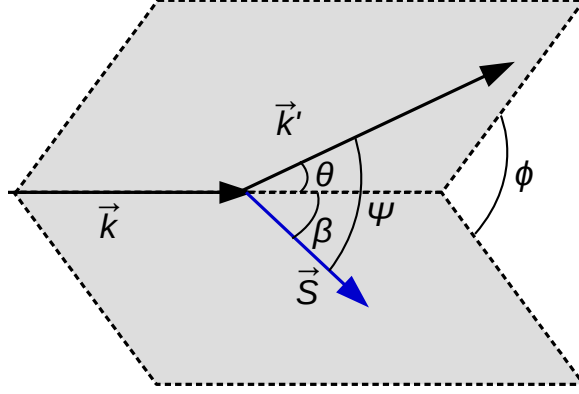


Figure 2.4: Electron scattering plane and relevant angles.

Eq. 2.43 is rewritten as the following,

$$\begin{aligned}
& \frac{d^2\sigma_{\rightarrow,S}}{d\Omega dE'} - \frac{d^2\sigma_{\rightarrow,-S}}{d\Omega dE'} \\
&= -\frac{4\alpha^2 E'}{Q^2 E} \left[\frac{(\vec{k}' \cdot \vec{S} + \vec{k} \cdot \vec{S})}{M_n \nu} g_1(x, Q^2) + \frac{2(E\vec{k}' \cdot \vec{S} - E'\vec{k} \cdot \vec{S})}{M_n \nu^2} g_2(x, Q^2) \right] \\
&= -\frac{4\alpha^2 E'}{Q^2 E} \left[\frac{1}{M_n \nu} (E \cos \psi + E' \cos \theta) g_1(x, Q^2) + \frac{2EE'}{M_n \nu^2} (\cos \theta - \cos \psi) g_2(x, Q^2) \right],
\end{aligned} \tag{2.48}$$

where θ is the electron scattering angle, ϕ is the azimuthal angle, β is the angle between the incident electron momentum and nucleon spin, and ψ is the angle between the scattered electron and the nucleon spin, so that,

$$\cos \psi = \sin \theta \sin \beta \cos \phi + \cos \theta \cos \beta. \tag{2.49}$$

The scattering plane, polarization plane and the angles are displayed in Fig. 2.4. In experiment E12-06-121, the nucleon spin was either longitudinal (\Rightarrow, \Leftarrow) or transverse (\Uparrow, \Downarrow) to the electron momentum, so that the angle β could have only four values: $0^\circ, 180^\circ, 90^\circ, 270^\circ$. This results in the longitudinal and transverse polarized cross-sections respectively as the following.

- $\beta = 0^\circ, 180^\circ$

$$\frac{d^2\sigma_{\rightarrow,\Rightarrow}}{d\Omega dE'} - \frac{d^2\sigma_{\rightarrow,\Leftarrow}}{d\Omega dE'} = -\frac{4\alpha^2 E'}{Q^2 E M_n \nu} \left[(E + E' \cos \theta) g_1(x, Q^2) - \frac{Q^2}{\nu} g_2(x, Q^2) \right] \tag{2.50}$$

- $\beta = 90^\circ, 270^\circ$

$$\frac{d^2\sigma_{\rightarrow,\Uparrow}}{d\Omega dE'} - \frac{d^2\sigma_{\rightarrow,\Downarrow}}{d\Omega dE'} = -\frac{4\alpha^2 E^2}{Q^2 E M_n \nu} \left[g_1(x, Q^2) + \frac{2E}{\nu} g_2(x, Q^2) \right] \sin \theta \cos \phi. \tag{2.51}$$

In Eq. 2.51 we can see that the transverse polarized cross-section is a maximum for $\phi = 0^\circ$ or, $\phi = 180^\circ$ and hence the target nucleon was always polarized in the scattering plane. However, the measurement of the polarized cross-section difference is difficult which makes the extraction of spin structure functions g_1 and g_2 more time consuming. There is a simpler way to study the g_1 and g_2 by the measurement of the double spin asymmetries (A_{\parallel} , A_{\perp}) and the unpolarized cross-section using the following relations.

$$g_1 = \frac{M_n Q^2}{4\alpha^2} \frac{2y}{(1-y)(2-y)} \frac{d^2\sigma^{Unpol}}{d\Omega dE'} \left[A_{\parallel} + \tan\left(\frac{\theta}{2}\right) A_{\perp} \right] \quad (2.52)$$

$$g_2 = \frac{M_n Q^2}{4\alpha^2} \frac{2y}{(1-y)(2-y)} \frac{d^2\sigma^{Unpol}}{d\Omega dE'} \left[-A_{\parallel} + \frac{1 + (1-y)\cos\theta}{(1-y)\sin\theta} A_{\perp} \right]. \quad (2.53)$$

The electron asymmetries are explained in more detail in the next section.

2.4 The Electron Asymmetries

The double spin asymmetries arise when both the incident electron and the target nucleon are polarized. The two types of electron asymmetries are described below.

Longitudinal electron asymmetry When the electron and nucleon spins are either parallel or antiparallel to each other, the longitudinal electron asymmetry is defined in terms of the longitudinal polarized cross-section differences ($\sigma^{\rightarrow\rightarrow}$, $\sigma^{\leftarrow\rightarrow}$) as,

$$A_{\parallel} \equiv \frac{\sigma^{\rightarrow\rightarrow} - \sigma^{\leftarrow\rightarrow}}{\sigma^{\rightarrow\rightarrow} + \sigma^{\leftarrow\rightarrow}} = \frac{1}{2} \frac{(\sigma^{\rightarrow\rightarrow} - \sigma^{\leftarrow\rightarrow})}{\frac{d^2\sigma^{Unpol}}{d\Omega dE'}}. \quad (2.54)$$

Transverse electron asymmetry When the electron is longitudinally polarized and the nucleon is transversely polarized, the transverse electron asymmetry is defined in terms of the transverse polarized cross-section differences ($\sigma^{\rightarrow\uparrow}$, $\sigma^{\leftarrow\downarrow}$) as,

$$A_{\perp} \equiv \frac{\sigma^{\rightarrow\uparrow} - \sigma^{\leftarrow\downarrow}}{\sigma^{\rightarrow\uparrow} + \sigma^{\leftarrow\downarrow}} = \frac{1}{2} \frac{(\sigma^{\rightarrow\uparrow} - \sigma^{\leftarrow\downarrow})}{\frac{d^2\sigma^{Unpol}}{d\Omega dE'}}. \quad (2.55)$$

The measurement of asymmetries is a relative measurement that results in cancellation of several systematic uncertainties while taking the ratio. Also, it is easy to control the electron polarization directions during the experiment. These factors make the extraction of the spin-structure functions from the asymmetry measurement less complicated.

2.5 Bjorken Scaling in One-Photon Exchange DIS

The electron scattering from the nucleon occurs by exchanging a virtual photon and that photon acts as a probe to the internal hadronic structure. The higher the momentum (Q^2) and the energy transfer (ν) is, the nucleon substructure is explored

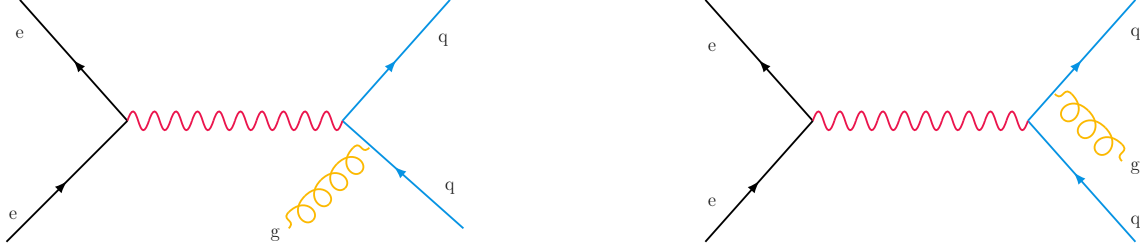


Figure 2.5: Examples of higher order radiative processes that contribute with the dominating one-photon exchange process in DIS.

with higher resolution ($\lambda \sim \frac{1}{\sqrt{Q^2}}$). In the case of deep inelastic scattering where the Q^2 and ν are very high, the electrons seem to scatter from the free quarks inside the nucleon. If the Q^2 and ν are increased further, the spatial resolution does not change anymore because the quarks are point-like, fundamental particles. This results in a scaling behavior of the structure functions in the Bjorken limit defined as,

$$Q^2 \rightarrow \infty \text{ and } \nu \rightarrow \infty, \text{ with fixed Bjorken } x = \frac{Q^2}{2M_n\nu} .$$

In this limit, the structure functions become independent of Q^2 and only depend on x , so that,

$$\begin{aligned} F_1(x, Q^2) &\rightarrow F_1(x) \\ F_2(x, Q^2) &\rightarrow F_2(x) \\ g_1(x, Q^2) &\rightarrow g_1(x) \\ g_2(x, Q^2) &\rightarrow g_2(x). \end{aligned}$$

This leads to the Callon-Gross relation [13] which is,

$$F_2(x) = 2xF_1(x). \quad (2.56)$$

This phenomenon is referred to as Bjorken scaling, first predicted by Bjorken and Paschos [14]. This scaling behavior of the structure functions is only exact for the one-photon exchange or the first-order approximation in α (Fig. 2.1) of the deep inelastic scattering.

2.6 Scaling Violation

In reality, Q^2 is finite and several higher order interactions contribute to the one-photon exchange process in DIS. In these processes, both the initial and scattered quarks emit gluons and the gluon radiation cannot be separated from the main one-photon exchange cross-section. In the Fig. 2.5, two leading order radiative contributions are illustrated. In order to take into account the radiative correction, the higher order terms are added to the first-order approximation that results in the scaling violation i.e. the cross-section now has a logarithmic dependence on Q^2 . The Q^2 evolution of the unpolarized structure function F_2 at different x values for proton is

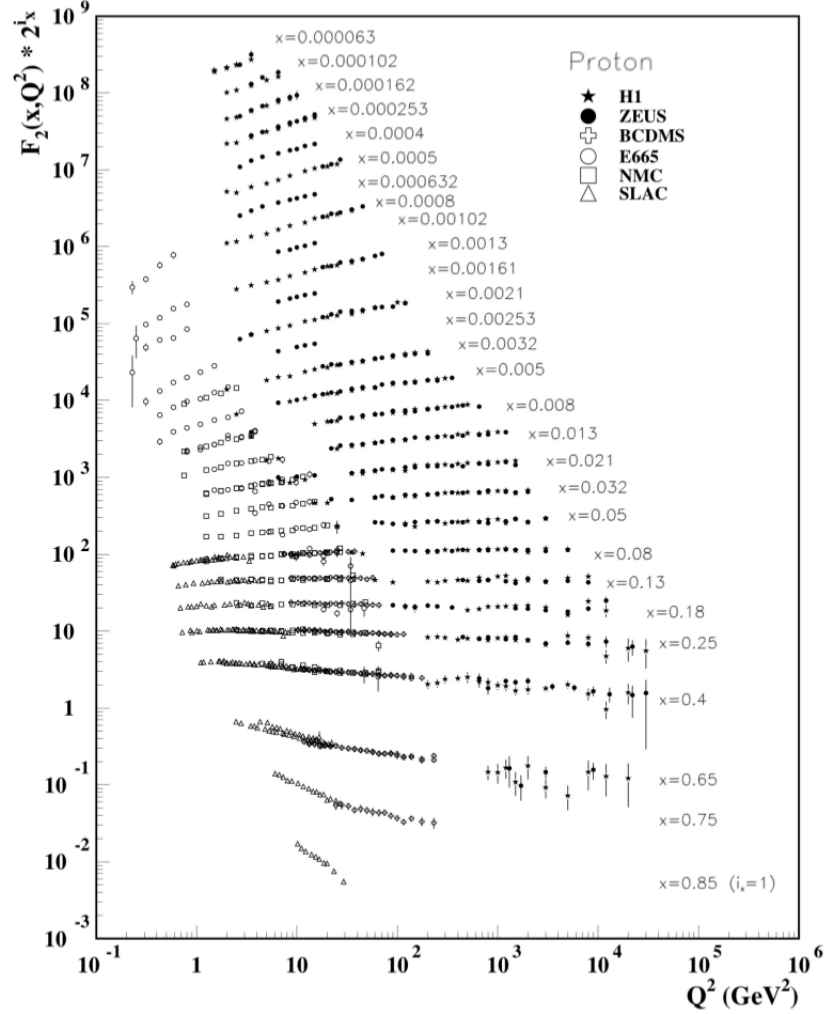


Figure 2.6: Q^2 evolution of $F_2^p(x, Q^2)$ at different x that shows scaling violation. [15]

shown in Fig. 2.6. So for higher energies, if the structure function is measured at any Q^2 for a particular x value, the structure function can be evolved in Q^2 very easily using its logarithmic dependence.

2.7 The Structure Functions in the Naive Parton Model

The structure functions can be understood physically in terms of the naive parton model developed by Feynman [16]. In this model, the nucleon is viewed as a collection of non-interacting, point-like constituents called partons. This model supports the scaling behavior of the structure functions predicted by Bjorken, which is, the nucleon must contain point-like objects to make the cross-section independent of the four-momentum transfer, Q^2 . The parton model assumes,

- The lepton scatters from an individual parton inside the nucleon (Fig. 2.7) and by simply adding the weighted cross-sections from the individual lepton-parton

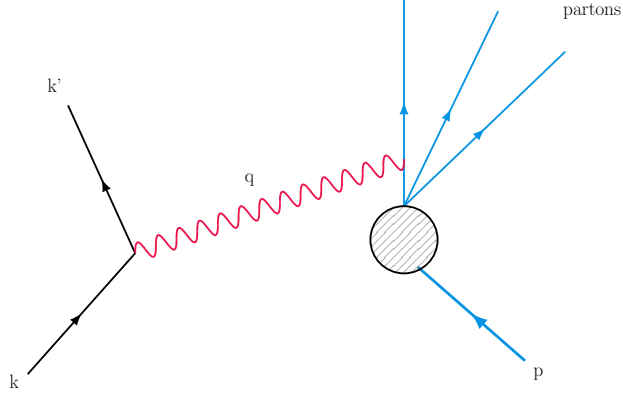


Figure 2.7: Electron scattering from an individual parton in the Naive Parton Model.

scattering, the total cross-section can be obtained.

- In the infinite momentum frame of the nucleon during scattering, the rest mass and transverse momenta of the partons are negligible compared to their longitudinal momenta. Hence, with the assumption of negligible parton masses,

$$\begin{aligned}
 (p_{parton} + q)^2 &\approx 0 \\
 \Rightarrow p_{parton}^2 + 2p_{parton} \cdot q - Q^2 &\approx 0 \\
 \Rightarrow M_{parton}^2 + 2p_{parton} \cdot q - Q^2 &\approx 0 \\
 \Rightarrow 2p_{parton} \cdot q &= Q^2 \\
 \Rightarrow \frac{2p_{parton} \cdot q}{2p \cdot q} &= \frac{Q^2}{2p \cdot q} \\
 \Rightarrow p_{parton} &= xp
 \end{aligned}$$

Based on the above expression, the Bjorken x is defined as the fraction of nucleon momentum (p) carried by the struck parton in the infinite momentum frame.

In the parton model, the unpolarized and polarized structure functions can be interpreted as the weighted average of parton distribution functions (PDF). In the case of unpolarized scattering, the spin averaged parton distribution function for each parton i can be defined as,

$$q_i(x) = q_i^\uparrow(x) + q_i^\downarrow(x) ,$$

where $q_i^\uparrow(x)/q_i^\downarrow(x)$ is defined as the probability that the spin of the i^{th} quark is parallel/anti-parallel to the nucleon momentum when it carries a fraction x of the nucleon momentum.

The unpolarized structure function $F_1(x)$ is defined as the charge weighted average of the spin-independent parton distribution functions.

$$F_1(x) = \frac{1}{2} \sum_i e_i^2 q_i(x) = \frac{1}{2} \sum_i e_i^2 \left(q_i^\uparrow(x) + q_i^\downarrow(x) \right). \quad (2.57)$$

Using the Callon-Gross relation in Eq. 2.56, the second unpolarized structure function $F_2(x)$ is defined as,

$$F_2(x) = x \sum_i e_i^2 q_i(x) = x \sum_i e_i^2 \left(q_i^\uparrow(x) + q_i^\downarrow(x) \right). \quad (2.58)$$

In the case of polarized scattering, the polarized parton distribution function for each parton i can be defined as,

$$\Delta q_i(x) = q_i^\uparrow(x) - q_i^\downarrow(x) .$$

The first spin-structure function $g_1(x)$ is defined as the charge weighted average of the polarized parton distribution functions.

$$g_1(x) = \frac{1}{2} \sum_i e_i^2 \Delta q_i(x) = \frac{1}{2} \sum_i e_i^2 \left(q_i^\uparrow(x) - q_i^\downarrow(x) \right). \quad (2.59)$$

Although the parton model can successfully interpret the three structure functions F_1 , F_2 and g_1 by considering the electron scattering from non-interacting partons, it fails to provide an explanation for the second spin-structure function g_2 . The experiment E12-06-121 will give insight into the study of g_2 which is related to the interactions of quarks and gluons inside the nucleon as a function of x and Q^2 . In the next chapter, I will discuss several theoretical advancements regarding g_2 along with the previous experimental measurements.

Chapter 3 The Neutron Spin Structure Function g_2 and the Quark-Gluon Correlations

3.1 g_2 , d_2 and Higher twist Effects

The second spin structure function g_2 can be measured from the measurement of longitudinal electron and transverse target double spin asymmetry. As mentioned in the last chapter, g_2 can be generated by the multi-parton interactions or, the higher twist effects. g_2 can be interpreted using the Operator Product Expansion (OPE)[17] of the local quark gluon operators in QCD. In OPE the product of two local operators with space-time separation z can be written as an expansion of local operators in the limit of $z \rightarrow 0$ (z has to be very small compared to the probed distance) as the following.

$$\lim_{z \rightarrow 0} \mathcal{O}_a(z) \mathcal{O}_b(0) = \sum_l c_{abl} \mathcal{O}_l(0). \quad (3.1)$$

The quark electromagnetic current which is related to the hadronic tensor $W_{\mu\nu}$ in forward Compton scattering can be written as,

$$T_{\mu\nu} = i \int \langle N | \mathcal{T}(j_\mu(z) j_\nu(0)) | N \rangle e^{iq \cdot z} d^4 z \quad (3.2)$$

where \mathcal{T} is the time ordering operator. By OPE the product $j_\mu(z) j_\nu(0)$ can be written as the sum of local gluon and quark operators with mass dimension, d and spin, n where the twist is defined as, $t = d - n$.

$$j_\mu(z) j_\nu(0) = \sum c_{\mu_1 \dots \mu_n} \mathcal{O}_{d,n}^{\mu_1 \dots \mu_n}. \quad (3.3)$$

The dimensional analysis of $c_{\mu_1 \dots \mu_n} \mathcal{O}_{d,n}^{\mu_1 \dots \mu_n}$ is shown below.

$$\begin{aligned} c_{\mu_1 \dots \mu_n} \mathcal{O}_{d,n}^{\mu_1 \dots \mu_n} &\rightarrow \frac{q_{\mu_1}}{Q} \dots \frac{q_{\mu_n}}{Q} Q^{2-d} M^{d-n-2} p^{\mu_1} \dots p^{\mu_n} \\ &\rightarrow \left(\frac{p \cdot q}{Q} \right)^n Q^{2-d} M^{d-n-2} \\ &\rightarrow \left(\frac{1}{x} \right)^n \left(\frac{Q}{M} \right)^{2+n-d} \\ &\rightarrow \left(\frac{1}{x} \right)^n \left(\frac{Q}{M} \right)^{2-t} \end{aligned}$$

The lowest possible twist for any gauge invariant operator is two because it must have at least two quark fields or two gluon operators. The twists of quark and gluon operators are listed in Table. 3.1.

Table 3.1: The spin, dimension, and twist of quark and gluon operators.

	Quark	Gluon
dimension (d)	3/2	2
spin (n)	1/2	1
twist (t)	1	1

As seen in the dimensional analysis, the higher twist terms have increasing powers of $\frac{M}{Q}$ that suppresses the higher twist terms and it becomes very difficult to separate the higher twist processes from the leading twist processes. Filippone and Ji [20] explained that the pre-existing quarks and gluons in the hadron wave function cannot be distinguished from those generated during the radiative processes. However, the interesting fact about g_2 is that it contributes at the same order as the leading twist to the measured double spin asymmetry makes it an exception and the cleanest higher twist observable.

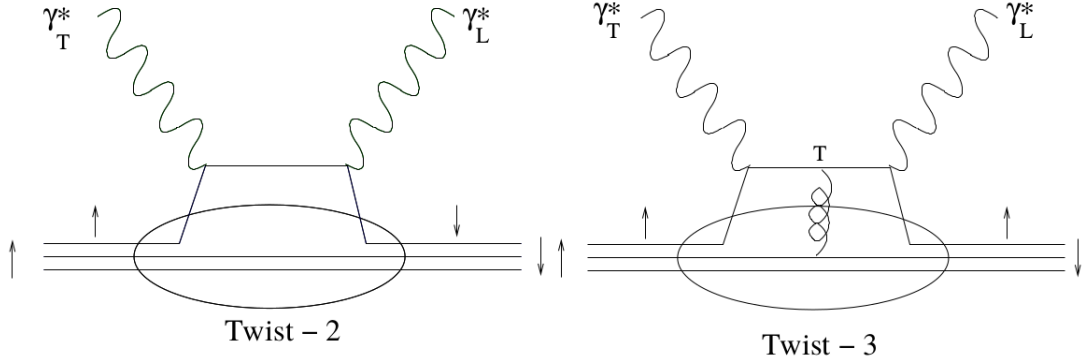


Figure 3.1: The helicity exchange in virtual Compton scattering by twist-2 and twist-3 processes. g_2 is the combination of these two processes.

Using optical theorem the spin structure functions can be interpreted in the Compton scattering process,

$$\gamma^{*(+1)} + N \left(\frac{1}{2} \right) \rightarrow \gamma^{*(0)} + N \left(\frac{-1}{2} \right),$$

where N and γ^* represent the target nucleon and the virtual photon respectively. The +1 helicity exchange in this scattering is allowed by the two processes (illustrated in the Fig. 3.1) which are combined to yield a gauge invariant result.

1. A single quark is scattered by carrying a single unit of orbital angular momentum via its transverse momentum wave function giving rise to a twist two operator.
2. A single quark is scattered by absorbing a transversely polarized gluon from another quark in the nucleon that gives rise to a twist three operator.

g_2 is related to the imaginary counterpart of the Compton scattering amplitude and is given by the sum of the above mentioned two processes. The function g_2 can be

decomposed into twist-2 and twist-3 parts as

$$g_2(x, Q^2) = g_2^{WW}(x, Q^2) + \bar{g}_2(x, Q^2), \quad (3.4)$$

where the first term is the twist-2 term that can be calculated from g_1 only by the Wandzura-Wilczek relation and it can be interpreted by the Quark parton Model.

$$g_2^{WW}(x, Q^2) = -g_1(x, Q^2) + \int_x^1 \frac{dy}{y} g_1(x, Q^2). \quad (3.5)$$

The second term is a combination of both twist-2 and twist-3 parts.

$$\bar{g}_2(x, Q^2) = - \int_x^1 \frac{\partial}{\partial y} \left[\frac{m_q}{M} h_T(y, Q^2) + \xi(y, Q^2) \right] \frac{dy}{y}, \quad (3.6)$$

where h_T describes the transversity (quarks's transverse polarization) distribution in the nucleon. This twist-2 quantity has a factor m_q/M multiplied with the h_T which results in a numerical suppression and can be neglected. The other part ξ is the twist-3 term generated by quark-gluon correlations in the nucleon. By subtracting the g_2^{WW} from the measured g_2 , the higher twist term ξ can be accessed easily in this experiment.

Another very interesting higher twist quantity to consider here is d_2 which is the third moment (in x) of the linear combination of g_1 and g_2 .

$$\begin{aligned} d_2(Q^2) &= \int_0^1 x^2 [2g_1(x, Q^2) + 3g_2(x, Q^2)] dx \\ &= 3 \int_0^1 x^2 [g_2(x, Q^2) - g_2^{WW}(x, Q^2)] dx \\ &= 3 \int_0^1 x^2 \bar{g}_2(x, Q^2) dx. \end{aligned} \quad (3.7)$$

As shown in Eq. 3.7, d_2 is very sensitive to the high x regions because of its x^2 weighting making it the cleanest higher twist observable. d_2 is also present in the twist expansion [22][23] of $\Gamma(Q^2)$, which is the first moment of $g_1(x, Q^2)$ as the following.

$$\begin{aligned} \Gamma(Q^2) &= \int_0^1 g_1(x, Q^2) dx \\ &= \frac{a_0}{2} + \frac{M^2}{9Q^2} (a_2 + 4d_2 + 4f_2) + O\left(\frac{M^4}{Q^4}\right), \end{aligned}$$

where,

- a_0 is the dominant twist-2 term [24] [25].
- a_2 is the second moment of g_1 that arises from the target mass correction [22].

- d_2 is the twist-3 reduced matrix element consisting of the local quark and gluon operators [20] [30][31] which can be expressed in light-cone coordinates as shown below.

$$2Mp^+p^+S^x d_2 = g \langle p, S | \bar{\psi}(0) \gamma^+ G^{+y}(0) \psi(0) | p, S \rangle \quad (3.8)$$

In Eq. 3.8 p and S are the nucleon momentum and spin respectively, g is the coupling constant, ψ and G^{+y} are the quark and gluon fields respectively, and the + superscript is used to denote the light-cone coordinate.

- f_2 is the twist-4 reduced matrix element [18] [19][27] and the twist-4 contribution was extracted by the measurement of proton and neutron f_2 separately and by combining high Q^2 world data and low Q^2 Jefferson Lab data [26] [27] [28] [29].

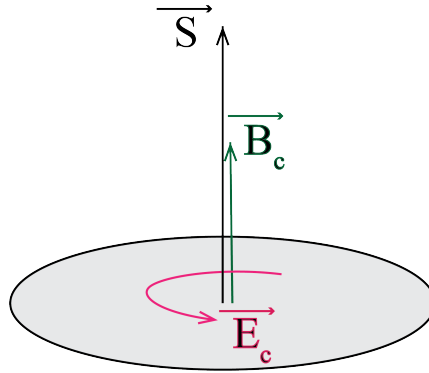


Figure 3.2: The induced color electric and magnetic field when the nucleon is transversely polarized and hit by the virtual photon.

d_2 is related to the electric (χ_E) and magnetic (χ_B) color polarizabilities [20] of the nucleon i.e. it represents how the color electric and magnetic fields are induced in a transversely polarized nucleon when struck by the virtual photon (Fig. 3.2).

$$d_2 = \frac{1}{4}(\chi_E + \chi_B) \quad (3.9)$$

According to the most recent interpretation of d_2 , the matrix element related to d_2 represents the color Lorentz force F^y on the struck quark by the remnant system when struck by the virtual photon. The gluon field G^{+y} in Eq. 3.8 is analogous to the electromagnetic Lorentz force (F^y) on charged particles and it can be expressed as $G^{+y} = \frac{1}{\sqrt{2}}(B^x - E^y) = F^y$. If the three momentum transfer of the virtual photon happens in z direction, then the E^y and B^x represent the transverse components of the color electric and magnetic fields respectively [30]. In the rest frame of nucleon, $d_2 = -F^y(0)/M^2$. The color electric and magnetic forces can be extracted from the measurements of d_2 and f_2 using the following relations [30].

$$d_2 = -\frac{1}{M^2}(F_E^y + F_B^y) \quad (3.10)$$

$$f_2 = -\frac{2}{M^2}(2F_E^y - F_B^y) \quad (3.11)$$

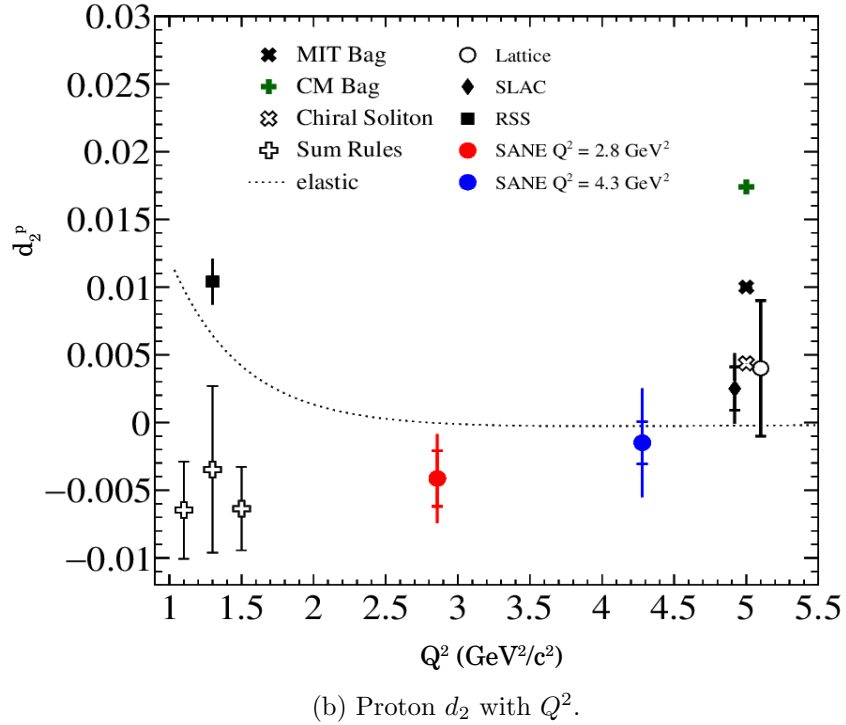
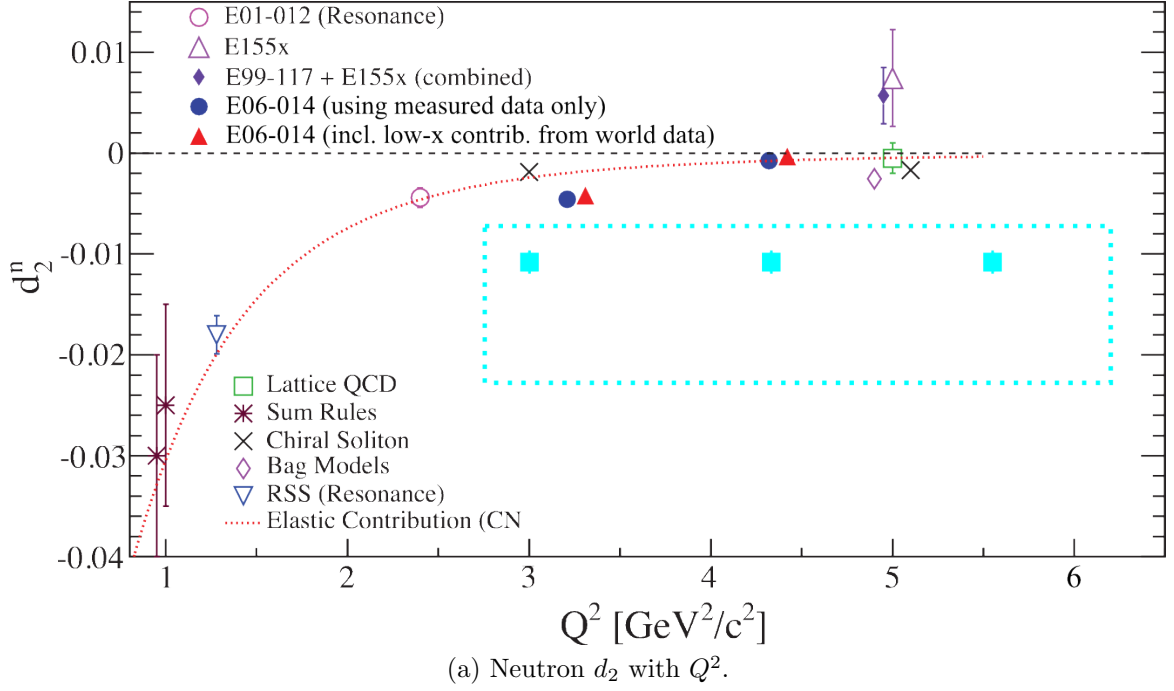


Figure 3.3: The theoretical predictions, previous experimental measurements of neutron and proton d_2 with Q^2 . The projections of d_2^n at three constant Q^2 values for the experiment E12-06-121 are also shown.

3.2 Theoretical Predictions and Existing Results

In this section a few theoretical predictions and previous experimental results of the neutron structure function g_2 and d_2 will be discussed. The Fig. 3.3 shows the d_2^n projections at constant $Q^2 = 3, 4.3, 5.6 \text{ GeV}^2/c^2$ for the experiment E12-06-121 and the model predictions and previous experimental results of both d_2^n and d_2^p . The Fig. 3.4 demonstrates the $x^2 g_2$ projections along x for the same three constant Q^2 values mentioned before.

3.2.1 d_2^n Models

A brief summary of the theoretical predictions shown in Fig. 3.3 is given below.

Lattice QCD

Lattice QCD is a theoretical framework to compute QCD observables in its non-perturbative regime [32] [33] [34]. Perturbative solutions cannot be used in the low energy region because of large coupling constant and non-linearity of the strong force. Lattice QCD is a very computation heavy approach where quarks are considered to be lattice points and the gluons are considered to be the connection between the lattice sites in space and time. Considering the lattice to be infinitely large and the distance between the sites to be infinitesimally small, the discrete equations are solved on a grid using computation. This is currently the most evolving and advanced field in theoretical QCD. However, there is only one prediction of d_2^n at $Q^2 = 5 \text{ GeV}^2/c^2$ [35] from Lattice QCD and more calculations are overdue. The lattice QCD predicts that $d_2^n = 0$ or very small within uncertainties at high Q^2 .

Chiral Soliton Model

Solitons are the solutions to nonlinear differential equations. The QCD lagrangian with N_f massless flavors holds a global symmetry called the chiral symmetry, under the unitary flavor transformation of left and right handed quark fields. The strong interactions are modeled on the basis of the spontaneous and explicit chiral symmetry breaking in hadron physics. If QCD is generalized to the $SU(N_c)$ gauge group of N_c number of colors, then a perturbative approach can be used by considering $1/N_c$ to be the expansion parameter in the low energy regime. In this scenario, the QCD transforms to an effective theory of mesons and glueballs which are weakly interacting. Also, baryons constructed from N_c quarks are the solitonic solutions of the nonlinear field equations. So, in the chiral soliton model [40] [41], the quarks are bound and localized by their interaction with chiral fields inside the nucleon which is viewed as a chiral soliton. This model successfully reproduced the twist-2 structure functions from EMC, SMC data for proton, neutron and deuteron [43] [44] [45] [46] and, NMC data for $F_2^p(x) - F_2^n(x)$ and $F_2^n(x)/F_2^p(x)$ [42]. While investigating the higher twist parton distributions, this model calculated[47] nonzero \bar{g}_2 at $Q^2 = 5 \text{ GeV}^2/c^2$ for small x . This model also predicts very small d_2^n and d_2^p similar to the Lattice QCD prediction.

Bag Model

In the bag model the massive quarks are considered to be bound in a deep potential to model the confinement mechanism (free quarks cannot exist outside the nucleon) of QCD. In the simplest bag model by Bogoliubov [48], the infinitely massive quarks with mass m (if finite) are placed in a finite spherical well with attractive scalar field. However, the more realistic MIT bag model [49] [50] includes both the asymptotically free and confined quarks in a bag separated into two regions: interior and exterior. In the interior region, the quarks are light and they only feel weak fields. In the exterior region the quarks have lower vacuum energy and they cannot propagate. The MIT bag model can be reduced to the Bogoliubov bag model in the limit of $m \rightarrow \infty$ and the bag is a spherical cavity. The twist-3 contribution was calculated [51] in the bag model where the bag boundary simulated the soft gluons and the twist-3 contribution was found to be non-negligible w.r.t. the twist-2 contribution. It predicts the sign of d_2^p is positive and d_2^n is negative.

Sum Rules

The sum rule method [36] relates the low and high energy regions of the QCD. The method of interpolation is used between the perturbative and non-perturbative regions using dispersion relation and OPE. The sum rule calculations [37] [38] [39] of d_2^p and d_2^n are 1-2 standard deviations away from the predictions by the bag model and the chiral soliton model. It predicts the signs of both d_2^n and d_2^p are negative and both of them are smaller than 0.03.

3.2.2 Previous d_2^n Measurements

The previous experimental data points of d_2^n and d_2^p shown in the Fig. 3.3, are briefly discussed in this section. The first data collection for the measurements of g_2 and d_2 was done in SLAC E143 [52], E154 [53] and E155 [54] experiments. Because of the very large statistical errors in this data, the first dedicated experiment on g_2 E155x [55] was performed in SLAC. This experiment extracted g_2 and d_2 for the proton and deuteron at high Q^2 ($\sim 5 \text{ GeV}^2/c^2$).

Two other experiments E99-117 [12] and E94-010 [56] [57] at the Jefferson Lab measured the neutron g_2 in the DIS and the resonance regions respectively. Experiment E99-117 had three data points in the DIS region: $(x, Q^2) = (0.33, 2.71)$, $(0.47, 3.52)$, $(0.6, 4.83)$ and, experiment E94-010 explored the lower Q^2 region: $Q^2 < 1 \text{ GeV}^2/c^2$. The neutron d_2 measurements from the SLAC E155x and Jefferson Lab experiment E99-117 were combined and the result is shown in the Fig. 3.3 (a) by the purple diamond marker around $Q^2 = 4.83 \text{ GeV}^2/c^2$. The error in this experimental data was dominated by statistics and the result was two standard deviations away from zero and the lattice QCD prediction.

To investigate the two spin structure functions g_1 and g_2 in the resonance region, two more experiments E01-012 [58] and RSS-E01-006 (Resonance Spin Structure) [59] were performed at Jefferson Lab. Experiment E01-012 used a polarized ^3He target, and it mainly focussed on extracting g_1 . The RSS experiment used polarized NH_3 and

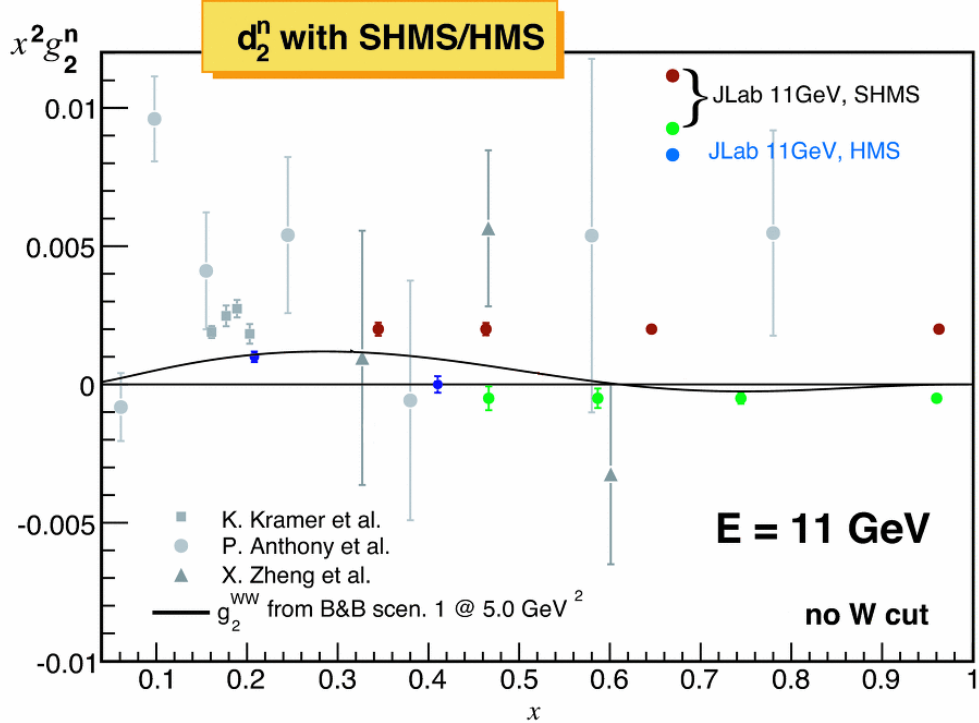


Figure 3.4: The projection of $x^2 g_2^n$ over the whole x region. The three sets of colored points (vertically offset from each other) represent the constant $Q^2=3, 4.3, 5.6$ GeV^2/c^2 where the d_2^n will be evaluated.

ND_3 targets to extract g_2^p and g_2^n at $\langle Q^2 \rangle = 1.3 \text{ GeV}^2/c^2$. Although the experimental results provided very high precision g_2^p data, g_2^n was limited by statistical precision.

In 2009 the Jefferson Lab 6 GeV era experiment E06-014 [60] [61] [62] used a polarized ^3He target to measure the double spin asymmetries and cross-section over $0.25 \leq x \leq 0.9$ and in both resonance and DIS regions. d_2^n was extracted at $\langle Q^2 \rangle = 3.21, 4.32 \text{ GeV}^2/c^2$ with an absolute precision of 10^{-5} . This result was in agreement with the lattice QCD prediction as shown in Fig. 3.3. A hint of a negative d_2^n value was noted in the moderate Q^2 region that dips below the elastic contribution (red dashed line in plot).

Another inclusive experiment, known as the SANE experiment (SANE-E07003) [63], was performed in Jefferson Lab around the same time as E06-014 to explore the proton spin structure over $0.3 \leq x \leq 0.8$ for $2.5 \leq Q^2 \leq 6.5 \text{ GeV}^2/c^2$. It also used polarized ^3He as the target. The results of this experiment is shown in Fig. 3.3 (b) by the red and blue markers. The similar hint of negative d_2^p was also noted here as it was seen in the case of neutron.

The projected data for the experiment E12-06-121 directly overlaps with the previous experimental measurements described above and as well as lattice QCD prediction. Our data will also verify the dip below the elastic contribution, observed previously for both the proton and neutron d_2 results. Also, the expected errors in the projected data points will be significantly smaller resulting in a very precise

measurement of d_2^n . Previously the measured g_2 data at one Q^2 value was evolved to a common Q^2 while evaluating d_2 . But due to lack of knowledge regarding the evolution of the twist-3 part \bar{g}_2 , the calculation with evolving the data at a common Q^2 was never precise. In the experiment E12-06-121, d_2^n will be calculated at three constant Q^2 values using the large momentum acceptance of the spectrometers that collected data over wide x ranges at three fixed Q^2 values.

Chapter 4 The Experimental Overview

The experiment E12-06-121 (measurement of g_2^n and d_2^n) was carried out in Hall C of the Thomas Jefferson National Accelerator Facility (known as Jefferson Lab or JLab) in Newport News, Virginia. The aerial view of the accelerator facility is shown in the Fig. 4.1. The standard Hall C spectrometers and detectors were used to detect the scattered electrons in this experiment but the polarized ^3He target system had to be installed in the hall. The target system installation for the experiment in Hall C was completed by November, 2019 before starting the production run for the sister experiment E12-06-110: “Measurement of Neutron Spin Asymmetry A_1^n in the Valence Quark Region Using an 11 GeV Beam and a Polarized Helium-3 Target in Hall C”. The modifications of the experimental setup (rotation of the main Helmholtz coils by 90° , upgrading to more stable power supply for the coils) for the d_2^n experiment was done in March, 2020 after the completion of the previous experiment. Although the production data taking started in the same month, data could only be taken for a couple of days. The laboratory had to shut down for four months because of the COVID-19 pandemic and it reopened in July, 2020. The production resumed right after that and the experiment E12-06-121 was successfully completed in September, 2020.



Figure 4.1: The aerial view of the Thomas Jefferson Accelerator Facility.

4.1 Goal of the Experiment

The goal of the experiment was to extract the spin structure function g_2^n over the kinematic range $0.2 < x < 0.95$ and $2.5 < Q^2 < 6 \text{ GeV}^2/c^2$. As g_2^n is not well understood at high x , the \bar{g}_2 (twist-3 part of g_2^n) will be extracted to evaluate the quantity $d_2^n = x^2 \int_0^1 \bar{g}_2 dx$ at three constant Q^2 values which are 3.0, 4.3, and 5.6 GeV^2/c^2 . The structure functions g_2 and d_2 of helium-3 will be accessed by measuring the unpolarized scattering cross-section, σ_0^{He3} and, the longitudinal and transverse electron asymmetries (A_{\parallel} , A_{\perp}) using Eq. 2.52 and, Eq. 2.53. Then nuclear correction will be performed to extract g_2^n and d_2^n . The combination of the spectrometers HMS and SHMS will cover a broad x region over constant Q^2 values leading to the first ever evaluation of d_2^n integrals at the aforementioned three constant Q^2 values.

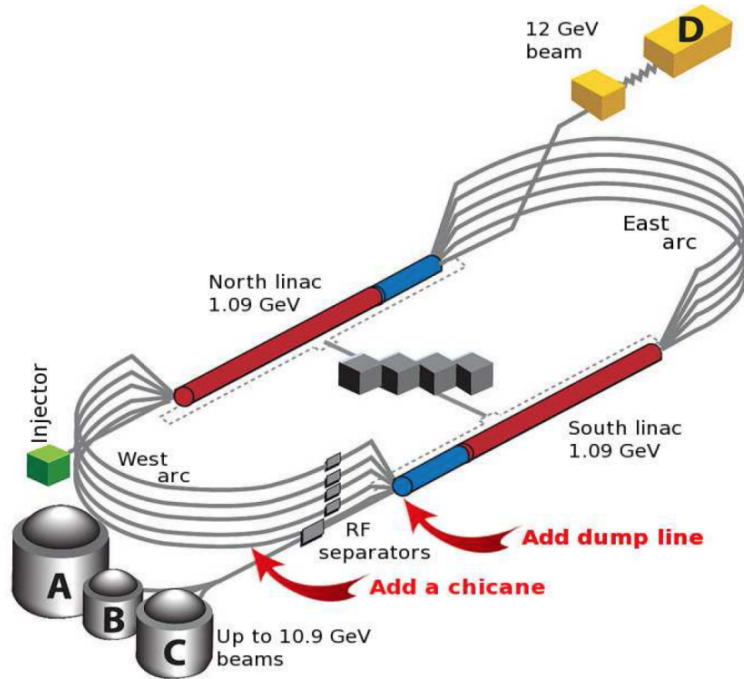


Figure 4.2: CEBAF after 12 GeV upgrade [64].

Table 4.1: List of important CEBAF parameters and their respective values.

Parameter Name	Value
Energy, max (GeV)	12
Beam current, max (mA)	0.1
Number of linacs	2
Linac passes	≤ 11
Linac energy (GeV)	1.09
Length of linac (m)	250
Number of cavities in each linac	200

4.2 The Experimental Setup

The Jefferson Lab Hall C is 150 feet in diameter and 60 feet tall and the layout of the hall is shown in Fig. 4.3. A longitudinally polarized, electron beam with an energy of 10.38 GeV was scattered from the polarized ^3He target which was placed inside an ~ 25 Gauss holding magnetic field. The scattered electrons were detected using the two spectrometers: the High Momentum Spectrometer (HMS) and the Super High Momentum Spectrometer (SHMS) which were installed on both sides of the electron beam line. Each component of the experimental setup will be discussed in more detail in the following sections.

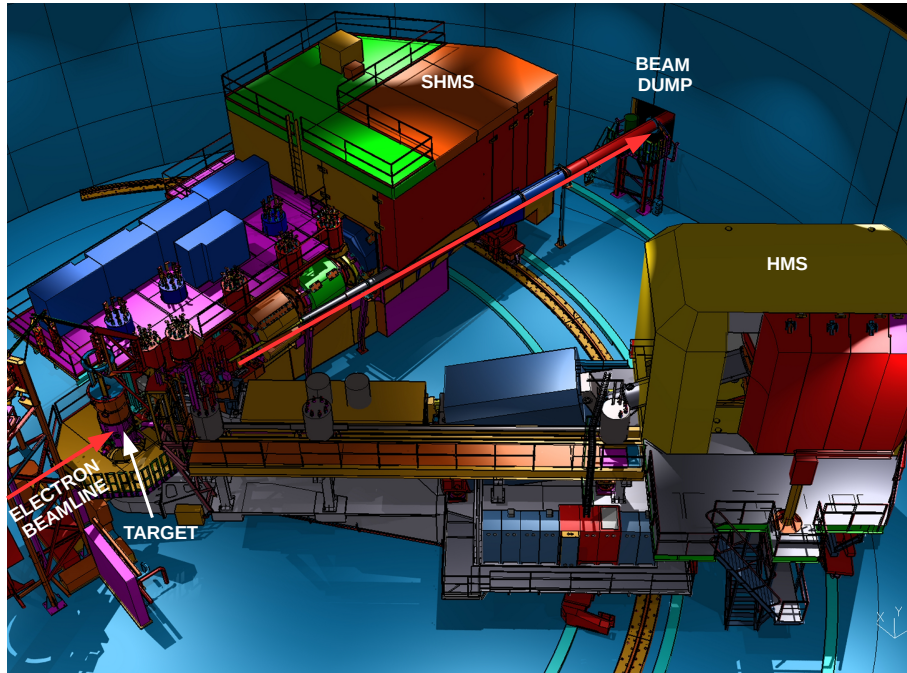


Figure 4.3: Experimental setup in Hall C.

4.2.1 The Polarized Electron Beam

The Continuous Electron Beam Accelerator Facility (CEBAF) currently delivers electron beams with energies up to 10.9 GeV to the experimental halls, Hall A, Hall B, Hall C, and up to 12 GeV electron beam to the fourth experimental hall, Hall D. This accelerator facility was founded in 1984 and it delivered electron beam to the experimental area for the first time in 1994. The name of CEBAF was changed to Thomas Jefferson Accelerator Facility (TJNAF) in 1996. By the year 1998, the accelerator was ready to send 4 GeV beams to the three initial experimental halls. The laboratory could achieve “enhanced design energy” of 6 GeV in the year of 2000 and the planning for the major 12 GeV upgrade and also the planning for the construction of Hall D were started in 2001. The 12 GeV CEBAF Upgrade Project was completed in 2017 and the experiment E12-06-121 was one of the first approved experiments of the 12 GeV era at the Jefferson Lab.

The basic principle of polarized electron beam delivery to the four experimental halls are demonstrated in the Fig. 4.2. The source of the continuous wave (CW) electron beam with very high polarization is a photocathode, made of strained super lattice gallium arsenide (GaAs)[65, 66, 15]. The different layers in the cathode are shown in Fig. 4.4. The shorter lattice spacing in the second layer made of $GaAs_{0.72}P_{0.28}$ causes a strain on the top pure GaAs layer, and an energy gap is created between the $P_{3/2}, m_j = \pm\frac{3}{2}$ and the $P_{3/2}, m_j = \pm\frac{1}{2}$ states. When left (or, right) circularly polarized laser light illuminates the photocathode, only the electrons in the $P_{3/2}, m_j = \frac{3}{2}$ (or, $m_j = -\frac{3}{2}$) state get excited to the $S_{1/2}, m_j = \frac{1}{2}$ (or, $m_j = -\frac{1}{2}$) state of the conduction band. These electrons are polarized in the same direction depending on the helicity (-1 or, $+1$) of the incident laser light.

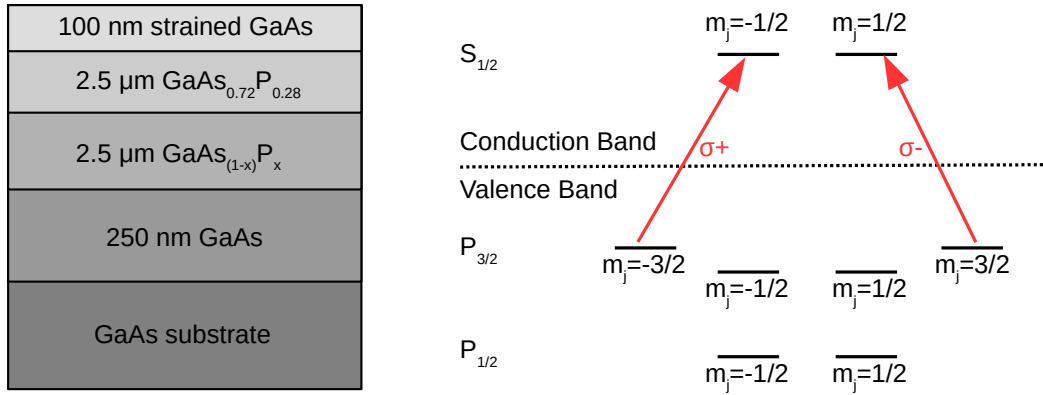


Figure 4.4: The source of the electron beam with high polarization

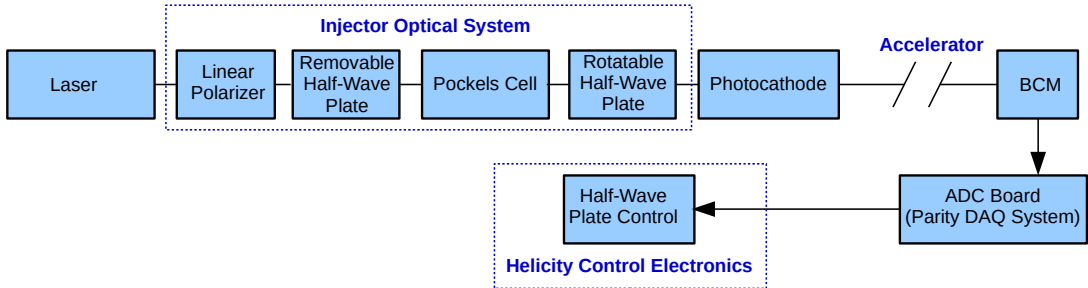


Figure 4.5: The diagram of the injector optics system and the helicity feedback system to compensate charge asymmetry.[68]

The optics system to control the helicity of the laser is shown in the Fig. 4.5. The unpolarized laser is converted to a linearly polarized light by the linear polarizer and it reaches the Pockels cell after passing (or not passing) through the removable half-wave plate. The removable half-wave plate is used to control the sign of the

laser beam helicity and it is inserted or removed periodically to cancel out several systematic errors. The Pockels cell is a crystal that is controlled by voltage inputs and it converts the linearly polarized laser light to a circularly polarized laser light, and the helicity of the circular polarization is also controlled by the helicity control electronics shown in the same figure. The rotatable half-wave plate after the Pockels cell compensates for charge asymmetries generated from residual linear polarization and it is generally kept under 200 ppm. Finally, the circularly polarized laser light reaches the photocathode and polarized electrons are extracted. The extracted electrons are accelerated towards the north linac after passing through the Wien filter which is used to rotate the electron polarization direction without changing the beam orbit. This allows optimized beam polarization to be delivered to each experimental hall. The next part of the accelerator consists of the north linac, the east arc, the south linac, and the west arc as shown in Fig. 4.2. Each linac is composed of 25 RF modules that provide acceleration to the electrons and they gain 1.09 GeV energy after passing through each linac. To keep the beam focused and to keep it on a precise trajectory, more than 2200 magnets are used. The beam is recirculated five times to reach the maximum energy, and it is delivered to the halls according to their energy requirement. So, pass-1 beam corresponds to ~ 2 GeV beam energy and pass-5 beam corresponds to a maximum of ~ 11 GeV beam energy in Hall C. The beamline instrumentation and the electron beam polarimetry will be discussed in Chapter 5.

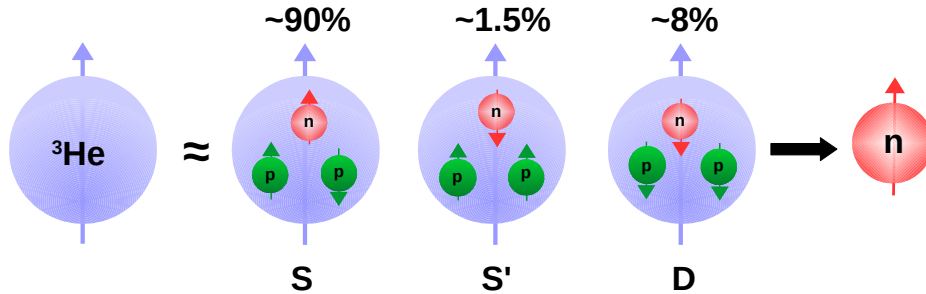


Figure 4.6: The components of the polarized ^3He ground states.

4.2.2 The Polarized Helium-3 Target

A polarized ^3He target was used as an effective neutron target in our experiment for the following reasons.

- A free neutron target does not exist because the lifetime of the neutron is very short ~ 880 seconds [67].
- The ground state of the polarized ^3He is composed of the three states: S, S', and D as shown in Fig. 4.6. In the dominating S state, the spins of the two protons cancel because they are anti-parallel (Pauli exclusion principle) to each other. The remaining neutron spin makes the nuclear correction in ^3He less model dependent as $\sim 90\%$ of the nuclear spin comes from the neutron spin

in helium-3. On the other hand, other polarized nuclear targets like deuteron (single proton and single neutron) can also serve as an effective neutron target but in that case $\sim 50\%$ of the nuclear spin comes from the neutron and the remaining $\sim 50\%$ of the nuclear spin comes from the proton. The uncertainty from the $\sim 50\%$ proton component increases the final uncertainty while extracting neutron spin structure from the deuteron data. Thus the polarized ^3He was an ideal candidate for our experiment to study the neutron spin structure.

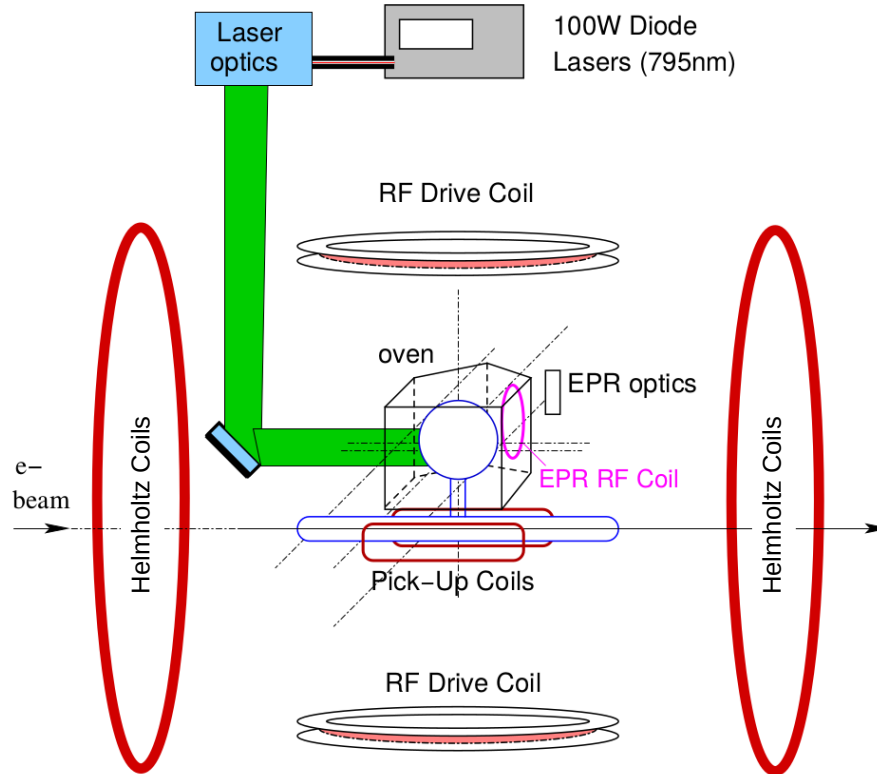


Figure 4.7: The layout of the target system in Hall C.

The polarized ^3He target system shown in Fig. 4.7, composed of several components and they were installed and optimized in Hall C before the experiment was started. The target cell geometry, all other components of the whole target system in the hall, the method of polarizing the target, target polarimetry and the precise target polarization direction measurement will be described in Chapter 6.

4.2.3 Spectrometers and Detectors

The high momentum spectrometer (HMS) and the super high momentum spectrometer (SHMS) were used to detect the scattered electrons in Hall C [76]. Both the spectrometers consist of a series of superconducting magnets followed by a set of particle detectors placed inside the detector huts which were used to trigger event

readout, particle identification (PID) and particle tracking [76]. The HMS and SHMS magnets and the detectors will be described in detail in the following sections. The design parameters for the HMS and SHMS are listed in the Table. 4.2.

Table 4.2: List of HMS and SHMS design parameters.

Parameter	HMS	SHMS
Range of central momentum (GeV/c)	0.5 to 7.5	2.0 to 11.0
Momentum acceptance, δ (%)	-8 to 8	-10 to 22
Range of scattering angle ($^{\circ}$)	10.5 to 90	5.5 to 40
Solid angle acceptance (msr)	8.0	5.0

4.2.3.1 HMS

The HMS is located on the beam right side of the electron beamline. It has three super conducting quadrupole magnets (Q_1, Q_2, Q_3) and a dipole magnet. The particle travels through the Q_1, Q_2, Q_3 to the dipole after scattering. The quadrupoles are used to focus the scattered particles towards the spectrometer focal plane and the dipole is used to bend the central momentum particle trajectories vertically by 25° in upward direction. The detector hut is located after the dipole and it has the following set of detectors inside it.

- Drift Chambers:** After exiting the dipole, the first detector encountered by the particles is a pair of drift chambers (DC) with six wire planes in each of them. They are used to measure the particle's position and angle in the detector hut very accurately. This information along with proper optics reconstruction gives the particle trajectory near the ^3He target. The HMS drift chambers cover an active region of 100 cm in vertical direction and 50 cm in horizontal direction. These drift chambers have an equal mixture (by weight) of argon and ethane gas, the wire planes in the first chamber are in the order U, U', X, X', V', V and, the wire planes in the second chamber are in the order V, V', X', X, U', U.
- Hodoscopes:** The HMS hodoscope has a set of four hodoscope planes and each plane has a set of scintillator bars covering the acceptance of the particles. One pair of planes (one with horizontal bars, S1X and one with vertical bars, S1Y) is located right after the DC and the second pair of planes (S2X, S2Y) is located 2 meter away from the first pair of planes. Photomultiplier tubes (PMT) are attached to the end of each bar to detect scintillating light from the particles. The hodoscopes provide a trigger to the data acquisition, the reference time for the drift chamber and they measure the time of flight between the two pairs of planes for PID.

- **Gas Cherenkov Detector:** The HMS Cherenkov detector is used for particle identification. If a charged particle has a speed greater than the speed of light in a particular medium, it polarizes the particles of the medium creating an electromagnetic disturbance. The excited molecules in the medium emit photons on returning to their ground state which is known as the Cherenkov radiation. The emission angle (θ) of the Cherenkov radiation is determined by the refractive index ($n = \frac{c}{u}$, c and u are the speed of light in the vacuum and the medium respectively) of the medium and the speed (v) of the charged particle in the medium.

$$\theta = \arccos\left(\frac{c}{nv}\right)$$

The threshold velocity (v_T) of the charged particle to generate Cherenkov radiation is determined by the refractive index of the medium which is proportional to the pressure ($n-1 \propto P$) of the gas used as the medium. If two charged particles with different masses travel with the same momenta, the velocities will be different in the medium. Thus by adjusting the gas pressure in the medium, the threshold velocity to produce Cherenkov radiation can be adjusted to distinguish between the two particles with different masses. This is used to identify electrons from the pion background. The HMS gas Cherenkov detector consists of a cylindrical tank (CO_2/N_2 gas at 1 atm operating pressure) with two mirrors that focus the Cherenkov light on two attached PMTs.

- **Calorimeter:** The HMS calorimeter has four stacks of TF1 lead glass with thirteen blocks in each stack. Two PMTs are attached to both ends of the first two stacks and the last two stacks have a single PMT attached to each of them. High energy particles generate a signal when passing through the lead glass and it is proportional to the sum of the path lengths traveled by all the particles above the Cherenkov threshold. The generation of photons from the bremsstrahlung process and the production of electron-positron pairs after that is known as the electromagnetic shower. The electrons or positrons deposit most of their energy in the shower counter which is analyzed to discriminate between electrons and pion background.

4.2.3.2 SHMS

The SHMS is located on the beam left side of the electron beamline. It has three superconducting quadrupole magnets (Q_1, Q_2, Q_3) and a dipole magnet similar to the HMS. It also has an additional dipole magnet known as the horizontal bender (HB) in front of the Q_1 . So, the scattered particles enter through the HB and then travel through the rest of the magnets. The quadrupoles are used to focus the scattered particles towards the spectrometer focal plane and the dipole is used to bend the central momentum particle trajectories vertically by 18.2° in upward direction. The HB is used to bend the central momentum particle trajectories to the left by 3° so that the SHMS can reach the smallest scattering angle (5.5°). The detector hut is located after the dipole (Fig. 4.8) and it has the similar set of detectors as the HMS.

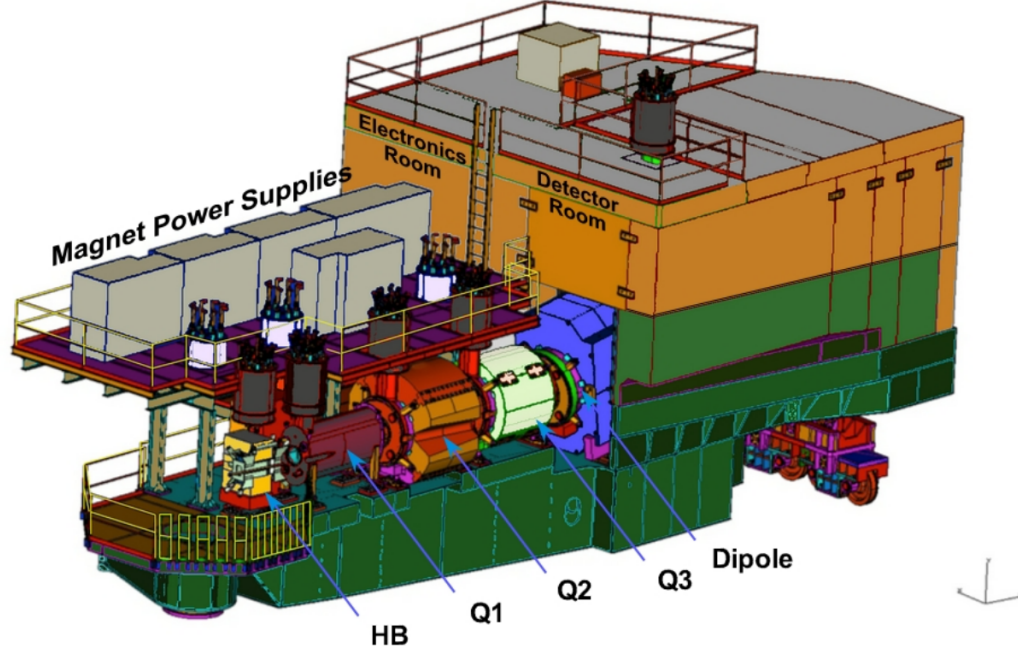


Figure 4.8: The CAD drawing of the SHMS showing the HB, quadrupoles, dipole and the detector hut [76].

- Drift Chambers:** The SHMS also has a pair of drift chambers (DC) with six wire planes in each of them. A cathode plane made of copper coated mylar is placed between each wire plane, also before the first wire plane and after the last wire plane. They are used to measure the particle's position and angle in the detector hut very accurately. The SHMS drift chambers cover an active region of 80 cm in vertical direction and 80 cm in horizontal direction. These drift chambers have an equal mixture (by weight) of argon and ethane gas, the wire planes in the first chamber are in the order U, U', X, X', V', V and, the wire planes in the second chamber are in the order V, V', X', X, U', U.
- Hodoscopes:** The SHMS hodoscope has a set of four hodoscope planes (S1X, S1Y, S2X, S2Y) and each plane has a set of scintillator bars covering the acceptance of the particles. The S1X and the S1Y planes have 13 scintillator paddles and the S2X plane has 14 scintillator paddles. On the other hand, the S2Y plane is composed of 21 bars of Corning HPFS 7980 Fused Silica (quartz) [76]. All the paddles and the bars have attached PMTs to read out the scintillating light and Cherenkov radiation from the quartz respectively.
- Noble Gas Cherenkov Detector:** The SHMS noble gas Cherenkov detector consist of a cylindrical tank (N_2 gas at 1 atm operating pressure and $20^\circ C$) with four mirrors that focus the Cherenkov light in four attached PMTs. The working principle of this detector is the same as that described in the previous HMS section. The threshold energies of the electron and pion are 21.6 MeV and 5.9 GeV respectively.

- **Calorimeter:** The last detector in the SHMS detector hut is the lead glass shower counter located behind the S2Y hodoscope plane. It has two parts: pre-shower and shower. The pre shower is located before the shower to augment PID by the early detection of the electromagnetic showers.

4.3 Kinematic Coverage

The kinematic coverage of the spectrometers are illustrated in Fig. 4.9 in $Q^2 - x$ space. Both the HMS and SHMS took data in three kinematic settings as listed in the Table. 4.3. Due to difficulties in accelerator performance and shortened run time, we could only complete production data taking (transverse and longitudinal target polarization) for the kinematic settings (HMS-A, SHMS-X) and (HMS-C, SHMS-Z). We had to skip the transverse production data taking for the middle kinematic setting (HMS-B, SHMS-Y), although we took the production longitudinal data in the same kinematic setting. The combination of data from both the spectrometers and extrapolation of previous JLab 6 GeV experimental data will allow us to meet the goal of the experiment as described in the Section 4.1.

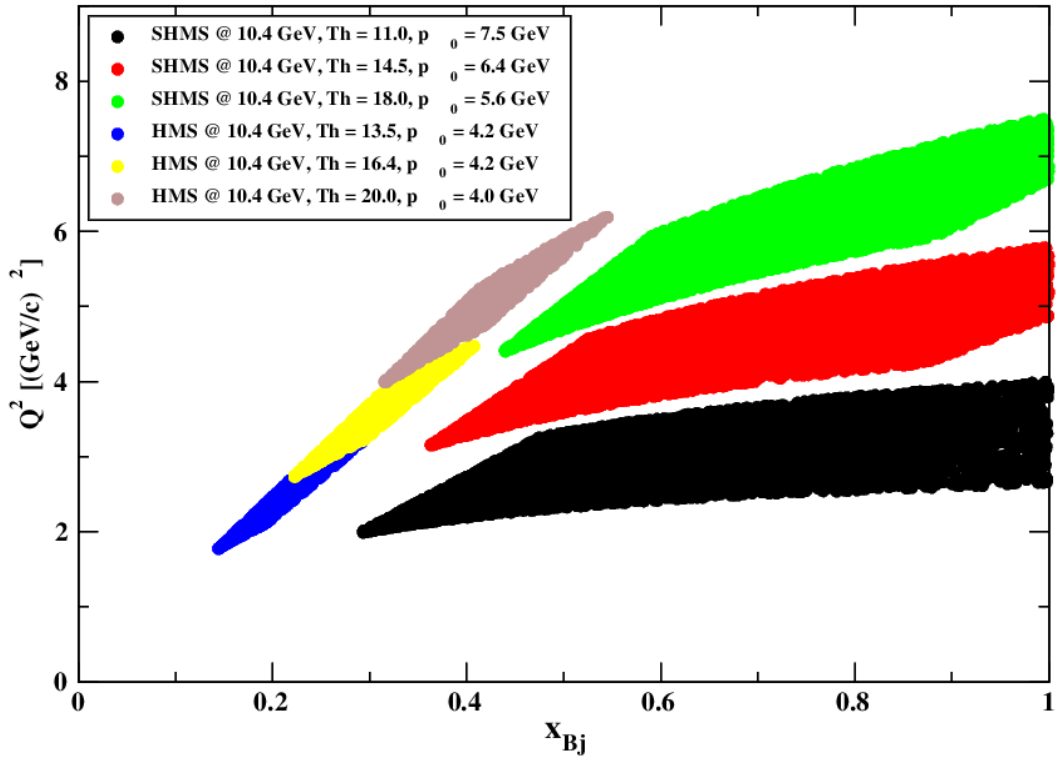


Figure 4.9: The kinematic coverage of HMS and SHMS for the experiment E12-06-121. The large momentum acceptance of SHMS is shown in the right part of the plot and the left part shows the HMS kinematic coverage.

Table 4.3: The list of HMS and SHMS production kinematic settings.

HMS Production					
Setting	P_0 (GeV/c)	Angle ($^\circ$)	x	Q^2	W
A	4.2	13.5	0.207	2.414	3.178
B	4.2	16.4	0.305	3.554	2.993
C	4.0	20.0	0.418	5.018	2.806
SHMS Production					
Setting	P_0 (GeV/c)	Angle ($^\circ$)	x	Q^2	W
X	7.5	11.0	0.527	2.866	1.859
Y	6.4	14.5	0.565	4.240	2.036
Z	5.6	18.0	0.633	5.701	2.046

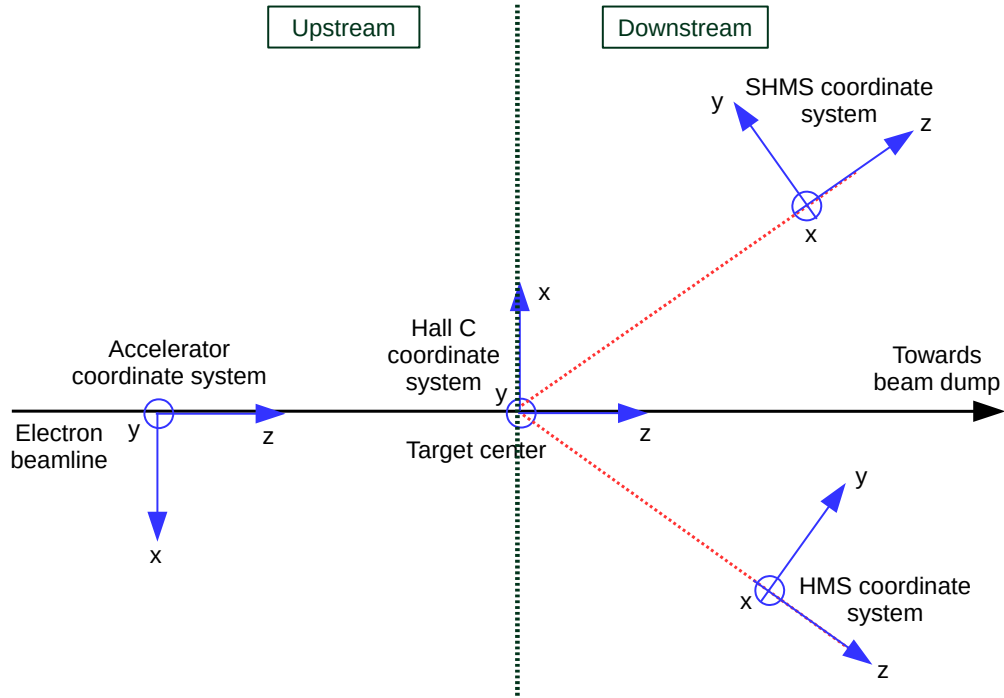


Figure 4.10: The different coordinate systems used in the experiment E12-06-121.

4.4 The Coordinate Systems

Different coordinate systems (Fig. 4.10) were used for the different parts of the experimental setup in Hall C. Two coordinate systems were used to define the incident electron beam before it scatters off the target: the accelerator coordinate system and the Hall C coordinate system. Another pair of coordinate systems, known as the spectrometer coordinate system and the target coordinate system were used to define and analyze the events after the scattering.

- **The accelerator coordinate system:**

Table 4.4: The definition of the accelerator coordinate system.

+x	Beam right	
+y	Pointing up	$-\hat{z} \times \hat{x}$
+z	Pointing downstream	Along electron beamline

- **The Hall C coordinate system:**

Table 4.5: The definition of the Hall C coordinate system.

+x	Beam left	
+y	Pointing up	$\hat{z} \times \hat{x}$
+z	Pointing downstream	Along electron beamline
Origin	Target center	x=0, y=0, z=0

- **The spectrometer coordinate system:**

Table 4.6: The definition of the spectrometer (HMS and SHMS) coordinate system.

+x	Pointing down	Vertical/ Dispersive
+y	Beam left	$\hat{z} \times \hat{x}$, Horizontal/ Non-dispersive
+z	Along the central ray of particle passing through detectors	Into the spectrometer/ Downstream
Origin	Center of the first drift chamber plane/ Focal plane	x=0, y=0, z=0

- **The target coordinate system:**

Table 4.7: The definition of the target coordinate system.

+x	Pointing down	Vertical/ Dispersive
+y	Beam left	$\hat{z} \times \hat{x}$, Horizontal/ Non-dispersive
+z	Along the central ray of particle passing through detectors	Into the spectrometer/ Downstream
Origin	Target center	x=0, y=0, z=0

Chapter 5 Electron Beamline Instrumentation and Polarimetry

The beamline instrumentation or the devices to measure the electron beam characteristics were located at the upstream side of the target. The most important devices were the beam position monitors (BPMs), beam current monitors (BCMs), and the Moller polarimetry setup which will be discussed in the following sections.

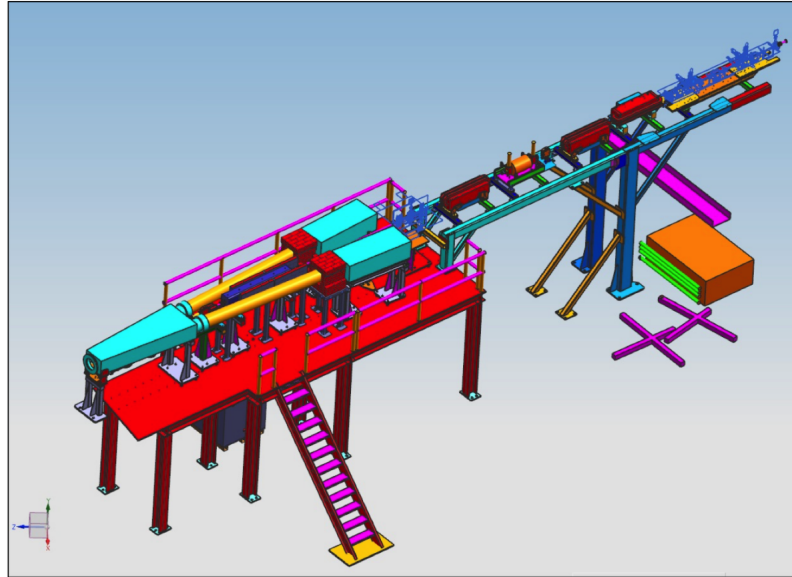


Figure 5.1: The view of the Hall C beamline looking from the entrance to the hall towards the target region [76].

5.1 Electron Beam Position Monitors

During the experiment E12-06-121, two beam position monitors (BPMs): IPM3H07A and IPM3H07C were used to monitor the electron beam trajectory and its position (x,y) on the target. The IPM3H07A and IPM3H07C were located 3.71 m and 1.23 m away from the target center in the upstream direction, respectively. Each BPM consisted of a 4-wire antenna array which was tuned to the fundamental beam RF frequency (1.497 GHz)[80]. The BPM signals were calibrated using harp scans where the harps were scanned across the beam to detect the resulting scattered particles. The relative position of the electron beam for currents above 1 μA were determined (within 100 microns) using the standard difference-over-sum technique [76]. The average beam positions (averaged over 0.3 seconds) from the BPMs were read out and updated in the EPICS database every few seconds with reference timestamps. In addition to that, event by event BPM information was also recorded in a Jefferson Lab software package named CODA (CEBAF online data acquisition package). The beam positions were recorded in the left handed, accelerator or EPICS coordinate system.

5.2 Electron Beam Current Monitors and Accumulated Charge

A number of beam current monitors were located (Fig. 5.2) on the upstream side of the target region named as: BCM1, BCM2, BCM4A, BCM4B, BCM4C and Unser monitor. All the BCMS were readout with EPICS. For experiment E12-06-121 BCM1, BCM2, and the Unser monitor were used as the primary system. The Unser monitor (parametric current transformer) provided an absolute reference for the beam current measurement. The offset from the calibrated Unser signal drifted significantly over a few minutes and that drift was measured during the calibration runs. The other BCMS were very stable RF cavity monitors tuned to the fundamental beam frequency (1.497 GHz). When calibrating the RF cavities, the Unser drift was removed and the readout from them was used for each run. The BCM runs were taken twice during the experiment and the BCM calibration [81] was performed by Dave Mack and verified by M. Cardona [82] during the offline experimental data analysis. The average beam current used in the production runs of the experiment E12-06-121 was $\sim 30 \mu\text{A}$ and the total accumulated charge for each run was determined from the BCM readouts.

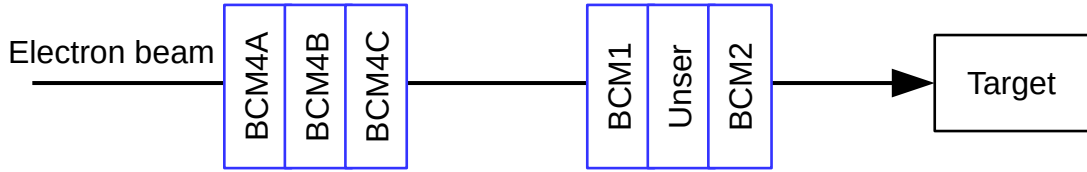


Figure 5.2: The schematic of the beam current monitor system located in Hall C.

5.3 Electron Beam Energy Measurement

The Hall C beam energy measurement was done by the Jefferson Lab Machine Control Center (MCC) during the experiment. The assumption was that the beam followed a central path through the dipole arc. The arc section in Hall C consisted of eight dipole magnets that deflected the electron beam with a bend angle of 37.5° at the entrance of the hall[76]. Combining the information of the beam positions and the bend angle at the entrance and exit of the arc, the beam energy was calculated using the following formula.[83]

$$E = \frac{k \int \vec{B} \cdot d\vec{l}}{\theta} \quad (5.1)$$

Where $k = 0.299792 \left(\frac{\text{GeV} \cdot \text{rad}}{\text{T} \cdot \text{m}} \right)$ was the speed of light, the field integral of the dipole magnets was $\int \vec{B} \cdot d\vec{l} (\text{T} \cdot \text{m})$, and the bend angle of the beam was θ (rad). The average beam energy was $\sim 10.38 \text{ GeV}$ for the 5-pass production running.

5.4 Electron Beam Polarization Measurement

In the experiment E12-06-121, the electron beam polarization was measured using Moller polarimetry. Moller scattering ($e + e \rightarrow e + e$) is a QED process and the cross section can be calculated to very high precision. For a longitudinally polarized electron beam ($P_b^z \parallel \hat{z}$) and longitudinally polarized target ($P_t^z \parallel \hat{z}$), the cross section in the center of mass frame (assuming that the scattering happens in x-z plane) can be written as,

$$\frac{d\sigma}{d\Omega} = \frac{d\sigma_0}{d\Omega} [1 + P_b^z P_t^z a_{zz}(\theta_{CM})]. \quad (5.2)$$

Where, $\frac{d\sigma_0}{d\Omega}$ is the unpolarized cross section and a_{zz} is the analyzing power. They are expressed as,

$$\frac{d\sigma_0}{d\Omega} = \left[\frac{\alpha(4 - \sin^2\theta_{CM})}{(2m_e\gamma\sin^2\theta_{CM})} \right]^2 \quad (5.3)$$

$$a_{zz}(\theta_{CM}) = \frac{-\sin^2\theta_{CM}(7 + \cos^2\theta_{CM})}{(3 + \cos^2\theta_{CM})^2} \quad (5.4)$$

$$a_{xx}(\theta_{CM}) = -a_{yy}(\theta_{CM}) = \frac{\sin^4\theta_{CM}}{(3 + \cos^2\theta_{CM})^2}, \quad (5.5)$$

with m_e = electron mass and, $\gamma = \frac{E}{m_e c^2}$. The electron beam polarization was effectively measured by measuring the cross section asymmetry when the beam and target spins were parallel and anti-parallel to each other.

$$\epsilon = \frac{\frac{d\sigma^{\uparrow\uparrow}}{d\Omega} - \frac{d\sigma^{\uparrow\downarrow}}{d\Omega}}{\frac{d\sigma^{\uparrow\uparrow}}{d\Omega} + \frac{d\sigma^{\uparrow\downarrow}}{d\Omega}} = P_b^z P_t^z a_{zz}(\theta_{CM}) \quad (5.6)$$

$$P_b^z = \frac{\epsilon}{P_t^z a_{zz}} \quad (5.7)$$

As shown in the Fig. 5.3a, the analyzing power, $a_{zz}(\theta_{CM})$ and, $\frac{d\sigma}{d\Omega_{lab}}$ are maximal at $\theta_{CM}=90^\circ$.

$$a_{zz}(\theta_{CM} = 90^\circ) = -\frac{7}{9} \quad (5.8)$$

$$\frac{d\sigma_0}{d\Omega_{lab}}(\theta_{CM} = 90^\circ) = 179 \frac{mbarn}{sr} \quad (5.9)$$

For a target and beam polarization of 100% , the cross-section asymmetry determines the effective analyzing power that includes effects from all the background contributions listed below.

- Radiative tail of the electron-nucleus scattering from the nuclei in the Moller target.
- The low energy electrons and photons produced in the bremsstrahlung process in the target and vacuum windows present in the setup.

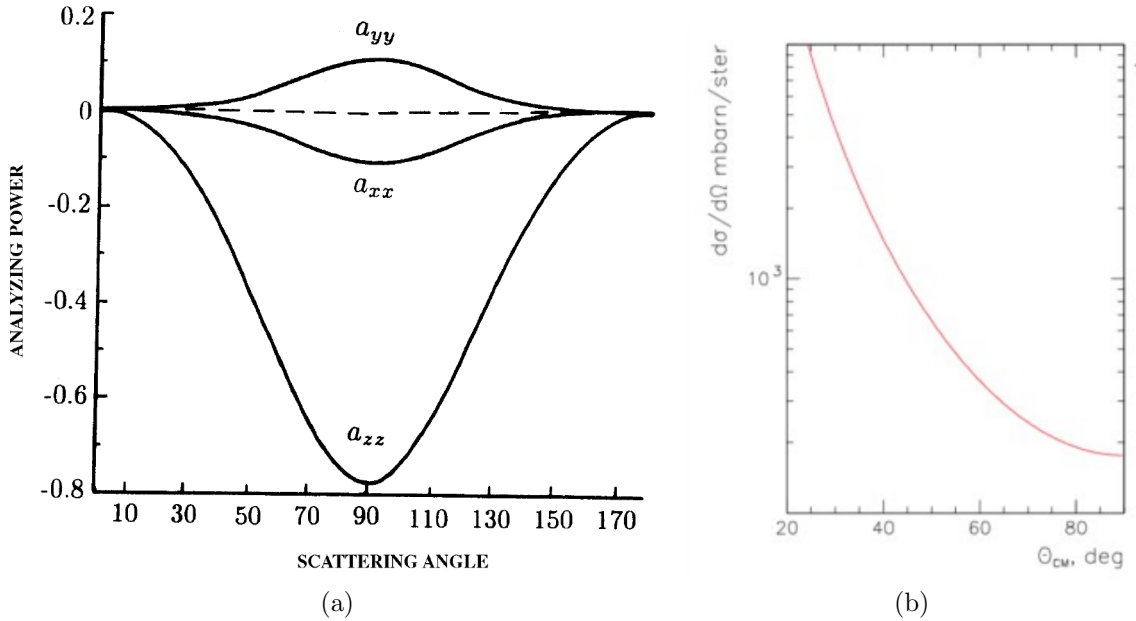


Figure 5.3: The analyzing powers (a_{xx} , a_{yy} , a_{zz}) as a function of scattering angle in the center of mass frame (θ_{CM}) in Moller scattering [84].

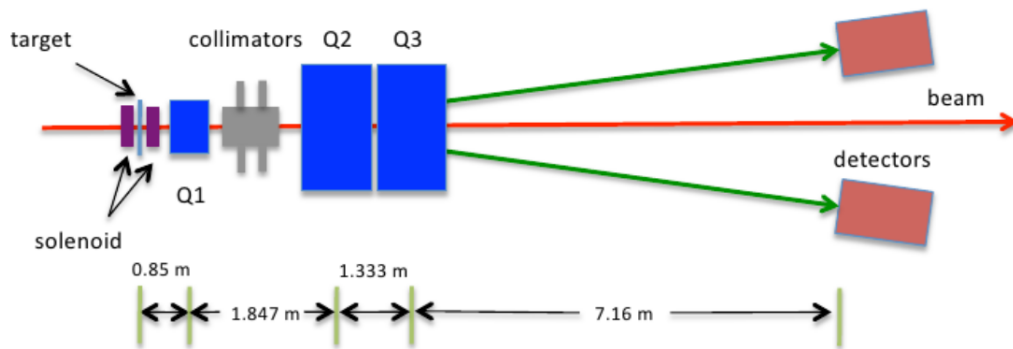
In addition to the background contributions, the other sources of uncertainties in the Moller polarimetry were:

- Error in determining the target polarization.
- Influence of the atomic motion of the target electrons on the effective analyzing power: The momentum distribution (\vec{p}_t) of the bound target electrons modified the lab scattering angle ($\theta_0 \rightarrow \theta'$) that resulted in an uncertainty. The inner shell electrons (unpolarized) had much larger momenta than those in the outer shells (polarized). So, the detector that could resolve the scattering angle of the electrons, had a different acceptance for scattering off a polarized vs. unpolarized electrons.

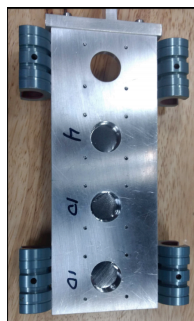
$$\theta' = \theta_0 \sqrt{\left(1 + \frac{\vec{p}_t \cdot \hat{z}}{m_e}\right)} \quad (5.10)$$

- Statistical precision of data.

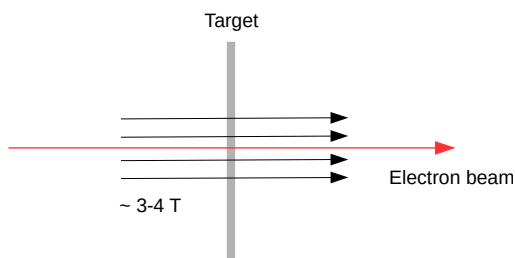
Using a detector with large acceptance, the influence of the atomic motion of the electrons on the analyzing power was reduced and a high statistical precision was achieved without increasing the data acquisition time significantly. The background contribution from Mott scattering was reduced by using the coincidence detection system. However, the dominating systematic uncertainty came from the Moller target polarization measurement.



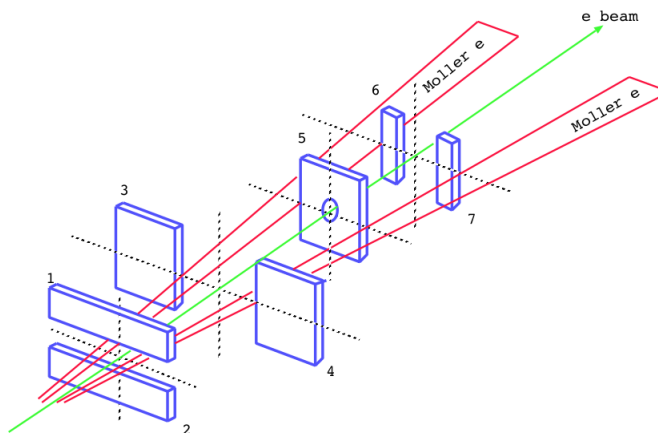
(a) The Moller setup in Hall C.



(b) Iron target.



(c) Target saturation.



(d) The Movable collimators.

Figure 5.4: (a) The layout of the target, quadrupoles, collimators, and the detectors are shown. (b) The iron targets with different thicknesses were placed in a target ladder which could be remotely moved horizontally into the beam. For the purpose of the experiment E12-06-121, only the $4\ \mu\text{m}$ thick target was used. (c) Target saturation using $\sim 3\text{-}4\ \text{T}$ magnetic field, the polarization was out-of-plane. (d) The movable collimators in the beamline are shown. [76].

5.4.1 Moller Polarimeter Setup

The Moller polarimeter in Hall C consisted of an iron target, target solenoid, movable collimators, four quadrupole magnets, and the detectors as shown in Fig. 5.4a. Each component will be discussed in detail in the following section.

- **Moller Target:** A thin foil of pure iron with thickness $4 \mu m$ was used as the Moller target (Fig. 5.4b). The target was polarized out-of-plane using a 3-4 T magnetic field as shown in Fig. 5.4c. During the experiment, the target polarization was 8.014% which was measured with $\sim 0.022\%$ accuracy.
- **Target Solenoid:** A superconducting solenoid was used to generate the high magnetic field for polarizing the target. It was a split-coil magnet that could generate a maximum of 4 T magnetic field. The liquid nitrogen and the liquid helium were used as the cryosystem for the solenoid.
- **Quadrupole Magnets:** A system of three quadrupole magnets (Q_1 , Q_2 , Q_3) were used to guide the scattered electrons towards the detectors. The quadrupole tuning was optimized using Monte-Carlo simulation to cover the whole energy range 0.8-12 GeV. However, the final quadrupole settings were determined from the Moller hodoscope left-right correlation and they were checked before every measurement to get an acceptable tune.
- **Collimators:** A set of seven collimators were used to reduce the singles rate and the accidental coincidences. They did not reduce real Moller coincidences. The collimator positions were first scanned in the Monte-Carlo simulation for the following two cases:
 - 1. Electron beam current = $1 \mu A$, target thickness = $10 \mu m$
 - 2. Electron beam current = $0.3 \mu A$, target thickness = $4 \mu m$

The simulation for the $10 \mu m$ target is shown in Fig. 5.5. However, we decided to use the $4 \mu m$ thick target, so the collimator scan was performed in Hall C with $0.3 \mu A$ beam current around the simulated values to get the optimum collimator position for the experiment. This study was done for all the collimators except collimator 5, which was a circular hole and it was fixed on the beamline. The collimator scan results and the simulation results for the $4 \mu m$ target are shown in the Fig. 5.6. The optimized values were chosen in the flat regions in the plot before the rate started to drop.

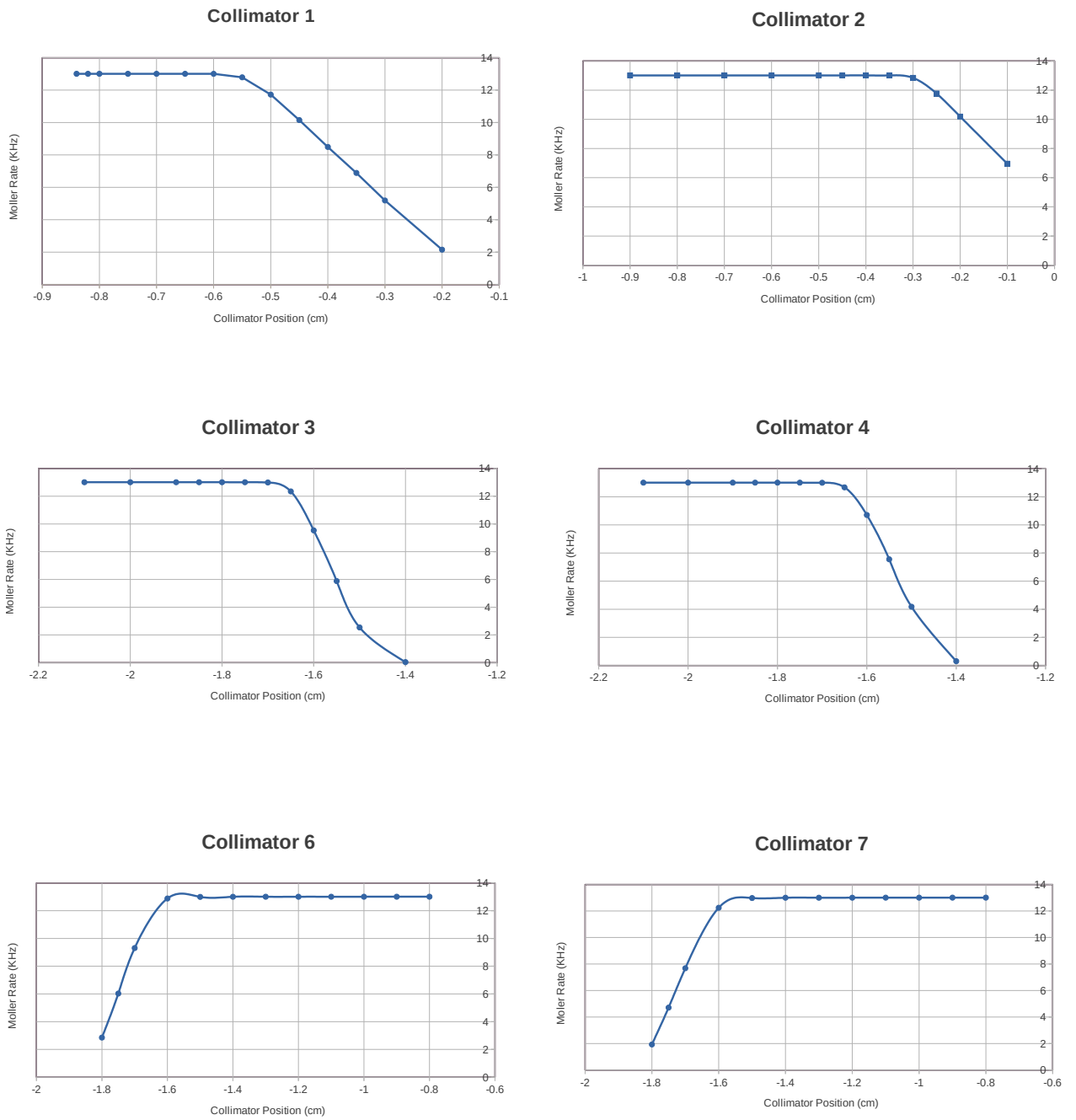


Figure 5.5: The results of the Monte-Carlo simulation of collimator scan for $10\ \mu\text{m}$ thick target and $1\ \mu\text{A}$ electron beam current.

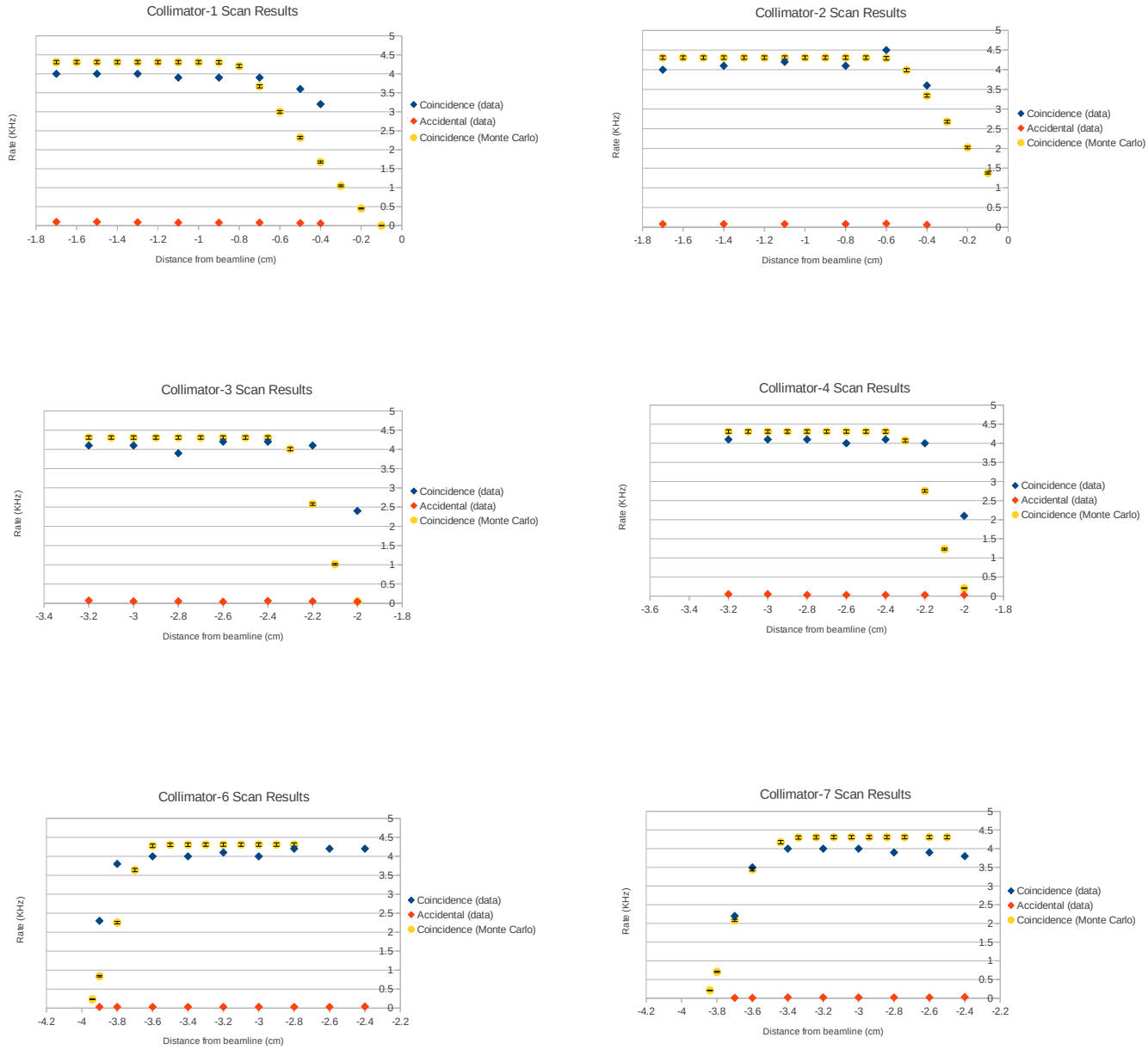


Figure 5.6: The results of the Monte-Carlo simulation of collimator scan and, the real collimator scans performed in Hall C before the experiment E12-06-121.

- Detectors:** The coincidence detection technique was used to detect the scattered electrons. So, two detectors were located on each side of the central electron beam path. As shown in the Fig. 5.7, a hodoscope and a lead glass shower counter were used to track the scattered electrons and to detect the electrons with appropriate energies respectively.

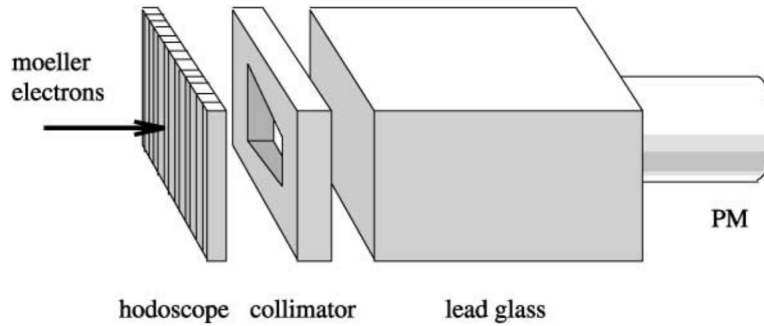


Figure 5.7: The Moller detector package consisting of the hodoscope, collimator, the lead glass counter and the photomultiplier tube [85].

5.4.2 Hall C Spin Dance

The accelerator at the Jefferson Lab sent longitudinally polarized electrons (with different degrees of polarization) simultaneously to all three experimental halls. The high degree of polarization in each hall was optimized by varying the initial electron spin direction at the beginning with a Wien filter. This procedure is known as “spin dance” and it was performed on February 3rd, 2020. Fig. 5.8 shows the four Wien angles at which the electron beam polarizations were measured in Hall C. The maximum possible polarization was $85.9\% \pm 0.3\%$.

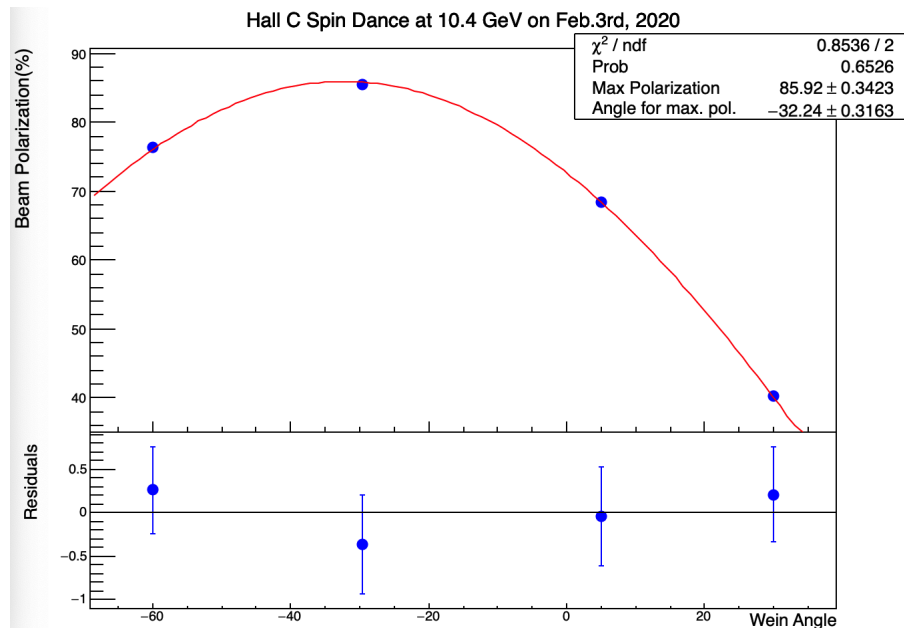


Figure 5.8: The results of the Hall C spin dance. Electron beam polarization was measured for four different Wien angle settings. The maximum polarization was obtained for the Wien angle of -32.24° [86].

5.4.3 Moller Measurement Results

Moller measurements were performed a number of times (once every week) during the experiment with a 10.38 GeV, 1 μ A electron beam. These were the first Moller measurements of the 12 GeV era and each measurement took 4-14 hours depending on the accelerator performance. The Fig. 5.9 shows the electron beam polarization values for each of the Moller measurements performed in 2020. Each point in the plot was the average of the several runs taken on a single day. Runs were taken with IHWP in the “IN” and “OUT” states. Then they were averaged with proper sign correction. This plot covers the electron beam polarization measurements for both the A_1^n and d_2^n experiments and it also shows the Jefferson Lab shutdown period during the Covid MEDCON6 phase. The bleed through (asymmetry measurement without any electron beam in Hall C) from the other experimental halls were measured and a correction of 0.0% to 1.0% was applied to each data point. The average beam polarization was $85.0\% \pm 0.3\%$ during the experiment.

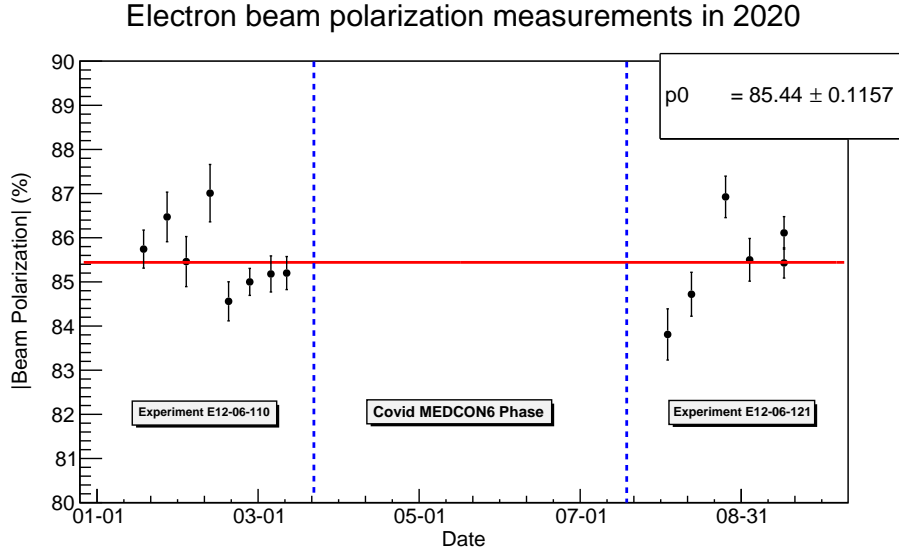


Figure 5.9: The Moller measurement results from that performed during the E12-06-110 and the E12-06-121 experiments.

The various relative systematic uncertainties associated with each parameter in the Eq. 5.7 that contributed to the total uncertainty in the electron beam polarization values in the plot are listed in the Table. 5.1. The time required to acquire the required statistics was very small and the statistical uncertainty was limited to $< 1.0\%$ in each measurement.

Table 5.1: The systematic uncertainties contributing to the electron beam polarization measurements.

Parameters	Uncertainty
Effective analyzing power	0.005%
Target polarization	3%

Chapter 6 The Polarized Helium-3 Target System

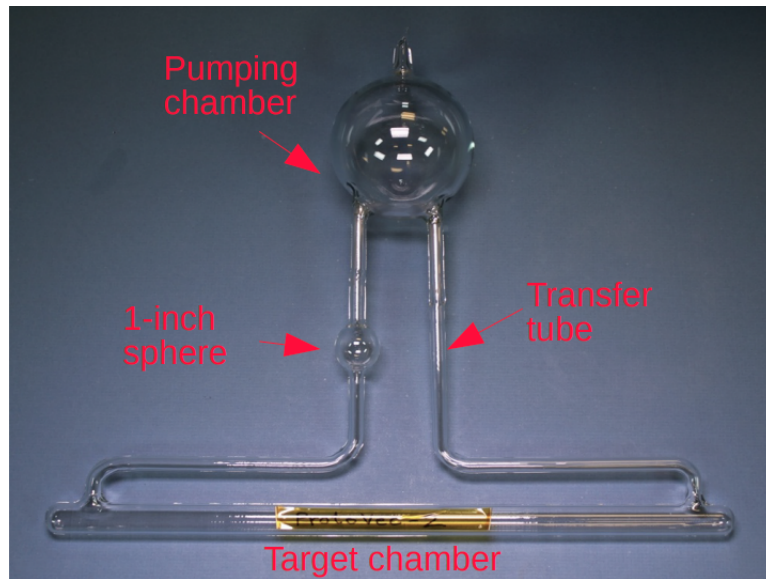
6.1 Target Cell

High pressure (fill density up to 8 amg) ^3He gas target cells were hand blown in Princeton and filled in the laboratory of University of Virginia. The target cells were made of GE180 aluminosilicate glass. As shown in Fig. 6.1, the target cell was composed of three chambers as follows.

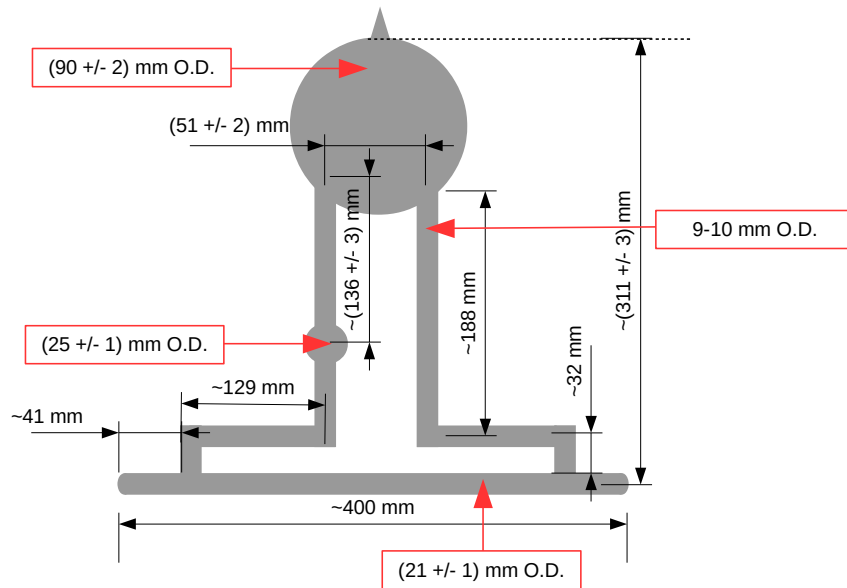
- **Pumping chamber:** The top spherical part of the target cell is known as the pumping chamber (pc). The diameter of the sphere was ~ 3 inches and it contained the alkali atoms (Rb, K), N_2 gas, and ^3He gas mixture. The little pull off on the top of the pumping chamber was used for sealing the target cell after it was filled and detached it from the filling apparatus. The pumping chamber was heated upto $\sim 230^\circ\text{C}$ to vaporize the present alkali metals (it will be discussed in details in the next section) and two temperature sensors (RTDs) were attached on the outer pc surface to monitor and log the pumping chamber temperature during the experiment. The resistance change of the RTD (Resistance Temperature Detector) sensors is proportional to the temperature change. The temperature was measured from the RTD resistance change with known calibration. A high power laser with a wavelength of ~ 795 nm was incident on this chamber to polarize the alkali atoms (SEOP method, will be discussed in next section).
- **Target chamber:** The cylindrical chamber at the bottom is known as the target chamber (tc) from where the polarized electron beam was scattered during the experiment. This chamber was ~ 40 cm long with an inner radius of ~ 0.95 cm. Two nitrogen cooling jets were used to cool down the end windows of the target chamber to $\sim 70^\circ\text{C}$ to create temperature gradient from the pumping chamber. Five temperature sensors (RTDs) were attached to the target chamber along its length.
- **Transfer tubes:** The two ~ 18 cm long tubes in the middle that connect the pumping chamber and the target chamber, are called the transfer tubes (tt). The polarized ^3He gas from the pumping chamber diffused through the transfer tubes towards the target chamber which was at a lower temperature than the pumping chamber. The tiny spherical blob with an outer diameter of ~ 2.5 cm in one of the transfer tubes was used for the pulsed NMR polarimetry measurements (will be discussed in Chapter 6).

Three ^3He cells named Austin, Briana, and Tommy were used during the experiment. Due to the radiation and the continuous high power laser beam on the pumping chamber, the cell performance decreased over time and after 3-4 weeks of use, they were replaced. The cell characterization for each cell was done at the University of

Virginia and Jefferson Lab. The target fill density and cell end window thickness measurements were performed at the University of Virginia. The measurement results are listed in Table. 6.1.



(a) The different chambers of the glass target cell.



(b) The dimensions of the target cell.

Figure 6.1: The ^3He gas target cell and the dimensions of its different chambers.

The cell wall thickness measurements was performed at Jefferson Lab using an

ultrasonic thickness gauge (Olympus 45 MG). The gauge measured the time difference between the incident and reflected ultrasonic pulses on the GE180 glass surface. A series of measurements was done at different locations of each target cell and the measurement locations are marked by numbers and letters in Fig. 6.2. The results for all three chambers of the target cell Briana are listed in Table. 6.2 and the results for the target cells Tommy and Austin are listed in Table. 6.3. The average target chamber wall and end window thickness was ~ 0.15 cm and ~ 0.014 cm respectively.

Table 6.1: The target chamber window thickness measurement results, volumes of the three chambers and the fill density measurement results for the cells Briana, Tommy, and Austin.

	Fill density (amagat)	PC volume (cc)	TC volume (cc)	TT volume (cc)
Briana	6.938	289.53	99.88	26.97
Tommy	7.940	284.00	110.000	33.00
Austin	7.498	305.87	106.46	37.92
	Downstream window thickness (μm)	Upstream window thickness (μm)	Cold lifetime (hr)	Max. polarization (no beam) (%)
Briana	130.8890	127.9760	15.3	52.1
Tommy	136.9530	145.1070	15.2	54.0
Austin	137.4248	156.2006	20.0	52.0

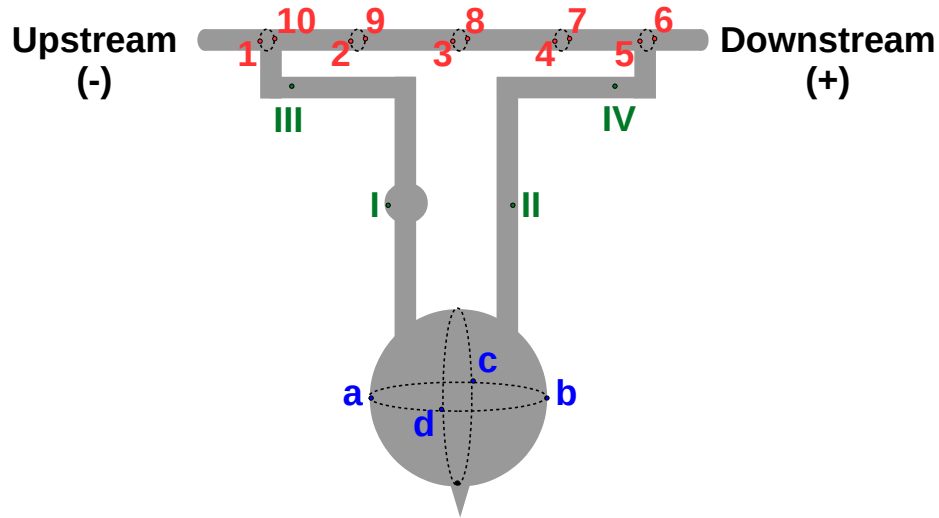


Figure 6.2: The locations where the target cell wall thickness was measured using the ultrasonic gauge (not to scale).

Table 6.2: The target cell wall thickness measurement results using the ultrasonic thickness gauge for the target cell Briana.

Target cell: Brianna			
Cell chamber	Measurement location	Position along z (cm)	Wall thickness (mm)
TC front	1	-12.50±0.16	1.49±0.01
	2	-6.25±0.16	1.50±0.01
	3	0.0±0.16	1.51±0.01
	4	+6.25±0.16	1.45±0.01
	5	+12.50±0.16	1.42±0.01
TC rear	6	-12.50±0.16	1.35±0.01
	7	-6.25±0.16	1.33±0.01
	8	0.0±0.16	1.33±0.01
	9	+6.25±0.16	1.35±0.01
	10	+12.50±0.16	1.29±0.01
PC	a	-4.37±0.16	3.73±0.01
	b	+4.37±0.16	3.75±0.01
	c	0.0±0.16	3.87±0.01
	d	0.0±0.16	3.64±0.01
TT	I	-2.70±0.16	2.19±0.01
	II	+2.70±0.16	2.13±0.01
	III	-6.25±0.16	1.99±0.01
	IV	+6.25±0.16	2.28±0.01

Temperature Corrected Target Density:

The fill density for the target cells listed in the Table. 6.1 were the extracted number densities at the room temperature. Under running conditions, the temperature of the ^3He cell was different from room temperature resulting in a different target density. The temperature gradient in different target chambers resulted in different number densities of the gas in the different chambers. The temperature correction to the density is essential to correctly analyze the experimental data and this was done by assuming that the ^3He gas behaved like an ideal gas. Considering the pressure was uniform in each chamber of the target cell,

$$\begin{aligned}
 P_{pc} &= P_{tc} \\
 \Rightarrow \frac{N_{pc}k_B T_{pc}}{V_{pc}} &= \frac{N_{tc}k_B T_{tc}}{V_{tc}} \\
 \Rightarrow N_{pc} &= \frac{V_{pc}}{V_{tc}} \frac{T_{tc}}{T_{pc}} N_{tc},
 \end{aligned} \tag{6.1}$$

Table 6.3: The target chamber wall thickness measurement results using the ultrasonic thickness gauge for the cells Tommy and Austin.

Target cell: Tommy			
Cell chamber	Measurement location	Position along z (cm)	Wall thickness (mm)
TC front	1	-12.50 ± 0.16	1.56 ± 0.01
	2	-6.25 ± 0.16	1.48 ± 0.01
	3	0.0 ± 0.16	1.51 ± 0.01
	4	$+6.25 \pm 0.16$	1.48 ± 0.01
	5	$+12.50 \pm 0.16$	1.45 ± 0.01
TC rear	6	-12.50 ± 0.16	1.34 ± 0.01
	7	-6.25 ± 0.16	1.26 ± 0.01
	8	0.0 ± 0.16	1.27 ± 0.01
	9	$+6.25 \pm 0.16$	1.27 ± 0.01
	10	$+12.50 \pm 0.16$	1.38 ± 0.01
Target cell: Austin			
Cell chamber	Measurement location	Position along z (cm)	Wall thickness (mm)
TC front	1	-12.50 ± 0.16	1.39 ± 0.01
	2	-6.25 ± 0.16	1.32 ± 0.01
	3	0.0 ± 0.16	1.33 ± 0.01
	4	$+6.25 \pm 0.16$	1.32 ± 0.01
	5	$+12.50 \pm 0.16$	1.52 ± 0.01
TC rear	6	-12.50 ± 0.16	1.43 ± 0.01
	7	-6.25 ± 0.16	1.29 ± 0.01
	8	0.0 ± 0.16	1.33 ± 0.01
	9	$+6.25 \pm 0.16$	1.32 ± 0.01
	10	$+12.50 \pm 0.16$	1.43 ± 0.01

$$\begin{aligned}
 P_{tc} &= P_{tt} \\
 \Rightarrow \frac{N_{tc} k_B T_{tc}}{V_{tc}} &= \frac{N_{tt} k_B T_{tt}}{V_{tt}} \\
 \Rightarrow N_{tt} &= \frac{V_{tt} T_{tc}}{V_{tc} T_{tt}} N_{tc}.
 \end{aligned} \tag{6.2}$$

Where, P, V, T, and N are the pressure, volume, temperature, and number of particles respectively in the target chamber, pumping chamber and transfer tubes of the target cell represented by the subscripts tc, pc, and tt respectively, and k_B is the Boltzmann constant. The total number of constituents in the target cell, N_{tot} can be written in terms of the fill density, η_{fill} as follows,

$$\begin{aligned}
N_{tot} &= N_{tc} + N_{pc} + N_{tt} \\
\Rightarrow \eta_{fill} V_{tot} &= N_{tc} + N_{pc} + N_{tt}.
\end{aligned} \tag{6.3}$$

Using the Eq. 6.1, Eq. 6.2, and Eq. 6.3 the ^3He number density in the target chamber (η_{tc}) can be derived as,

$$\begin{aligned}
\Rightarrow \eta_{fill} V_{tot} &= N_{tc} \left[\frac{V_{pc} T_{tc}}{V_{tc} T_{pc}} + \frac{V_{tt} T_{tc}}{V_{tc} T_{tt}} + 1 \right] \\
\Rightarrow \eta_{fill} V_{tot} &= \eta_{tc} V_{tc} \left[\frac{V_{pc} T_{tc}}{V_{tc} T_{pc}} + \frac{V_{tt} T_{tc}}{V_{tc} T_{tt}} + 1 \right] \\
\Rightarrow \eta_{fill} V_{tot} &= \eta_{tc} \left[\frac{V_{pc} T_{tc}}{T_{pc}} + \frac{V_{tt} T_{tc}}{T_{tt}} + V_{tc} \right] \\
\Rightarrow \eta_{tc} &= \frac{\eta_{fill} V_{tot}}{\left[\frac{V_{pc} T_{tc}}{T_{pc}} + \frac{V_{tt} T_{tc}}{T_{tt}} + V_{tc} \right]}.
\end{aligned} \tag{6.4}$$

A similar calculation for the pumping chamber gives,

$$\eta_{pc} = \frac{\eta_{fill} V_{tot}}{\left[\frac{V_{tc} T_{tc}}{T_{pc}} + \frac{V_{tt} T_{pc}}{T_{tt}} + V_{pc} \right]}. \tag{6.5}$$

The RTD readings from the pumping and target chambers with proper corrections were used to determine the temperature inside those chambers under running conditions. The temperatures inside the different chambers were different from the surface because of the pumping laser shining from two different directions (longitudinal, and transverse) on the pumping chamber, location of the target oven, cooling jets to cool the target windows and so on. The final temperature corrected ^3He densities in the target chamber are listed in the Table. 6.4 below.

Table 6.4: The temperature corrected ^3He densities in the target chamber of the cells Brianna, Tommy, and Austin.

Target Cell	T_{pc} ($^{\circ}\text{C}$)	T_{tt} ($^{\circ}\text{C}$)	T_{tc} ($^{\circ}\text{C}$)	η_{tc} (amg)
Brianna	240.0	38.0	30.0	9.70
Tommy	240.0	38.0	30.0	10.82
Austin	240.0	38.0	30.0	10.40

6.2 The Holding Magnetic Field

The holding magnetic field for the experiment was generated using two pairs of orthogonal Helmholtz coils as shown in Fig. 6.3. The axis of the large pair of Helmholtz coils was parallel to the electron beam line and the axis of the small pair of Helmholtz

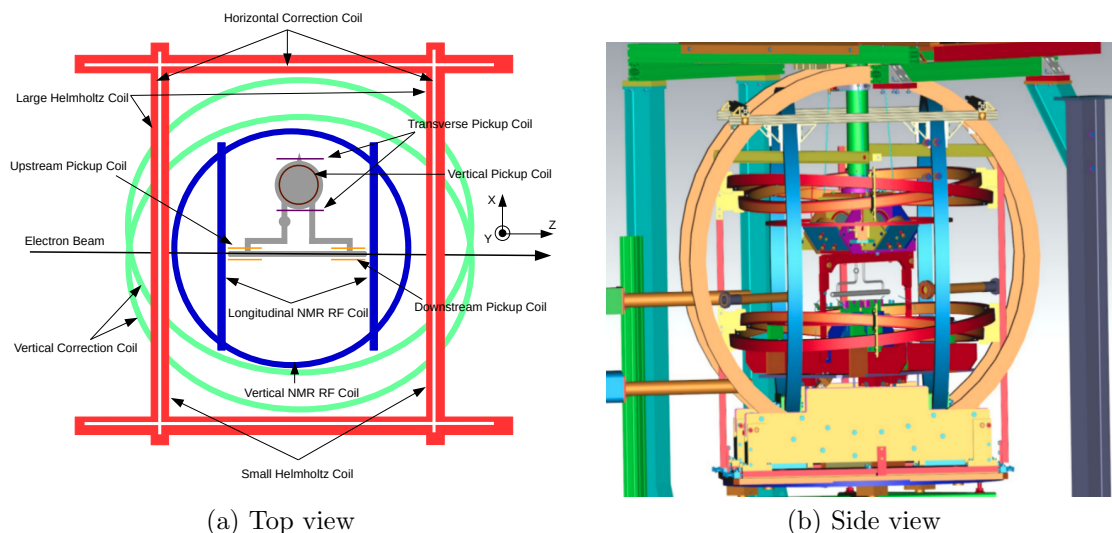


Figure 6.3: The target magnetic field system.

coils was perpendicular to the same. These coils were used to generate ~ 25 Gauss magnetic field either in longitudinal ($+Z$, $-Z$) or in transverse ($+X$, $-X$) direction to align the ^3He spins either parallel or anti-parallel to the electron spin. The characteristics of the main Helmholtz coils are listed in the Table. 6.5. Longitudinal and

Table 6.5: The characteristics of the main Helmholtz coils.

Coil Name	Inner Radius (m)	No. of Turns	Resistance(Ω)
Large Coil	0.725	272	3
Small Coil	0.635	256	3

transverse horizontal correction coils were used to reduce the magnetic field gradient in the horizontal direction. Those coils were added to the main Helmholtz coils (100 turns each). Two pairs of vertical correction coils were used to correct the vertical fringe field from the horizontal bender (HB) magnet of the Super High Momentum Spectrometer. These coils were tilted by $\sim 6^\circ$ about the X-axis. The power supplies for all the coils were controlled remotely during the experiment.

6.3 The Target Optics

The target laser system is composed of eight monochromatic, infrared (795 nm), narrow-band (spectral width less than 0.3 nm) diode lasers that could provide up to 120 W laser power in longitudinal and transverse direction (four lasers in each direction). The laser controllers with the interlock system were placed in a laser room outside the hall close to the counting house to prevent accidental laser exposure. The operating current and the temperature of the laser diodes were 35-40 A and 15°C -

26.5°C respectively. All the lasers were controlled and monitored through EPICS remotely during the experiment.

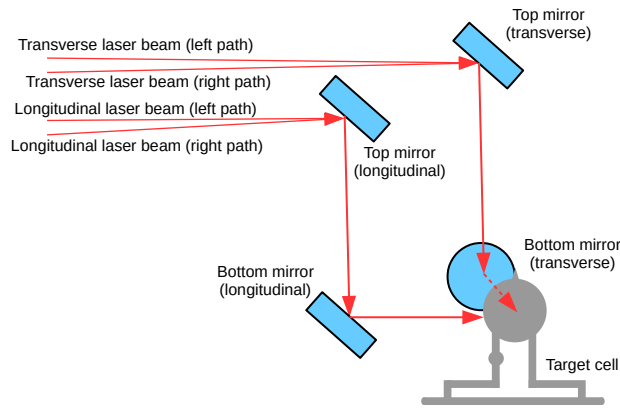
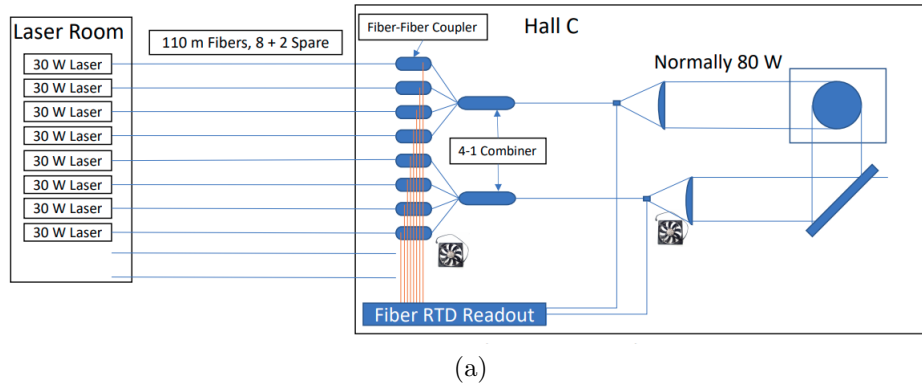
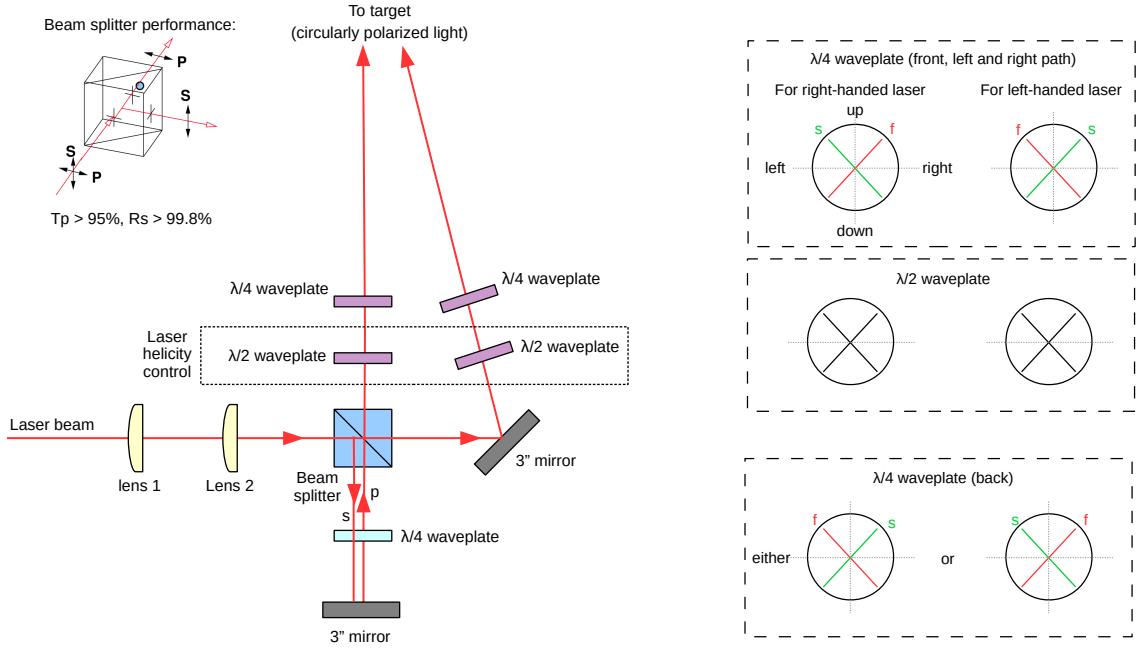


Figure 6.4: (a) The laser transport from the laser room to Hall C via optical fibers. (b) The top and bottom mirror orientations reflect the laser beam towards the pumping chamber for the longitudinal and transverse directions.

The laser beam was transported to the hall via eight ~ 110 meter long optical fibers (radius of aperture = 0.6 mm, output divergence angle = 0.22 radians) which resulted in a 10% power loss. As shown in Fig. 6.4, four laser beams were combined using a 4-to-1 combiner, and then it passed through a series of 2-3 inches diameter optics containing lenses, polarizers, and mirrors towards the pumping chamber of the target cell to produce transverse and longitudinal polarization of the target. The goal was to get a beam spot with 3.5 inches diameter on the pumping chamber of the target cell. As shown in Fig. 6.5, the whole optics system was installed on two tables. The top table contained the longitudinal optics and the bottom table had the transverse optics. For each direction, a pair of convex lenses was used to focus the laser beam to the beam splitter where it was splitted into two paths. The direct beam (p-wave) was reflected from a mirror with 3 inches diameter and was directed to the pumping chamber. The s-wave part of the beam was first passed through a quarter waveplate

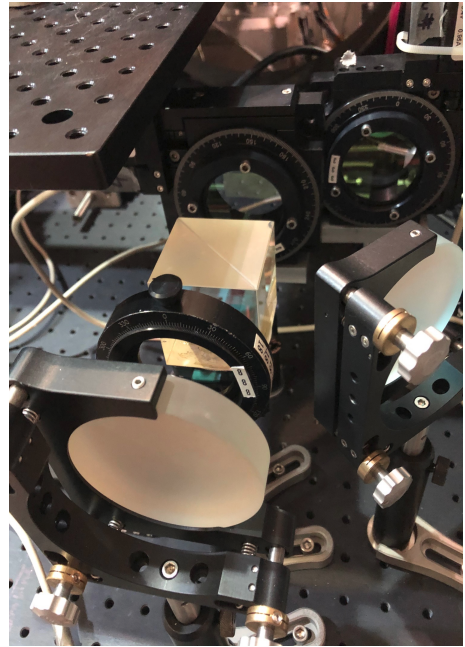


(a) Top view of the optics setup inside the optics enclosure.

(b) Waveplate orientation (facing the target).



(c) Longitudinal optics alignment on the top table.



(d) Transverse optics alignment on the bottom table.

Figure 6.5: The longitudinal and transverse optics setup in Hall C.

(fast and slow axes oriented at 45° w.r.t. the horizontal or vertical direction), then it was reflected from a mirror with 3 inches diameter and, it was passed through the same quarter waveplate again. This way the s-wave was transformed into p-

wave before passing through the beam splitter again without any reflection. So, both the left and right laser beams approaching the target in Fig. 6.5 had the same linear polarization before passing through the next set of half and quarter waveplates. The quarter waveplates in the right and left beam path were used to transform the linear polarization to circular polarization. The Fig. 6.5(b) shows the orientation of the quarter waveplates to get the maximum circular polarization (95-100%) on the pumping chamber. However, the angles were further optimized remotely around the set angle using the laser absorption spectrum.

The half-wave plates were used to change the helicity of the laser beam (σ_+ , σ_-) during the experiment. The resulting laser beams from the left and the right paths were then reflected off two adjustable dielectric mirrors with diameter 6 inches, aligned in such a way that the laser beam spot hits the center of the pumping chamber. When the laser beam was reflected from a dielectric mirror, an additional phase was introduced in its circular polarization. As shown in Fig. 6.4(b), in case of the transverse direction, the phase introduced from the top and the bottom mirrors cancel each other. On the other hand in case of the longitudinal direction, the parallel orientation of the top and the bottom mirrors results in addition of the phases from each of them. As shown in Fig. 6.5(c), an extra pair of quarter wave plates was installed in front of the remaining longitudinal setup to compensate for that extra phase. All the half waveplates, and the quarter waveplates were motor controlled and the angles could be set remotely. RTDs were attached to every fiber coupling to monitor the temperature through EPICS. The whole optics system was enclosed in a box on top of the target region and it was kept completely sealed when the lasers were turned on to full power. A camera was also placed inside the optics box to monitor the quarter waveplate angles periodically.

6.4 The Target Oven and the Heating System

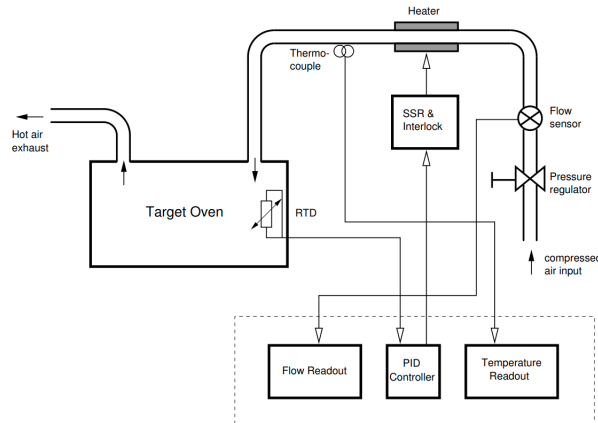


Figure 6.6: The target oven control system. The instruments inside the dashed box were located far away from the target region and the rest were located on top of the target cell.

The pumping chamber of the target cell was inserted inside an oven made of non-magnetic, heat resistant material CS85. The oven had four circular glass windows (6 inches diameter) which allowed the laser beam to enter the oven, pass through the pumping chamber, and finally exit the oven. The heating system layout is displayed in the Fig. 6.6. The air was inserted through a shut-off valve with a pressure regulator and passed through a pair of resistive heaters. The hot air entered the oven through insulated copper tubing and exited from the other side where it was cooled down. RTDs were attached to the oven to monitor the oven temperature and the temperature readings were connected to a PID feedback system to maintain the oven temperature to about $\sim 240^\circ\text{C}$ throughout the experiment.

6.5 Polarizing The Target

The ^3He target was polarized using the hybrid spin exchange optical pumping (HSEOP) method which was based on the optical pumping of the Rb alkali vapor following the spin exchange between the polarized alkali atoms (Rb and K) and the ^3He nuclei. The goal was to generate a source of polarized electrons which will collide with the ^3He nuclei to transfer their polarization. HSEOP is better than SEOP because it transfers the polarization of the alkali atoms to the ^3He nuclei with much greater efficiency. The collision between K and ^3He transfers the spin quicker than the collision between Rb and ^3He [74].

- **Optical Pumping:** The electron configuration of ^{85}Rb is, $1s^2 2s^2 2p^6 3s^2 3p^6 3d^{10} 4s^2 4p^6 5s^1$ with a single electron in the outer shell. The nuclear spin of ^{85}Rb is $\frac{5}{2}$, which results in the following ground state Hamiltonian operator when interacting with the holding magnetic field \vec{B} [69][70]:

$$\hat{H} = Ag\vec{I}\cdot\vec{S} + g_e\mu_B S_z B_z - \frac{\mu_I}{I} I_z B_z.$$

The first term represents the vector coupling between the electron spin and the nuclear spin. The second term describes the coupling of the electron spin to the magnetic field \vec{B} with strength $\mu_e = g_e\mu_B$, where g_e is the the electron g value ($g_e = 2.00232$) and μ_B is the Bohr magneton ($\mu_B = 0.0579 \text{ MeV T}^{-1}$). The third term represents the coupling of the nuclear spin with the magnetic field where the nuclear magneton, $\mu_I = 4.26426 \times 10^{-12} \text{ MeV T}^{-1}$. The eigenstates of the total angular momentum of the ^{85}Rb atom are labeled by the quantum number, $F = I \pm S$ of the total spin vector $\vec{F} = \vec{I} + \vec{S}$. The presence of the external magnetic field causes the splitting of the F state into $2F+1$ sublevels as shown in the Fig. 6.7. the energy levels are labeled by $m_F = -F, -F + 1, \dots, F - 1, F$ resulting from $m_F = m_I + m_S$ with $m_I = -I, -I + 1, \dots, I - 1, I$ and, $m_S = -S, -S + 1, \dots, S - 1, S$. The 795 nm circularly polarized laser light corresponds to the D_1 transition ($5S_{\frac{1}{2}} \rightarrow 5P_{\frac{1}{2}}$) of the ^{85}Rb . The laser light is absorbed by all the $S_{\frac{1}{2}}$ substates of the ^{85}Rb atoms and get excited to the $P_{\frac{1}{2}}$ state following the selection rule, $\Delta m_F = \pm 1$ for the right (σ_+) and the left (σ_-) circularly polarized light respectively. As there is no $m_F = 4$ substate of the $P_{\frac{1}{2}}$

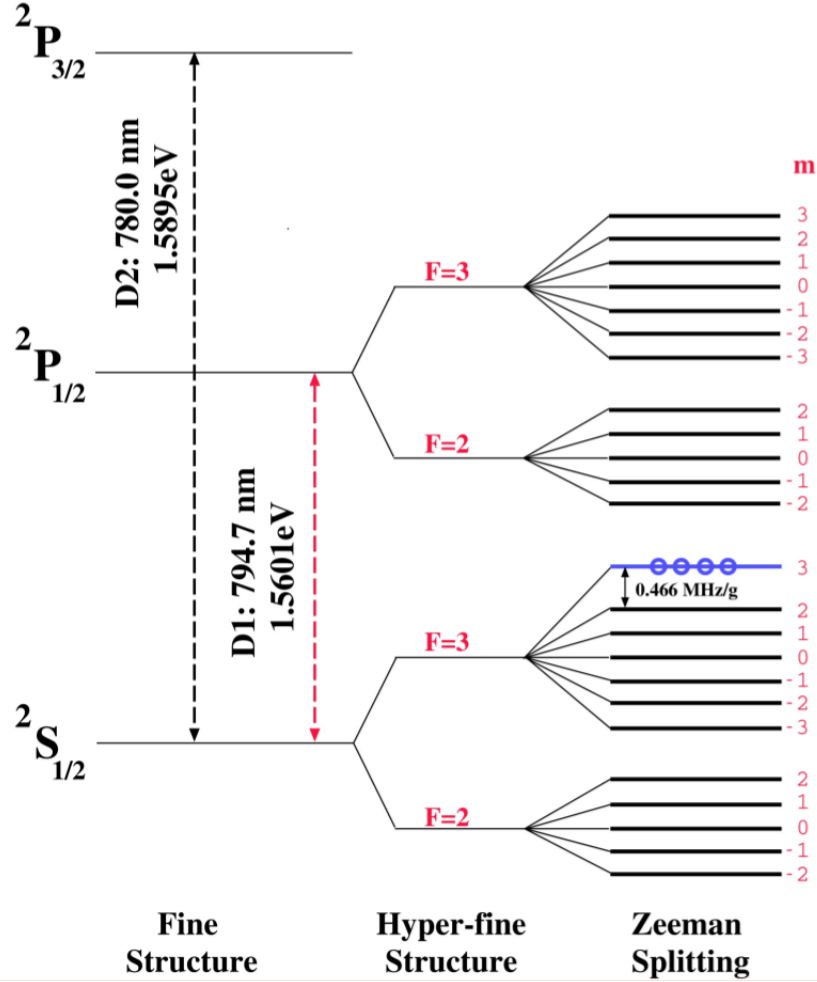


Figure 6.7: The splitting of the energy levels of ^{85}Rb in presence of the external magnetic field [72].

state, the electrons from the $m_F = 3$ substate of the $S_{\frac{1}{2}}$ state cannot get excited and get trapped in that level when right circularly polarized light is incident on the cell. On the other hand the spontaneous and stimulated emission happen following the selection rule, $\Delta m_F = \pm 1, 0$. The highest magnetic sublevel gets depopulated by collision and most of the electrons decay back to the $m_F = 3$ substate of the $S_{\frac{1}{2}}$ level. This is known as pumping of the $m_F = 3$ level of the ground state. Similarly, for the left circularly polarized laser, all atoms are polarized into the $m_F = -3$ state. When the electrons decay to the $S_{\frac{1}{2}}$ state, they emit unpolarized photons with wavelength corresponding to the D_1 transition which can excite electrons from the $m_F = +3$ state. To minimize this depolarization effect, the nitrogen gas is used in the target cell to provide a channel for the excited electrons to decay to ground state without emitting photons.

- **Spin Exchange:** The spin exchange between the Rb and K atoms transfers the polarization of the Rb atoms to the K atoms. Another subsequent spin exchange

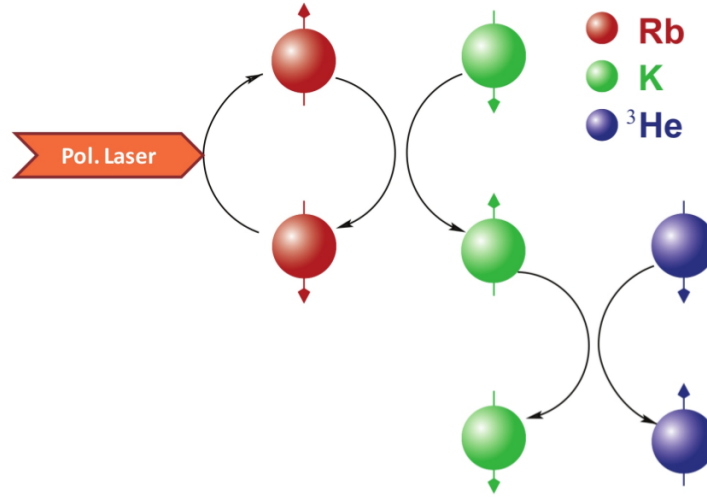


Figure 6.8: The demonstration of the spin exchange polarization transfer from the alkali atoms to the ^3He nuclei. [15]

collision between K atoms and the ^3He nuclei transfers the polarization to the ^3He nuclei through a weak hyperfine Fermi contact interaction as shown in the Fig. 6.8.

Step 1: $\text{Rb}(\uparrow) + \text{K}(\downarrow) = \text{Rb}(\downarrow) + \text{K}(\uparrow)$.

The interaction potential ($\sim\text{eV}$) for this collision is of electrostatic nature and it can be written as,

$$V(r) = V_0(r) + \vec{S}_{\text{Rb}}\vec{S}_{\text{K}}V_1(r),$$

where r is the interatomic separation and \vec{S}_{Rb} and \vec{S}_{K} are the spin operators. In this case, even if the atoms exchange their individual spins during the collision, the total spin of the colliding pair is always conserved.

Step 2: The next step is the binary collisional transfer of the polarization between the K atoms and the ^3He nuclei. The interaction potential for this collision can be written as,

$$V(R) = \gamma(R)\vec{N}\cdot\vec{S} + A(R)\vec{I}\cdot\vec{S},$$

where R is the interatomic separation. The first term describes the interaction between the electron spin \vec{S} and the rotational angular momentum of the K- ^3He system. The second term describes the hyperfine interaction between the electron spin \vec{S} and the ^3He nuclear spin \vec{I} . In this collision process, van der Waals molecules are produced which live until they are broken apart by a subsequent collision. This is the dominating relaxation mechanism. However, due to the high pressure in the target cell, most of the molecules break up before they depolarize the nucleus.

For any SEOP, two types of efficiencies are important:

Photon Efficiency (η_γ): This represents the number of ^3He nuclei polarized by each photon that is absorbed.

Spin Exchange Efficiency (η_{SE}): This is the ratio of the rate at which the polarization is transferred to the ^3He to the rate at which it is depolarized through collisions with the alkali atoms in the target cell. The rate of change of ^3He polarization in HSEOP is given by the following equation [73]:

$$\frac{dP_{^3\text{He}}}{dt} = \gamma_{SE}(P_A - P_{^3\text{He}}) - \Gamma_{^3\text{He}}P_{^3\text{He}}, \quad (6.6)$$

where P_A and the $P_{^3\text{He}}$ are the spin polarization of the alkali atoms and the ^3He , respectively. $\Gamma_{^3\text{He}}$ is the depolarization rate of the ^3He nuclei via various processes (target polarimetries, magnetic field gradients, wall collisions [71]). $\gamma_{SE} = \kappa_K + \kappa_{Rb}$ with the spin exchange coefficients $\kappa_K = (6.1 \pm 0.4) \times 10^{-20} \text{ cm}^3\text{s}^{-1}$ and $\kappa_{Rb} = (6.8 \pm 0.2) \times 10^{-20} \text{ cm}^3\text{s}^{-1}$ [73]. With the typical densities of 10^{14} cm^{-3} , the K-Rb spin exchange rate is 10^5 per second which is much greater than the typical alkali spin relaxation rate, 500 per second. The target cells used in the experiment E12-06-121 had a hybrid gas mixture with ratio of $\frac{[K]}{[Rb]} = 5$ based on the efficiency study done in the Reference[74].

6.6 Target Polarimetries

The ^3He target polarization was measured using three polarimetries: nuclear magnetic resonance (NMR), electron paramagnetic resonance (EPR) and, pulse nuclear magnetic resonance (PNMR). Although the NMR was the primary polarimetry technique, it was a relative measurement. So, EPR was done to calibrate the NMR measurements periodically. PNMR was also periodically performed to cross check the NMR results with its advantage of low ^3He polarization loss. The NMR polarimetry was performed both in the pumping and the target chamber and the EPR polarimetry was performed in the pumping chamber. The PNMR measurements were done on the small blob (~ 136 mm below the pumping chamber) in one of the transfer tubes.

- **Nuclear Magnetic Resonance (NMR)**: In NMR polarimetry, the ^3He polarization was determined from the magnetic field produced by the nuclear spins when they were modulated. The principle of NMR polarimetry is described below. When a free particle with magnetic moment $\vec{\mathcal{M}} = \gamma\vec{I}$ is placed in an external magnetic field \vec{B}_0 , it experiences a torque, τ in the laboratory frame as follows.

$$\begin{aligned} \tau &= \vec{\mathcal{M}} \times \vec{B}_0 \\ \left(\frac{d\vec{I}}{dt}\right)_{lab} &= \vec{\mathcal{M}} \times \vec{B}_0 \\ \left(\frac{d\vec{\mathcal{M}}}{dt}\right)_{lab} &= \gamma\vec{\mathcal{M}} \times \vec{B}_0. \end{aligned} \quad (6.7)$$

The magnetic moment of the the particle then starts precessing about the holding magnetic field with frequency, $\omega_L = \gamma B_0$, which is known as the Larmor frequency. In our case the holding field \vec{B}_0 is pointing in \hat{z} direction. Now, a RF field \vec{B}_{RF} oscillating with frequency $\pm\omega$ is applied in the vertical direction \hat{x} to the holding field and it has two components as following.

$$\begin{aligned}\vec{B}_{RF} &= B_{RF}\hat{e}_+ + B_{RF}\hat{e}_- \\ &= B_{RF}(\cos\omega t\hat{x} + \sin\omega t\hat{y}) + B_{RF}(\cos\omega t\hat{x} - \sin\omega t\hat{y}) \\ &= 2B_{RF}\cos\omega t\hat{x}.\end{aligned}$$

The negative frequency component of the RF field will be ignored using the positive frequency approximation. To make the situation conceptually simpler, the Eq. 6.7 is transformed into a frame of reference which is rotating with the same frequency ($+\omega$) as the external RF field. In that rotating frame, the rate of change of magnetic moment is expressed as,

$$\begin{aligned}\left(\frac{d\vec{\mathcal{M}}}{dt}\right)_{rot} &= \left(\frac{d\vec{\mathcal{M}}}{dt}\right)_{lab} + \vec{\omega} \times \vec{\mathcal{M}} \\ &= \gamma\vec{\mathcal{M}} \times \vec{B}_0 + \vec{\omega} \times \vec{\mathcal{M}} \\ &= \gamma\vec{\mathcal{M}} \times \left(\vec{B}_0 - \frac{\vec{\omega}}{\gamma}\right).\end{aligned}\tag{6.8}$$

With the external RF field the Eq. 6.8 can be written as,

$$\begin{aligned}\left(\frac{d\vec{\mathcal{M}}}{dt}\right)_{rot} &= \gamma\vec{\mathcal{M}} \times \left(\vec{B}_0 - \frac{\vec{\omega}}{\gamma} + \vec{B}_{RF}\right) \\ &= \gamma\vec{\mathcal{M}} \times \vec{B}_{eff},\end{aligned}\tag{6.9}$$

where, $\vec{B}_{eff} = \left(\vec{B}_0 - \frac{\vec{\omega}}{\gamma} + \vec{B}_{RF}\right)$. Two methods can be used to flip the nuclear spin in a NMR measurement which are,

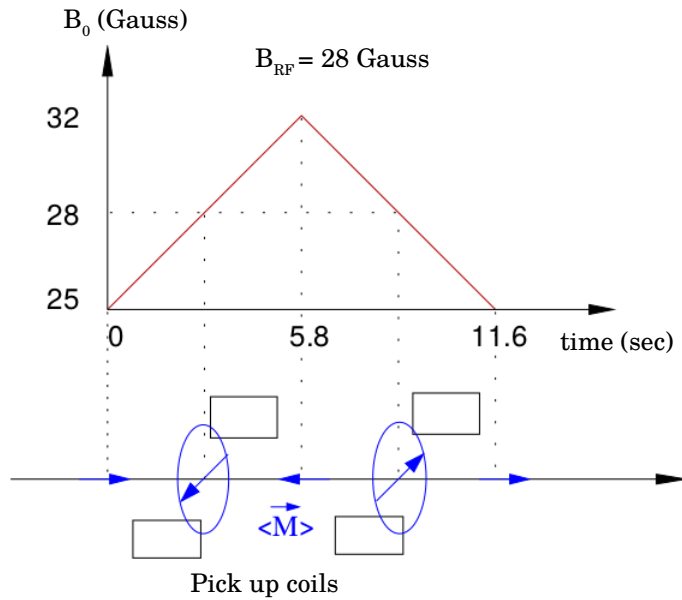
1. Frequency Sweep Method: The frequency of the external RF field is varied about the Larmor frequency, from $\omega < \omega_L$ to $\omega > \omega_L$.
2. Field Sweep Method: The amplitude of the holding field is swept about the resonance field, $B_0 = \frac{\omega}{\gamma}$.

Both of these methods have to follow the Adiabatic Fast Passage conditions (AFP) for a successful spin flip and the AFP condition can be expressed as the following.

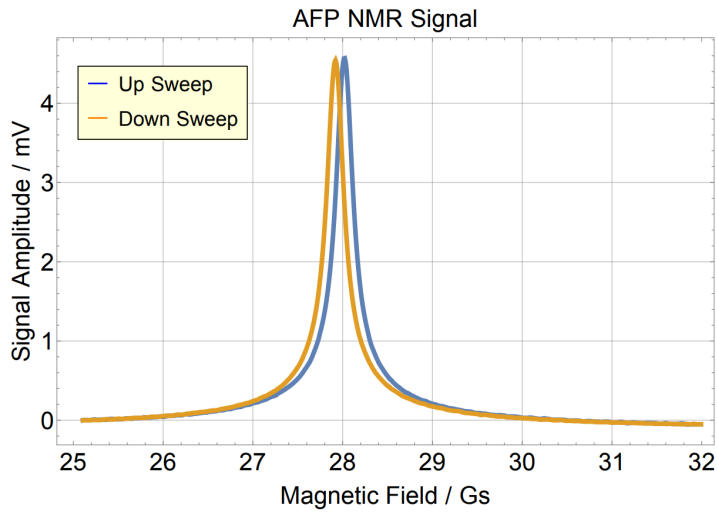
Frequency sweep method: $\frac{1}{T_2} \ll \frac{1}{\gamma B_{RF}} \left| \frac{d\omega}{dt} \right| \ll \gamma B_{RF}$

Field sweep method: $\frac{1}{T_2} \ll \frac{1}{B_{RF}} \left| \frac{dB_{RF}}{dt} \right| \ll \omega$

Where T_2 is the ^3He nuclear spin relaxation time in the transverse plane. The AFP conditions require that, the field or frequency sweep has to be fast enough that the nuclear spins do not get enough time to relax and the field or frequency



(a) Helium-3 spin flip using AFP.



(b) Typical NMR signal in the pick up coil.

Figure 6.9: The oscillating voltage induced in the pick up coils as a result of NMR spin flip and a typical NMR up-sweep and down-sweep signal peaks are shown.

sweep has to slow enough that the nuclear spins can follow that sweep. For the experiment E12-06-121, the field sweep method was used and it was performed periodically every ~ 5 hours. As demonstrated in Fig. 6.9, during the NMR flip, the motion of the nuclear spin results in a changing magnetic field which is proportional to the ^3He polarization value. The changing flux from the oscillating magnetic field induces an oscillating voltage in the NMR pickup coils around the target cell. This voltage is detected by a lock-in amplifier with its reference

frequency set at $f_L = \omega_L/2\pi$. The detected voltage is maximum for $\omega = \omega_L$ and a peak in the magnetic field is observed at resonance. The peak height (s) is proportional to the ^3He polarization and is given by,

$$s \propto \frac{P_{He3}\mu_{He3}B_{RF}}{\sqrt{\left(B_0 - \frac{\omega}{\gamma}\right)^2 + B_{RF}^2}}, \quad (6.10)$$

where P_{He3} is the value of the ^3He polarization and μ_{He3} is the magnetic moment of ^3He , $\mu_{He3}=6.706984 \times 10^{-14} \frac{\text{MeV}}{\text{T}}$.

In our experiment, the RF frequency was 91 KHz that corresponds to a resonance at $B_0=28$ Gauss. The field sweep was done from 25 Gauss to 32 Gauss range. as the NMR measurement is a relative measurement, the EPR measurements were performed to calibrate the NMR peak heights for both transverse and longitudinal ^3He polarization directions. An example NMR signal plot is demonstrated in Fig. 6.9(b) where the up-sweep signal corresponds to the first NMR flip ($0^\circ \rightarrow 180^\circ$) and the down-sweep signal corresponds to the second spin flip ($180^\circ \rightarrow 0^\circ$) The ^3He polarization measurements from all the calibrated NMR measurements are shown in Fig. 6.10. The different colored points represent the different ^3He polarization directions. The average target polarization was $\sim 45\% \pm 3\%$ during the experiment. The NMR analysis was performed by J. Chen.

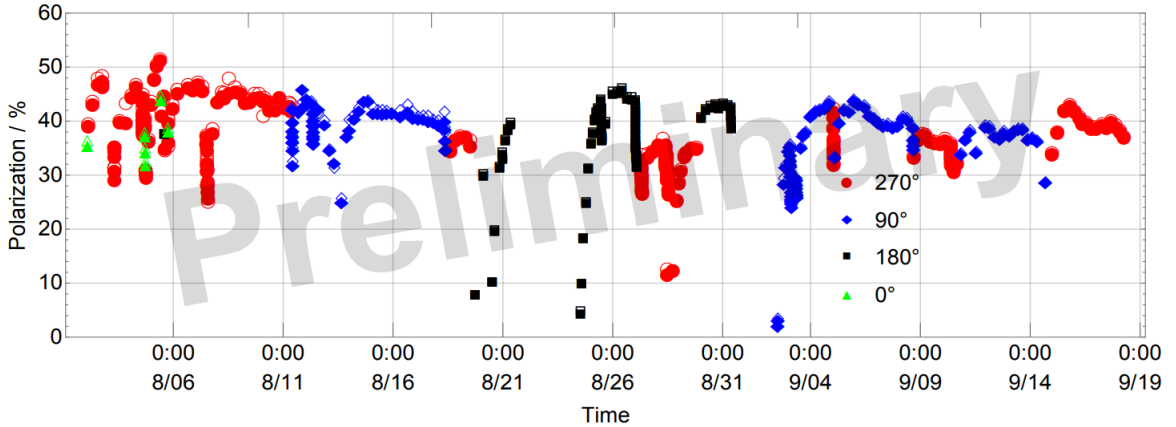


Figure 6.10: ^3He polarization measurement results from all NMR measurement performed during experiment E12-06-121.

- **Electron Paramagnetic Resonance (EPR):** In EPR polarimetry, the ^3He polarization is measured by the Zeeman splitting of atomic energy levels with unpaired electron when placed in the external magnetic field. The EPR is performed on the alkali atoms in the target cell to measure the absolute ^3He polarization and this is used to calibrate NMR measurements. The Zeeman splitting of Rb energy levels are shown in Fig. 6.7. If 795 nm right (or left)

circularly polarized laser is incident on the pumping chamber, all the Rb atom will be polarized into the $m_F=3$ (or, -3) substate of $S_{\frac{1}{2}}$ level. The splitting between the $m_F=3$ and the $m_F=2$ (or, $m_F=-3$ and the $m_F=-2$) levels is known as the EPR transition frequency and it depends on the external magnetic field \vec{B}_0 , the spin exchange (SE) collision between the alkali atom and ^3He and, the small magnetic field induced from the polarization of ^3He .

$$\Delta\nu_{EPR} = \Delta\nu_{B_0} + \Delta\nu_{SE} + \Delta\nu_{He3}. \quad (6.11)$$

The fact that the EPR frequency can change as result of a change in the induced magnetic field from ^3He spins, is used to measure the ^3He polarization in EPR polarimetry. During the EPR measurement, ^3He spins are flipped by AFP to reverse their orientation w.r.t. the external magnetic field. When the spins are parallel to \vec{B}_0 , the effective magnetic field becomes $\vec{B}_0 - \vec{B}_{He3}$ where \vec{B}_{He3} is the magnetic field from the ^3He spins. Again, when the spins are flipped back to their original orientation, the effective magnetic field becomes $\vec{B}_0 + \vec{B}_{He3}$. By making sure the holding magnetic field is reasonably stable, the effect from the holding magnetic field in the frequency shift can be eliminated. The frequency shift due to ^3He polarization can be written as,

$$\Delta\nu_{EPR} = \left(\frac{d\nu_{EPR}}{dB_0} \right) (\Delta B_{He3} + \Delta B_{SE}). \quad (6.12)$$

The change in EPR frequency due to the holding magnetic field, $\frac{d\nu_{EPR}}{dB_0}$ is calculated from Breit-Rabi formula [77]. The effective magnetic field from the spin exchange collisions, ΔB_{SE} is written as,

$$\Delta B_{SE} = \frac{2K_{He3}\Gamma_{SE}\hbar K_z}{g_3\mu_B}, \quad (6.13)$$

where g_e is the gyromagnetic ratio, μ_B is the Bohr magneton, Γ_{SE} is the spin exchange (Rb- ^3He) rate per Rb atom, K_z is the z component ^3He spin and, K_{He3} is called the frequency shift parameter (described in [78]). The magnetic field from the polarized ^3He , ΔB_{He3} is written as,

$$\Delta B_{He3} = c\eta_{He3}\mu_{He3}P_{He3}, \quad (6.14)$$

where the factor c comes from the shape of the pumping chamber, η_{He3} is the ^3He number density, and P_{He3} is the ^3He polarization. By expanding the ΔB_{SE} and ΔB_0 terms in the Eq. 6.12 in terms of Eq. 6.13 and Eq. 6.14, the frequency shift ($\Delta\nu_{EPR}$) can be related to the ^3He polarization as follows.

$$\Delta\nu_{EPR} = c \left(\frac{d\nu_{EPR}}{dB_0} \right) \kappa_0 \eta_{He3} \mu_{He3} P_{He3}, \quad (6.15)$$

where $\kappa_0 = \kappa_{00}T_{ref} + \kappa_{0T}(T - T_{ref})$ depends on the cell geometry and temperature (largest source of error). The University of Virginia group provided

the κ_0 values for the target cells used in the experiment [79]. For the spherical pumping chamber, $c = \frac{8\pi}{3}$. Finally the absolute ^3He polarization is extracted using the following formula.

$$P_{He3} = \frac{\Delta\nu_{EPR}}{\frac{8\pi}{3} \left(\frac{d\nu_{EPR}}{dB_0} \right) \kappa_0 \eta_{He3} \mu_{He3}}. \quad (6.16)$$

To measure the frequency shift, the RF coil placed next to the pumping chamber and perpendicular to both the holding field coils, was driven by a function generator which was set to the Rb/K EPR transition frequency. As an example, consider that the RF function generator was set to the EPR transition frequency corresponding to the $m_F=3$ and $m_F=2$ splitting. Due to optical pumping, all the Rb electrons were polarized to $m_F=3$ state before the EPR RF field was applied. The RF field de-excited the Rb electron to the $m_F=2$ state and then they were re-excited to $P_{\frac{1}{2}}$ level by absorbing the 795 nm laser light. Due to this repolarization process, when the Rb electrons decayed back to $S_{\frac{1}{2}}$ level, it resulted in increased photon emission corresponding to D_1 transition ($P_{\frac{1}{2}} \rightarrow S_{\frac{1}{2}}$) at 795 nm wavelength. Due to the thermal mixing between the $P_{\frac{1}{2}}$ and $P_{\frac{3}{2}}$ levels, there were an photon emission corresponding to the D_2 transition ($P_{\frac{3}{2}} \rightarrow S_{\frac{1}{2}}$) at 780 nm wavelength. Although there was same amount of D_1 and D_2 light emission, D_1 photons could not be distinguished from the huge D_1 background from the incident pumping laser. So only the D_2 photons were detected by a photodiode with a narrow bandpass filter. When the RF function generator frequency was modulated, the voltage from the photodiode had a shape of Lorentzian function while scanned through the EPR transition frequency.

A lock in amplifier was locked at the transition frequency and that frequency was read out by the computer. After the EPR AFP flip, the EPR transition frequency readout value was shifted. By measuring the difference, $\Delta\nu_{EPR}$, the ^3He polarization value was calculated using the Eq. 6.16.

Fig. 6.11 shows an example of an EPR AFP flip performed on ^{39}K ($F=2$, $m_F=-2 \rightarrow F=2$, $m_F=-1$) in target cell Tommy during the experiment. For this particular EPR measurement,

- κ_0 ($T_{PC}=265.4 \pm 5^\circ\text{C}$) = 6.55 ± 0.18 , provided by the University of Virginia group
- $\eta_{PC} = 6.47 \pm 0.05$, calculated using Eqn. 6.5 (uncertainty yet to be finalized)
- $2\Delta\nu_{EPR} = 62.61 \pm 1.78$ kHz, calculated from the EPR flip in Fig. 6.11
- $\frac{d\nu_{EPR}}{dB_0} = 883.21$ kHz/Gauss

Using this information the ^3He polarization was calculated using Eq. 6.16 and the ^3He polarization inside the pumping chamber was $34.6 \pm 1.4\%$. As mentioned before the EPR measurement is an absolute measurement and the NMR measurements were calibrated using EPR. To do the calibration, NMR measurements were taken before and after one EPR measurements periodically

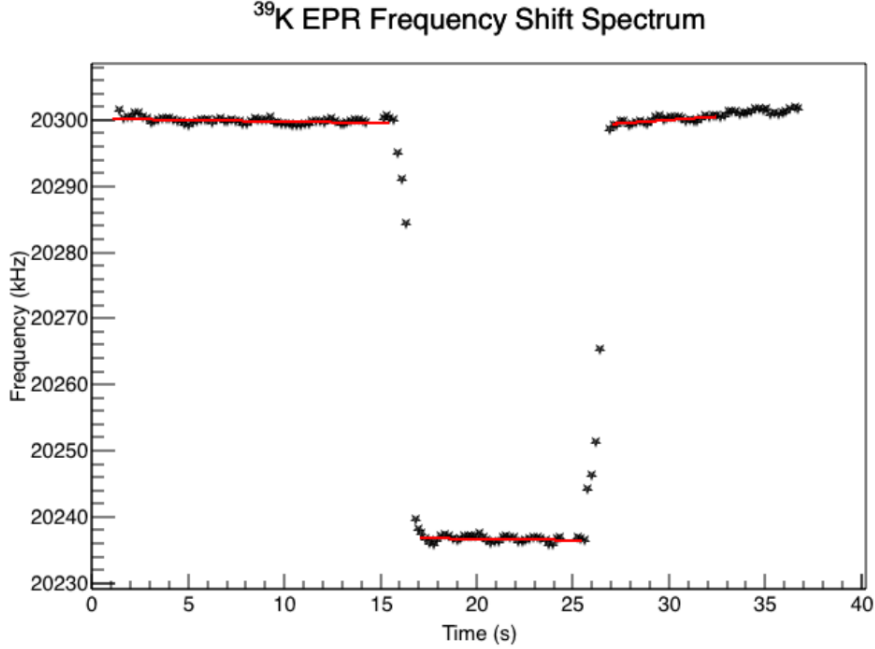


Figure 6.11: The EPR AFP signal for the target cell Tommy with target polarization direction 270° w.r.t. the electron beamline.

once every month or when there was any configuration change (eg. polarization direction rotation, spectrometer rotation). The following formula was used to determine the EPR-NMR calibration constant, $C_{EPR-NMR}$.

$$P_{He3}^{EPR} = C_{EPR-NMR} * C_{diff} * s. \quad (6.17)$$

Where, s was the height of NMR signal peak and C_{diff} was the diffusion constant that was determined from transforming the EPR polarization value from pumping chamber to target chamber. The EPR analysis was performed by M. Cardona.

- **Pulsed Nuclear Magnetic Resonance (PNMR):** The PNMR polarimetry was performed at the spherical blob on the transfer tube of the target cell. During a PNMR measurement an RF pulse at Larmor frequency was applied in the blob and it tipped the ^3He spins away from the holding field direction with an angle $\theta_{tip} = \frac{1}{2}\gamma H_{RF} t_{pulse}$. After the pulse ended after time, $t = t_{pulse}$, the ^3He spin precessed back to the original state, experiencing a free induction decay (FID). The PNMR pick up coil attached surrounding the blob picked up this FID signal as shown in Fig. 6.12. This signal was related to the transverse component of the magnetic moment which was proportional to the ^3He polarization.

$$S(t) \propto M_z \sin(\theta_{tip}) \cos(\omega t + \phi_0) e^{-\frac{t}{T_2}}. \quad (6.18)$$

This polarimetry required significantly uniform magnetic field (gradient < 10 mG/cm) around the blob and very stable Helmholtz coil power supply. Due to

these constraints, the holding field magnitude drifted with time that resulted in drift in PNMR signal amplitude. Currently, the polarization from PNMR measurements agrees to the NMR within $\sim 2\%$. Additional systematic studies and PNMR-NMR calibrations are being performed by M. Chen to reduce the uncertainty.

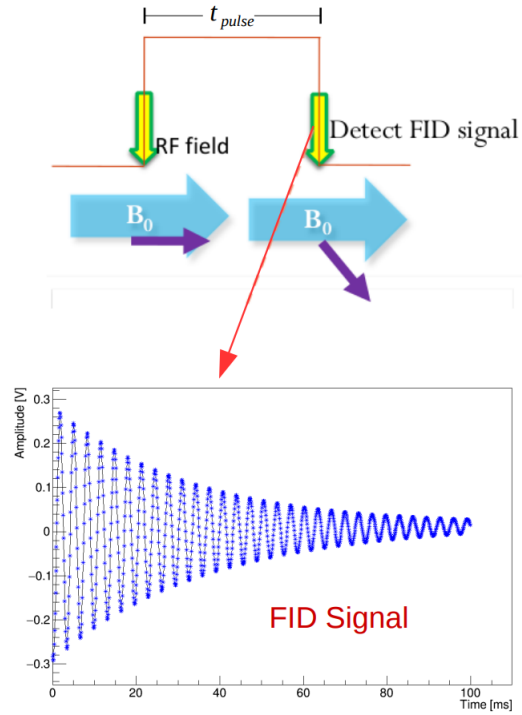


Figure 6.12: An example PNMR FID signal after the RF pulse ends.

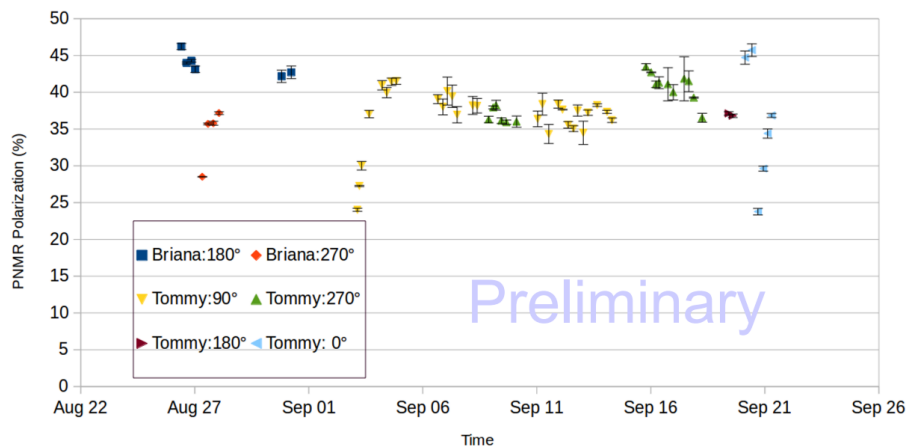
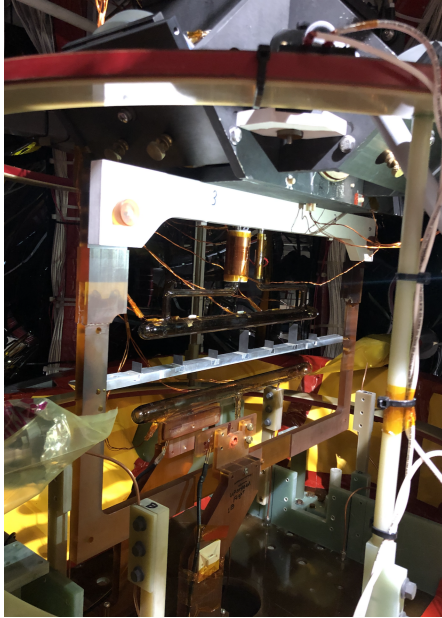


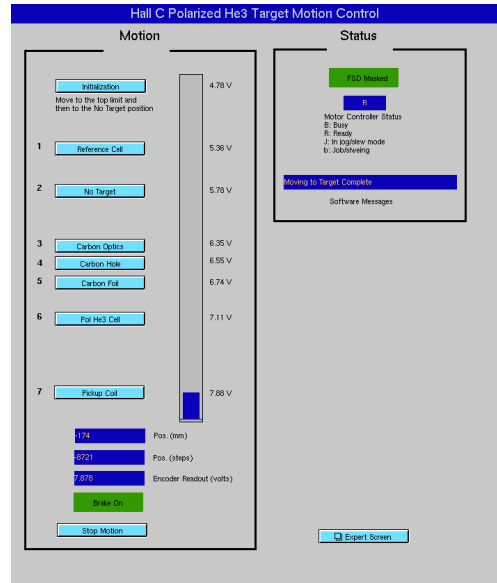
Figure 6.13: The target polarization measurement results from all the PNMR measurements during the experiment E12-06-121.

6.7 The Target Ladder

The target ladder shown in Fig. 6.14 was developed at Jefferson Lab to set the position of the different targets used in the experiment, and all the targets were mounted on it. The list of target positions used are as follows.



(a) The target ladder.



(b) The target ladder EPICS control screen.

Figure 6.14: The target ladder with different targets mounted on it. From top to bottom: The ³He cell, carbon foils, and the reference cell can be seen in the picture.

- **Polarized ³He position:** The target ladder was always set to this position during production data taking. In this case, the electron beam was passed through the center of the target chamber.
- **Reference cell position:** The target ladder was moved to this position when we required reference cell data taking. Four types of reference cell data were taken: empty cell data, nitrogen data, hydrogen data, and ³He data for detector calibration and background contamination studies.
- **Carbon foil position:** Two carbon foils were used for the optics calibration and electron beam adjustment.
- **Carbon hole position:** The two carbon foils had holes which were used to fine tune the electron beam position on target.
- **Carbon optics position:** Five carbon targets were used for the optics calibration.

- **Pick up coil position:** The target ladder was moved to this position before each NMR measurement. In this case, the target cell sits between the pairs of pick up coils to get a good NMR signal.
- **“No target” position:** The target ladder was moved in this position when we had to take cosmic data which required absolutely no target in the electron beam path.

The stepper motor used for the motion of the target ladder resulted in a position accuracy of $\pm 40 \mu\text{m}$ with a maximum range of 45.7 cm. The target ladder position was also monitored and controlled remotely through EPICS.

6.8 The Target Enclosure

The whole target region was enclosed by lexan polycarbonate panels with interlocks attached to each panel. This was used to prevent target hazard such as the exposure to the high power target laser or radiation in case of the high pressure target cell explosion.

6.9 The Target Polarization Direction Measurement

6.9.1 The Target Holding Magnetic Field Mapping

Experiments E12-06-110 and E12-06-121 required magnetic field mapping to optimize the correction coil currents to get a nearly homogeneous ~ 25 G magnetic field near the target region. The goal was to reduce the magnetic field gradient to < 30 mG/cm and also to correct for the vertical fringe field coming from the spectrometer magnets. However, studies showed that only the fringe field from the SHMS horizontal bender was affecting the target holding field.

A 3D magnetometer (Metrolab THM1176HF) was used to measure the magnetic field in all directions. This probe was mounted on the field mapping device shown in Fig. 6.15. The device was made of aluminum and the bottom square frame with 40 pin holes 1 cm apart on each of the four sides, was mounted on the target base. A horizontal bar with 45 pin holes (1 cm apart) was mounted to the square frame and a vertical bar with 45 pin holes (1 cm apart) was mounted on the horizontal bar. The 3D magnetometer was attached to a probe holder which was mounted on the vertical bar and it could be moved vertically. This device could cover the field mapping of the whole target region in all three directions. The full magnetic field mapping was performed along the following 18 lines after the correction coil currents were optimized (optimized currents are listed in Table. 6.7, Table. 6.8 and Table. 6.11).

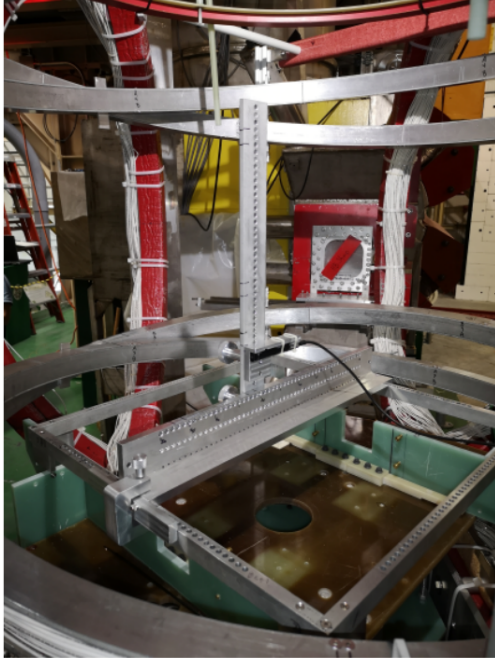


Figure 6.15: The magnetic field mapping device used in experiment E12-06-121.

- **line 1:** $x=0; y=0; z=20, 18, -3, -5, -18, -20$ (cm)
- **line 2:** $x=0; y=2; z=20, 18, -3, -5, -18, -20$ (cm)
- **line 3:** $x=0; y=10; z=20, 18, -3, -5, -18, -20$ (cm)
- **line 4:** $x=0; y=10; z=20, 18, -3, -5, -18, -20$ (cm)
- **line 5:** $x=0; y=30; z=20, 18, -3, -5, -18, -20$ (cm)
- **line 6:** $x=0; y=32; z=20, 18, -3, -5, -18, -20$ (cm)
- **line 7:** $x=-2; y=0; z=20, 18, -3, -5, -18, -20$ (cm)
- **line 8:** $x=-2; y=2; z=20, 18, -3, -5, -18, -20$ (cm)
- **line 9:** $x=-2; y=10; z=20, 18, -3, -5, -18, -20$ (cm)
- **line 10:** $x=-2; y=10; z=20, 18, -3, -5, -18, -20$ (cm)
- **line 11:** $x=-2; y=30; z=20, 18, -3, -5, -18, -20$ (cm)
- **line 12:** $x=-2; y=32; z=20, 18, -3, -5, -18, -20$ (cm)
- **line 13:** $x=2; y=0; z=20, 18, -3, -5, -18, -20$ (cm)
- **line 14:** $x=2; y=2; z=20, 18, -3, -5, -18, -20$ (cm)
- **line 15:** $x=2; y=10; z=20, 18, -3, -5, -18, -20$ (cm)

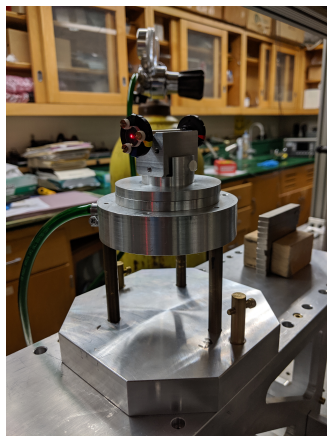
- **line 16:** $x=2; y=10; z=20, 18, -3, -5, -18, -20$ (cm)
- **line 17:** $x=2; y=30; z=20, 18, -3, -5, -18, -20$ (cm)
- **line 18:** $x=2; y=32; z=20, 18, -3, -5, -18, -20$ (cm)

The magnetic field magnitude was measured with an uncertainty of 0.12 Gauss and the optimized coil currents were used during the magnetic field direction measurements (Section 6.9) and also during the production data taking.

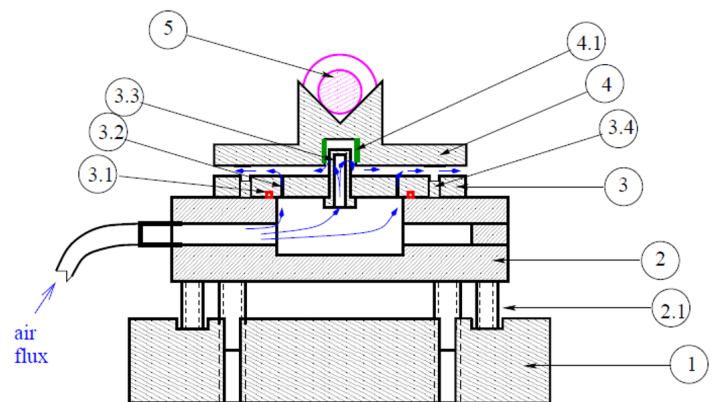
6.9.2 The Horizontal Compass

Experiments E12-06-110 and E12-06-121 required the target holding field direction to be measured precisely to about $\pm 0.1^\circ$ in absolute Hall C coordinate system. In the experimental Hall C, the longitudinal polarization direction is the direction of the target spins pointing parallel or antiparallel to the beam direction in the horizontal plane and the transverse polarization direction is the direction of the target spins pointing perpendicular to the beam direction in the horizontal plane. If the target polarization direction is slightly different from 90° or 270° (the horizontal transverse polarization directions) w.r.t the electron beam direction, the longitudinal asymmetry contributes to the total asymmetry in same order as the transverse asymmetry. To account for the contribution of the longitudinal asymmetry, the holding field direction needed to be measured very precisely.

In order to measure the horizontal magnetic field directions, a novel air-compass was conceptualized and developed at the University of Kentucky and subsequently modified at Jefferson Lab as the commercially available compasses cannot achieve the desired level of precision.



(a) The compass.



(b) Sectional view through center.

Figure 6.16: Design of the horizontal compass.

The horizontal compass (Fig. 6.16a) consisted of a cylindrical magnet mounted on a floating disk made of aluminum. The length and diameter of the neodymium

magnetic cylinder were 2 inches and 0.25 inches, respectively. The compass magnet was placed inside a V-groove as it was ideal for positioning a cylindrical magnet. It provided two lines of contact along the bottom and it allowed access to both ends of the cylinder.

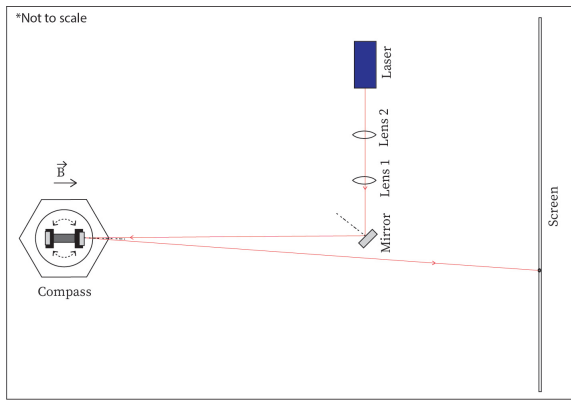
The disk was floated by passing compressed nitrogen gas through an air inlet shown in Fig. 6.16b. The bottom aluminum disk with the air-inlet was placed on three brass legs. The height of the compass was adjusted by adjusting the legs on the octagonal base plate. The compass magnet had two caps with circular scales and 1 mm deep pockets attached to both ends. Two mirrors (diameter 0.5 inches and 3 millimeter thick) were placed inside the pockets on top of a neoprene sponge cut in circular shape (0.5 inches diameter) with the help of three brass screws. The magnetic field direction was measured by reflecting a laser beam off the compass mirrors, aligned perpendicular to the magnetic axis of the magnet as precisely as possible. The circular scales had markings every 30° to reproduce the same angular position of the cylinder for every reading. The magnetic field direction was given by the surface normal of the compass mirror.

6.9.3 Compass Mirror Alignment

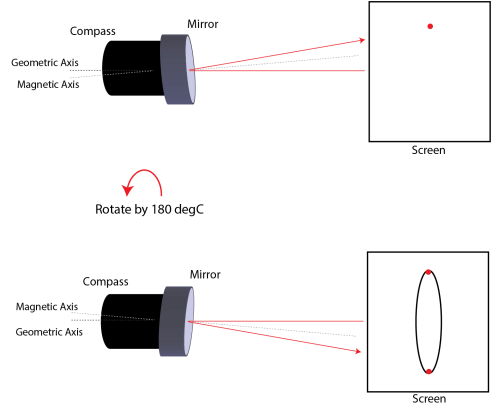
The misalignment of the surface normal of the compass mirrors and the unknown magnetic axis of the cylindrical magnet gave rise to systematic errors in the magnetic field direction measurements. This error was minimized by aligning the surface normal of the compass mirrors parallel to the magnetic axis of the magnet with the help of the three brass screws and the neoprene sponge used as a spring material.

The compass mirror alignment was done in the target lab (Fig. 6.17a) at the Jefferson Lab before the field direction measurements in Hall C. A laser beam was reflected off the compass mirrors and the reflected beam spot was monitored on a screen placed $s = 2$ meter away from the compass. A laser pointer was fixed for the whole procedure so that the plane of incidence was always horizontal. Two lenses were used to reduce the beam spot diameter to 2 millimeters on the screen. To ensure the perfect flotation of the disk, a Starrett 98 series Mechanists' level was used to level the compass to the precision of 0.024° . The cylindrical magnet was rotated about its axis from the other end and the reflected beam spots were marked for all angular positions of the magnet. It inscribed an ellipse on the screen (Fig. 6.17b). This process was repeated until the minor axis of the ellipse was reduced to get a vertical straight line by fine tuning the angle of the mirrors attached.

The alignment data from both the compass mirrors were fitted to straight lines. The two mirrors were named mirror-1 and mirror-2 depending on which direction they face in Hall C when the magnetic field is turned on. Mirror-1 was used to measure the magnetic field directions in $-X$ (beam right) and $+Z$ (downstream) directions and mirror-2 was used to measure the magnetic field directions in $+X$ (beam left) and $-Z$ (upstream) directions. In Fig. 6.18, Fig. 6.19, and Fig. 6.20 the straight lines were fitted after a 90° rotation of each data point so that the x and y axes correspond to the vertical and horizontal directions respectively. The y-spread of the data points about the fitted straight line determined the horizontal error in the magnetic field



(a) Setup in the target lab.



(b) Incribed ellipse from the 360° scan of the compass magnet.

Figure 6.17: Compass mirror alignment in the target lab.

angle measurement generated from the compass mirror alignment. The total error in angle $\pm (\theta_M \pm d\theta_M)$ was calculated from $D_y \pm dD_y$ using the following equations.

$$D_y = \frac{y_{max} - y_{min}}{2} \quad (6.19)$$

$$D_x = \frac{x_{max} - x_{min}}{2} \quad (6.20)$$

$$dD_x = \sqrt{2x_{err}^2} \quad (6.21)$$

$$dD_y = \sqrt{\left(\frac{\partial D_y}{\partial p_1}\right)^2 dp_1^2 + \left(\frac{\partial D_y}{\partial D_x}\right)^2 dD_x^2 + \left(\frac{\partial D_y}{\partial p_0}\right)^2 dp_0^2} \quad (6.22)$$

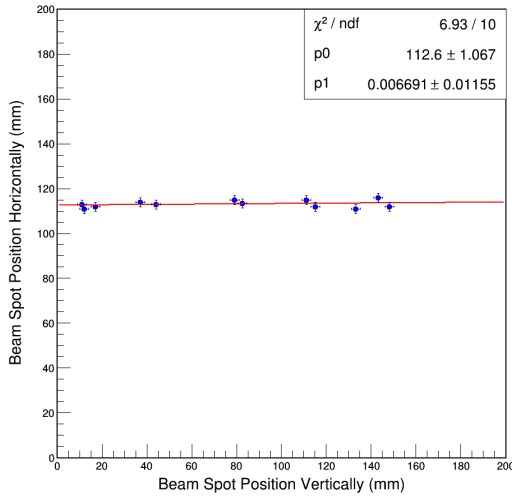
$$\theta_M = \frac{D_y}{2s} \quad (6.23)$$

$$d\theta_M = \sqrt{\left(\frac{\partial \theta_M}{\partial D_y}\right)^2 dD_y^2 + \left(\frac{\partial \theta_M}{\partial s}\right)^2 ds^2} \quad (6.24)$$

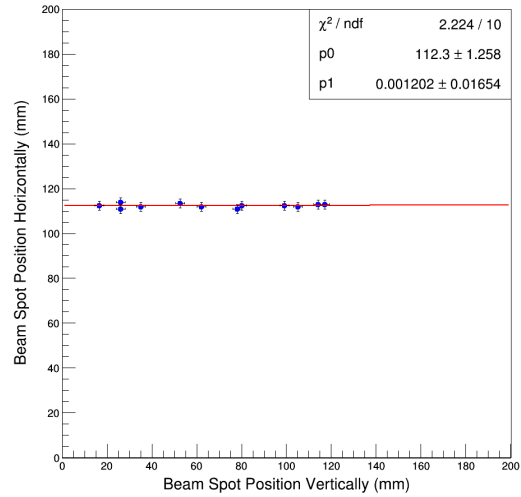
Where p_0 and p_1 are the fit parameters, dp_0 and dp_1 are the fit parameter errors, x_{err} was the error associated with each data point which was given by the laser beam spot diameter and D_y and dD_y are the y-spread and error in the y-spread, respectively. The results of the compass mirror alignment for both the A_1^n and d_2^n experiments (March and September measurements) are listed in Table. 6.6.

6.9.4 Compass Measurements in Hall C

The compass measurements were performed in Hall C in October, 2019 for a couple of A_1^n kinematic settings before starting the experiment. The measurements for d_2^n

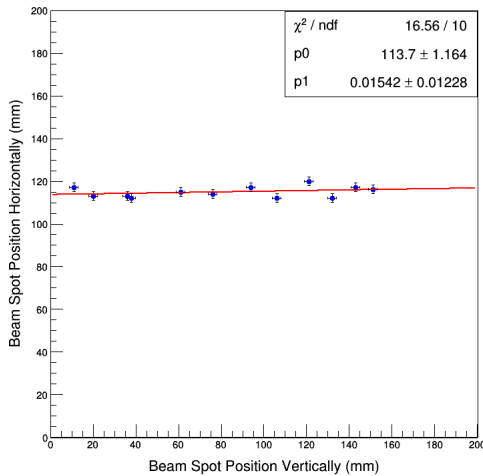


(a) Mirror-1

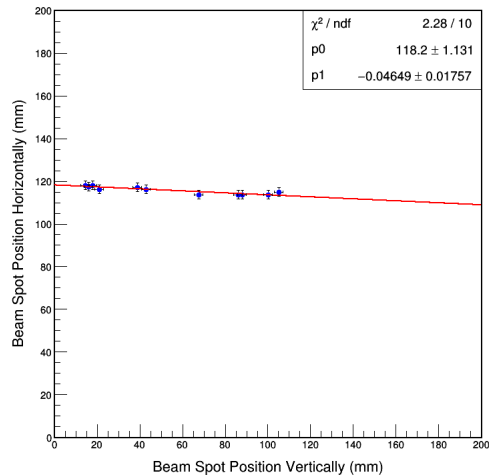


(b) Mirror-2

Figure 6.18: Straight line fits to the compass mirror alignment data for A_1^n experiment (October, 2019).



(a) Mirror-1

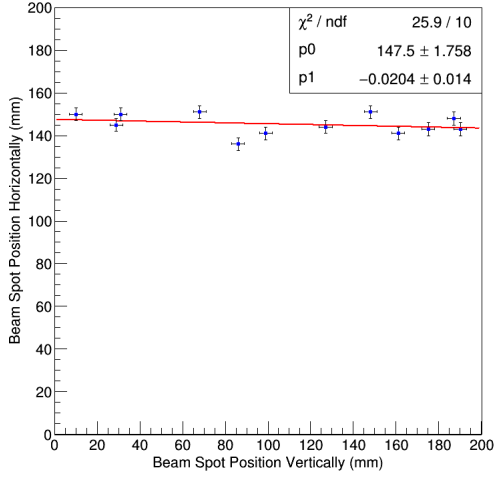


(b) Mirror-2

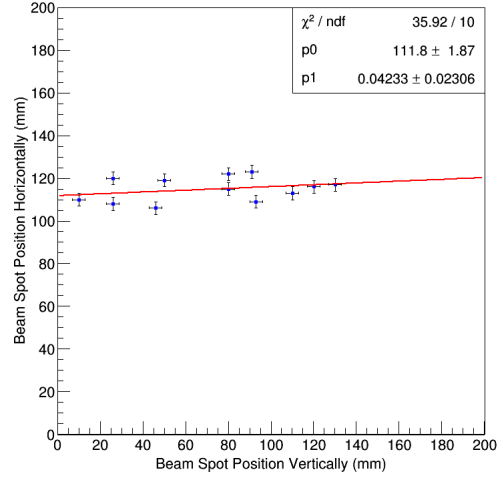
Figure 6.19: Straight line fit to the compass mirror alignment data for d_2^n experiment (March, 2020).

kinematic settings were done once in March, 2020 before the experiment and were repeated in September, 2020 after the completion of the experiment.

The Helmholtz coil (MainL and MainS) and correction coil current settings (VL, VS, HL, HS) for all measured kinematic settings are listed in Table. 6.7, Table. 6.8, and Table. 6.11. The magnetic field directions were measured for all four polarization directions as shown in Table. 6.10. The compass was mounted on an aluminum fixture (Fig. 6.21a) with the help of two brass dowel pins. The fixture had eleven holes which



(a) Mirror-1.



(b) Mirror-2.

Figure 6.20: Straight line fit to the compass mirror alignment data for d_2^n experiment (September, 2020).

Table 6.6: Systematic uncertainties from the compass mirror alignment.

Experiment	Mirror	D_y (mm)	dD_y (mm)	θ_M ($^\circ$)	$d\theta_M$ ($^\circ$)
A_1^n	1	0.4584	0.9541	0.0128	0.0266
	2	0.0604	1.0422	0.0018	0.0290
d_2^n (March)	1	1.0563	1.0380	0.0294	0.0289
	2	2.1342	0.9794	0.0594	0.0273
d_2^n (September)	1	1.8362	1.5373	0.0511	0.0428
	2	2.5397	1.6722	0.0707	0.0466

Table 6.7: Helmholtz coil and correction coil settings used during compass measurements for A_1^n kinematic settings with the Helmholtz coils at 45° w.r.t. electron beam direction.

Kin. settings	Pol. directions	MainL current (A)	MainS current (A)	VL current (A)	VS current (A)	HL current (A)	HS current (A)
SHMS at 12.5° , 7.5 GeV/C	+X	+5.2306	+5.1632	8.7	6.7	-1.0	1.0
	-X	-5.2306	-5.1632	8.7	5.4	-1.0	1.0
	+Z	+5.2306	-5.1632	8.7	5.9	0.0	0.0
	-Z	-5.2306	+5.1632	8.7	5.9	0.0	0.0
SHMS at 30° , 3.4 GeV/C	+X	+5.2306	+5.1632	2.3	2.3	0.0	0.0
	-X	-5.2306	-5.1632	4.5	2.8	0.0	0.0
	+Z	+5.2306	-5.1632	4.5	3.5	0.0	0.0
	-Z	-5.2306	+5.1632	2.8	1.6	0.0	0.0

Table 6.8: Helmholtz coil and correction coil settings used during compass measurements in March, 2020 for d_2^n kinematic settings with the Helmholtz coils at 0° w.r.t. electron beam direction.

Kin. settings	Pol. directions	MainL current (A)	MainS current (A)	VL current (A)	VS current (A)	HL current (A)	HS current (A)
SHMS at 11° , 7.5 GeV/C	+X	7.407	0.137	6.0	4.0	0.0	0.0
	-X	-7.364	-0.237	6.0	4.1	0.0	0.0
	+Z	0.000	7.225	6.5	4.5	0.0	0.0
	-Z	0.000	-7.305	6.9	4.7	0.0	0.0
SHMS at 14.5° , 6.4 GeV/C	+X	7.406	0.139	6.1	4.2	0.0	0.0
	-X	-7.385	-0.239	6.1	4.2	0.0	0.0
	+Z	0.000	7.298	6.3	4.6	0.0	0.0
	-Z	0.000	-7.398	7.0	4.9	0.0	0.0

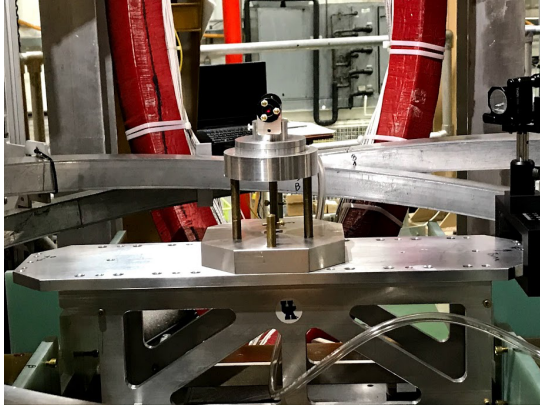
Table 6.9: Helmholtz coil and correction coil settings used during compass measurements for d_2^n kinematic setting with the Helmholtz coils at 45° w.r.t. electron beam direction.

Kin. settings	Pol. directions	MainL current (A)	MainS current (A)	VL current (A)	VS current (A)	HL current (A)	HS current (A)
SHMS at 18° , 5.6 GeV/C	+X	+5.2306	+5.1632	2.3	2.3	0.0	0.0
	-X	-5.2306	-5.1632	4.5	2.8	0.0	0.0
	+Z	+5.2306	-5.1632	4.5	3.5	-1.0	1.0
	-Z	-5.2306	+5.1632	2.8	1.6	0.0	0.0

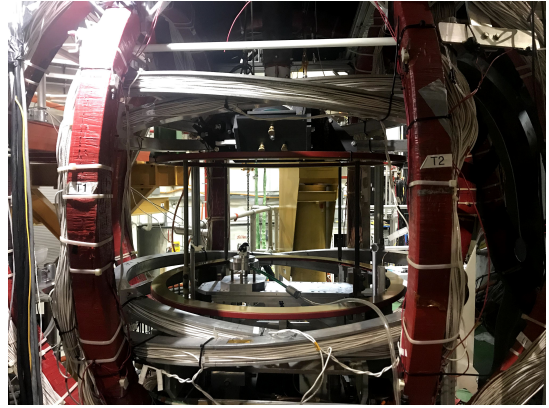
were 4 cm apart from each other. Both the transverse and longitudinal field directions were scanned in three different positions, 0 (target center), +12 cm and -12 cm along the beam direction. The beam direction was defined by two fiducials mounted on two posts (upstream and downstream) at the same height as the compass. by the alignment group. The three compass locations and the fiducials were surveyed by the Jefferson Lab alignment group before proceeding with the magnetic field direction measurements. All the optics and a transparent screen were installed (Fig. 6.21c) on an optics table, 2 meter away from the target region.

Table 6.10: Definition of target polarization directions in Hall C.

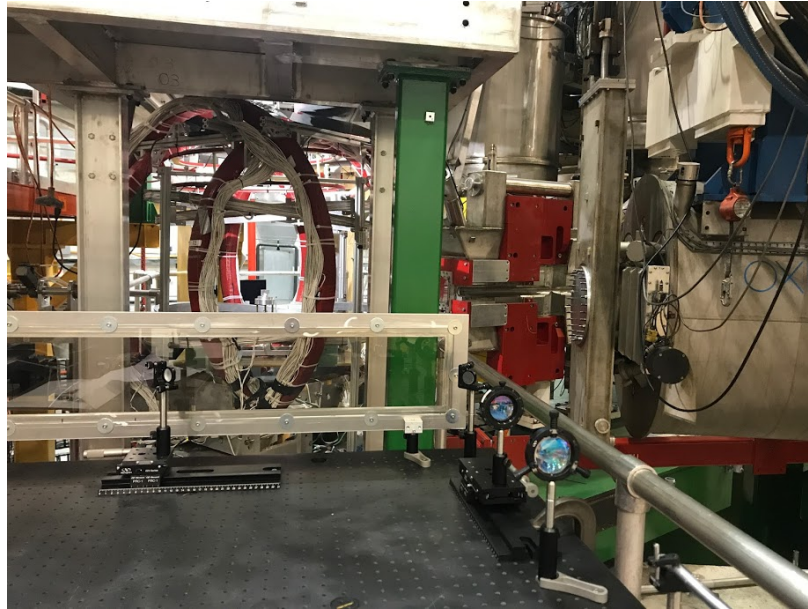
Polarization	Direction	Angle with beamline
Transverse	Beam right: +X	90°
	Beam left: -X	270°
Longitudinal	Downstream: +Z	0°
	Upstream: -Z	180°



(a) Installation of the horizontal compass for the A_1^n experiment.



(b) Installation of the horizontal compass for the d_2^n experiment.

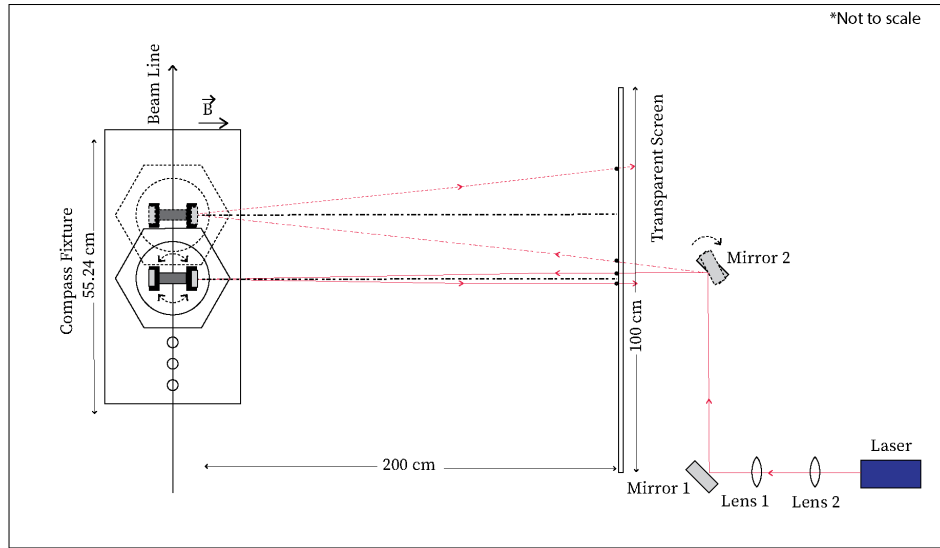


(c) Optics setup for compass measurements.

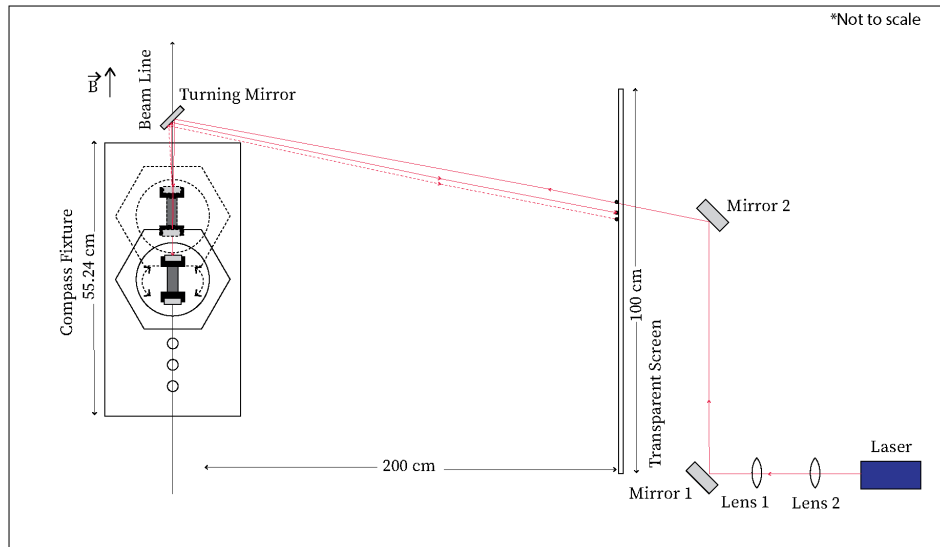
Figure 6.21: The compass measurement setup in Hall C.

6.9.4.1 Transverse Magnetic Field Direction Measurement Procedure

The laser beam was incident at the center of the compass mirror from the beam right direction (Fig. 6.22a). The mirror-1 and mirror-2 were facing the beam right direction when the polarization directions were $-X$ and $+X$ respectively. While the compass was floating, the incident and reflected beam spots were marked on the transparent screen and they were surveyed by the alignment group after all the measurements were completed. This procedure was repeated for all three locations of the compass along the target length. The angular bisector of the incident and reflected laser beams determined the transverse magnetic field direction in the absolute Hall C coordinate system.



(a) Transverse direction.



(b) Longitudinal direction.

Figure 6.22: The magnetic field direction measurement procedures in Hall C.

6.9.4.2 Longitudinal Magnetic Field Direction Measurement Procedure

In order to measure the longitudinal magnetic field direction, a turning mirror of 1 inch diameter was mounted on the same aluminum fixture (Fig. 6.21a) as the compass for the A_1^n kinematics. The downstream fiducial was replaced with an aluminum post which had the turning mirror (Fig. 6.21b) attached to it, during the compass measurements for the d_2^n kinematics. Before beginning the longitudinal field direction measurement the angle of the turning mirror was aligned to define the beamline and it was fixed at that orientation which helped in determining the longitudinal field direction from the surveyed points. The turning mirror alignment was checked periodically during the whole longitudinal field direction measurement procedure.

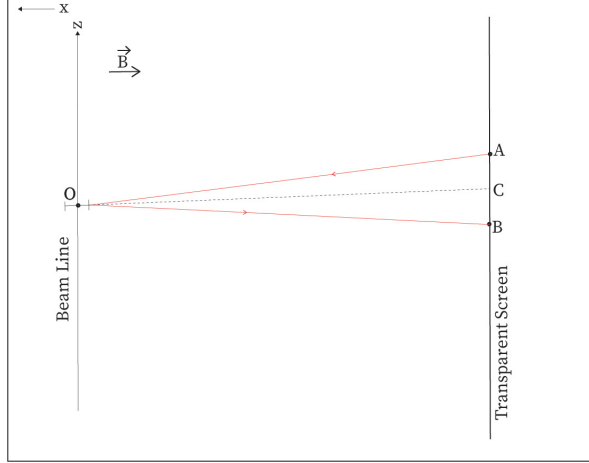


Figure 6.23: Determining the transverse magnetic field direction.

The incident laser beam was reflected from the turning mirror to hit the center of the compass mirror and the reflected laser beam was reflected back to the transparent screen for all three compass locations (Fig. 6.22b). Mirror-1 and mirror-2 were facing the turning mirror when the polarization directions were $+Z$ and $-Z$ respectively. The angular bisector of the incident and reflected laser beams determined the longitudinal magnetic field direction.

6.9.5 Survey Data Analysis and Results

The three compass locations and the upstream and downstream fiducials were surveyed at the beginning of the compass measurements. The incident and reflected points on the transparent screen for all kinematic settings were surveyed after the magnetic field direction measurements were completed. The survey reports were analyzed and the angles between the magnetic field directions and the electron beam direction were calculated for all the kinematic settings.

6.9.5.1 Determining the Transverse Magnetic Field Direction

As shown in Fig. 6.23, the coordinates of the compass center (O), the incident (A) and the reflected (B) points on the transparent screen were surveyed in the absolute Hall C coordinate system. The transverse field direction was given by \overrightarrow{OC} , where C was the midpoint of A and B. The angle made by the transverse magnetic field with the beam line (w.r.t. $+Z$ direction) was calculated as,

$$\alpha = \arccos \left(\frac{z_c - z_0}{\sqrt{(x_c - x_0)^2 + (z_c - z_0)^2}} \right) \quad (6.25)$$

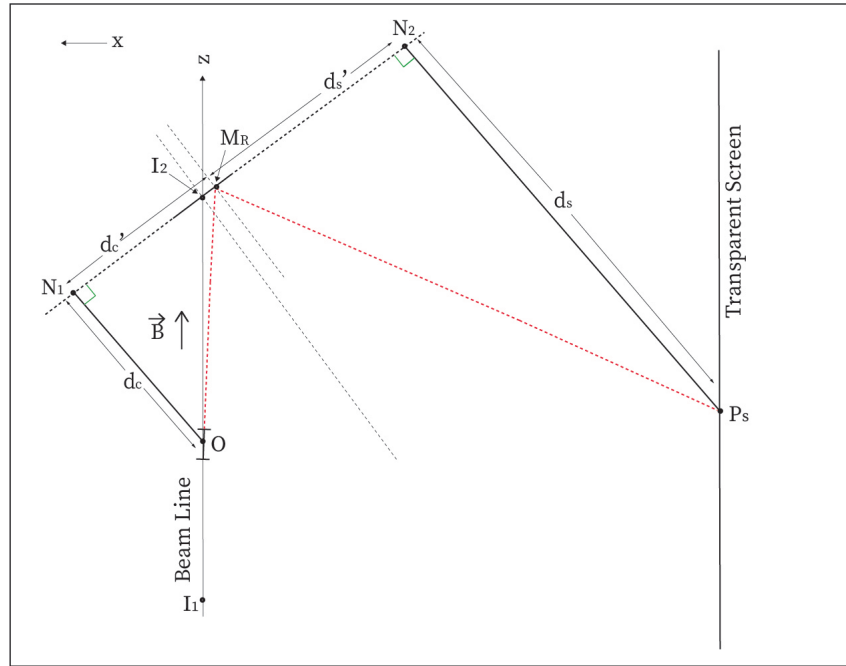
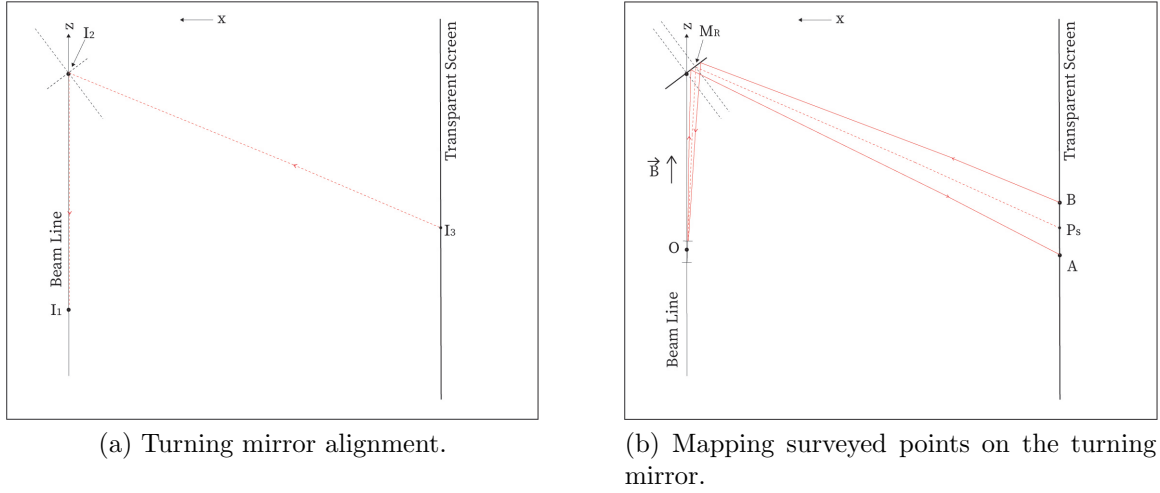


Figure 6.24: Determining the longitudinal magnetic field direction.

6.9.5.2 Determining the Longitudinal Magnetic Field Direction

The center of the turning mirror coincided with the center of the fiducial I_2 as shown in Fig. 6.24a. The fiducials I_1 and I_2 were aligned to define electron beam direction. The turning mirror was aligned such that the laser beam coming from I_3 followed the beamline after reflecting off the turning mirror. The coordinates of the points I_1 , I_2 , and I_3 were surveyed to determine the surface normal of the turning mirror, which was given by the angular bisector of $\overrightarrow{I_1 I_2}$ and $\overrightarrow{I_2 I_3}$. The surveyed incident and reflected beam spots on the screen were A and B respectively. The point M_R on the

turning mirror corresponded to P_s (midpoint of A and B) on the transparent screen (Fig. 6.24b). The longitudinal magnetic field direction was given by $\overrightarrow{OM_R}$.

Geometric analysis (Fig. 6.24c) was used to determine the coordinate of M_R from all the information available for each case and the angle β that $\overrightarrow{OM_R}$ made with positive Z direction was calculated. All calculations were done in the x-z plane as the compass was only sensitive to the horizontal angle. Perpendicular line to the angular bisector of $\overrightarrow{I_1I_2}$ and $\overrightarrow{I_2I_3}$ passing through I_2 lying in the x-z plane was $\overrightarrow{N_1N_2}$. The equation of $\overrightarrow{N_1N_2}$:

$$(z - z_{I_2}) = \left(\frac{-1}{m}\right) (x - x_{I_2}), \quad (6.26)$$

where the slope of the angular bisector is,

$$m = \tan \left(\frac{\arctan \left(\frac{z_{I_2} - z_{I_1}}{x_{I_2} - x_{I_1}} \right) + \arctan \left(\frac{z_{I_2} - z_{I_3}}{x_{I_2} - x_{I_3}} \right)}{2} \right). \quad (6.27)$$

The equations of $\overrightarrow{ON_1}$ and $\overrightarrow{P_sN_2}$ (perpendiculars drawn to $\overrightarrow{N_1N_2}$ from O and P_s respectively) were,

$$z - z_0 = m (x - x_0), \quad (6.28)$$

$$z - z_{P_s} = m (x - x_{P_s}). \quad (6.29)$$

The coordinates of N_1 and N_2 were determined by solving $(\overrightarrow{ON_1}, \overrightarrow{N_1N_2})$ and $(\overrightarrow{P_sN_2}, \overrightarrow{N_1N_2})$, respectively. Length of $\overrightarrow{ON_1}$:

$$d_c = \sqrt{(x_0 - x_{N_1})^2 + (z_0 - z_{N_1})^2}. \quad (6.30)$$

Length of $\overrightarrow{P_sN_2}$:

$$d_s = \sqrt{(x_{P_s} - x_{N_2})^2 + (z_{P_s} - z_{N_2})^2}. \quad (6.31)$$

Length of $\overrightarrow{N_1N_2}$:

$$L = \sqrt{(x_{N_1} - x_{N_2})^2 + (z_{N_1} - z_{N_2})^2}. \quad (6.32)$$

The following equations were solved to determine the coordinates of M_R .

$$d'_c = \sqrt{(x_{N_1} - x_{M_R})^2 + (z_{N_1} - z_{M_R})^2} = L - d'_s, \quad (6.33)$$

$$d'_s = \sqrt{(x_{N_2} - x_{M_R})^2 + (z_{N_2} - z_{M_R})^2} = \frac{L}{1 + \frac{d_c}{d_s}}. \quad (6.34)$$

The angle made by the longitudinal magnetic field with the beam line (w.r.t. +Z direction) was calculated as,

$$\beta = \arccos \left(\frac{(z_{M_R} - z_0)}{\sqrt{(x_{M_R} - x_0)^2 + (z_{M_R} - z_0)^2}} \right). \quad (6.35)$$

Table 6.11: Helmholtz coil and correction coil settings used during compass measurements in September, 2020 for d_2^n kinematic settings with the Helmholtz coils at 0° w.r.t. electron beam direction.

Kin. settings	Pol. directions	MainL current (A)	MainS current (A)	VL current (A)	VS current (A)	HL current (A)	HS current (A)
SHMS at 11° , 7.5 GeV/C	+X	7.418	0.136	6.04	4.03	0.0	0.0
	-X	-7.366	-0.240	6.04	4.10	0.0	0.0
	+Z	0.000	7.227	6.55	4.49	0.0	0.0
	-Z	0.000	-7.308	6.95	4.72	0.0	0.0
SHMS at 14.5° , 6.4 GeV/C	+X	7.418	0.138	6.15	4.31	0.0	0.0
	-X	-7.386	-0.238	6.15	4.20	0.0	0.0
	+Z	0.000	7.294	6.32	4.60	0.0	0.0
	-Z	0.000	-7.406	7.05	4.89	0.0	0.0
SHMS at 18° , 5.6 GeV/C	+X	7.418	0.145	6.04	4.43	0.0	0.0
	-X	-7.387	-0.243	6.66	4.82	0.0	0.0
	+Z	0.000	7.293	4.13	2.82	0.0	0.0
	-Z	0.000	-7.406	7.05	5.21	0.0	0.0
SHMS at 8.5° , 2.12 GeV/C	+X	N/A	N/A	N/A	N/A	N/A	N/A
	-X	N/A	N/A	N/A	N/A	N/A	N/A
	+Z	0.000	7.227	0.04	0.00	0.0	0.0
	-Z	0.000	-7.309	4.52	3.62	0.0	0.0

6.9.5.3 Results

The angles between the electron beam direction and the magnetic field directions were determined and plotted along the z-axis for all measured kinematic settings of both the A_1^n and d_2^n experiments. The compass measurements for the A_1^n kinematic settings were performed in October, 2019 before the experiment started. At that time, the Helmholtz coils were rotated by 45° with respect to the electron beamline. The magnetic field directions were also scanned for one of the d_2^n kinematic settings ($18^\circ, -5.6$ GeV/c) with this Helmholtz coil orientation. The results of the October measurements are shown in Fig. 6.25. After the A_1^n data collection was completed, the Helmholtz coil setup was rotated to make the large coils parallel to the electron beamline.

The compass measurements were performed twice for the d_2^n experiment, once before the experiment (March, 2020) and once after the experiment (September, 2020) with the aforementioned Helmholtz coil orientation (large coil parallel to the beamline). The results are shown in Fig. 6.26 and Fig. 6.27 respectively.

The field direction at different locations along the ^3He target cell deviated from that at the center due to the presence of different steel structures close to the target region and also due to the fringe field effect of the SHMS Horizontal Bender magnet. The effect of the other SHMS and HMS magnets were tested and there was no change

Table 6.12: Helmholtz coil and correction coil settings used during d_2^n production run with the Helmholtz coils at 0° w.r.t. electron beam direction.

Kin. settings	Pol. directions	MainL current (A)	MainS current (A)	VL current (A)	VS current (A)	HL current (A)	HS current (A)
SHMS at 11° , 7.5 GeV/C	+X	7.407	0.137	6.00	4.00	0.0	0.0
	-X	-7.364	-0.237	6.00	4.10	0.0	0.0
	+Z	0.000	7.225	6.50	4.50	0.0	0.0
	-Z	0.000	-7.305	6.90	4.70	0.0	0.0
SHMS at 14.5° , 6.4 GeV/C	+X	7.406	0.139	6.10	4.30	0.0	0.0
	-X	-7.385	-0.239	6.10	4.20	0.0	0.0
	+Z	0.000	7.298	6.30	4.60	0.0	0.0
	-Z	0.000	-7.398	7.00	4.90	0.0	0.0
SHMS at 18° , 5.6 GeV/C	+X	7.406	0.139	6.00	4.40	0.0	0.0
	-X	-7.385	-0.239	6.60	4.80	0.0	0.0
	+Z	0.000	7.298	4.10	2.80	0.0	0.0
	-Z	0.000	-7.398	7.00	5.20	0.0	0.0
SHMS at 8.5° , 2.12 GeV/C	+X	N/A	N/A	N/A	N/A	N/A	N/A
	-X	N/A	N/A	N/A	N/A	N/A	N/A
	+Z	0.000	7.225	0.00	0.00	0.0	0.0
	-Z	0.000	-7.305	4.50	3.60	0.0	0.0

in the target magnetic field due to the different settings of those SHMS and HMS magnets.

All the systematic uncertainties from different sources (section 6.9.6) were propagated to generate the error bars on each data point in the shown plots. The total uncertainty in the magnetic field direction measurement was within $\pm 0.1^\circ$ for each set of measurements satisfying the requirement of the experiments.

6.9.6 Sources of Systematic Uncertainties

Several systematic uncertainties contributed to generate the total error in the compass measurements and they are listed below.

1. **Error propagation from the surveyed points** (Error_{Survey}): The uncertainty in surveying the compass center (O) and the locations of the two fiducials (I_1 and I_2) was ± 0.28 millimeters and that in the mapped points (I_3 , A and B) on the transparent screen was ± 0.50 millimeters. The error propagation for the transverse ($d\alpha$) and longitudinal ($d\beta$) field direction measurements were calculated using the following formulas.

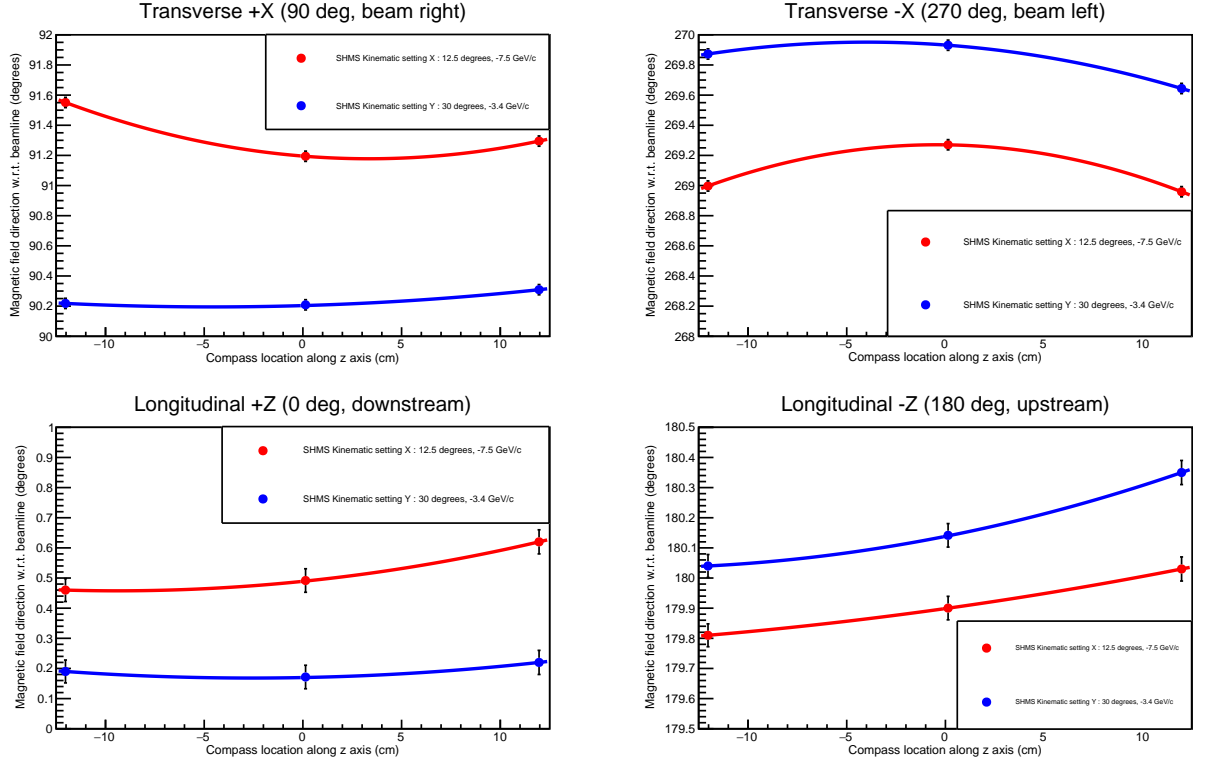


Figure 6.25: The magnetic field direction measurement results for the A_1^n experiment. All angles were calculated w.r.t. +Z direction in absolute Hall C coordinate system. The results from one of the d_2^n kinematic settings (SHMS at 18° , 5.6 GeV/C) were added to this plot because of the similar Helmholtz coil orientation in Hall C.

a) Transverse direction:

$$d\alpha^2 = \left(\frac{\partial\alpha}{\partial x_0}\right)^2 dx_0^2 + \left(\frac{\partial\alpha}{\partial z_0}\right)^2 dz_0^2 + \left(\frac{\partial\alpha}{\partial x_A}\right)^2 dx_A^2 + \left(\frac{\partial\alpha}{\partial z_A}\right)^2 dz_A^2 + \left(\frac{\partial\alpha}{\partial x_B}\right)^2 dx_B^2 + \left(\frac{\partial\alpha}{\partial z_B}\right)^2 dz_B^2 \quad (6.36)$$

b) Longitudinal direction:

$$d\beta = \sqrt{\sum_j \left(\frac{\partial\beta}{\partial x_j}\right)^2 dx_j^2} \quad (6.37)$$

Where $x_j = x_0, z_0, x_A, z_A, x_B, z_B, x_{I_1}, z_{I_1}, x_{I_2}, z_{I_2}, x_{I_3}, z_{I_3}$ were the surveyed coordinates and dx_j was the survey error associated with the particular coordinate.

- Compass mirror alignment** ($\text{Error}_{\text{Mirror}}$): The misalignment between magnetic axis of the cylindrical magnet and compass mirror generated additional errors as described in section 6.9.3 .

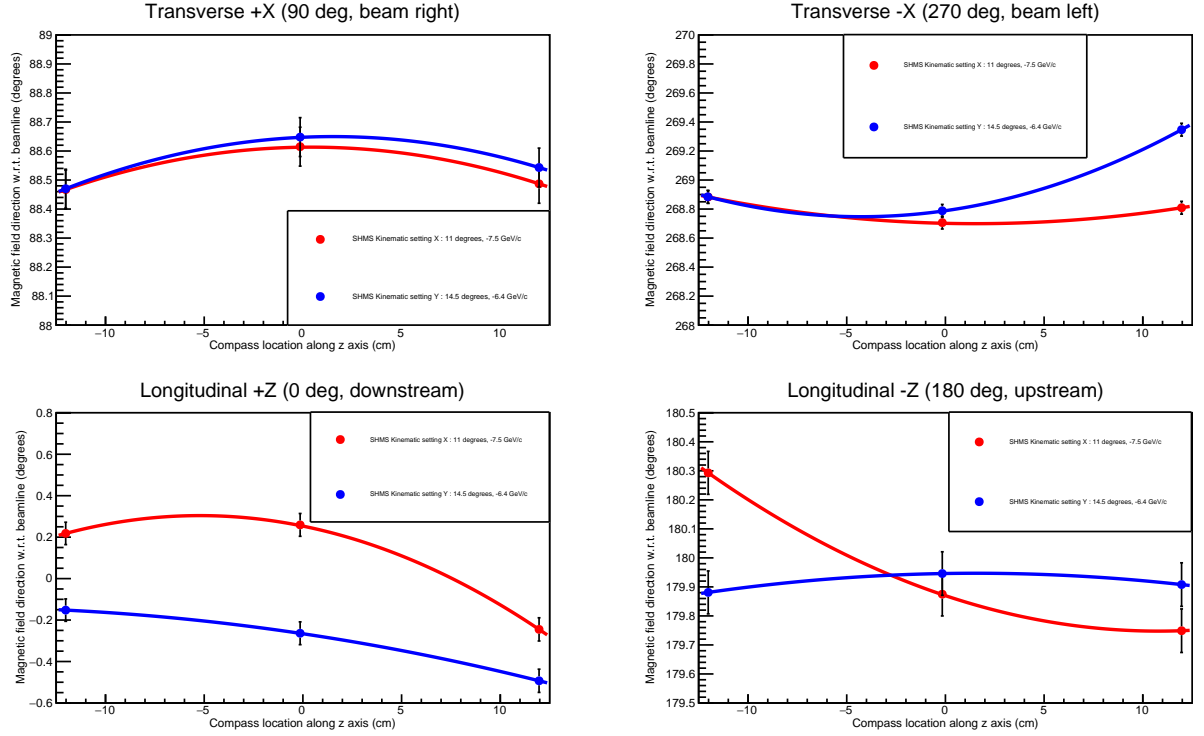


Figure 6.26: The magnetic field direction measurement results for the d_2^n experiment (March, 2020). All angles were calculated w.r.t. +Z direction in absolute Hall C coordinate system.

- a) Projection of the fitted straight line on the horizontal axis.
- b) Fit parameter errors.

3. **Laser beam spot size** ($\text{Error}_{\text{Spot size}}$): The laser beam spot size was reduced to 2 millimeters diameter with the help of a pair of lenses. This beam spot size contributed $\pm 0.006^\circ$ systematic uncertainty in the horizontal angle measurements.
4. **Position of the incident laser beam on the compass mirror** ($\text{Error}_{\text{Center}}$): The laser beam was always reflected off the center of the compass mirror within ± 0.5 millimeter uncertainty that generated $\pm 0.01^\circ$ uncertainty in the horizontal angle measurements.

6.9.7 Studies Done to Investigate the Differences in the March and September Data

The results from the March and September compass measurements were compared and the results agreed within $\pm 0.5^\circ$ (Fig. 6.28). A series of studies were performed to investigate the difference in the March and September results.

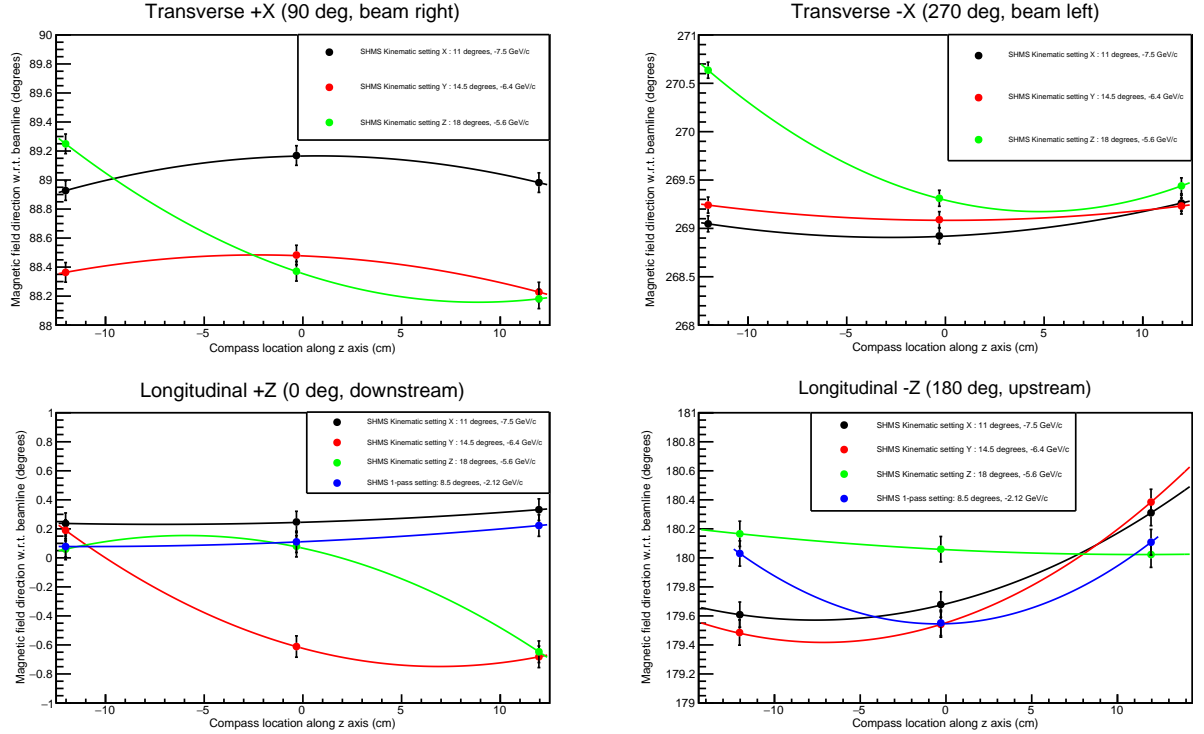


Figure 6.27: The magnetic field direction measurement results for the d_n^0 experiment (September, 2020). All angles were calculated w.r.t. +Z direction in absolute Hall C coordinate system.

- **Hall C condition:**

Hall C was shut down after the March compass measurements for five months. All the instruments were powered off during that period and they were powered back on in September, 2020. The power supplies for the Helmholtz coils that generate the target holding magnetic field were replaced with more stable ones. Non-magnetic electron beam pipe was installed before the September measurements which was not present in March.

- **Check if the compass was placed at the surveyed locations everytime:** The holes on the aluminum fixture were 4 cm apart. To check if the compass was placed in a wrong hole in one of the measurements, the September data was analyzed by assuming the compass was shifted by 1 hole either in the upstream or downstream directions. The transverse direction measurement results (Fig. 6.29) for both the SHMS 11° and 14.5° kinematic settings showed that the magnetic field direction will change by 2° if the compass location was shifted by a single hole. As the March and September results agreed within 0.5° , we could eliminate this possibility.
- **Check if there was any consistent offset introduced during the survey of the compass locations:**

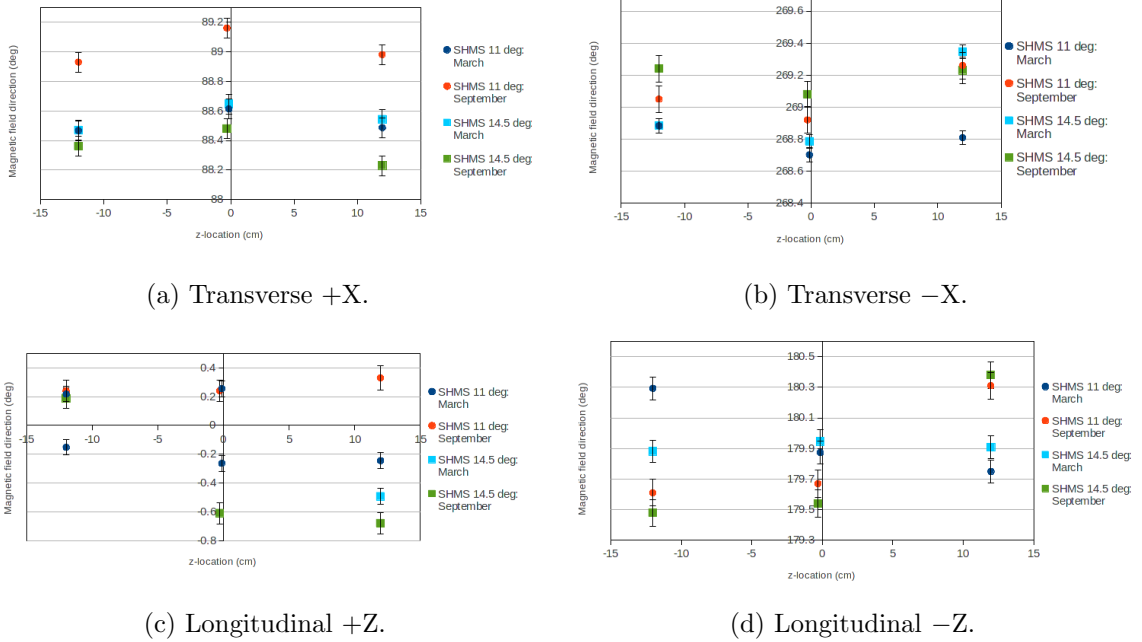


Figure 6.28: Comparison of March and September compass measurement results.

The x and z locations of the compass for the September data were scanned over a wide range. The particular x and z-coordinates for which the September results will agree to the March results within $\pm 0.1^\circ$ were found for the transverse direction measurement settings. The determined offsets were not consistent for all the kinematic settings as shown in Fig. 6.30. Based on this study, possibility of any constant offset in compass location survey results during the September measurements was eliminated.

- **Check if there was any consistent offset introduced during the survey of the fiducial locations:**

Two fiducials (upstream and downstream) were used to define the electron beam line as a reference for the magnetic field direction in Hall C. The downstream fiducial location was varied 2 cm about the surveyed location and looked for any x and z-coordinates, that will make the March and September results agree within $\pm 0.1^\circ$. While doing this the upstream fiducial location, compass locations and the mapped point locations on the transparent screen were fixed to the values provided by the survey group. The same procedure was repeated for the upstream fiducial location. In both the cases, no x and z-locations were found within ± 2 cm of the surveyed data that could match the September results with the March results.

The March and September compass measurements were performed under different hall and hardware conditions. The two sets of results were not be combined and each measurement was applied to the production runs taken with the same configu-

ration. The angle of the magnetic field w.r.t. electron beam direction was calculated in Hall C coordinate system with less than $\pm 0.01^\circ$ for each set of measurements, satisfying the requirement of the experiments.

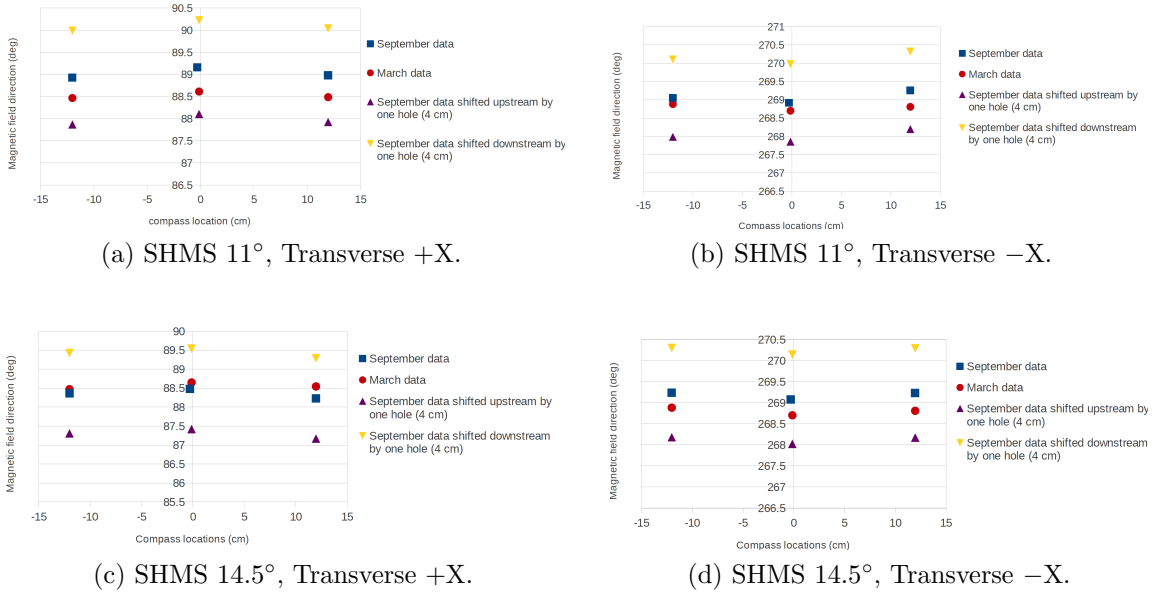


Figure 6.29: Magnetic field direction if the compass was placed in the wrong location.

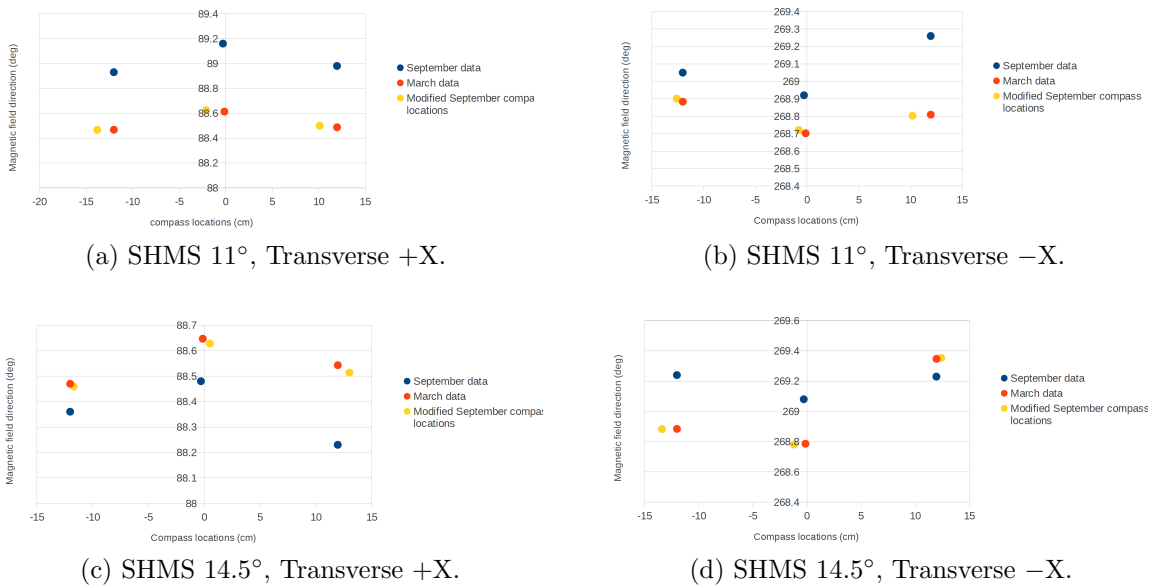


Figure 6.30: Check for consistent offset in compass locations to match the March and September results.

Chapter 7 Experimental Data Analysis

The goal of the data analysis for experiment E12-06-121 was to extract the g_1 and g_2 of ^3He from the measurement of the double spin asymmetries and the unpolarized cross-section. The neutron g_2 and d_2 will be extracted by performing nuclear corrections to the ^3He structure functions. The analysis flowchart is shown in Fig. 7.1 and each step after the completion of raw data taking will be discussed in this chapter.

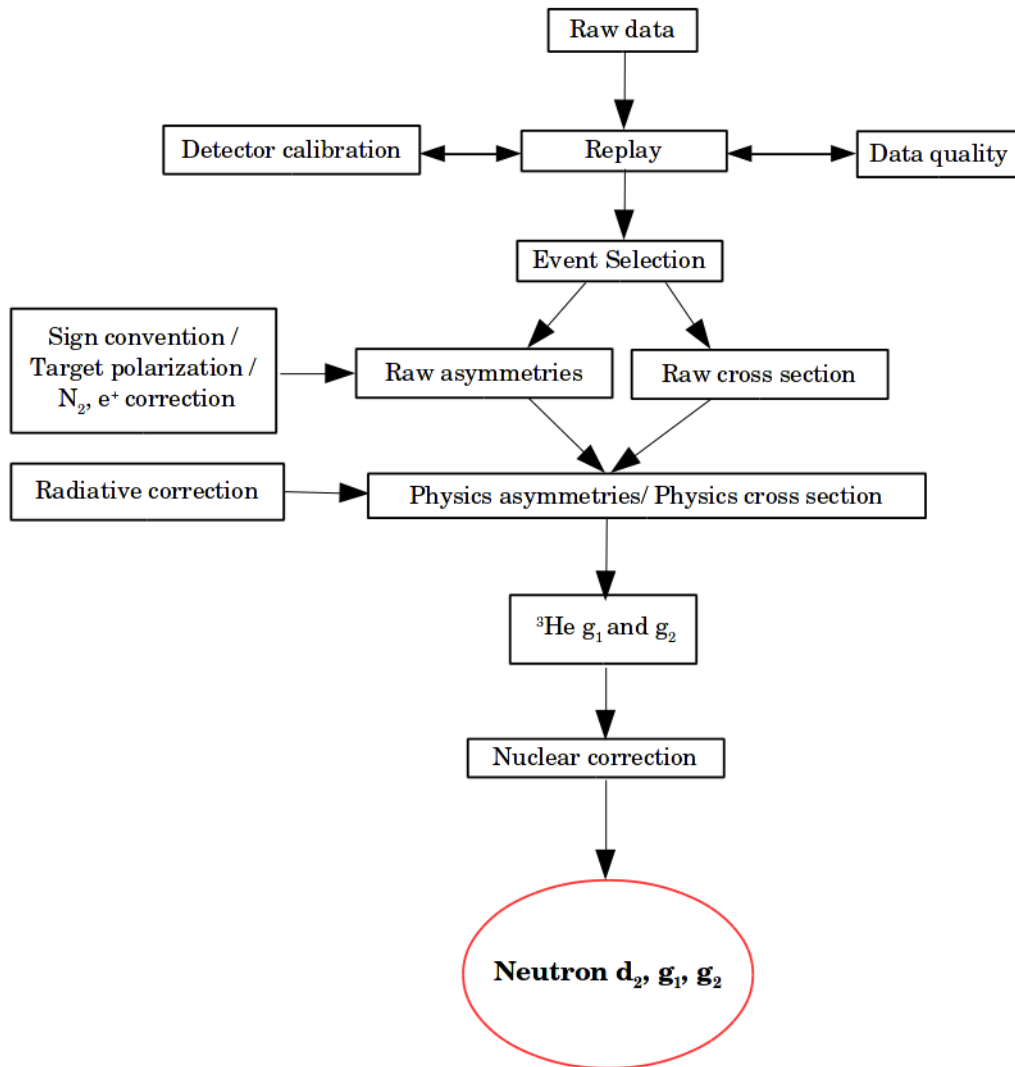
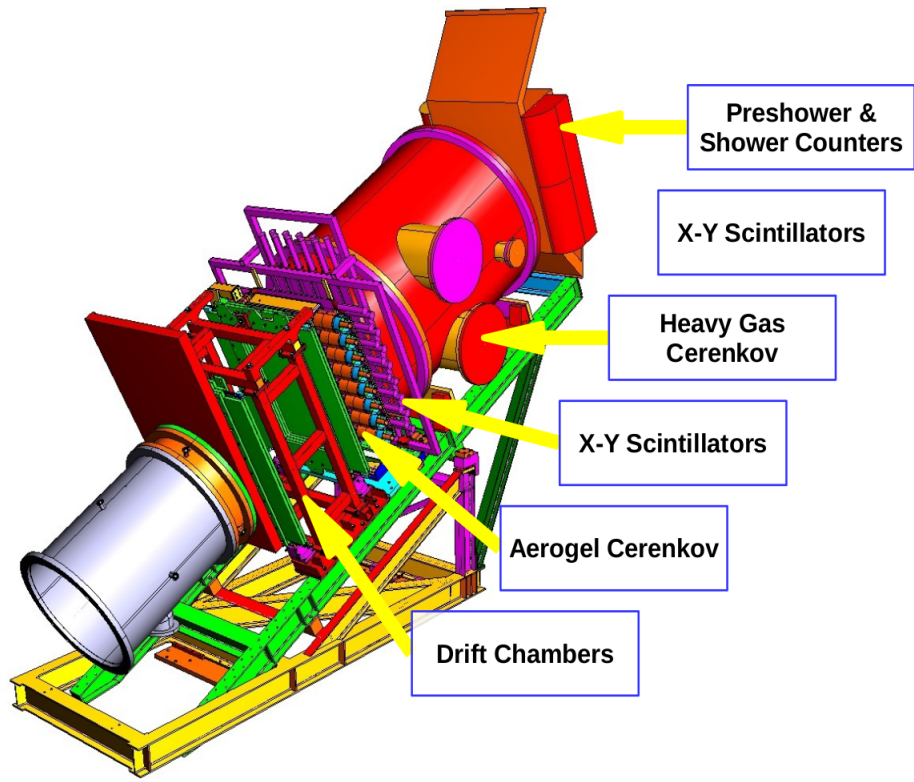
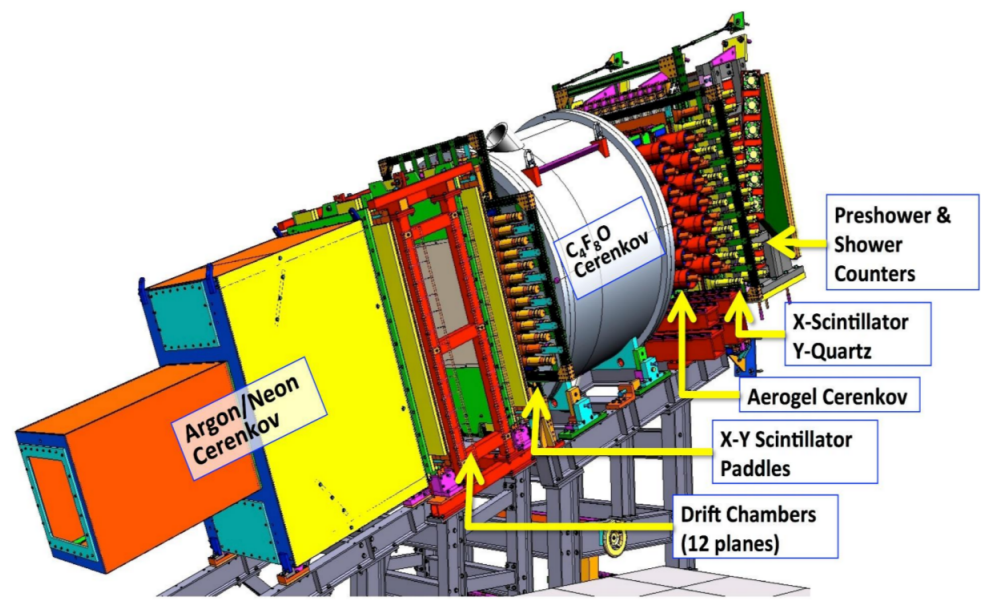


Figure 7.1: The experimental data analysis flowchart that is being followed to extract g_2^n and d_2^n .



(a) Detectors inside HMS.



(b) Detectors inside SHMS.

Figure 7.2: The HMS and SHMS detector stacks showing the order of the particle tracking and particle identification (PID) detectors [88].

7.1 Data Acquisition

The data acquisition for the experiment E12-06-121 was performed by a Jefferson Lab software package named CODA (CEBAF online data acquisition package). The duration of each run was ~ 1 hour and the data was recorded in three different ways [88].

- The scaler readings were taken every few seconds.
- The ADC, TDC and FADC readings were recorded for each event.
- The EPICS database containing the target, beamline, and detector instrumentation settings was updated every 10 seconds.

At the beginning of a run the PRETRIG (pedestals were triggered to start recording the ADC outputs) signaled the data acquisition system to start recording physics events and the ADC, TDC, FADC outputs were recorded event by event.

Table 7.1: The list of HMS and SHMS reference times associated with the detectors.

(a) HMS

Detector Name	Reference Time Name
Calorimeter [ADC]	hFADC_TREF_ROC1
Cherenkov [ADC]	hFADC_TREF_ROC1
Drift Chamber [TDC]	hDCREF1-5
Hodoscope [ADC]	hFADC_TREF_ROC1
Hodoscope [TDC]	hTref2

(b) SHMS

Detector Name	Reference Time Name
Calorimeter [ADC]	pFADC_TREF_ROC2
Cherenkov [ADC]	pFADC_TREF_ROC2
Drift Chamber [TDC]	pDCREF1-10
Hodoscope [ADC]	pFADC_TREF_ROC2
Hodoscope [TDC]	pTref1-2

7.2 Reference Time Cuts

The first step of the data analysis was to determine the reference time cuts. All the ADC, TDC, and FADC of every detector received a copy of PRETRIG which is known as the reference time at run start. Both the reference time and the triggers were recorded during data acquisition and analyzed later during Hall C data replay by subtracting the reference time from the detector signal. The analyzer package of Hall C is known as hcana which assumed the first hit to be the good hit in case of

Table 7.2: The list of HMS and SHMS reference time variables in the hcana leaf.

(a) HMS

Reference Time Name	hcana Leaf Name
hFADC_TREF_ROC1	T.hms.hFADC_TREF_ROC1_adcPulseTimeRaw
hTref1	T.hms.hT1_tdcTimeRaw
hTref2	T.hms.hT2_tdcTimeRaw
hDCREF1	T.hms.hDCREF1_tdcTimeRaw
hDCREF2	T.hms.hDCREF2_tdcTimeRaw
hDCREF3	T.hms.hDCREF3_tdcTimeRaw
hDCREF4	T.hms.hDCREF4_tdcTimeRaw
hDCREF5	T.hms.hDCREF5_tdcTimeRaw

(b) SHMS

Reference Time	hcana Leaf Name
pFADC_TREF_ROC2	T.shms.hFADC_TREF_ROC2_adcPulseTimeRaw
pTref1	T.shms.pT1_tdcTimeRaw
pTref2	T.shms.pT2_tdcTimeRaw
pDCREF1	T.shms.pDCREF1_tdcTimeRaw
pDCREF2	T.shms.pDCREF2_tdcTimeRaw
pDCREF3	T.shms.pDCREF3_tdcTimeRaw
pDCREF4	T.shms.pDCREF4_tdcTimeRaw
pDCREF5	T.shms.pDCREF5_tdcTimeRaw
pDCREF6	T.shms.pDCREF6_tdcTimeRaw
pDCREF7	T.shms.pDCREF7_tdcTimeRaw
pDCREF8	T.shms.pDCREF8_tdcTimeRaw
pDCREF9	T.shms.pDCREF9_tdcTimeRaw
pDCREF10	T.shms.pDCREF10_tdcTimeRaw

multiple hits. But if the first hit was not a good hit, then it will result in a wrong reference time subtraction in the detector ADC, TDC, or FADC spectra. So, a proper determination of reference time cuts were necessary to select the good hit. The reference time variables associated with each detectors of the HMS and SHMS are listed in the Table. 7.1 and, the hcana leaf names of the reference time variables are listed in the Table. 7.2.

Before determining the reference time cuts, the multiplicity variables were looked at to see the number of ADC and TDC hits happening per event. For a good physics event, the multiplicity is generally 1 or, it can be n=2,3.. if the reference time was the OR of n number of PRETRIGs. After making the TDC time window bigger (0 to 100000), the multiplicity cuts were determined from the hcana multiplicity leaf and the multiplicity=1,2,3 cuts were then applied to the reference time variables. The conversion factors of TDC and ADC channels to time are 0.1 ns and 0.0625 ns per channel, respectively. In the Fig. 7.3 one example of the multiplicity leaf for HMS

1-pass elastic run 2608 and the corresponding reference time plots are shown.

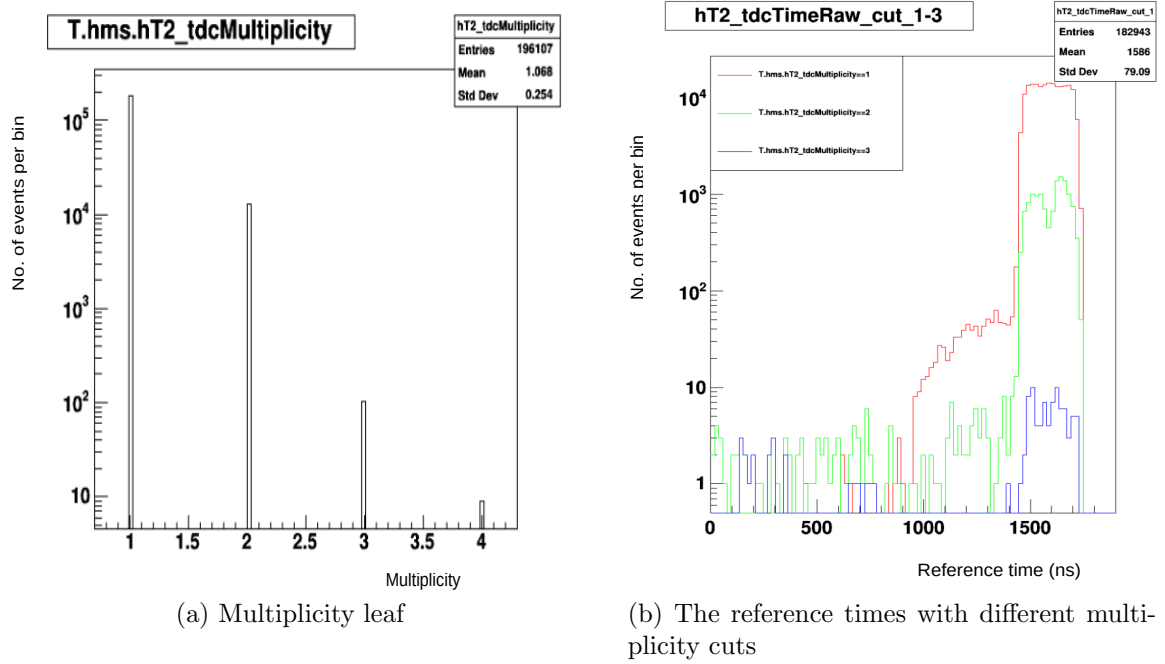


Figure 7.3: The hcana multiplicity leaf of HMS 1-pass elastic run 2608 and the corresponding reference time variable with the three multiplicity cuts.

This procedure was performed for several HMS and SHMS runs to determine the reference time cuts by selecting the clean signal. Fig. 7.4 shows the determined reference time cuts by analyzing HMS production run 4195 (Kin-A) and SHMS production run 11395 (Kin-X). All the reference time cuts are listed in Table. 7.3, and they were updated in the corresponding parameter file.

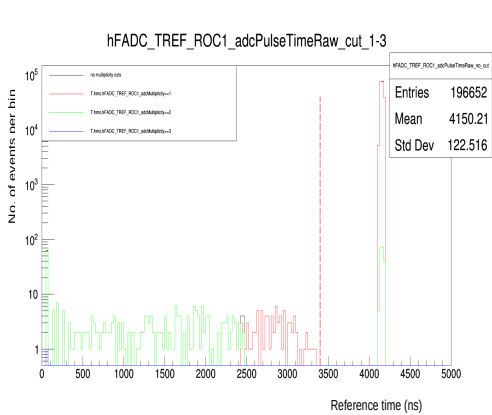
Table 7.3: The list of final HMS and SHMS reference time cuts.

(a) HMS

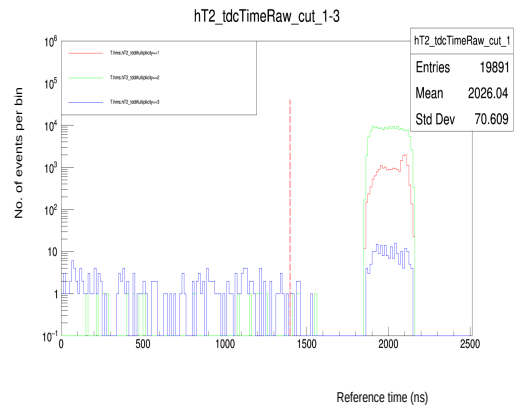
Reference Time Name	Reference Time Cut
hFADC_TREF_ROC1	3400
hDCREF1-5	20000
hT1-2	1400

(b) SHMS

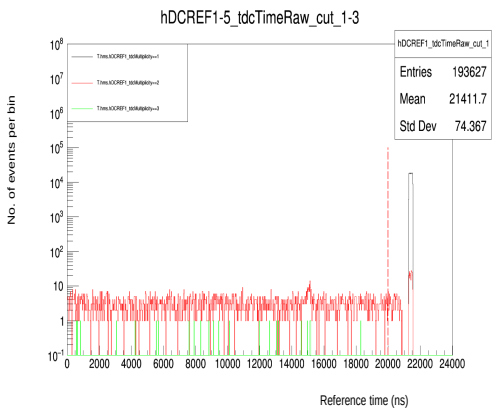
Reference Time Name	Reference Time Cut
pFADC_TREF_ROC2	4200
pDCREF1-10	14400
pT1-2	3400



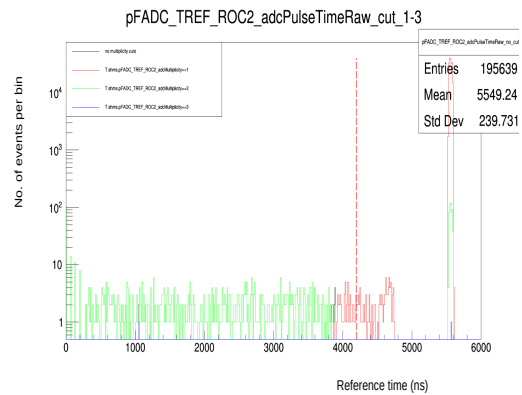
(a)



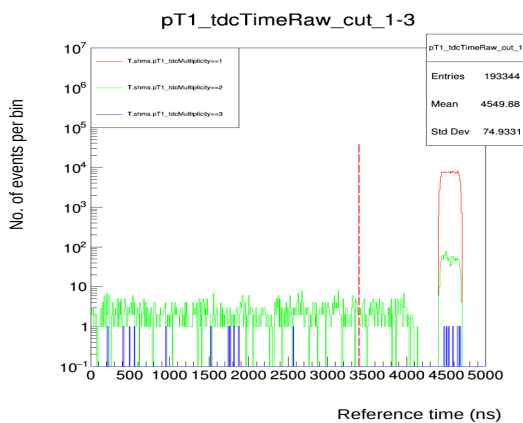
(b)



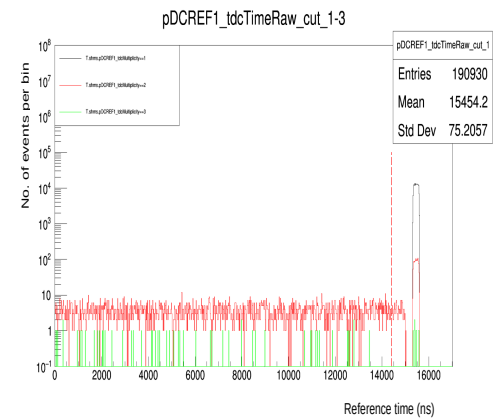
(c)



(d)



(e)



(f)

Figure 7.4: The determination of HMS (a, b, c) and SHMS (d, e, f) reference time cuts, the determined cuts are shown by a red dashed line in each plot.

7.3 Detector Analysis

The detector analysis was done in two steps: determining the detector time window cuts and, detector calibration. Once the reference time cuts were determined, the determination of the detector time window cuts were necessary to eliminate any background slipped into the detector time windows. The time difference between ADC and TDC hit times for each PMT was plotted for the Cherenkov, calorimeter, and hodoscopes to determine the time windows. For the drift chamber the time window cuts were made on the raw drift times for each plane. In hcana the time difference was defined as follows.

- Hodoscope: $\text{AdcTdcDiffTime} = \text{TdcTime}[\text{ipmt}] - \text{AdcPulseTime}[\text{ipmt}]$
- Calorimeter, Cherenkov: $\text{AdcTdcDiffTime} = \text{HodoStartTime} - \text{AdcPulseTime}[\text{ipmt}]$

Where the $\text{AdcPulseTime}[\text{ipmt}]$ was the pulse time for a particular PMT in the detector and, the HodoStartTime was the projection of the hodoscope time in the focal plane of the spectrometers. The determined time window cuts were applied to the corresponding detector parameter files before proceeding with the detector calibration.

The Hodoscope Calibration

The hodoscopes provided the trigger for the data acquisition in the experiment. For particle tracking, the time when the particle hits the hodoscope paddle is required. Hardware calibrations were performed before the experiment to convert the TDC values to the time of the hit.

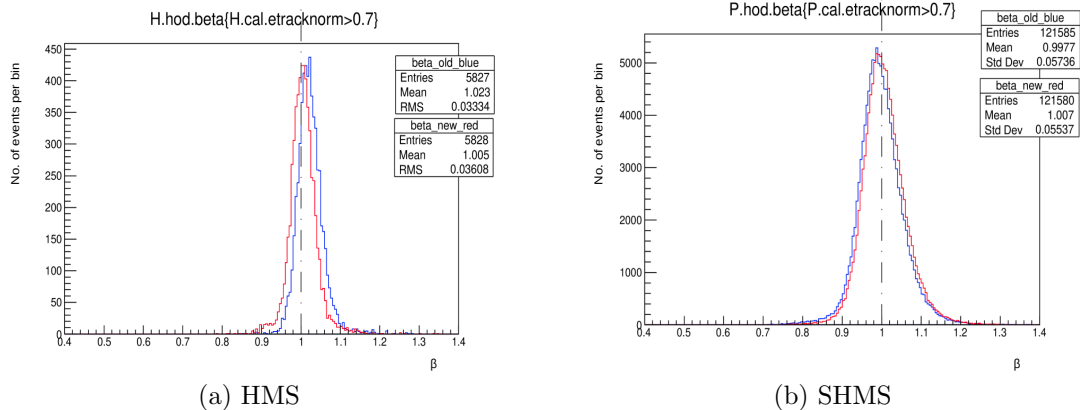


Figure 7.5: The β distribution plots after HMS and SHMS hodoscope calibration. The blue and red plots are the uncalibrated and the calibrated β distributions respectively. (Plots generated by M. Chen)

However, software calibration was also required before the data analysis to correct for the delays when the hodoscope scintillation light passed through various compo-

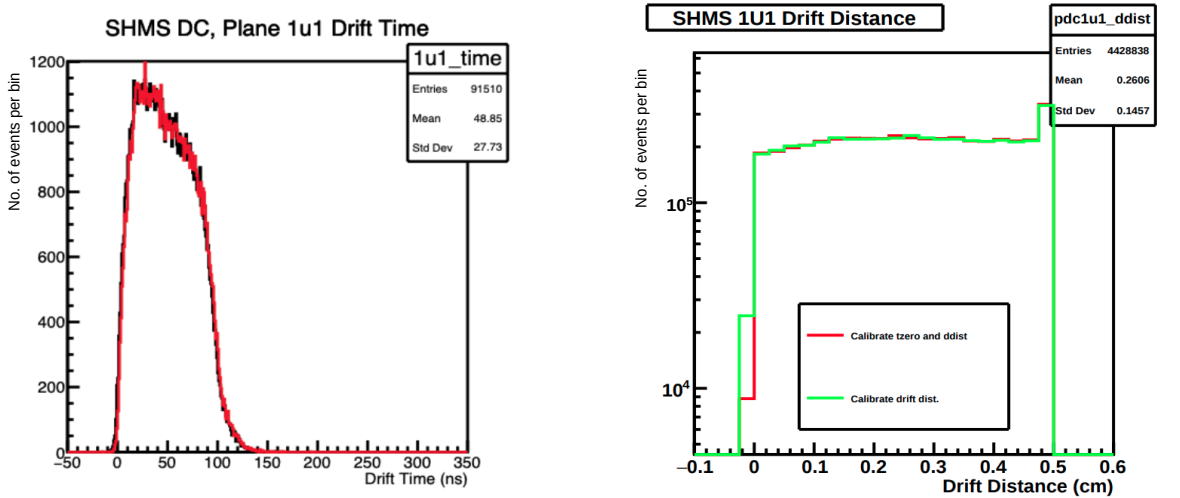
nents of the detector to reach the PMTs. If these corrections were applied correctly, the relativistic velocity ($\beta = \frac{v}{c}$) of the particle should match the same calculated from the distance between the hodoscope scintillator planes and the time of flight. For high energy electrons, the β distribution should have a peak at unity and that was verified as part of the hodoscope calibration (Fig. 7.5).

The Drift Chamber Calibration

The drift chamber signal was used for particle trajectory reconstruction. The drift chamber TDC values of the hits were converted to drift time (the time when the particle traveled through the focal plane of the spectrometer) using the information from the hodoscopes. The positions of the particle w.r.t. the drift chamber sense wires were determined from the drift time distribution, $F(t)$ using the following formula.

$$D(t) = D_{max} \frac{\int_{t_{min}}^t F(t) dt}{\int_{t_{min}}^{t_{max}} F(t) dt} \quad (7.1)$$

Where, $D(t)$ is the drift distance, D_{max} is half of the cell width (maximum drift distance), t is time from TDC value and, t_{min} and, t_{max} are the minimum and maximum of the time range in the drift time distribution fit. During this calibration, the assumption was that the drift position distribution was uniform when all cells were combined. An example of the drift time distribution and the corresponding drift distance distribution is shown in Fig. 7.6. This calibration was performed for all drift chamber planes and all kinematic settings of the experiment.



(a) Drift time distribution, $F(t)$

(b) Drift distance distribution, $D(t)$

Figure 7.6: The drift time and drift distance distribution plots for the SHMS first drift chamber wire plane U. The analysis was done using a SHMS defocused run 9644. (Plots generated by J. Chen.)

The Cherenkov Calibration

The components of the HMS and SHMS Cherenkov detectors were described in Section 4.2.3. The HMS gas Cherenkov (CER) had two PMTs and the SHMS noble gas Cherenkov (NGCER) had four PMTs attached. The detector variables for the CER and NGCER time windows are listed in the Table. 7.4.

The time difference of the Cherenkov pulse time and the hodoscope start time was calculated with multiplicity==1 cut that resulted in good AdcTdcTimeDiff. This calculated time difference was plotted on top of the pre calculated good AdcTdcTimeDiff in hcana (root tree variable: H.cer.goodAdcTdcTimeDiff) as a cross-check. The CER and NGCER time window plots for HMS run 4195 (Kin-A) and SHMS run 11395 (Kin-X) are shown in Fig. 7.8. The determined time window cuts for all PMTs for a particular detector were the same and they are listed below.

- HMS CER: minimum 60 ns, maximum 200 ns
- SHMS NGCER: minimum -20 ns, maximum 80 ns

Table 7.4: The list of HMS and SHMS Cherenkov detector variables used in determining the time window cuts.

(a) HMS

Detector Variable Name	Description
H.hod.starttime	hodoscope start time
H.cer.adcPulseTime [ipmt]	gas Cherenkov pulse time
H.cer.goodAdcMult [ipmt]	multiplicity of gas Cherenkov hits
H.cer.goodAdcTdcDiffTime [ipmt]	pre calculated good difference time

(b) SHMS

Detector Variable Name	Description
P.hod.starttime	hodoscope start time
P.ngcer.adcPulseTime [ipmt]	noble gas Cherenkov pulse time
P.ngcer.goodAdcMult [ipmt]	multiplicity of noble gas Cherenkov hits
P.ngcer.goodAdcTdcDiffTime [ipmt]	pre calculated good difference time

Once the Cherenkov time window cuts were applied to the parameter files, the data was replayed again to perform the Cherenkov calibration. The electrons generated Cherenkov light or photons in the operating condition while traveling through the Cherenkov detector. Those photons hit the photocathode of the PMT to extract photoelectrons which were read out as demonstrated in the Fig. 7.7. The purpose of the calibration was to determine the charge output (pC) of each PMT when one photoelectron was extracted.

In the case of the HMS gas Cherenkov (CER), the single photoelectron peak (SPE) was clearly visible in the ADC spectra. The SPE peak in the pulse integral histogram

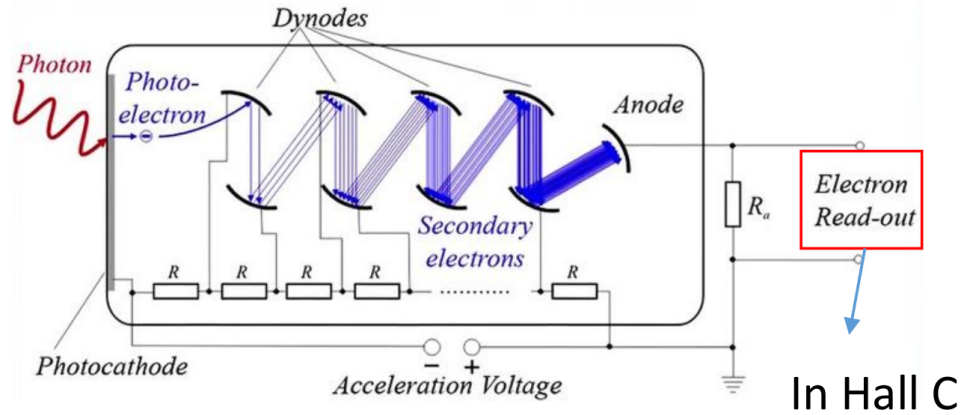
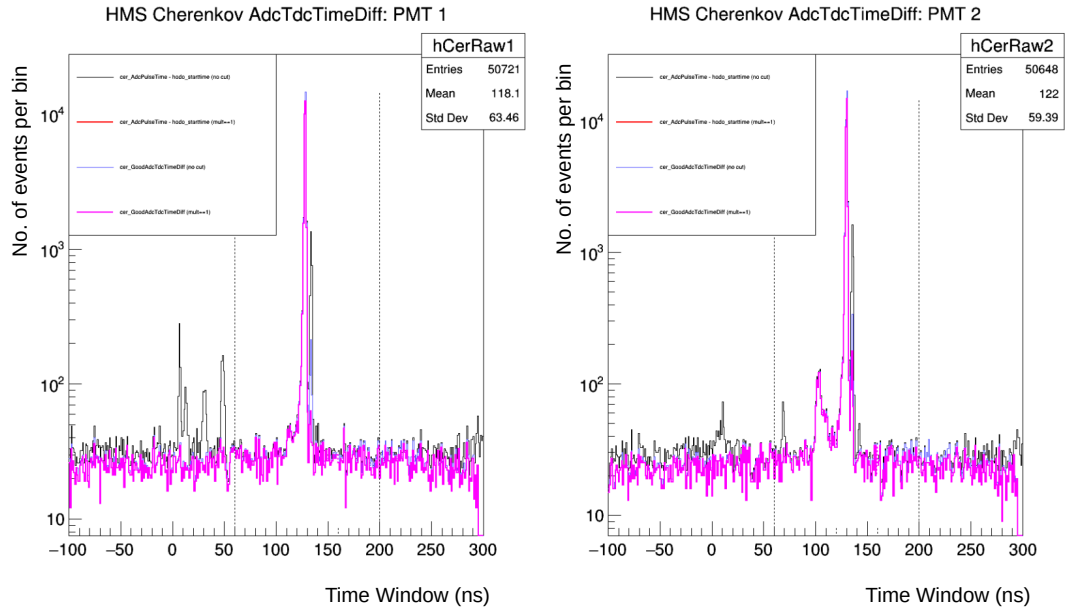


Figure 7.7: The electron read out of Cherenkov PMTs when one photoelectron is extracted from the photocathode.

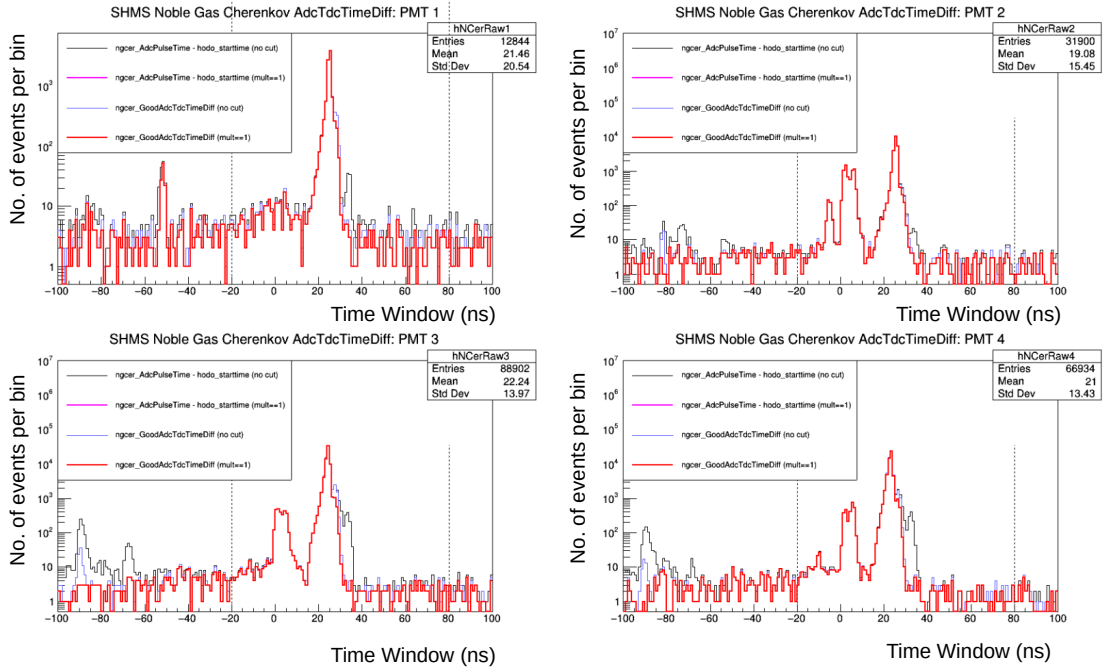
(hcana leaf name: H.cer.goodAdcPulseInt) was fitted with a Gaussian distribution with a goodAdc multiplicity==1 cut. The fitted mean gave us the conversion factor so that $1/\text{mean}$ was the charge per photoelectron extraction. The HMS Cherenkov calibration was performed for different runs (1-pass quasi-elastic, C-optics, DIS, and cosmic) for both the PMTs (Fig. 7.9 and Fig. 7.10). The calibration constant ($1/\text{mean}$) was very close for all the analyzed runs. However, the cosmic run had the lowest background that resulted in a more reliable peak location. So the calibration constant from the cosmic run was chosen and the determined HMS Cherenkov calibration constants were $1/7.664$ (PMT1) and $1/7.904$ (PMT2).

In the case of SHMS noble gas Cherenkov (NGCER), the SPE spectrum was not clearly visible in the ADC pulse integral spectra. Because of that, the electrons were selected with particle identification cuts in the calorimeter energy. The cuts used in the SHMS ADC pulse integral histogram are listed below.

- P.ngcer.goodAdcMult==1 for the PMT under calibration.
- $0.8 < P.\text{cal.etoctracknorm} < 1.4$, PID cut on total energy (E/P) to choose electrons (determined from Fig. 7.12).
- Momentum acceptance cut: $-10 < P.\text{gtr.dp} < 22$ (%).
- NGCER mirror plane cuts (determined from Fig. 7.13):
 - PMT1: $0 < X_{\text{atCer}} < 5.5$ (cm), $0 < Y_{\text{atCer}} < 12$ (cm)
 - PMT2: $0 < X_{\text{atCer}} < 3.8$ (cm), $-13.7 < Y_{\text{atCer}} < -2.2$ (cm)
 - PMT3: $-17 < X_{\text{atCer}} < 0.2$ (cm), $1.5 < Y_{\text{atCer}} < 16$ (cm)
 - PMT4: $-13 < X_{\text{atCer}} < -1$ (cm), $-16 < Y_{\text{atCer}} < 0$ (cm)
- Cuts to consider signals in single PMT only.



(a) HMS CER



(b) SHMS NGCER

Figure 7.8: The detector time window cuts for the HMS CER and the SHMS NGCER. The precalculated goodAdcTdcDiffTime (red) with multiplicity==1 overlapped with the calculated time difference (magenta) with multiplicity==1.

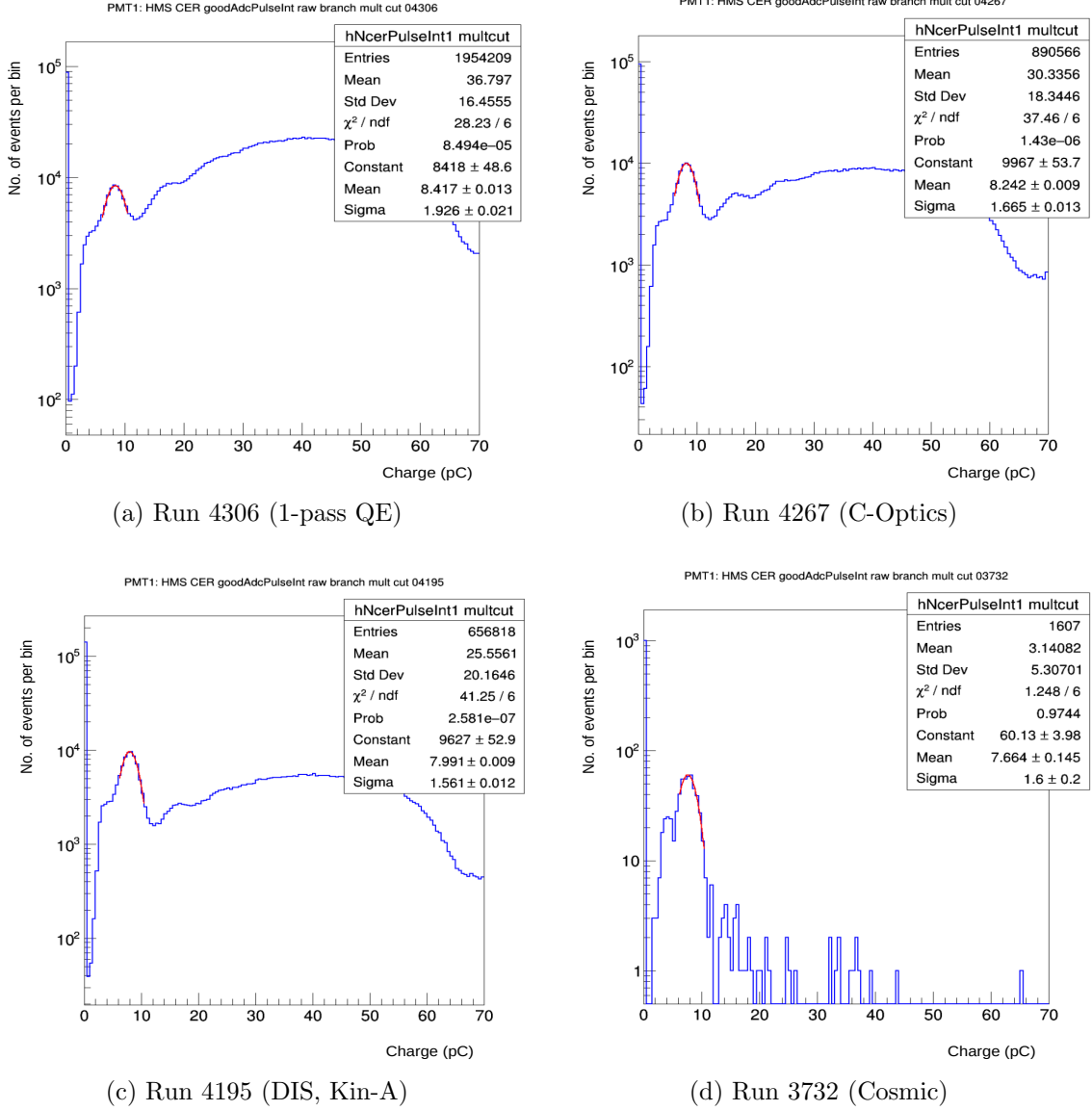


Figure 7.9: The calibration of HMS gas Cherenkov for PMT1.

The npe signal (number of photo electrons extracted from the photocathode) should follow a Poisson distribution as follows.

$$P(npe) = \frac{\lambda^{npe} e^{-\lambda}}{npe!}. \quad (7.2)$$

Where, λ is the mean value of the npe. If λ is not an integer, the npe! is replaced with a Gamma function, $\Gamma(npe + 1)$ resulting in the following distribution.

$$P(npe) = \frac{\lambda^{npe} e^{-\lambda}}{\Gamma(npe + 1)}. \quad (7.3)$$

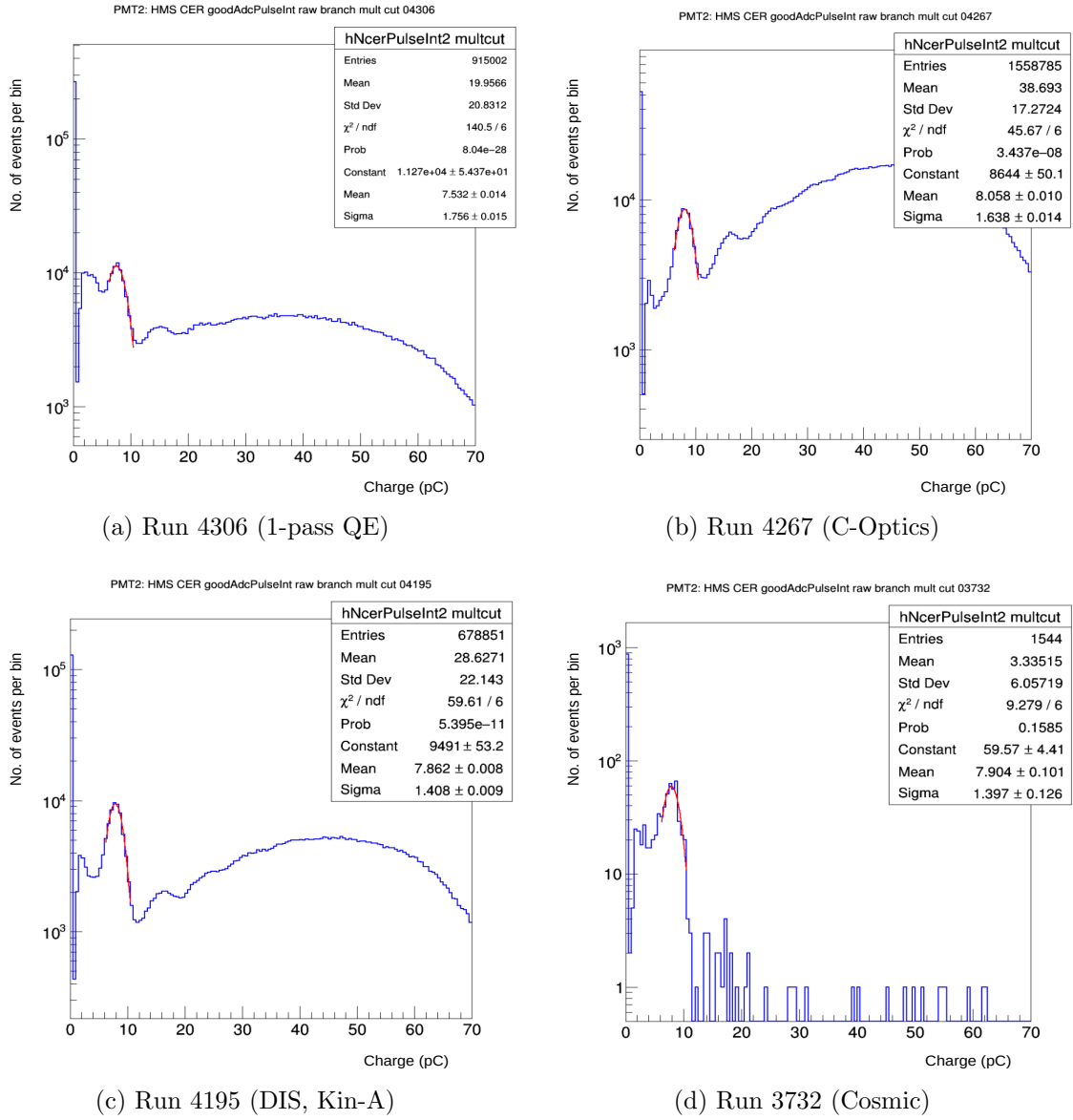


Figure 7.10: The calibration of HMS gas Cherenkov for PMT2.

The uncalibrated PMT signal was a spectrum $x = npe / \text{gain}$ where gain is the charge per photo electron. x also follows a Poisson like distribution, so that,

$$P(npe) = \frac{\lambda^{\frac{x}{\text{gain}}} e^{-\lambda}}{\Gamma(\frac{x}{\text{gain}} + 1)}. \quad (7.4)$$

The ngcer spectra were fitted with the following fit function as shown in Fig. 7.11.

$$f = p_0 \left(\frac{p_1}{p_2} \right)^{\frac{x}{p_2}} \frac{e^{-\frac{x}{p_2}}}{\Gamma\left(\frac{x}{p_2} + 1\right)}. \quad (7.5)$$

Where, p_2 was the gain and, $\frac{p_1}{p_2}$ was the average number of photoelectrons (λ). The determined calibration constants were 1/5.054 (PMT 1), 1/3.521 (PMT 2), 1/4.419 (PMT 3), 1/3.788 (PMT 4).

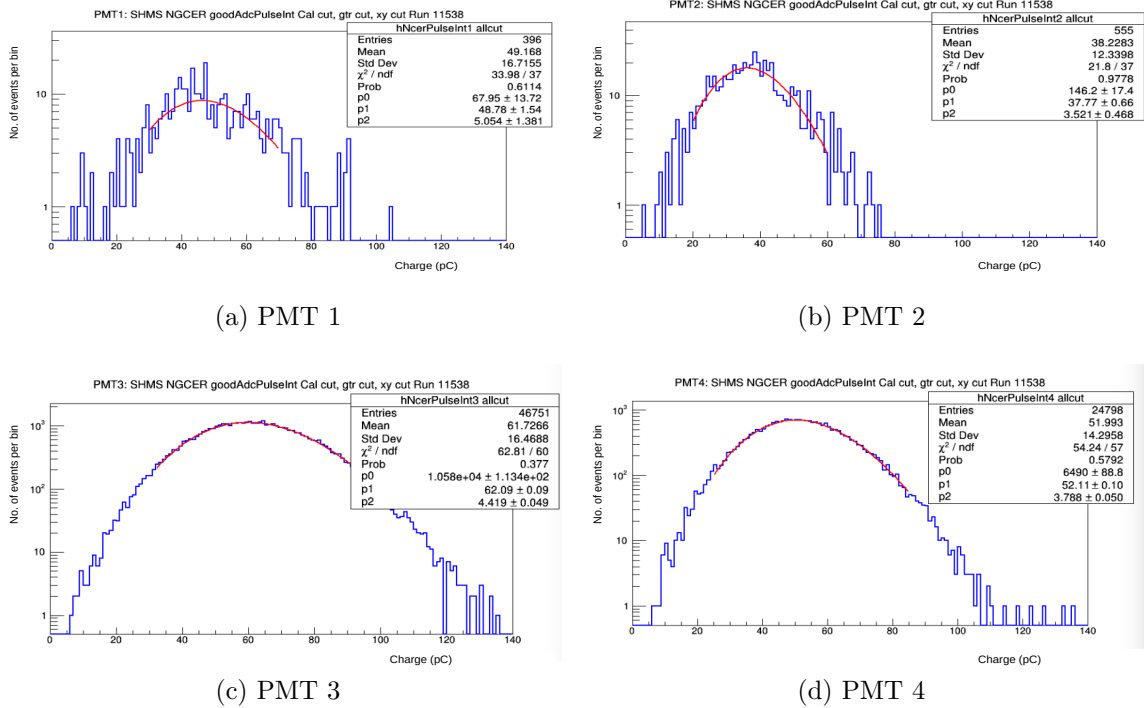


Figure 7.11: The SHMS Cherenkov calibration for all four PMTs for run 11538 (13° , -2.1286 GeV/c). The x-axis has unit pC and the inverse of the fit parameter p_2 was the calibration constant.

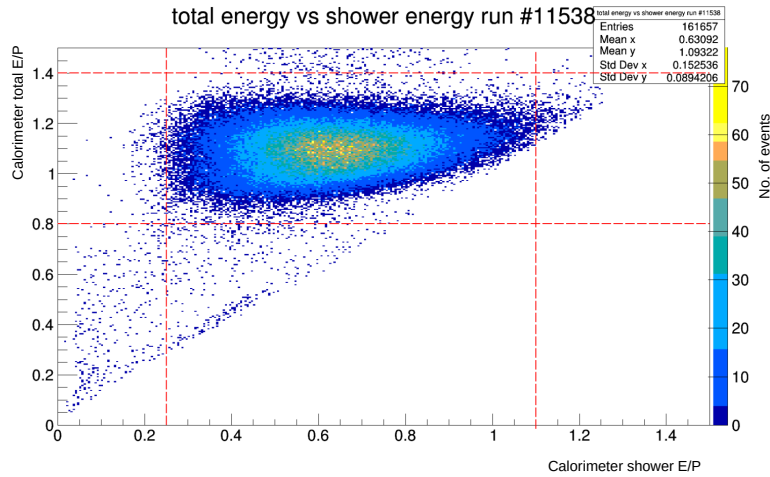
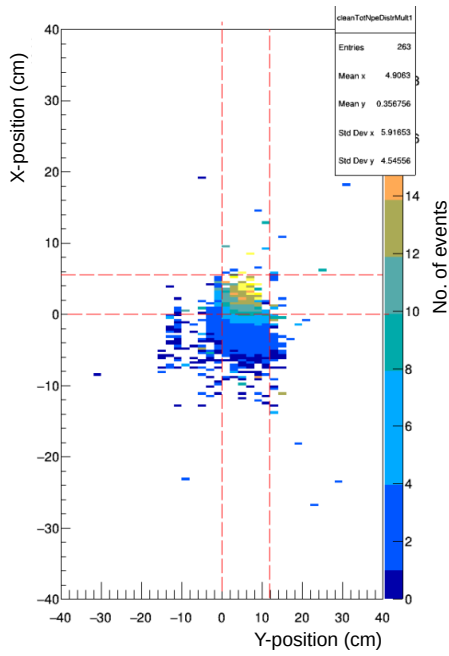
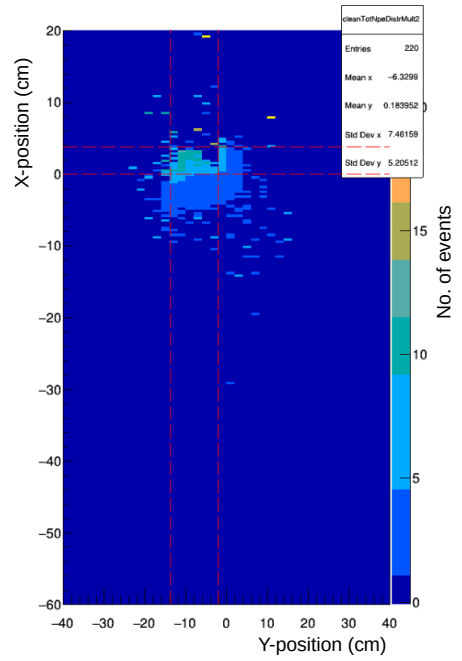


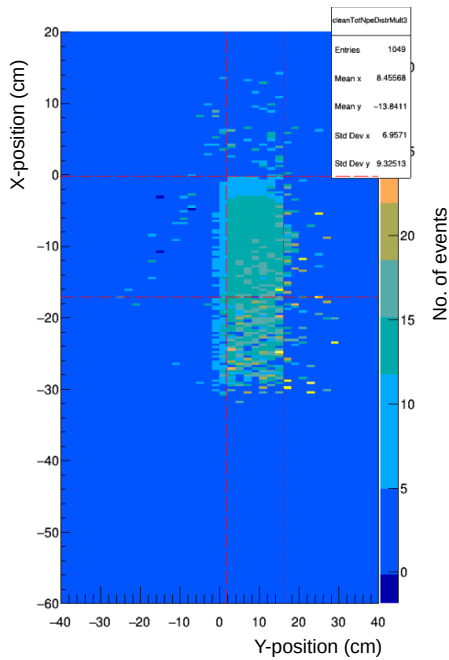
Figure 7.12: The determination of the total energy cut from the 2D histogram of total energy in calorimeter and the energy in shower.



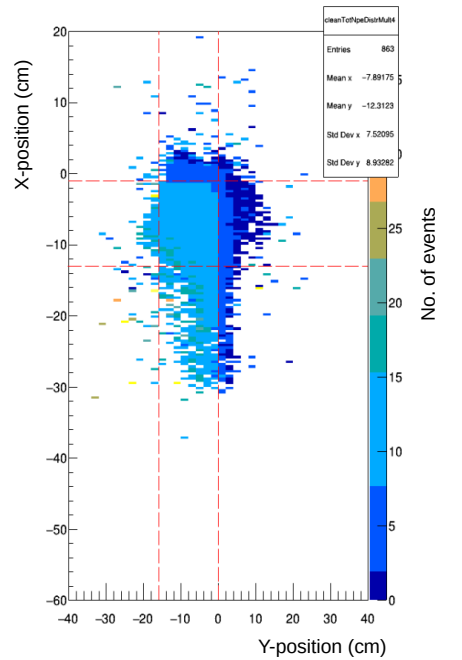
(a) PMT 1



(b) PMT 2

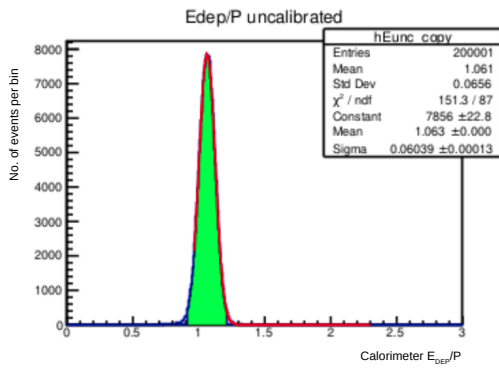


(c) PMT 3

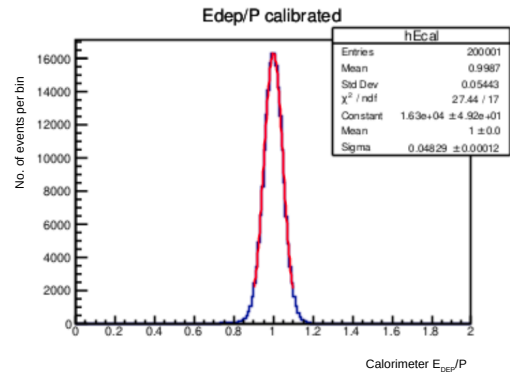


(d) PMT 4

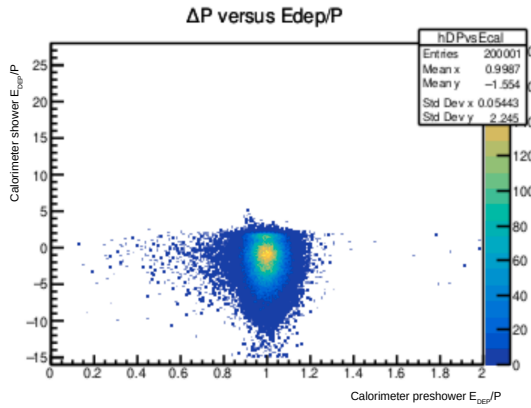
Figure 7.13: The average number of photo electron distributions in the NGCER mirror plane is shown that was used to determine the mirror plane cuts. This was calculated by dividing the PMT good pulse integral weighted events in X-Y by pure event distribution in mirror X-Y.



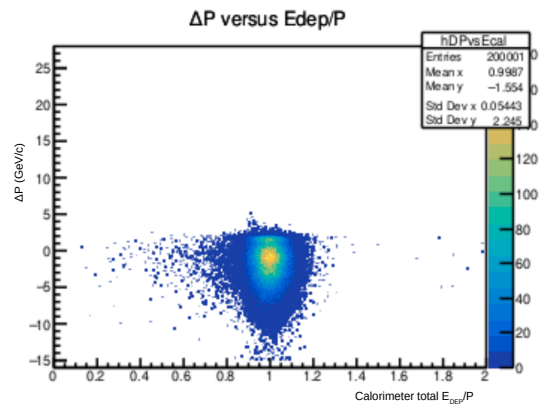
(a) E_{DEP}/P before calibration.



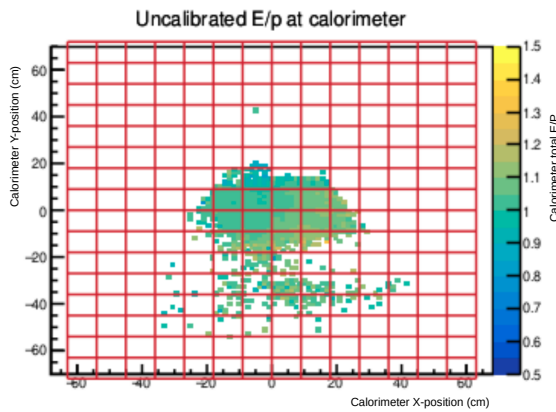
(b) E_{DEP}/P after calibration.



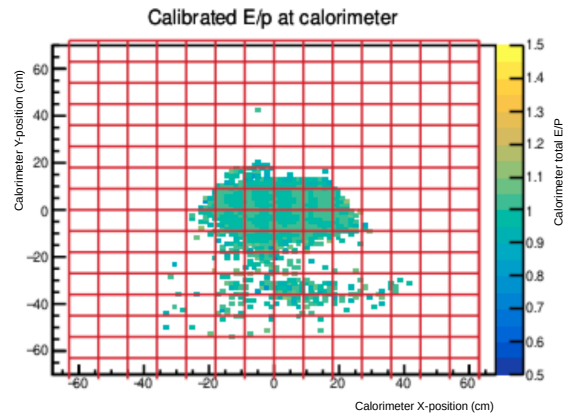
(c) Energy deposit in shower counter vs. pre-shower counter.



(d) Minimization of the deviation of ΔP .



(e) The projected E_{DEP}/P distribution over the calorimeter plane before calibration (x, y in cm).



(f) The projected E_{DEP}/P distribution over the calorimeter plane after calibration (x, y in cm).

Figure 7.14: Representative plots of SHMS calorimeter calibration. By minimizing the ΔP , the calibration constants to transform ADC pulse integral to energy deposition was determined and the calibrated E_{DEP}/P histogram was centered at 1. (Plots generated by M. Cardona.)

The Calorimeter Calibration

The particles lose their energy while traveling through the calorimeter and the particle identification was done based on that deposited energy by each particle. The calorimeter time window cuts were determined to be -100 ns to 0 ns (HMS), -30 ns to 70 ns (SHMS preshower) and, -20 ns to 80 ns (SHMS shower). Once these time windows were updated, the ADC pulse integrals from the PMTs had to be converted into energy and this is known as the calorimeter calibration. If the electrons surviving after the Cherenkov cuts hit the i^{th} calorimeter lead block and the corresponding ADC gives a signal ADC_i , then the total energy can be written as,

$$E_{DEP} \sim \sum_i c_i ADC_i \quad (7.6)$$

Where c_i is the calibration constant for i^{th} lead glass block and E_{DEP} is the total deposited energy of the electrons. The calibration constant was determined by minimizing the difference (ΔP) of the electron momentum (P) and the deposited energy E_{DEP} with the following constraint.

$$\langle P \rangle = \langle E_{DEP} \rangle \quad (7.7)$$

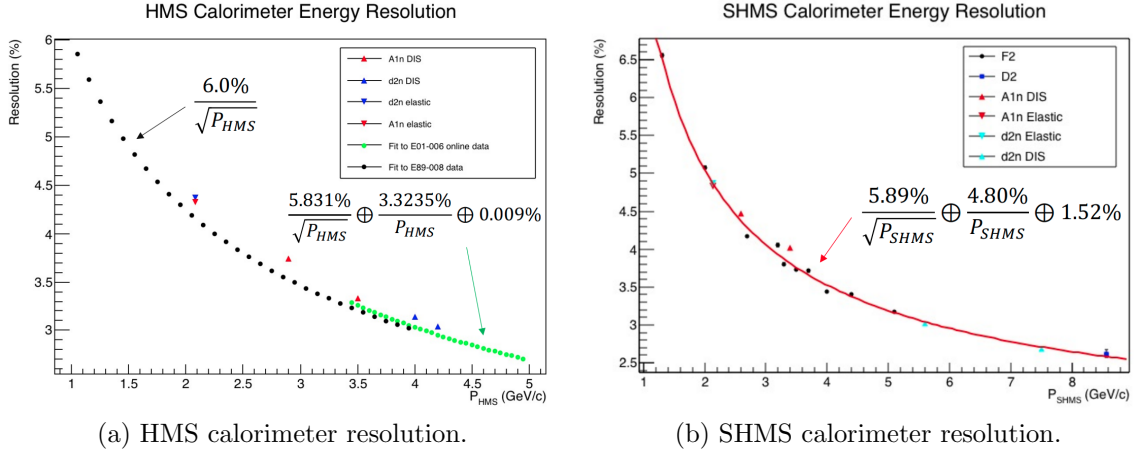


Figure 7.15: The energy dependence of the HMS and SHMS calorimeter resolution. (Plots generated by M. Cardona.)

Fig. 7.14 shows one representative calorimeter calibration plots for SHMS run 9839 (^3He elastic run, 8.5° at -2.129 GeV). The calorimeter resolutions for all the HMS and SHMS kinematic settings were calculated and the resolution for each spectrometer momentum was plotted as shown in the Fig. 7.15. The calorimeter resolution was defined by the standard deviation of the Gaussian fit to the calibrated E_{DEP}/P histogram (Fig. 7.14). To obtain the energy dependence of the resolution, the spectrometer resolution data was fitted using a function of the following form:

$$\frac{\sigma_{E'}}{E'} = \frac{A}{\sqrt{E'}} + B + \frac{C}{E'}, \quad (7.8)$$

where, A is purely stochastic term containing shower fluctuations and, photon/electron statistics in photon detector (intrinsic), B represents a combination of calibration error and, the systematics from detector non-uniformity/ leakage and, C is the electronic noise.

7.4 Particle Identification Studies

The particle identification studies were performed using the Cherenkov detector and the calorimeter as described in 4.2.3. The dominating background came from the pions in the experiment E12-06-121. The efficiency of particle identification was depicted by two variables: electron efficiency and pion rejection factor.

- **Electron efficiency:** The electron efficiency is defined as the ratio of number of electrons selected by the detector of interest (e.g. Cherenkov) to the same selected by another detector (e.g. calorimeter). This variable indicates how well the detector of interest can distinguish electrons from pions.
- **Pion rejection factor:** The pion rejection factor is defined as the ratio of number of pions selected by the detector of interest (e.g. Cherenkov) to the same selected by another detector (e.g. calorimeter). This variable indicates how well the detector of interest can reject pions over the electrons.

The electron efficiency and pion rejection studies were performed for both the Cherenkov and the calorimeter and they are described below.

7.4.1 Cherenkov efficiency and pion rejection factor:

The Cherenkov efficiency, ε_{cheren} and the Cherenkov pion rejection factor, PRF_{cheren} are defined as follows:

$$\varepsilon_{cheren} = \frac{N_{e^-}^{cherenkov}}{N_{e^-}^{calorimeter}} \quad (7.9)$$

$$PRF_{cheren} = \frac{N_{\pi}^{calorimeter}}{N_{\pi}^{cherenkov}}, \quad (7.10)$$

where, $N_{e^-}^{cherenkov}$ and $N_{\pi}^{cherenkov}$ are the electron and pion samples respectively, that passed the Cherenkov cut and $N_{e^-}^{calorimeter}$ and $N_{\pi}^{calorimeter}$ are the electron and pion samples respectively, that were selected by the calorimeter. In this case, the electron and pion samples were determined by the calorimeter and the Cherenkov was used for the PID study.

As an example, the Cherenkov PID study for HMS run 4101 (Kin-C: 20°, -4.0 GeV/c) will be described. To select the electron and pion samples, the calorimeter preshower, shower and total energy distribution were plotted (Fig. 7.16) and the calorimeter cuts were determined to distinguish between electron and pions.

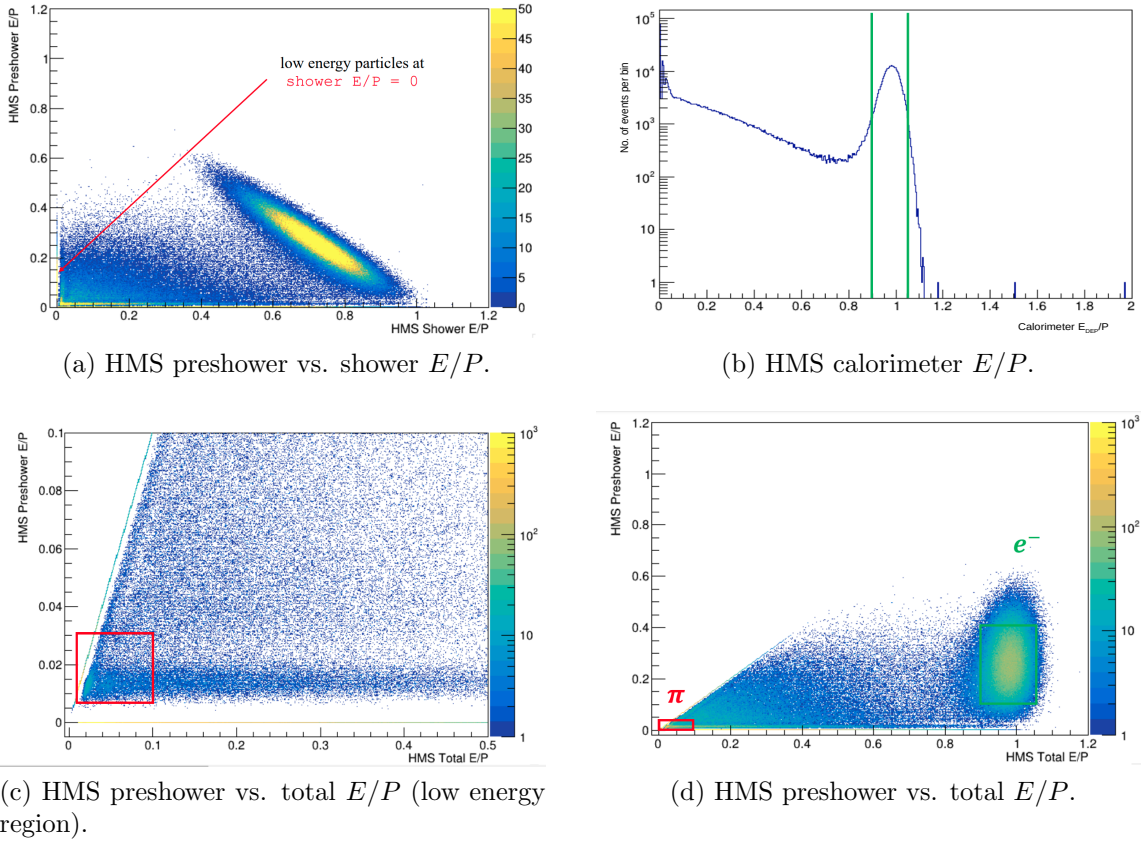


Figure 7.16: The calorimeter cuts to separate electron and pion samples in HMS run 4101 (20° , -4.0 GeV/c). The nominal acceptance cuts used: $-8 < H.gtr.dp < 8$ (momentum acceptance), $abs(H.gtr.th) < 0.1$ (out-of-plane angle), $abs(H.gtr.ph) < 0.06$ (in-plane angle) and, $abs(H.react.z) < 22$ (target z cut). (Plots generated by M. Cardona.)

From the above Fig. 7.16 the calorimeter sample cuts were determined as the following.

- **Electron sample:** $0.90 < \text{Total } E/P < 1.05$, $0.10 < \text{Preshower } E/P < 0.40$
- **Pion sample:** $0.01 < \text{Total } E/P < 0.1$, $0.005 < \text{Preshower } E/P < 0.03$

In the next step, these calorimeter cuts were used to look at the Cherenkov npe (number of photoelectrons) distribution as shown in Fig. 7.17. For different npe cuts the number of electrons and pions that passed those cuts were determined and the $\varepsilon_{\text{cheren}}$ and PRF_{cheren} were calculated using Eq. 7.9 and Eq. 7.10. The optimal npe cut (H.cer.npeSum=1) was determined from the plot shown in Fig. 7.18 where the $\varepsilon_{\text{cheren}}$ and PRF_{cheren} were $98.85 \pm 0.02\%$ and $36.27 \pm 1.20\%$, respectively.

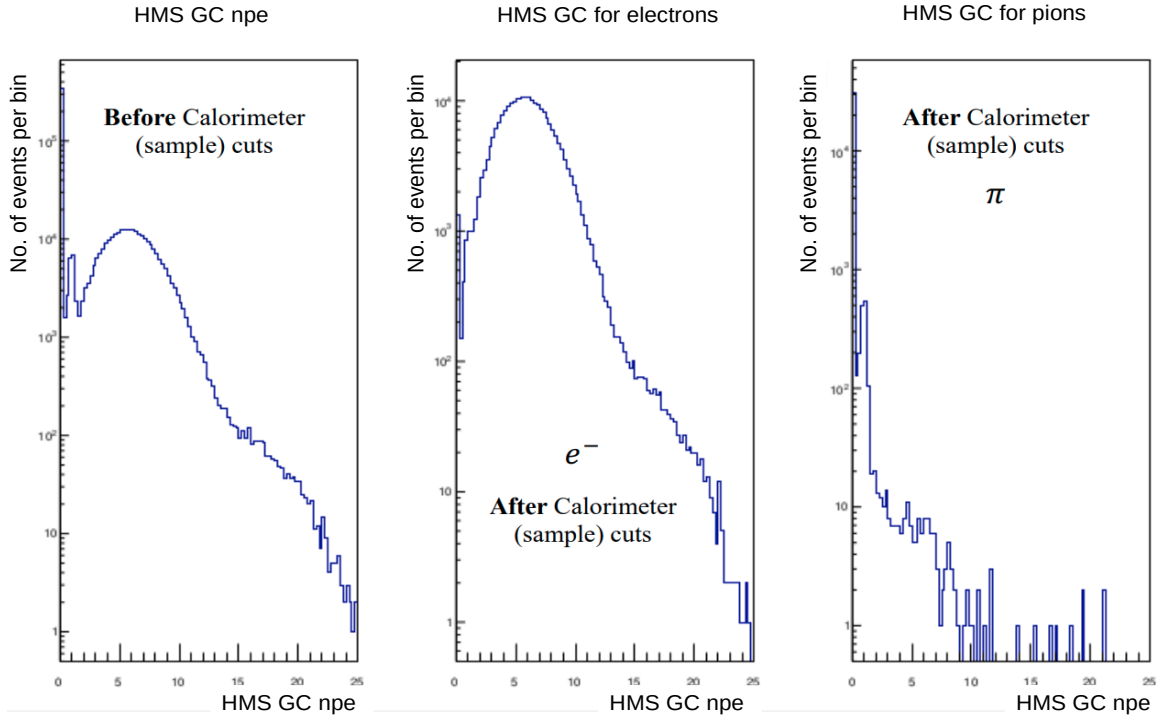


Figure 7.17: The Cherenkov npe distribution of electrons and pions for HMS run 4101 (20° , -4.0 GeV/c). The nominal acceptance cuts used: $-8 < H.gtr.dp < 8$ (momentum acceptance), $abs(H.gtr.th) < 0.1$ (out-of-plane angle), $abs(H.gtr.ph) < 0.06$ (in-plane angle) and, $abs(H.react.z) < 22$ (target z cut). (Plots generated by M. Cardona.)

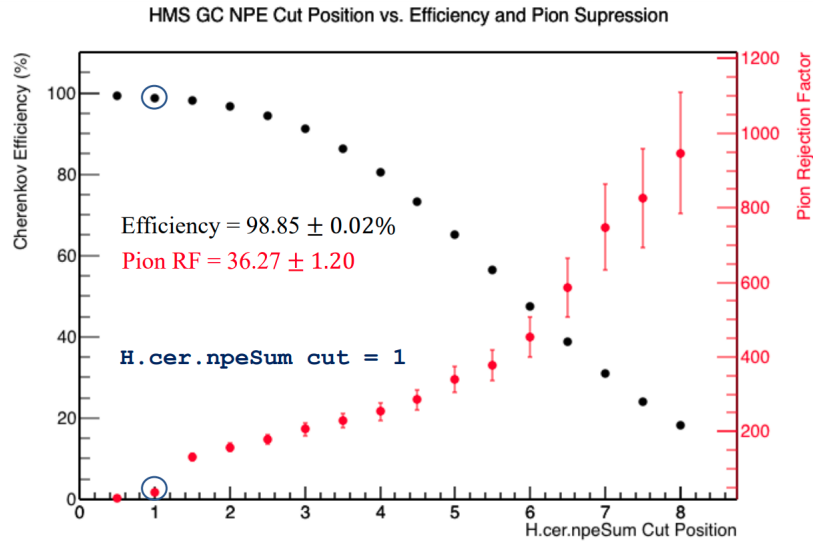


Figure 7.18: Determining npe cut position for optimal ε_{cheren} and PRF_{cheren} . (Plot generated by M. Cardona.)

7.4.2 Calorimeter efficiency and pion rejection factor:

The calorimeter efficiency, ε_{cal} and, the pion rejection factor, PRF_{cal} are defined as follows:

$$\varepsilon_{cal} = \frac{N_{e^-}^{\prime calorimeter}}{N_{e^-}^{\prime cherenkov}} \quad (7.11)$$

$$PRF_{cal} = \frac{N_{\pi}^{\prime cherenkov}}{N_{\pi}^{\prime calorimeter}}, \quad (7.12)$$

where, $N_{e^-}^{\prime calorimeter}$ and $N_{\pi}^{\prime calorimeter}$ are the electron and pion samples respectively that passed the calorimeter shower and preshower cuts and $N_{e^-}^{\prime cherenkov}$ and $N_{\pi}^{\prime cherenkov}$ are the electron and pion sample respectively that were selected by the Cherenkov. In this case, the electron and pion samples were determined by the Cherenkov and the calorimeter was used for the PID study.

As an example, the calorimeter PID study for SHMS run 11445 (Kin-Z: 18° , -5.6 GeV/c) will be described. In the first step, the npe distribution was plotted (Fig. 7.19) and the npe cuts were used to determine the electron and pion samples as follows.

- **Electron sample:** npeSum > 11
- **Pion sample:** npeSum < 0.1

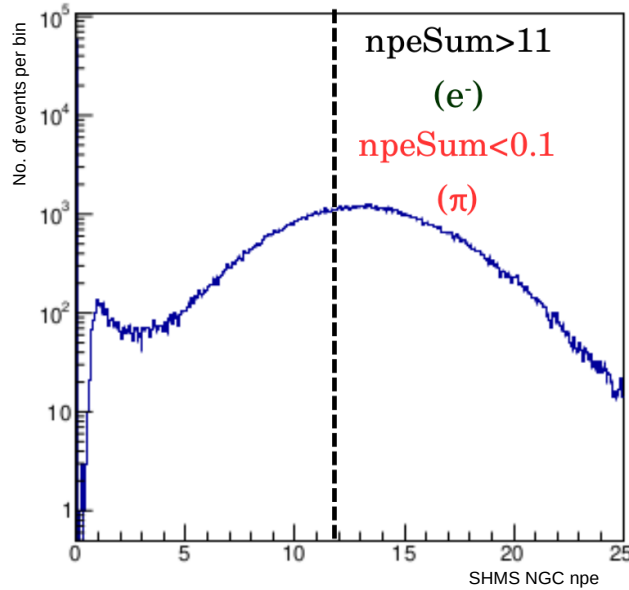


Figure 7.19: Determining npe cut position to distinguish between electron and pion sample for SHMS run 11445 (Kin-Z: 18° , -5.6 GeV/c). (Plot generated by M. Cardona)

In the next step, the calorimeter energy distribution was plotted (Fig. 7.20) for electrons and pions with the determined npe cuts. In the electron sample, the low energy

electrons survived the Cherenkov cut but did not make the total calorimeter cut (they were completely absorbed in the pre shower). To ensure the counting of only good electrons, a shower energy cut was used: shower $E/P > 0$. In this step, the number of electrons and pions that passed the total energy cut (total $E/P > 0.8$) were calculated and the calorimeter efficiency was determined for different shower E/P cuts. As shown in Fig. 7.21, the calorimeter efficiency and pion rejection factor were found to be $99.74 \pm 0.01\%$ and $35.10 \pm 0.85\%$, respectively, for shower $E/P > 0$ cut.

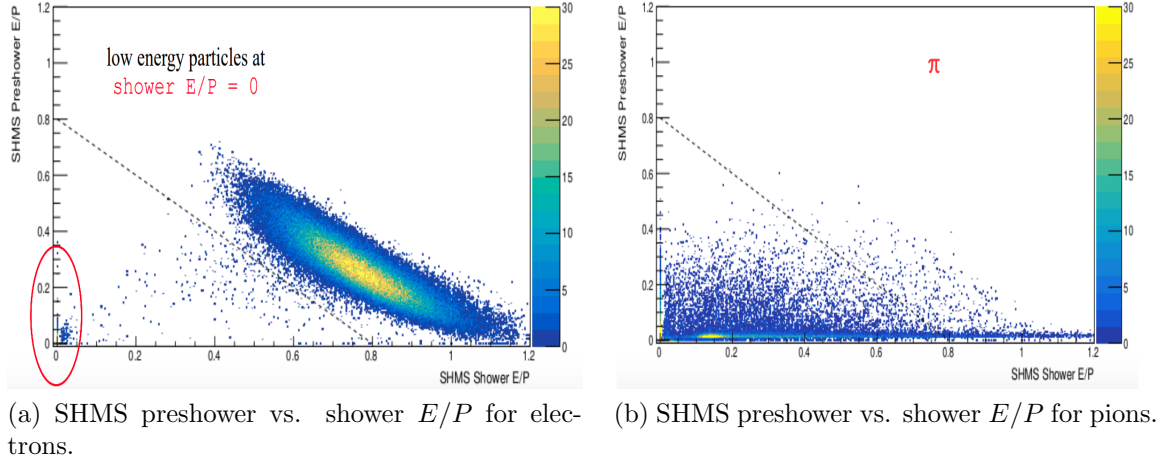


Figure 7.20: The calorimeter energy distribution of electrons and pions for SHMS run 11445 (Kin-Z: 18° , -5.6 GeV/c). The nominal acceptance cuts used: $-10 < H.gtr.dp < 22$ (momentum acceptance), $abs(H.gtr.th) < 0.05$ (out-of-plane angle), $abs(H.gtr.ph) < 0.07$ (in-plane angle) and, $abs(H.react.z) < 22$ (target z cut). (Plot generated by M. Cardona.)

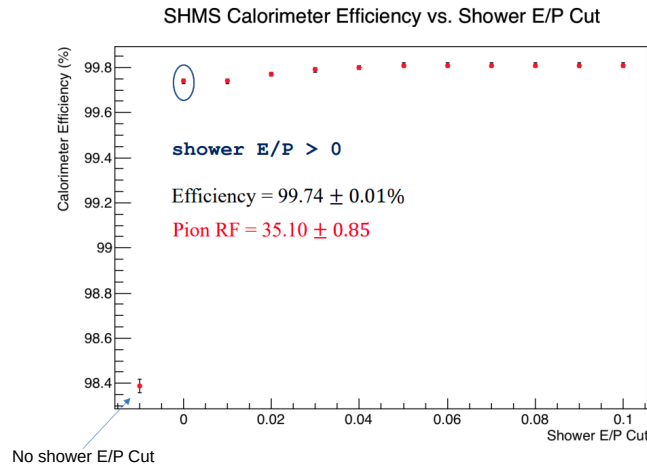


Figure 7.21: SHMS calorimeter efficiency plot with different calorimeter shower energy cuts. A shower energy cut > 0 was applied to ensure selection of good electrons (Plot generated by M. Cardona.)

The study of ε_{cal} and PRF_{cal} with different preshower cut positions was performed as shown in Fig. 7.22. It was noticed that, adding a preshower cut (Preshower $E/P > 0.05$) resulted in a PRF_{cal} boost. The final results were: $\varepsilon_{cal} = 99.33 \pm 0.02\%$ and, $PRF_{cal} = 146.39 \pm 7.36\%$.

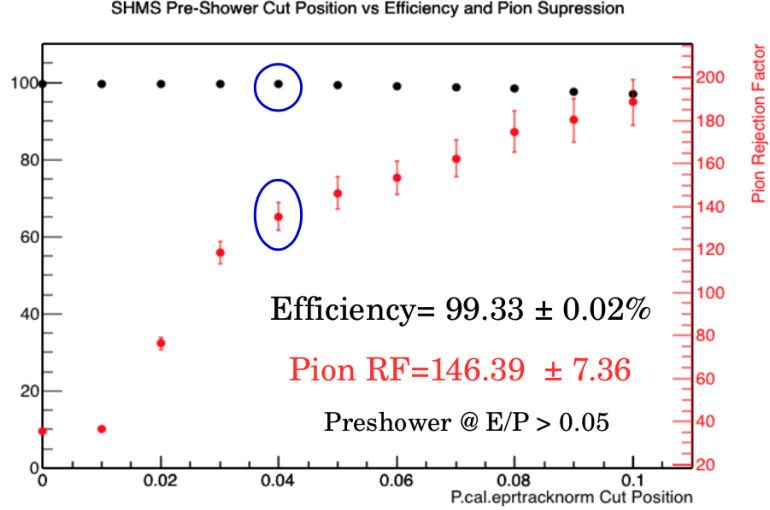


Figure 7.22: Determining calorimeter preshower energy cut for optimum efficiency and pion rejection factor for SHMS run 11445 (Kin-Z: 18° , -5.6 GeV/c). (Plot generated by M. Cardona.)

Pion contamination:

Although the good electrons were selected using the PID cuts described before, some pion background might not get completely removed from the electron sample. Even if those pions did not produce any Cherenkov light themselves, they might have generated some knock-on high energy electrons that resulted in Cherenkov radiation and passing the Cherenkov cut. So, the percentage pions present in the electron sample after applying all the PID cuts had to be determined to correct for the pion background for all momentum settings of the spectrometers. This is known as pion contamination and is defined as the following.

$$PC = \frac{N_\pi}{N_{e^-}} \quad (7.13)$$

As shown in Fig. 7.23 the calorimeter total energy distribution for electrons and pions were integrated over the E/P range $[0.8, 1.5]$ and the calorimeter pion contamination (PC_{cal}) was determined using Eq. 7.13. Then the Cherenkov pion rejection factor (PRF_{cheren}) was used as a normalization factor for the pion sample in Fig. 7.23 and the combined pion contamination (PC_{comb}) after the normalization was given by,

$$PC_{comb} = \frac{PC_{cal}}{PRF_{cheren}}.$$

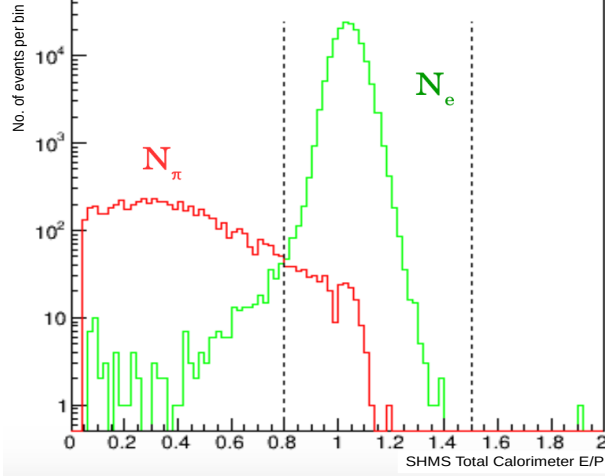


Figure 7.23: Pion contamination in good electron sample for SHMS run 11445 (Kin-Z: 18° , -5.6 GeV/c). The nominal acceptance cuts used: $-10 < H.gtr.dp < 22$, $abs(H.gtr.th) < 0.05$, $abs(H.gtr.ph) < 0.07$ and, $abs(H.react.z) < 22$, the PID cut used: preshower $E/P > 0.05$, preshower $E/P > 0$, $npeSum > 11$ for electrons and preshower $E/P > 0.05$, $npeSum < 0.1$ for pions.(Plot generated by M. Cardona.)

The list of electron efficiency, pion rejection factor and pion contamination for all momentum settings of the HMS and SHMS are listed in Table. 7.5.

Table 7.5: The list of Cherenkov and calorimeter particle identification results.

(a) The Cherenkov and calorimeter PID cuts

Spec, P_0 (GeV/c)	Cherenkov cut	Calorimeter cut
SHMS, 5.6	$npe > 2$	Total $E/P > 0.8$, Preshower $E/P > 0.05$
SHMS, 6.4	$npe > 2$	Total $E/P > 0.8$, Preshower $E/P > 0.05$
SHMS, 7.5	$npe > 2$	Total $E/P > 0.8$
HMS, 4.0	$npe > 1$	Total $E/P > 0.8$

(b) The Cherenkov and calorimeter efficiency and pion contamination

Spec, P_0 (GeV/c)	ϵ_{cheren}	PRF_{cheren}	ϵ_{cal}	PRF_{cal}	PC_{comb}
SHMS, 5.6	99.82 $\pm 0.01\%$	21.00 $\pm 0.55\%$	99.33 $\pm 0.03\%$	146.36 $\pm 7.36\%$	0.012%
SHMS, 6.4	99.80 $\pm 0.01\%$	N/A	99.33 $\pm 0.02\%$	103.24 $\pm 4.51\%$	0.102%
SHMS, 7.5	99.73 $\pm 0.01\%$	N/A	99.29 $\pm 0.01\%$	28.11 $\pm 1.13\%$	0.101%
HMS, 4.0	99.85 $\pm 0.02\%$	36.27 $\pm 0.20\%$	99.11 $\pm 0.02\%$	82.88 $\pm 1.27\%$	0.063%

7.4.3 Background Estimation

There are three main sources of backgrounds in the experiment.

- **Charge Symmetric Background:** The neutral pions are produced during the electron scattering and each pion decays into two photons and the photons then decay into electron-positron pairs.

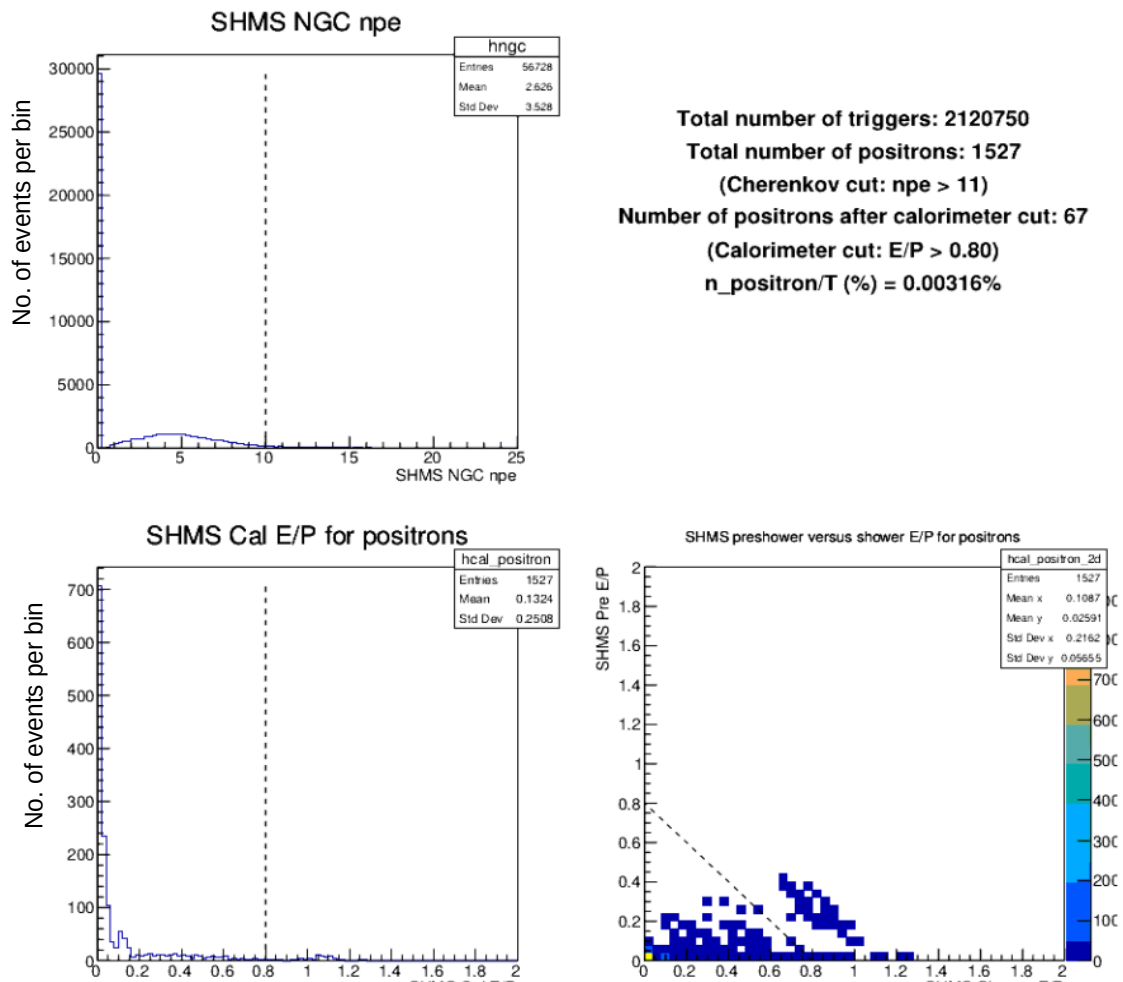
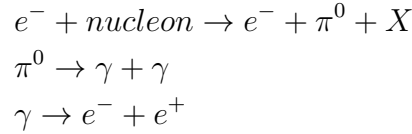


Figure 7.24: The ratio of positrons to the total number of triggers for SHMS positive polarity run 11090. The top left plot shows where the SHMS NGCER very restrictive PID cut ($npe > 11$) was applied, the bottom left and right plots show the calorimeter PID cut ($E/P > 0.8$) position. The number of positrons that passed the PID cuts was calculated.

These processes result in secondary electrons which are detected with the primary scattered electrons. The production of electrons and positrons in pairs is known as the charge symmetric background and must be subtracted from the inclusive DIS cross-section. However, this background becomes important only for smaller momentum and larger scattering angles.

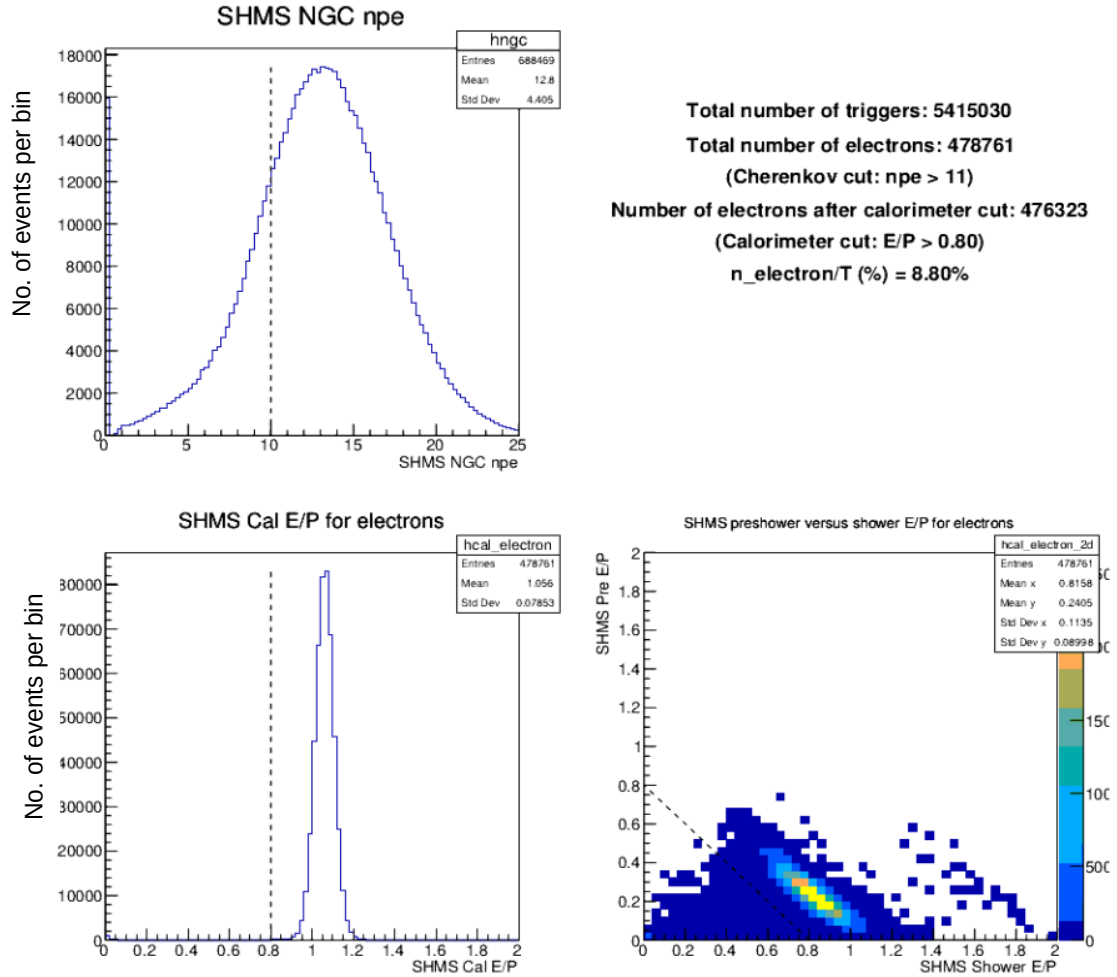


Figure 7.25: The ratio of positrons to the total number of triggers for SHMS negative polarity run 11085. The top left plot shows where the SHMS NGCER very restrictive PID cut ($npe > 11$) was applied, the bottom left and right plots show the calorimeter PID cut ($E/P > 0.8$) position. The number of electrons that passed the PID cuts was calculated.

A few positive polarity runs were taken during the experiment for SHMS Kin-X. Fig. 7.24 shows that the $e^+/T = 0.00316\%$ and Fig. 7.25 shows that the $e^-/T = 8.80\%$ for SHMS at 11° and -7.5 GeV/c where T represents the total number of triggers. The positron to electron (e^+/e^-) ratio in that kinematic setting was found to be 0.036% . Also, the e^+/e^- analysis from the experiment E12-10-002 (“Precision measurements of the F_2 structure function at large x ”

in the resonance region and beyond”) shows that the ratio gets significantly smaller with higher momentum and smaller angle as shown in Fig. 7.26[87]. In our experiment, the largest spectrometer angle was 20° and the smallest momentum was -4.0 GeV/c. So, it was concluded that the charge symmetric background in our experiment was insignificant and can be neglected.

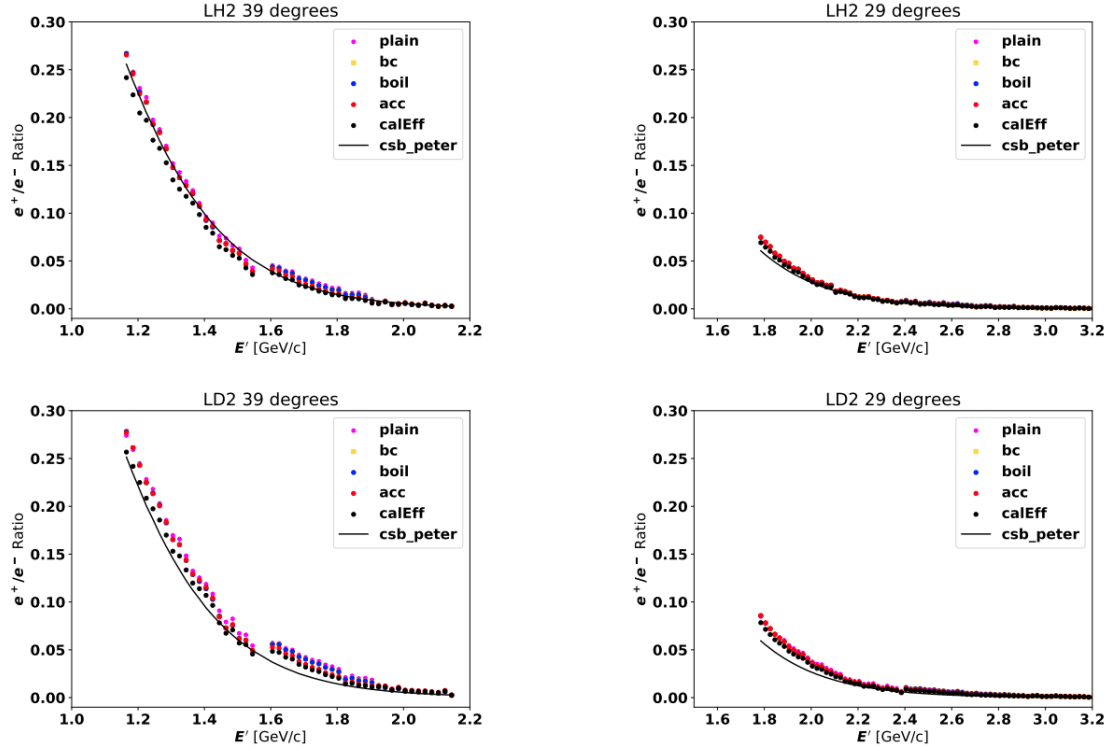


Figure 7.26: The ratio of positrons to electrons from E12-10-002 experimental data analysis. This data was also compared with the P. Bosted model that shows that the e^+/e^- ratio decreases with higher momentum and smaller spectrometer angle [87].

- **Pion Background:** The pion background for the experiment E12-06-121 was estimated as described in Section. 7.4.2. The pion contamination value ranged between 0.012% to 0.102% for all the kinematic settings which was insignificant w.r.t. other systematics of the experiment.
- **Nitrogen Scattering Contribution:** To estimate the nitrogen scattering contribution from the nitrogen present in the target cell, a reference cell was used which had the same geometry as the target chamber. The reference cell was filled with nitrogen gas to measure the electron scattering from it and the cross section was scaled down to the fraction of nitrogen present in the target chamber of the production cell. This dilution cross-section was later subtracted from the measured ^3He raw cross-section.

7.4.4 Live time

In case of high trigger rate, few events could not be recorded as opposed to the ideal case where each event generating a trigger would be recorded. The time during which the events were not recorded is known as dead time and the time during which the events were recorded is known as the live time of a detector. The live time was calculated for each run by counting the number of good triggers and the total number of triggers generated in that run. The computer live time was calculated using the following formula.

$$livetime = \frac{T * ps}{S}, \quad (7.14)$$

where T is the total number of recorded triggers, ps is the prescale factor for the run and S is the number of triggers from the scaler. The error was calculated as,

$$\frac{\delta livetime}{livetime} = ps * \frac{\sqrt{T * (1 - T/S)}}{S} \quad (7.15)$$

The average live times for the good SHMS and HMS runs are shown in Fig. 7.27. The runs that had live time $> 85\%$ were considered as good. The average live times and the statistical errors associated with the live time were $\sim 99.9\%$ and $\sim 0.07\%$ absolute, respectively, for the runs used in the cross-section analysis in this dissertation.

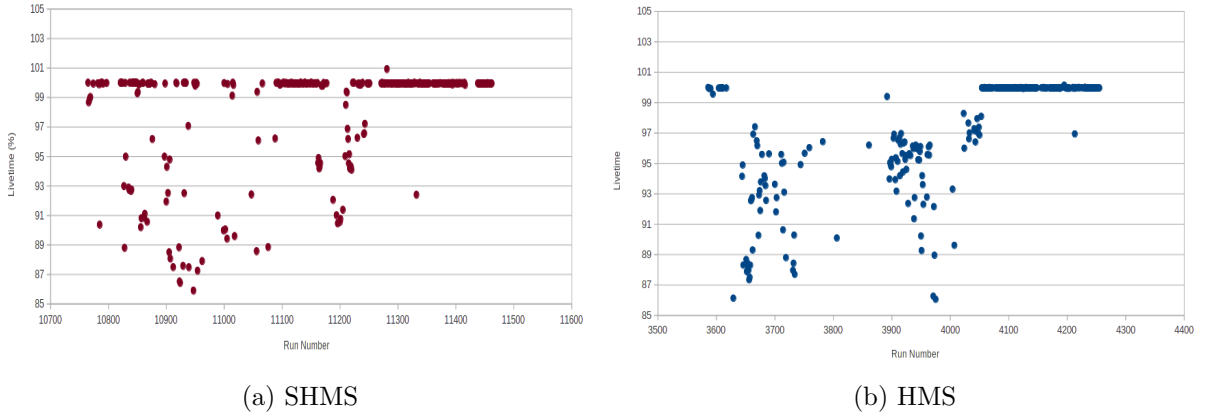


Figure 7.27: The computer live times for good SHMS and HMS runs.

7.4.5 Trigger Efficiencies

During data collection the trigger might not be generated for some time that can result in event loss. This is known as trigger inefficiency and the data yield should be corrected for that. In our experiment mostly T1 (3/4) and sometimes T3 (EL-CLEAN) triggers were used for both the HMS and SHMS. The trigger efficiency was determined by the following equations.

$$\epsilon_{T1} = \frac{N_{T1}}{N_{T1} + N_{T3}}, \quad (7.16)$$

$$\epsilon_{T3} = \frac{N_{T3}}{N_{T1} + N_{T3}}, \quad (7.17)$$

where N_{T_i} is the number of events from trigger T_i after prescale correction. These efficiencies were $>99.9\%$ and they were calculated with a relative uncertainty of 0.03% . The yield was corrected on a run-by-run basis with the trigger efficiency.

7.4.6 Tracking Efficiency

During data collection sometimes the track reconstruction algorithm might not be able to reconstruct a track even if the trigger occurs. In case of very few hits in the drift chamber, only a few wires will generate a signal which might not be sufficient for track reconstruction. On the other hand, if the drift chamber has too many hits, it might introduce a noise preventing the track reconstruction algorithm from working. If N_{found} is the number of events for which the track was found and $N_{expected}$ is the number of events for which track reconstruction is expected (events that passed the calorimeter total energy cut and the Cherenkov PID cut), then the tracking efficiency is defined as,

$$\epsilon_{tr} = \frac{N_{found}}{N_{expected}}. \quad (7.18)$$

The average tracking efficiency was 99.6% and the relative error was 0.2% . The yield was corrected on a run-by-run basis with the tracking efficiency.

7.4.7 Spectrometer Acceptance

The acceptance of a spectrometer is defined as the probability that a scattered electron will reach the detector after passing through the spectrometer magnets and other components. The acceptances of the spectrometers were determined to correct for the fact that they had finite angle and momentum acceptance for a fixed central angle and momentum. The scattering happened over a 40-cm long ^3He target resulting in different acceptances for the scattered electrons from the upstream and the downstream of the target center. Moreover, scattered particles with momentum and scattering angle away from the central spectrometer values might be lost if they hit the edges of the apertures and collimators. To account for these effects, the HMS and SHMS acceptances were studied. The acceptance (A) depends on the full target coordinates (x, y, z) and also the spectrometer coordinates (δ, xp, yp) where δ represents the momentum acceptance and xp, yp represent the out-of-plane and in-plane angles, respectively.

$$A = A(x, y, z, \delta, xp, yp). \quad (7.19)$$

If the fraction of particles at each vertex is known, the acceptance can be averaged over the target coordinates (x, y, z) and, it can be written as,

$$A = A(\delta, xp, yp). \quad (7.20)$$

The scattering angle θ is a combination of the angles xp and yp and it is determined by the following equation.

$$\theta = \text{acos}(\cos(\theta_0 - yp) * \cos(xp)) \quad (7.21)$$

where, θ_0 is the spectrometer central angle. As the physics only depends on the momentum ($E' = p_0 (1 + \frac{\delta}{100})$) and the scattering angle, θ , the acceptance function is conveniently expressed as,

$$A = A(E', \theta). \quad (7.22)$$

The acceptance function was generated using a Monte Carlo simulation written to simulate the Hall C spectrometers. The simulation program, mc-single-arm had the three following components.

- **Event generator:** Each scattered electron is called an event and the events were generated with random flat distribution in z , δ , xp and yp with reasonable bounds in each variable as shown below.
 1. $-20 < z < 20$ (HMS, SHMS) in cm
 2. $-12 < \delta < 12$ (HMS), $-15 < \delta < 25$ (SHMS) in %
 3. $-100 < xp < 100$ (HMS, SHMS) in mrad
 4. $-100 < yp < 100$ (HMS, SHMS) in mrad
- **Transport matrices:** The generated events were passed through the magnets to hit the detectors which is known as forward transportation of the particles. This was handled by a magneto-optics simulation package known as COSY that generates a series of matrices to simulate the particle transportation through the collimators, vacuum pipes and magnet apertures. The particle tracks were fitted in the focal plane from the drift chamber hits and the target quantities were reconstructed from the focal plane tracks. If the particles passed through all the mentioned components and hit all the detectors in the stack, it was considered as “success” and if the particles did not hit every detector, it was considered as “failure”.
- **Spectrometer geometry:** The spectrometer geometry part had the thickness and size of different materials and apertures listed for HMS and SHMS.

The first step was to compare the Monte Carlo simulation results with the data. In order to do that the charge normalized yield from the simulation was calculated using the following formula.

$$\text{yield} = \frac{N}{Q_{tot}}, \quad (7.23)$$

where N was the number of events generating a total charge of Q_{tot} over a time period, t . The total number of events, N is written in terms of the differential cross-section ($\frac{d^2\sigma}{dE'd\Omega}$) and the integrated luminosity (L) as follows.

$$N = \frac{d^2\sigma}{dE'd\Omega} * \Delta E' * \Delta \Omega * L. \quad (7.24)$$

The integrated luminosity is expressed as,

$$L = \frac{\eta_{tar} * l_{tar} * Q_{tot}}{|e|}, \quad (7.25)$$

where, η_{tar} is the number density of the target, l_{tar} is the length of the target and $|e|$ is electronic charge. Substituting Eq. 7.24 and Eq. 7.25 in Eq. 7.23, the charge normalized yield can be written as,

$$yield = \frac{d^2\sigma}{dE'd\Omega} * \Delta E' * \Delta\Omega * \frac{\eta_{tar} * l_{tar}}{|e|}. \quad (7.26)$$

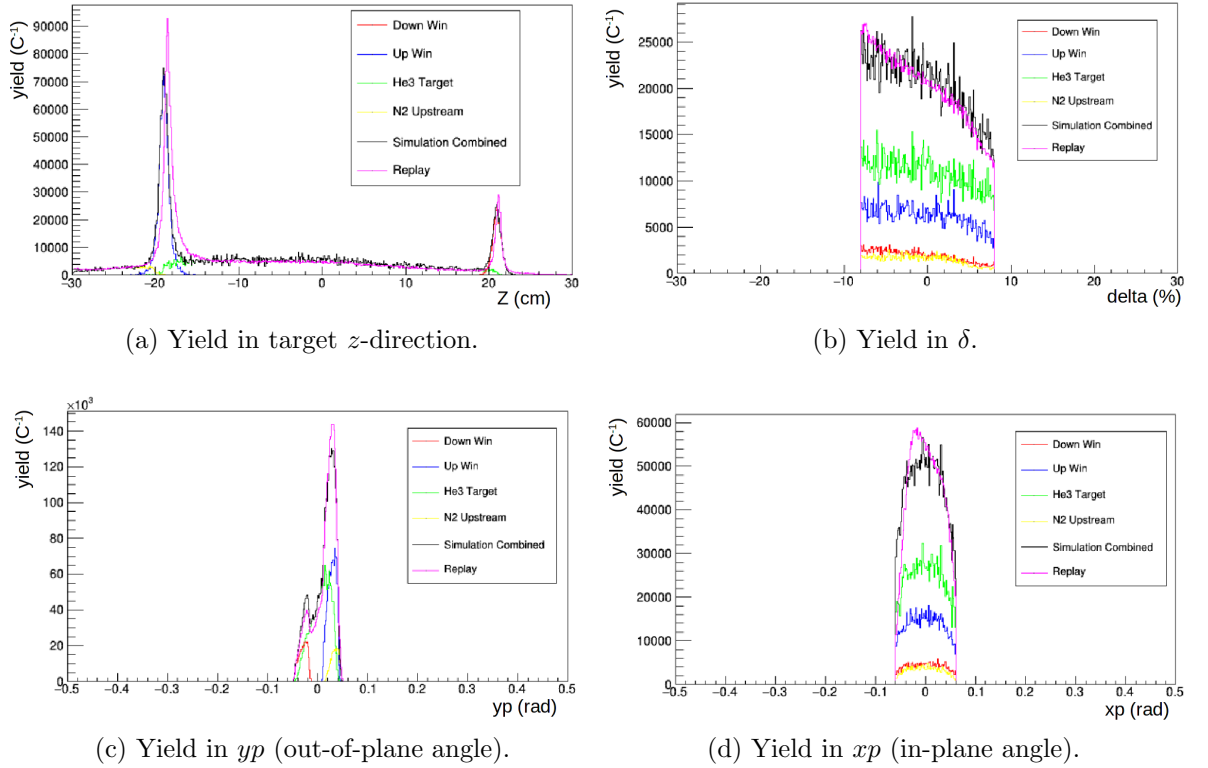
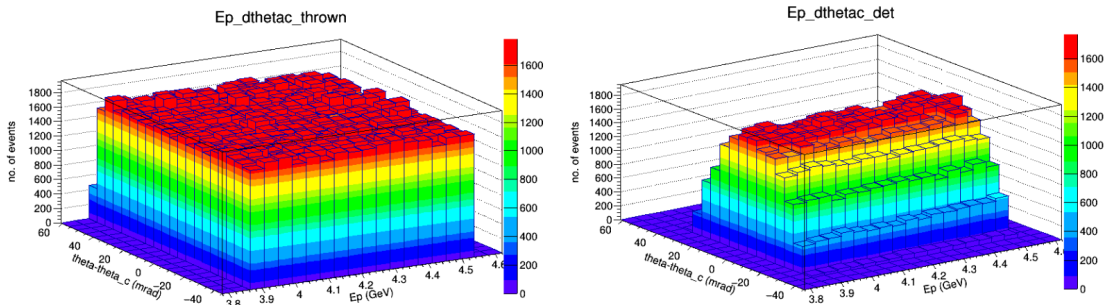


Figure 7.28: Comparison of data (magenta) and simulated yield (black) in z , δ , yp and xp for HMS run 4233 (Kin-C: 20° , -4.0 GeV/c). The upstream window (blue), downstream window (red), ^3He target (green) and the nitrogen gas (yellow) between the beam window and cell upstream window were simulated separately and everything was combined to get the combined simulated yield histogram (black).

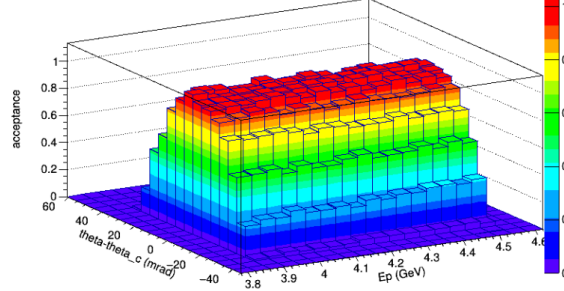
The yield histograms were generated for the GE-180 target cell upstream and downstream windows and the ^3He target region using the cross-section model F1F2IN09 and an example comparison with data for HMS Kin-C is shown in Fig. 7.28. The simulation shown in these histograms did not have radiative correction applied. The spectrometer optics was only well understood for $-8 < \delta < 8$ (%) for HMS and

$-10 < \delta < 22$ (%) for SHMS, hence the delta cut was always applied in the analysis. As the central ${}^3\text{He}$ simulation (z-yield) agreed with the data very well, we decided to use a tight z-cut to completely eliminate the window contributions in the next part of the analysis (cross-section extraction). The spectrometer acceptance is cross-section model independent. If N_{thrown} number of particles were generated or, thrown initially in the volume described by the event generator limits mentioned above and, $N_{detected}$ number of particles were detected with “success” flag in the spectrometer, then the two dimensional acceptance function calculated for each E' and θ bin can be expressed as,

$$A(E', \theta) = \frac{N_{detected}(E', \theta)}{N_{thrown}(E', \theta)}. \quad (7.27)$$



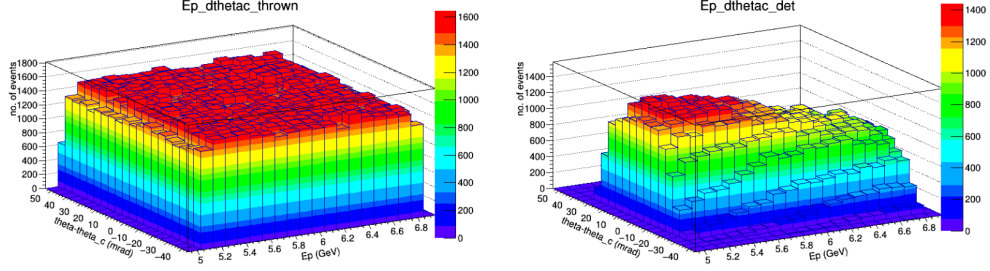
(a) Number of thrown and detected events in $E' - \theta$ space.



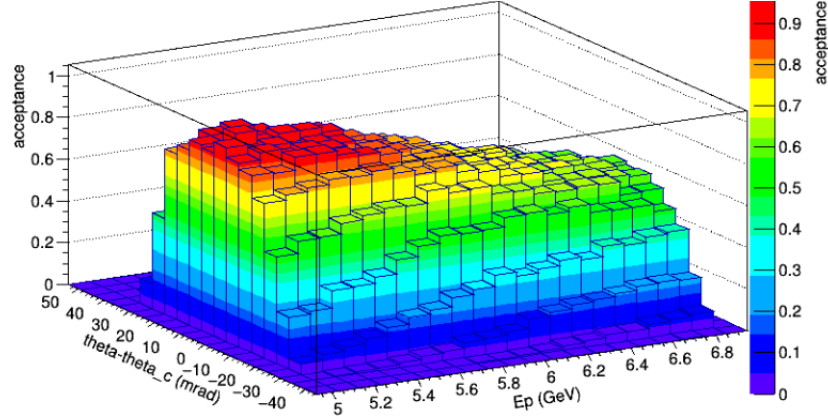
(b) Two dimensional acceptance function.

Figure 7.29: The acceptance function is generated in $E' - \theta$ space for HMS Kin-A. The x-axis is the energy of the scattered electron (E') and the y axis is the deviation of scattering angle from the spectrometer’s central momentum ($\theta - \theta_0$).

The events in the Monte Carlo simulation were generated for different HMS and SHMS kinematic settings of the experiment. During the acceptance analysis, the simulated events were binned in 20 bins in E' (range of $\pm 10\%$ about the central spectrometer momentum) and 20 bins in θ (range of ± 100 mrad) that covered the whole spectrometer acceptance. The generated two dimensional $A(E', \theta)$ for HMS Kin-A (13.5° , -4.2 GeV/c) is shown in Fig. 7.29 with $-10 < z < 10$ (cm) and, $-8 < \delta < 8$ (%) cuts and the same for SHMS Kin-Z (18° , -5.6 GeV/c) is shown in Fig. 7.30 with $-10 < z < 10$ (cm) and, $-10 < \delta < 22$ (%) cuts. An acceptance study was performed to determine proper xp and yp cuts that generate uniform,



(a) Number of thrown and detected events in $E' - \theta$ space



(b) Two dimensional acceptance function

Figure 7.30: The acceptance function is generated in $E' - \theta$ space for SHMS Kin-Z. The x axis is the energy of the scattered electron (E') and the y axis is the deviation of scattering angle from the spectrometer central momentum ($\theta - \theta_0$).

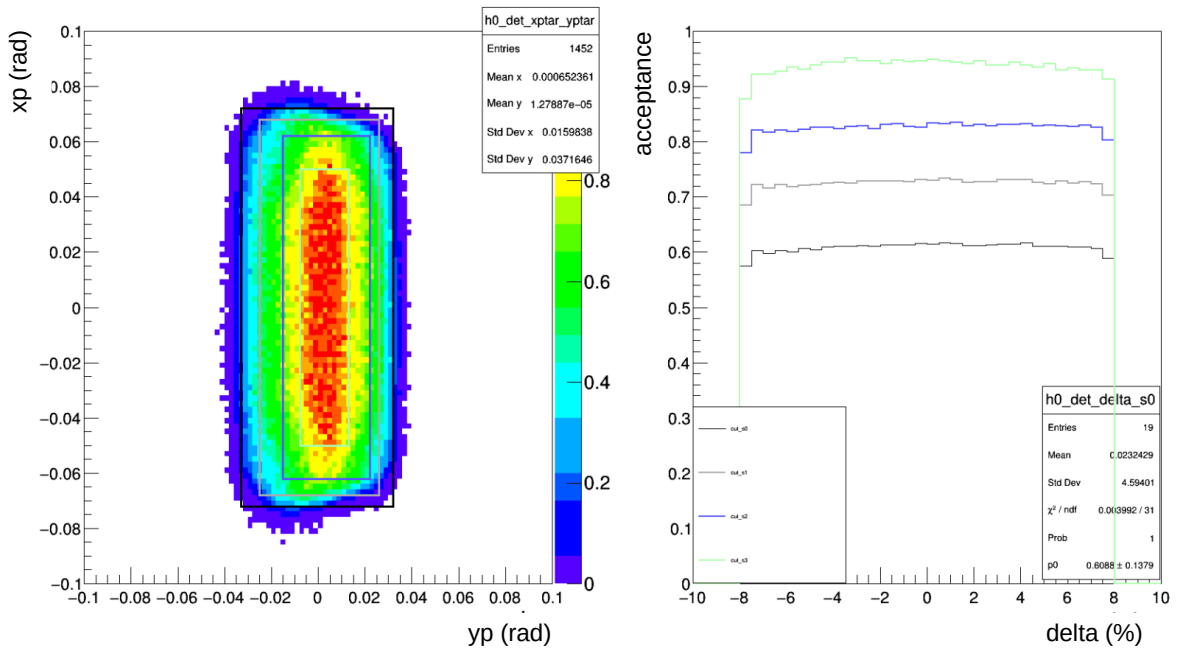
one dimensional δ acceptance (single θ bin). The Fig. 7.31 demonstrates how the one dimensional δ acceptance changes with different sets of rectangular xp and yp cuts. The HMS δ acceptance was very uniform with all the xp , yp cuts. The SHMS δ acceptance became uniform only with tighter xp , yp cuts and the acceptance dropped significantly over the δ for loose xp , yp cuts.

In the Fig. 7.31(a) the following sets of xp , yp acceptance cuts were used.

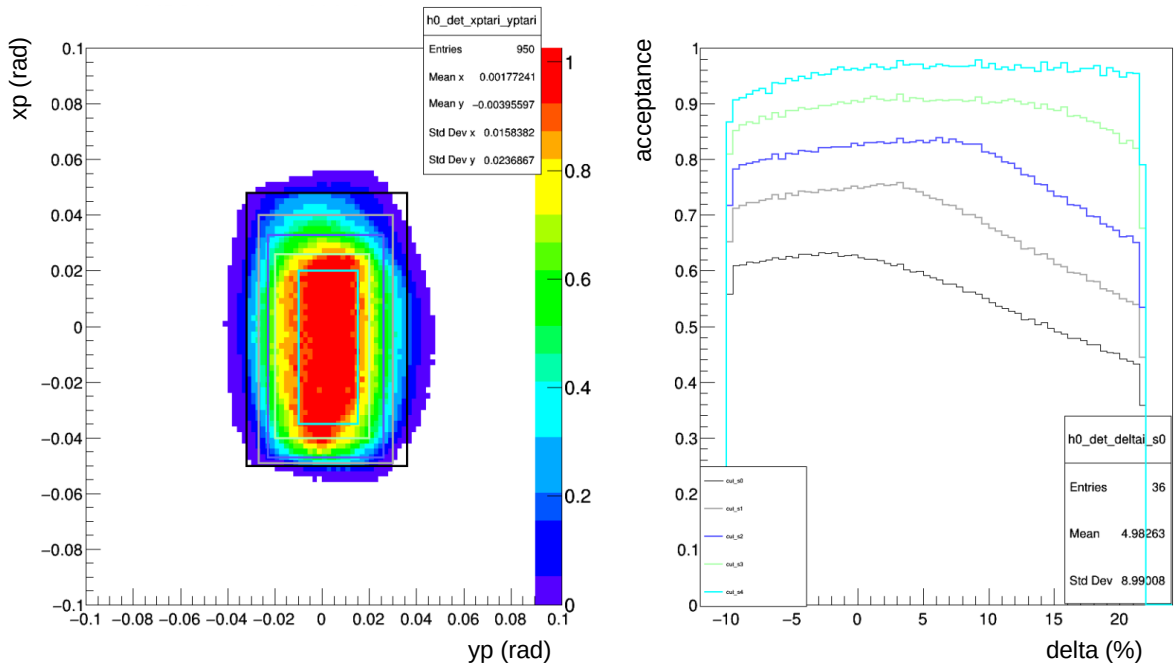
1. $xp < 0.072$, $xp > -0.072$, $yp < 0.032$, $yp < -0.033$
2. $xp < 0.068$, $xp > -0.068$, $yp < 0.026$, $yp < -0.025$
3. $xp < 0.062$, $xp > -0.062$, $yp < 0.022$, $yp < -0.015$
4. $xp < 0.050$, $xp > -0.050$, $yp < 0.013$, $yp < -0.008$

In the Fig. 7.31(b) the following sets of xp , yp acceptance cuts were used.

1. $xp < 0.048$, $xp > -0.050$, $yp < 0.036$, $yp < -0.032$
2. $xp < 0.040$, $xp > -0.049$, $yp < 0.049$, $yp < -0.027$
3. $xp < 0.033$, $xp > -0.047$, $yp < 0.026$, $yp < -0.023$
4. $xp < 0.026$, $xp > -0.040$, $yp < 0.020$, $yp < -0.020$
5. $xp < 0.020$, $xp > -0.035$, $yp < 0.015$, $yp < -0.010$



(a) HMS Kin-A



(b) SHMS Kin-Z

Figure 7.31: The one dimensional delta acceptances for different sets of rectangular x_p and y_p cuts.

7.5 Cross-section Extraction

The raw cross-section (σ_{raw}) can be extracted using from the data yield using the following formula:

$$\sigma_{raw}(E', \theta) = \frac{yield_{cor}(E', \theta)}{L * \Delta E' * \Delta \Omega_{eff}}, \quad (7.28)$$

where, $yield_{cor}(E', \theta)$ is the efficiency (ϵ) corrected yield, L is the integrated luminosity and, $\Delta \Omega_{eff}$ is the effective acceptance as seen by the spectrometer.

$$yield_{cor}(E', \theta) = \frac{yield(E', \theta)}{\epsilon_{cal} * \epsilon_{cheren} * \epsilon_{tr} * \epsilon_{trig} * livetime}. \quad (7.29)$$

The raw cross-section extraction can be performed using the following two methods.

- **Acceptance correction method:** In this method the acceptance correction is performed on a bin-by-bin basis in the Eqn. 7.28 where,

$$\Delta \Omega_{eff}(E', \theta) = \Delta \Omega * A(E', \theta). \quad (7.30)$$

The acceptance function is determined for each $E' - \theta$ bin from the Monte-Carlo simulation as described in Section. 7.4.7 and the extracted cross-section is written as,

$$\sigma_{raw}(E', \theta) = \frac{yield_{cor}(E', \theta)}{L * \Delta E' * \Delta \Omega * A(E', \theta)}.$$

- **Monte-Carlo ratio method:** In this method, the simulated yield is generated ($yield_{MC}$) using a cross-section model and the ratio of the simulated yield and the data yield is taken to extract the cross-section as shown below.

$$\begin{aligned} yield_{MC} &= L * \sigma_{model} * \Delta E' * \Delta \Omega_{eff} \\ yield_{data} &= L * \sigma_{raw} * \Delta E' * \Delta \Omega_{eff} \\ \sigma_{raw}(E', \theta) &= \sigma_{model} * \frac{yield_{data}(E', \theta)}{yield_{MC}(E', \theta)}. \end{aligned}$$

As the acceptance correction method was model independent, it eliminates any uncertainty due model dependence of the extracted raw cross-section. So, the acceptance correction method was used to extract the cross-section for experiment E12-06-121 and it will be described in detail. For the HMS the raw cross-section was extracted for each run binned in E' and θ . Then the weighted average was taken for n runs for each $E' - \theta$ bin to obtain,

$$\langle \sigma_{raw} \rangle = \frac{\sum_{i=0}^n \frac{\sigma_{raw}^i}{\delta \sigma_i^2}}{\sum_{i=0}^n \frac{1}{\delta \sigma_i^2}}, \quad (7.31)$$

where σ_i and $\delta \sigma_i$ are the i^{th} cross-section and statistical error on that cross-section. The combined statistical error was calculated as,

$$\delta \sigma_{stat} = \langle \sigma_{raw} \rangle \sqrt{\sum_{i=1}^p \left(\frac{\delta a_i}{a_i} \right)^2}, \quad (7.32)$$

where a_i is each component of the cross section that has a statistical error. In our case the statistical uncertainty came from the yield, acceptance (MC events), and live time calculations. All the systematic errors were combined in quadrature to obtain $\delta\sigma_{sys}$ which will be listed with the final results.

While analyzing data taken by HMS, the cross-section was binned over 10 E' and 10 θ bins. The range of E' was $\pm 10\%$ about the central spectrometer momentum of a particular HMS setting and the θ range was ± 25 mrad about the central angle of the spectrometer. The whole cross-section extraction procedure will be discussed for one HMS kinematic setting and the results for all other kinematic settings will be reported. The extracted acceptance corrected raw cross section (σ_{raw}) for HMS Kin-C is shown in Fig. 7.32. The correction factors and charge normalization applied to the yield on run by run basis are listed in Table. 7.6.

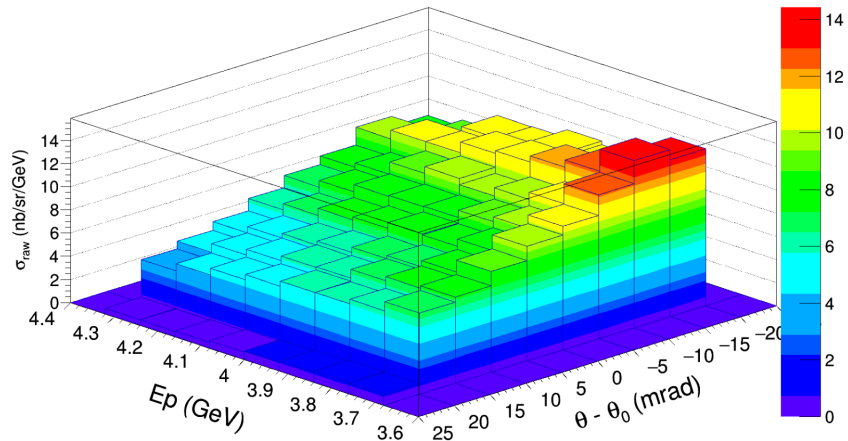


Figure 7.32: The acceptance corrected raw cross-section for HMS Kin-C.

Table 7.6: The list normalization and correction factors to the HMS yields for Kin-C.

Correction factor	Run 4233	Run 4234	Run 4235
ϵ_{cal}	0.9985	0.9985	0.9985
ϵ_{cheren}	0.9911	0.9911	0.9911
ϵ_{tr}	0.9962	0.9962	0.9962
ϵ_{trig}	0.9993	0.9993	0.9993
$livetime$	0.9997	0.9997	0.9997
$Q_{tot}(\mu C)$	76123.5	91630.7	75091.3

The following cuts were used on the HMS data yield for the cross-section analysis.

1. $-9 < z < 9$ (cm)
2. $-8 < \delta < 8$ (%)
3. $abs(xp) < 0.04$ (rad)
4. $abs(yp) < 0.02$ (rad)
5. Calorimeter cut : $0.2 < \frac{E}{P} < 2$
6. Cherenkov cut : $npe > 1$

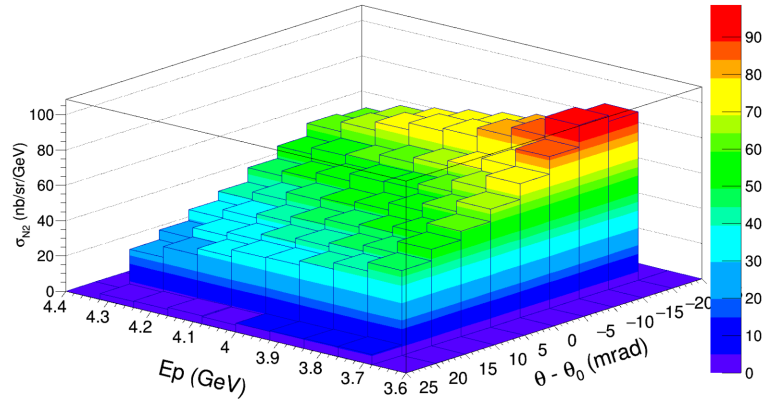
7.5.1 Background Correction to Obtain σ_{rad}

The acceptance corrected nitrogen scattering cross-section (σ_{N_2}) was measured using nitrogen reference cell data following the same procedure as extracting raw cross-section (Eq. 7.5). Then the σ_{N_2} was scaled down by a factor of $\frac{\eta_{N_2}}{\eta_{N_2} + \eta_{He3}}$ to account for the number density of nitrogen present in the production cell where, η_{N_2} and η_{He3} are the number densities of the nitrogen and 3He in the target cell. So the nitrogen dilution contribution was calculated by the following formula.

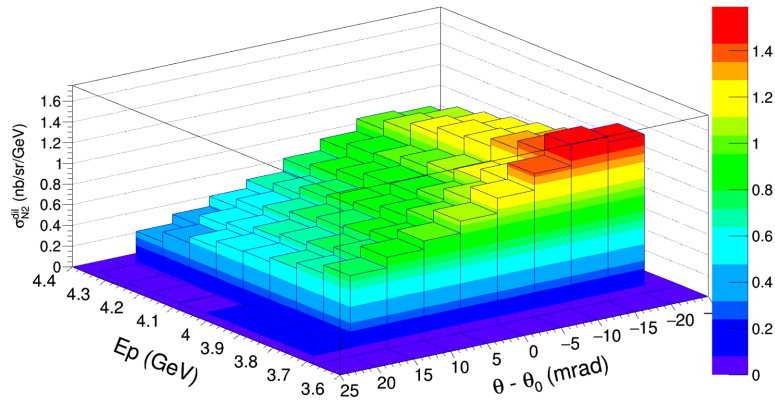
$$\sigma_{N_2}^{dil} = \frac{\eta_{N_2} * \sigma_{N_2}}{\eta_{N_2} + \eta_{He3}}. \quad (7.33)$$

This dilution was subtracted from the σ_{raw} to obtain the actual measured experimental cross-section, σ_{rad} as follows:

$$\sigma_{rad} = \sigma_{raw} - \sigma_{N_2}^{dil}. \quad (7.34)$$



(a)



(b)

Figure 7.33: The nitrogen dilution cross-section for HMS Kin-C. (a) Nitrogen cross-section extracted from reference cell data, (b) The nitrogen dilution correction to the raw cross-section.

The nitrogen dilution for HMS Kin-A is demonstrated in Fig. 7.33. The top plot shows the measured σ_{N_2} using the reference cell run 3808. The bottom plot shows the dilution cross-section $\sigma_{N_2}^{dil}$ which was subtracted from σ_{raw} to extract the measured radiative cross-section. In the case of production cell Tommy, the number densities of nitrogen and ^3He were 0.13 amagat (η_{N_2}) and 7.76 amagat (η_{He3}) respectively. The Fig. 7.34 shows the background subtracted cross-section, σ_{rad} binned in $E' - \theta$.

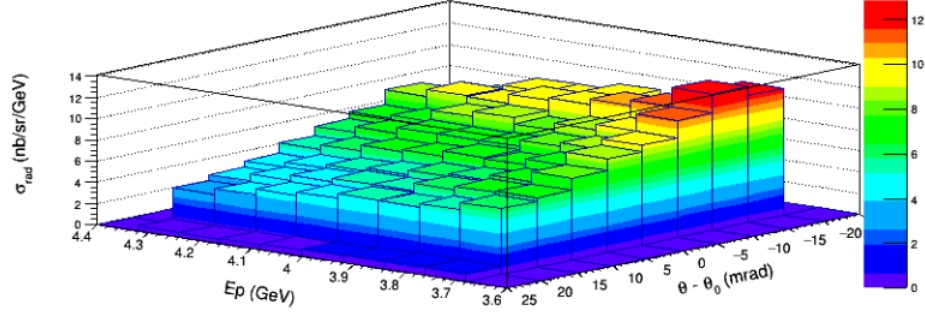


Figure 7.34: The measured acceptance corrected radiative cross-section after background subtraction for HMS Kin-C.

7.5.2 Radiative Correction

During the scattering process, the electrons lose some energy due to various processes like scattering from the glass cell windows, bremsstrahlung, vertex processes and so on. Because of these interactions the actual incident energy of the electrons and also the scattered electron energy get shifted from their true values which results in a different measured cross-section from the true scattering cross-section. The procedure of correcting for these higher order effects is known as radiative corrections. The radiative corrections can be classified in two ways: internal radiative corrections and external radiative corrections.

Internal radiative corrections

In the QED perturbative expansion of scattering cross-section, the leading order is the Born cross section. The next order has interference of Born cross section along with higher order interactions. The higher order processes that occur at the scattering vertex are known as the internal radiative processes. These corrections include bremsstrahlung when photons are emitted in the nucleon field during scattering, vertex corrections like emission and reabsorption of the virtual photons, the creation of particle-antiparticle pairs or vacuum polarization and multiple photon exchange corrections. The Fig. 7.35 shows the different internal radiative processes that contribute in the scattering. In case of our analysis, the internal radiative corrections used the equivalent radiator approximation [91] where the internal bremsstrahlung effect is considered to be equivalent to placing two radiators of same thicknesses before and after the scattering.

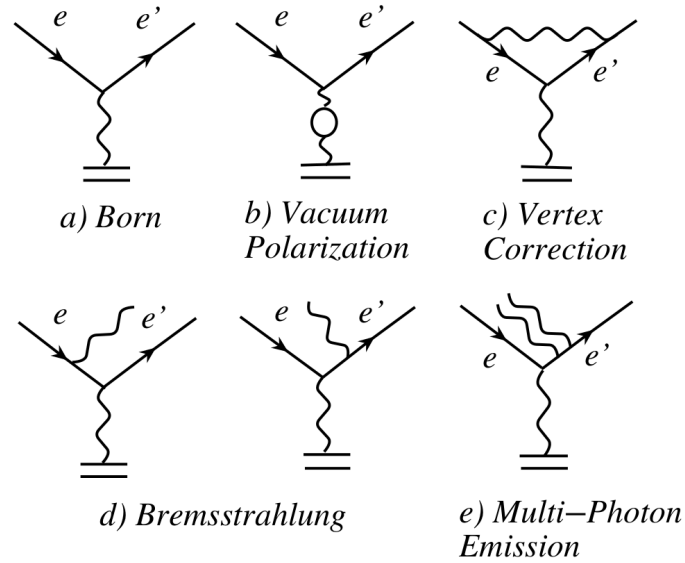


Figure 7.35: Different internal radiative processes that contribute to the inclusive electron scattering [90].

External radiative corrections

The external radiative corrections come from the interaction of the electrons with different materials before and after the scattering from the target. The main external radiation process is the bremsstrahlung and it depends on the thickness and radiation lengths of the different materials present in the electron path. The energy loss of high energy electrons through bremsstrahlung is characterized by radiation length (X_0 in g cm^{-2}) which is the depth of material traversed by the electrons. The thicknesses of the pre target materials, target cell wall, ^3He target, and the post- target materials present in the electron beam path are listed below.

- **Pre target materials:**

- Be Window: Thickness 10 mil (0.0254 cm)
- Nitrogen gas: Thickness 11 cm (10 cm + 1 cm target z offset downstream for Tommy)
- Upstream window, GE-180: Thickness 0.0137 cm (Tommy), raster correction factor = 1.014 [89]

- **Target:** Helium-3, thickness 40 cm

- **Cell wall:** GE-180, thickness 0.15 cm

- **Post target materials (HMS):**

- Nitrogen gas: Thickness 44 cm
- Lexan polycarbonate panels: Thickness 0.1588 cm

- Air: Thickness 24.61 cm
- Kevlar: Thickness 15 mil (0.0381 cm)
- Mylar: Thickness 5 mil (0.0127 cm)

• **Post target materials (SHMS):**

- Nitrogen gas: Thickness 44 cm
- Lexan polycarbonate panels: Thickness 0.1588 cm
- Air: Thickness 57.27 cm
- Aluminum: Thickness 10 mil (0.0254 cm)

The radiation lengths of different materials present in the electron path are listed in Table. 7.7.

Table 7.7: The list of radiation lengths of different materials present in the electron beam path.

Material	X_0 (g cm^{-2})	Density (g cm^{-3})	Radiation length, R (cm)
Helium-3	67.42	1.50×10^{-3}	44947
GE-180	19.5	2.77	7.040
N_2	37.9879	1.1602×10^{-3}	32742.54
Be Window	35.28	1.848	19.091
Air	36.62	1.20×10^{-3}	30420
Lexan Polycarbonate	41.46	1.14	34.6
Aluminum	24.01	2.10	8.89
Kevlar			74.6
Mylar			28.7

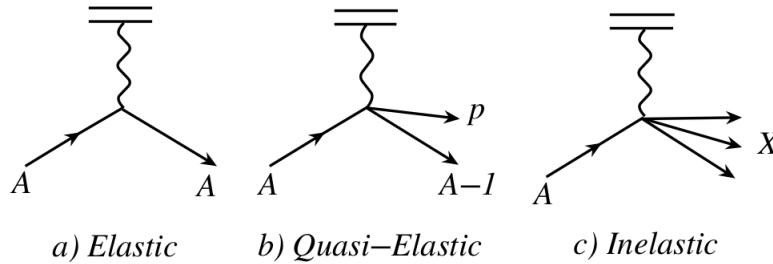


Figure 7.36: The processes contributing to the measured scattering cross section in experiment E12-06-121 [90].

The measured cross-section σ_{rad} is a combination of the three contributions, shown in Fig. 7.36.

$$\sigma_{rad} = \sigma_{rad}^{elastic} + \sigma_{rad}^{quasielastic} + \sigma_{rad}^{inelastic}. \quad (7.35)$$

The Jefferson Lab radiative correction program called rc-externals was used to generate the radiated elastic, quasi elastic and inelastic contributions. This code calculated both the internal and external radiative corrections. Although the elastic scattering peak is well separated from the inelastic region at Born level, the radiative tail reaches the inelastic regime. In the rc-externals code, the elastic radiative tail was calculated by Mo and Tsai's formula [91]. In this analysis the exact formula for the elastic radiative tail was directly integrating over all photon emission angles without the peaking approximation where the photon emission is assumed to happen only in the direction of incident and scattering electrons. The quasi elastic tail was computed using the ^3He quasi-elastic model with radiative effects [92][93]. The elastic, quasi-elastic tail contributions for HMS Kin-C of experiment E12-06-121 are shown in Fig. 7.37. In the inelastic spectrum, the radiative correction was done by integrating all possible final states at a particular kinematic setting. The measured radiative cross section (σ_{rad}) is expressed in terms of the following integral:

$$\sigma_{rad}(E_s, E_p) = \int_0^T \frac{dt}{T} \int_{E_s^{min}}^{E_s} dE'_s \int_{E_p}^{E_p^{max}} dE'_p I(E_s, E'_s, t) \sigma_r(E'_s, E'_p) I(E_p, E'_p, T - t), \quad (7.36)$$

where E_s , E_p are incident and scattered electron energy respectively, σ_r is the internally radiated cross-section (calculated using equivalent radiator model) and, $I(E, E', t)$ is the probability that the electrons lose their energy through bremsstrahlung after traveling a length t in the material [91][93].

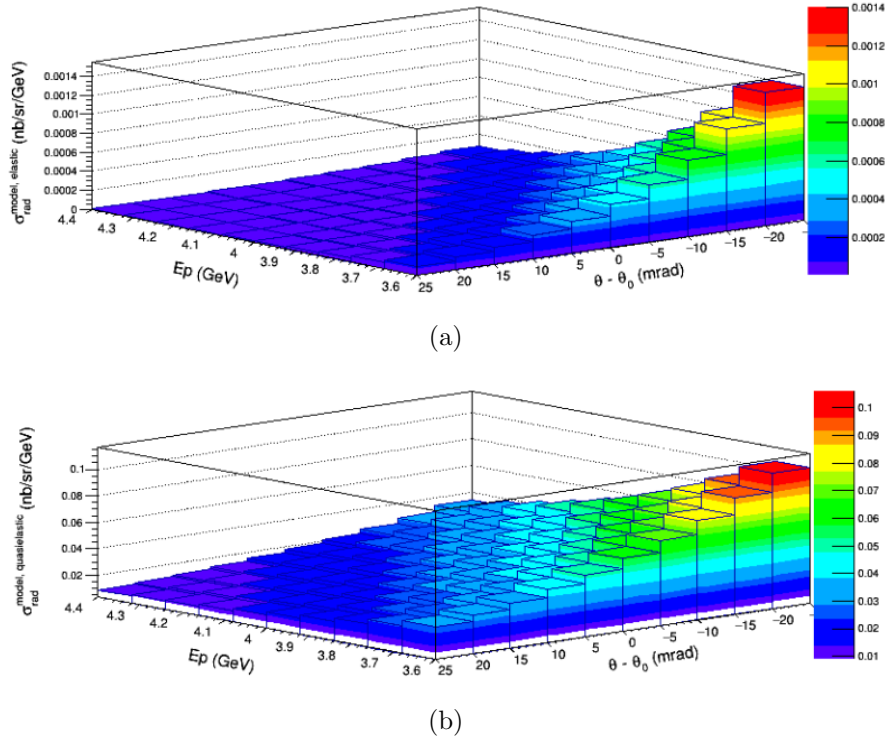


Figure 7.37: The elastic and quasi-elastic tail contributions calculated using rc-externals code binned in $E' - \theta$ for HMS Kin-C.

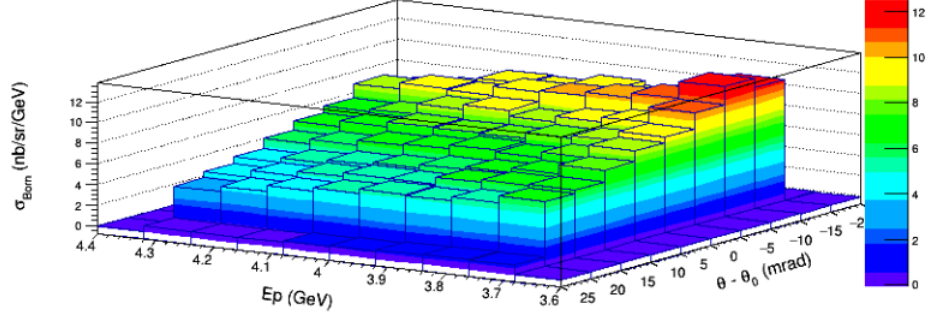


Figure 7.38: The extracted Born cross-section for HMS Kin-C.

To unradiate the measured radiated cross section the following formula was used:

$$\sigma_{Born} = \left(\sigma_{rad} - \sigma_{rad}^{elastic,model} - \sigma_{rad}^{quasielastic,model} \right) \frac{\sigma_{Born}^{model}}{\sigma_{rad}^{inelastic,model}}. \quad (7.37)$$

The first step was to subtract all elastic and quasi-elastic contributions from the experimental cross-section. Then a multiplicative radiative correction using cross-section parametrization F1F2IN21 [94] was applied to extract the Born cross-section (σ_{Born}).

These corrections were performed on a bin-by-bin basis on the $\sigma_{rad}(E', \theta)$ histogram to extract the $\sigma_{Born}(E', \theta)$. The Fig. 7.38 shows the unradiated cross-section σ_{Born} for HMS Kin-C binned in $E' - \theta$. The scattering angle (θ) dependence of both the measured radiated and Born cross-sections for each E' bin is shown in Fig. 7.39 for the same kinematic settings.

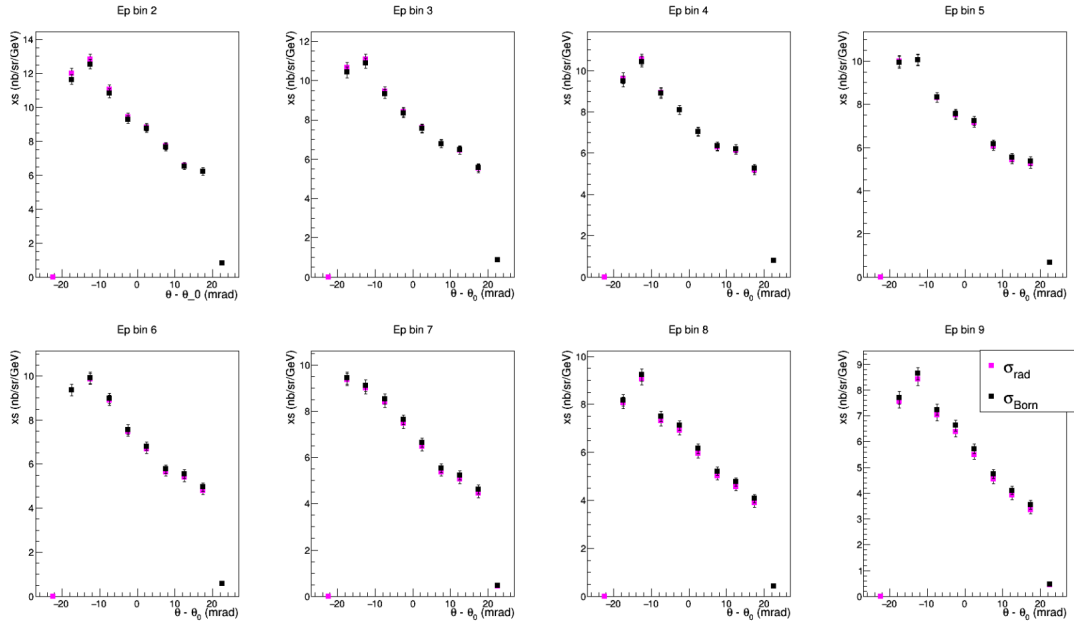


Figure 7.39: The scattering angle dependence of the measured radiated and Born cross-sections for each E' bin. The error bars are statistical only.

7.5.3 Bin Centering Correction

The measured Born cross-section was extracted binned in δ and θ . If the cross-section varies non-linearly with the scattering angle, a correction has to be applied to correctly average the cross-sections over θ . The θ dependence of the cross-section is removed by normalizing the cross-sections to the central spectrometer angle. For each δ bin one gets,

$$[\sigma_{Born}(\theta_0)]_{BC,i} = \sigma_{Born}(\theta_i) \frac{\sigma_{Born}^{model}(\theta_0)}{\sigma_{Born}^{model}(\theta_i)}, \quad (7.38)$$

where θ_i and θ_0 are the i^{th} and central θ bins and the superscript *model* represents the F1F2IN21 model cross-sections for each bin. The bin centering of Born cross-sections are shown in Fig. 7.40. The momentum acceptance cuts $abs(\delta) < 8\%$ on data fall on the first and the last E' bins in this plot, so these two bins will not be analyzed in cross-section extraction. After that the bin centering corrected Born cross-sections were averaged over θ for each δ bin as shown in Fig. 7.41. This averaging was performed after the background subtraction and radiative correction were done bin-by-bin basis. The Fig. 7.42 shows the bin-centering correction for the radiative cross-section. This was done to directly compare the radiative and Born cross-sections binned in E' which is shown in Fig. 7.43. The radiative correction was kinematics dependent and it ranged from ~ 1 -10% for different kinematic settings.

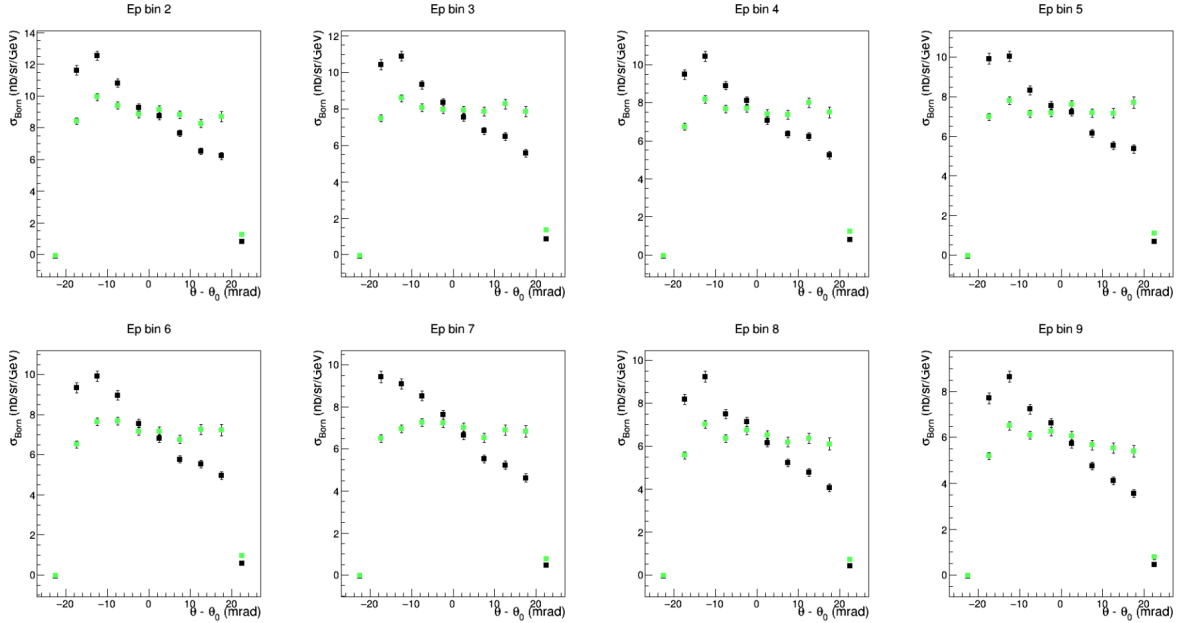


Figure 7.40: The θ bin centering corrections on Born cross-sections for each E' bin. The error bars are statistical only.

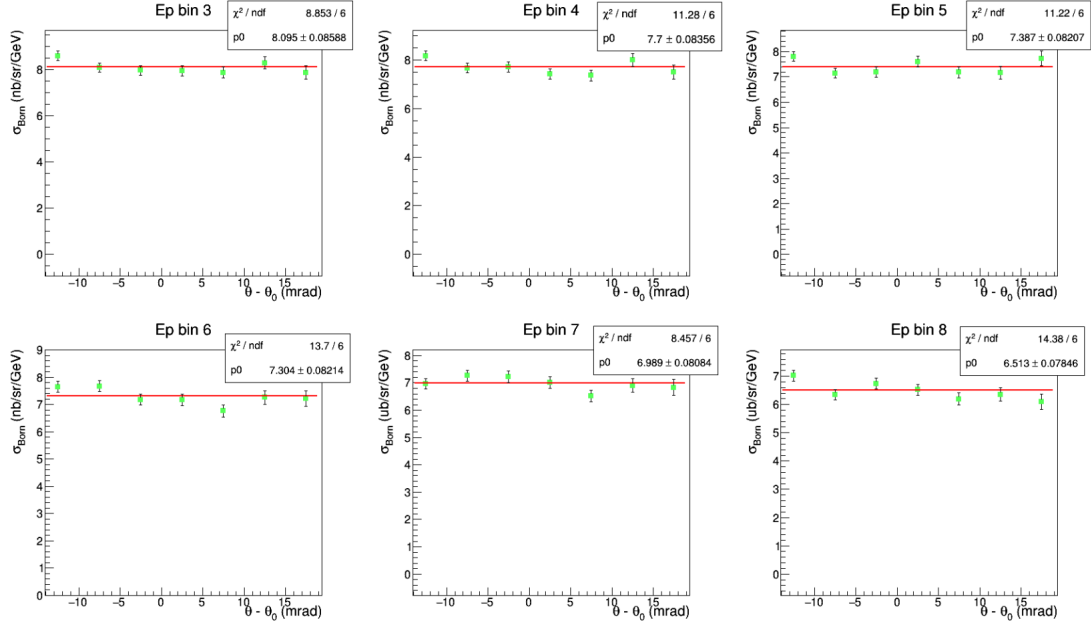


Figure 7.41: The average of θ bin centered Born cross-sections for each E' bin. The error bars are statistical only.

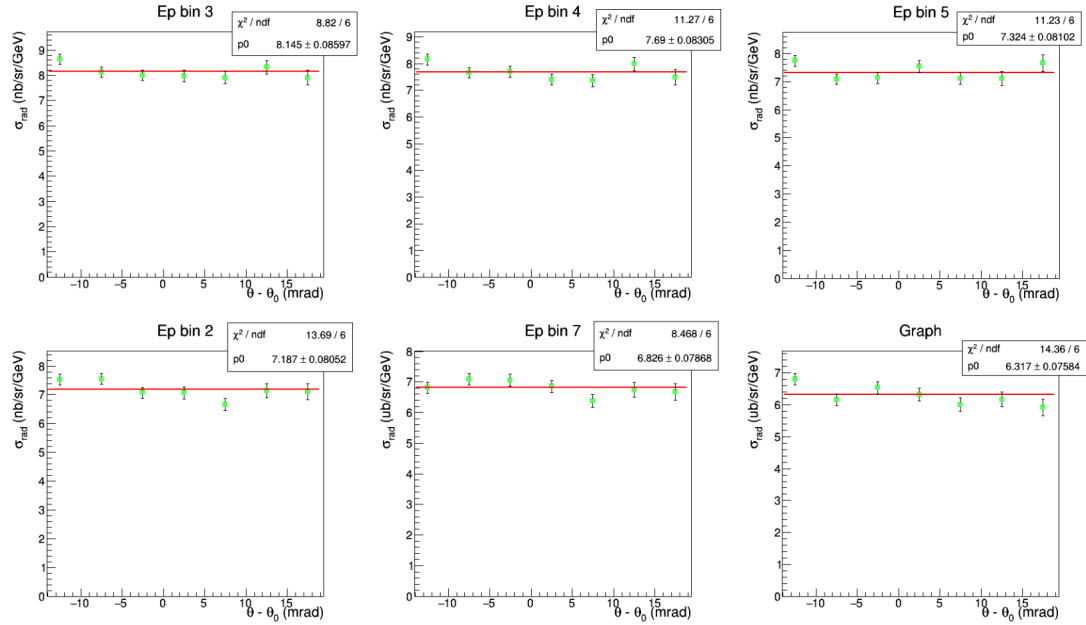
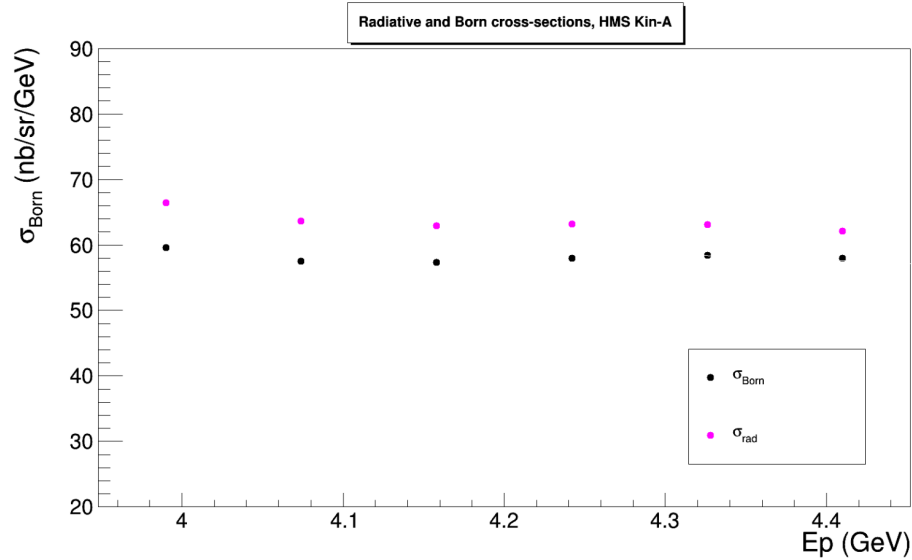
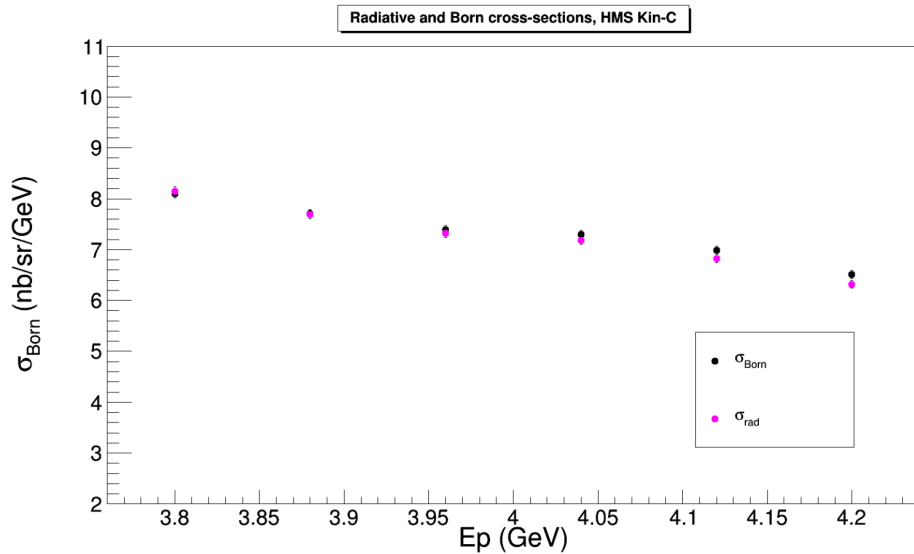


Figure 7.42: The average of θ bin centered radiative cross-sections for each E' bin. The error bars are statistical only.



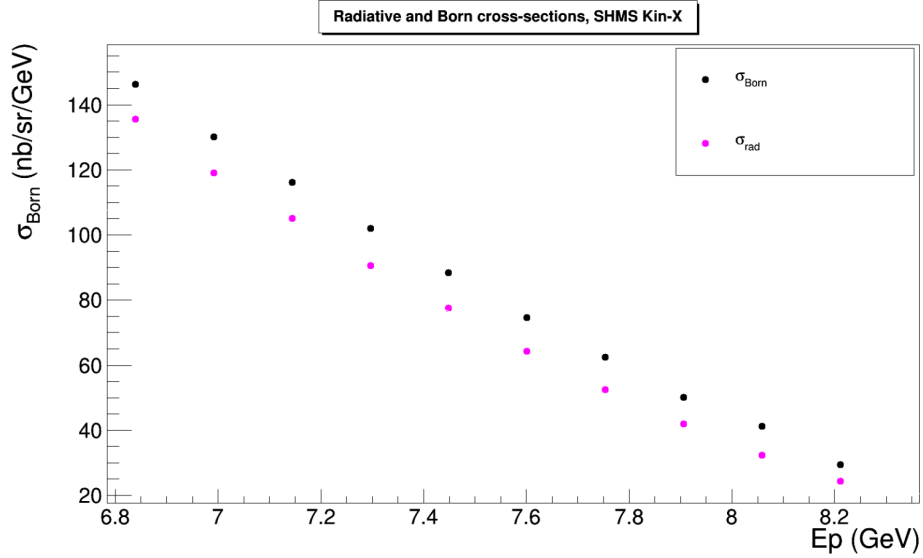
(a) HMS Kin-A



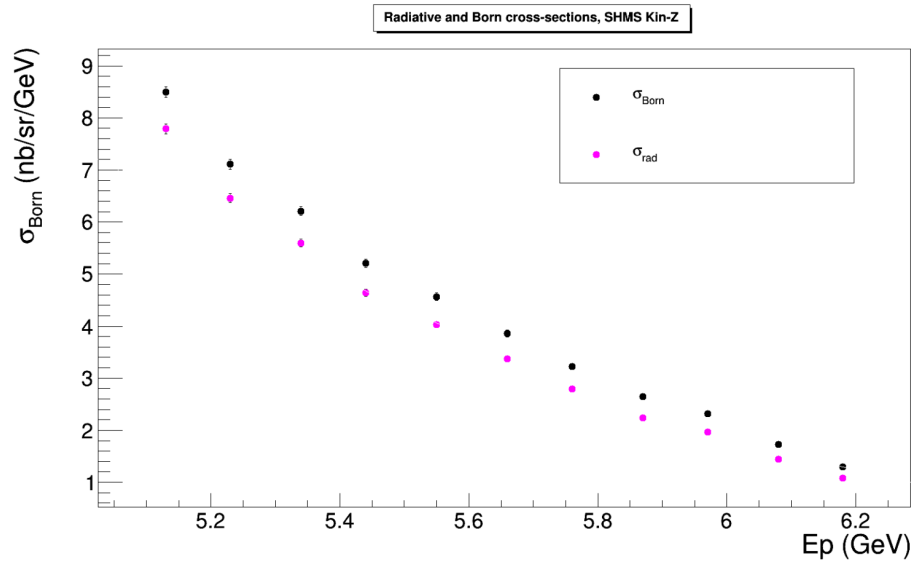
(b) HMS Kin-C

Figure 7.43: The θ bin centering corrected radiative and Born cross-sections binned in E' for HMS kinematic settings.

This procedure was performed for all HMS and SHMS kinematic settings. Fig. 7.45 and 7.46 show the extracted Born cross-section for HMS (Kin-A, Kin-C) and SHMS (Kin-X, Kin-Z) respectively, with statistical and systematic uncertainties. The systematic errors are shown by gray bands which are the quadrature sum of all error sources and it will be discussed in Section 7.5.4.



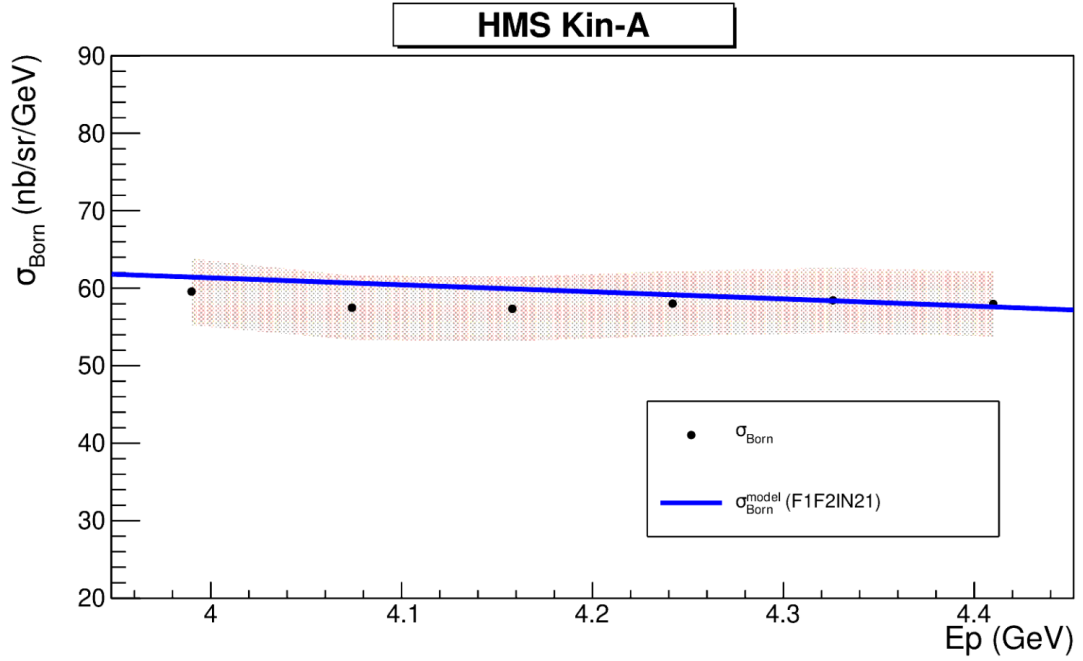
(a) SHMS Kin-X



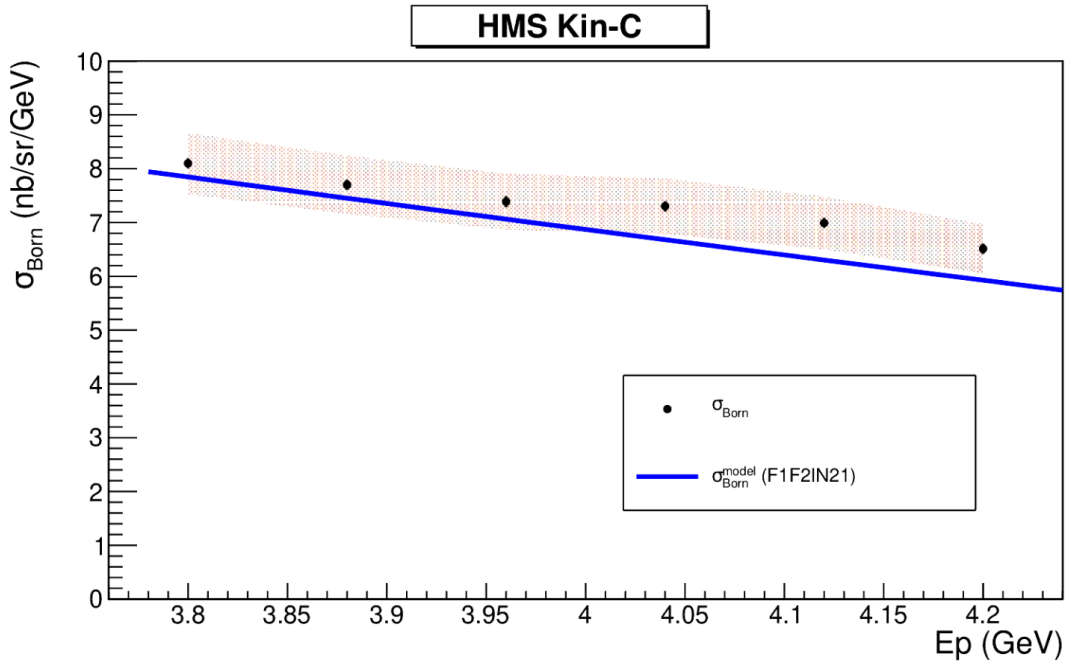
(b) SHMS Kin-Z

Figure 7.44: The θ bin centering corrected radiative and Born cross-sections binned in E' for SHMS kinematic settings.

The data was limited for HMS Kin-B and SHMS Kin-C. The livetime correction for the HMS runs also needs to be re-analyzed. An exceptionally low computer livetime was reported, so the cross-section result for that particular kinematics is not reported in this dissertation. The θ bin-centered corrected radiative and Born cross-sections for each E' bin are reported in Appendix E.

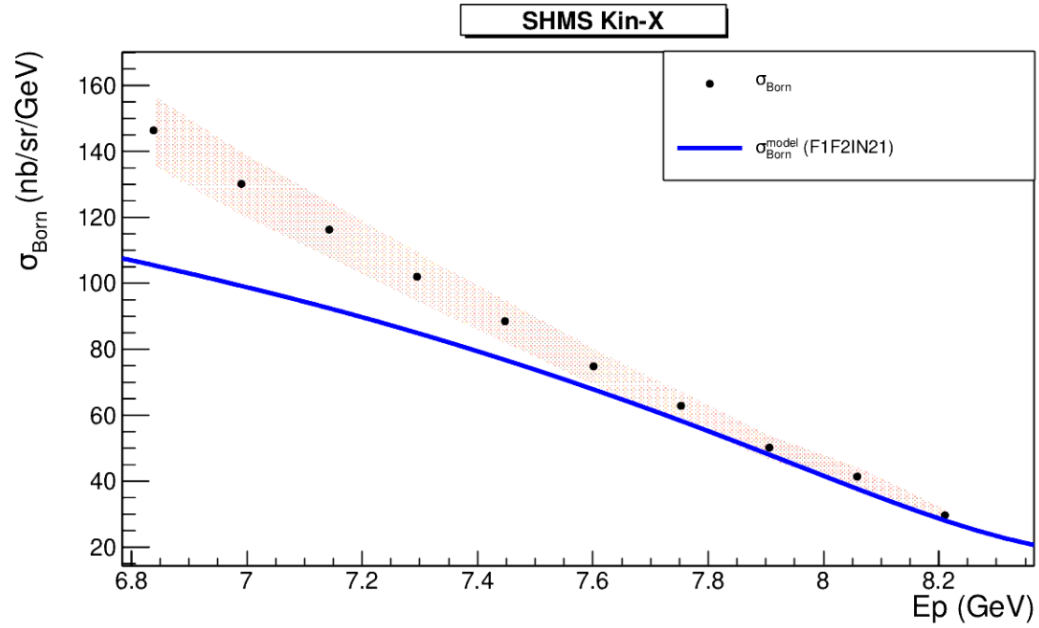


(a) HMS Kin-A: $\langle x \rangle = 0.207$, $\langle Q^2 \rangle = 2.409 \text{ GeV}^2/c^2$

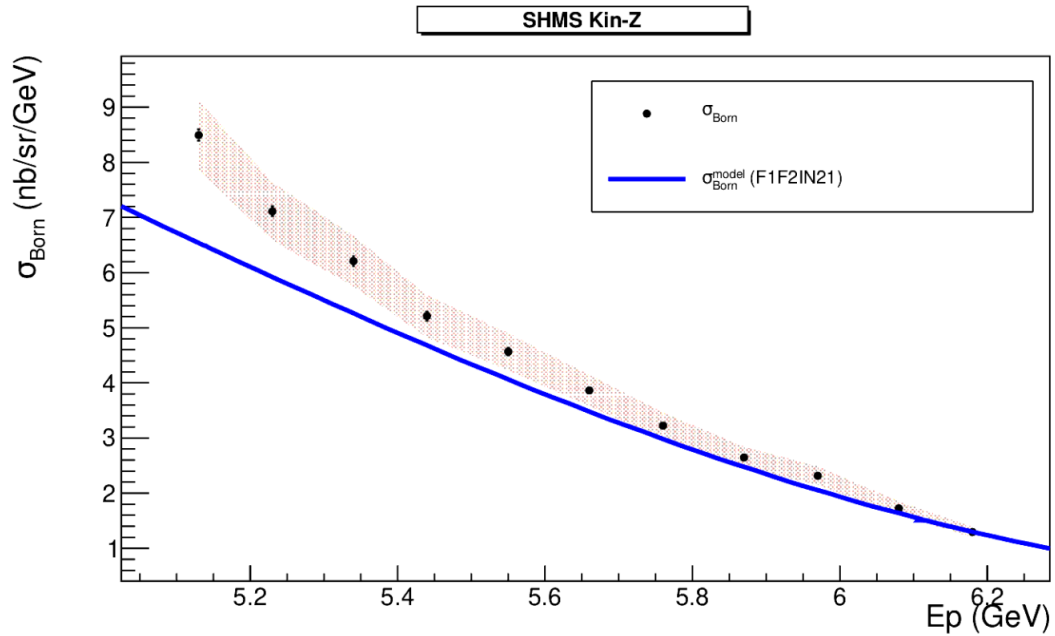


(b) HMS Kin-C: $\langle x \rangle = 0.418$, $\langle Q^2 \rangle = 5.008 \text{ GeV}^2/c^2$

Figure 7.45: The extracted Born cross-sections for HMS kinematic settings. The statistical error on each data point is shown by bars and the systematic errors are shown by gray band. The prediction from the F1F2IN21 model is shown by the blue line on the same plot.



(a) SHMS Kin-X: $\langle x \rangle = 0.53$, $\langle Q^2 \rangle = 2.86 \text{ GeV}^2/c^2$



(b) SHMS Kin-Z: $\langle x \rangle = 0.63$, $\langle Q^2 \rangle = 5.69 \text{ GeV}^2/c^2$

Figure 7.46: The extracted Born cross-sections for SHMS kinematic settings. The statistical error on each data point is shown by bars and the systematic errors are shown by gray band. The prediction from the F1F2IN21 model is shown by the blue line on the same plot.

7.5.4 Systematic Uncertainties

There are systematic uncertainties associated with various parameters that go into the radiative and Born cross-sections. Firstly, the raw cross section had systematic errors from the charge normalization, yield correction factors, target density, PID cuts and spectrometer acceptances. The systematic errors in the raw cross section, the error from background correction and the error due to radiative corrections were added in quadrature to calculate the total systematic error in the Born cross-section.

The total beam charge error was estimated to be $\pm 1\%$ relative during the experiment. For the cross-section analysis, the charge from BCM-2 was used because it was found to be more stable during the d_2^m run period. The calibration of BCM-1 and BCM-2 were conservatively good to $\sim 1\%$. The next systematic error came from the target density correction. The temperature corrected target density was calculated using the method described in Chapter 6. The systematic error from density correction in this dissertation was conservatively estimated to be $\sim \pm 2\%$ based on previous ^3He experimental results. However, the University of Virginia group is working on finalizing this systematic error. The systematic error from the PID cut was $\sim \pm 3\%$. The calorimeter PID cut was varied about the optimum one by about $\pm 7\%$ making sure good electrons are being selected. Then the variation of the efficiency corrected yields for different PID cuts were calculated and it was $\sim \pm 3\%$. The point-to-point errors from the Cherenkov and calorimeter efficiencies were also included in the systematic error and those errors were small ($\sim \pm 0.02\%$). One of the dominant systematic errors came from the spectrometer acceptance and the following systematic study was performed to estimate that error.

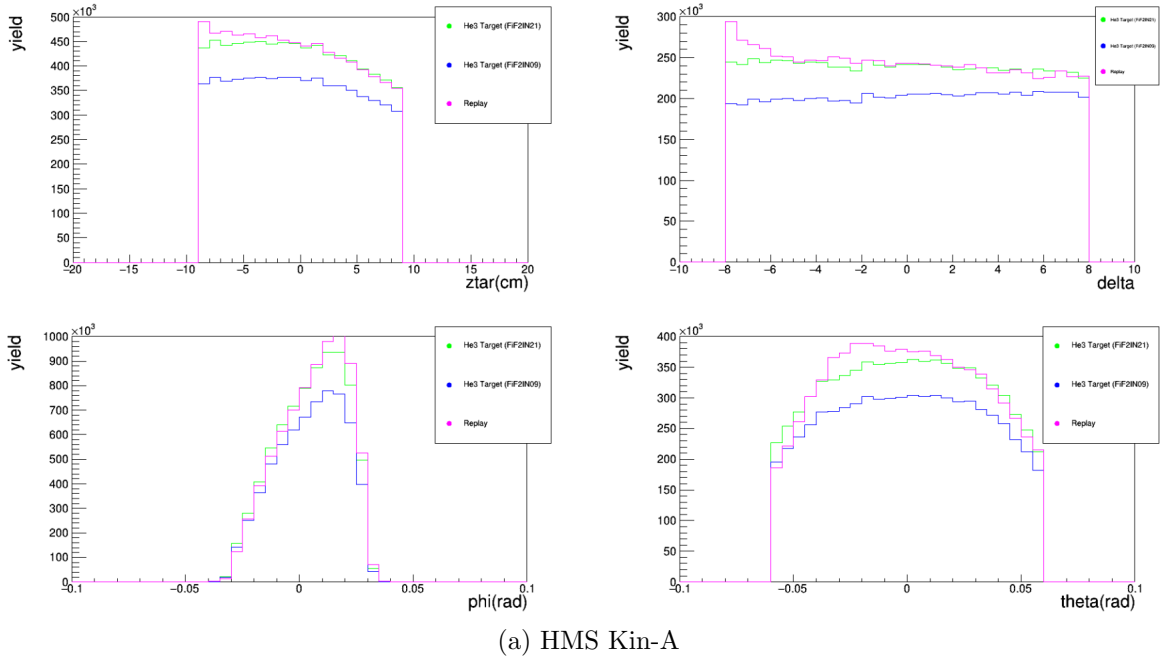
Acceptance Uncertainty

The acceptance uncertainty analysis required an absolute comparison of the data with the Monte-Carlo simulation. The radiative cross sections were generated to apply forward radiative corrections to the simulated yield for the absolute comparison with data. Before that the unradiated cross-section weighted yields from the F1F2IN09 [95] and the F1F2IN21 (upgraded version of F1F2IN09) cross-section model were compared with the data.

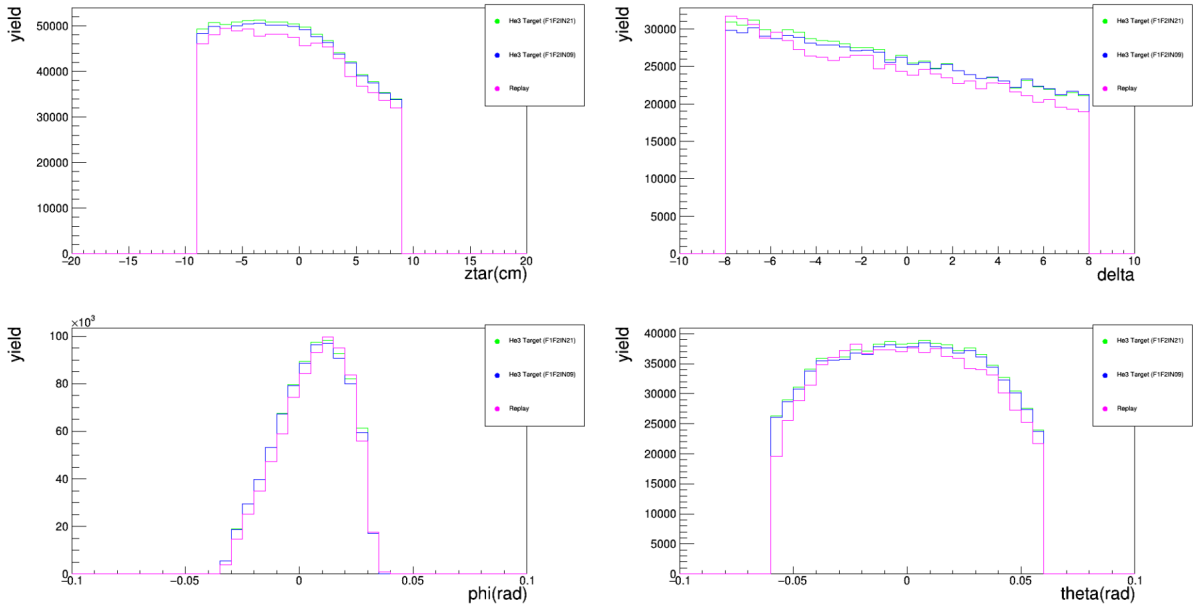
The Fig. 7.47 shows the model comparisons for one smaller and one larger spectrometer angle settings with the following acceptance cuts.

1. $-9 < z < 9$ (cm)
2. $-8 < \delta < 8$ (%)
3. $\text{abs}(xp) < 0.06$ (rad)
4. $\text{abs}(yp) < 0.04$ (rad)
5. PID cuts on data: calorimeter cut ($0.8 < E/P < 2$) and Cherenkov cut ($n_{pe} > 1$)

Significant improvement in data-simulation agreement was noticed for smaller scattering angle setting when the F1F2IN21 model was used. So it was decided to use the F1F2IN21 model while generating the radiative cross-section.



(a) HMS Kin-A



(b) HMS Kin-C

Figure 7.47: The comparison of data yield (magenta) with F1F2IN09 (blue) and F1F2IN21 (green) cross-section models for smaller (HMS Kin-A, 13.5°) and larger (HMS Kin-C, 20°) spectrometer angles.

The Fig. 7.48 shows the Born and radiative cross-section for HMS Kin-A, generated using the Jefferson Lab programming package called rc-externals. The Born cross-section weighted yield and the radiative cross-section weighted yield for HMS Kin-A are shown in Fig. 7.49. The radiated yield was 7% higher than the Born yield

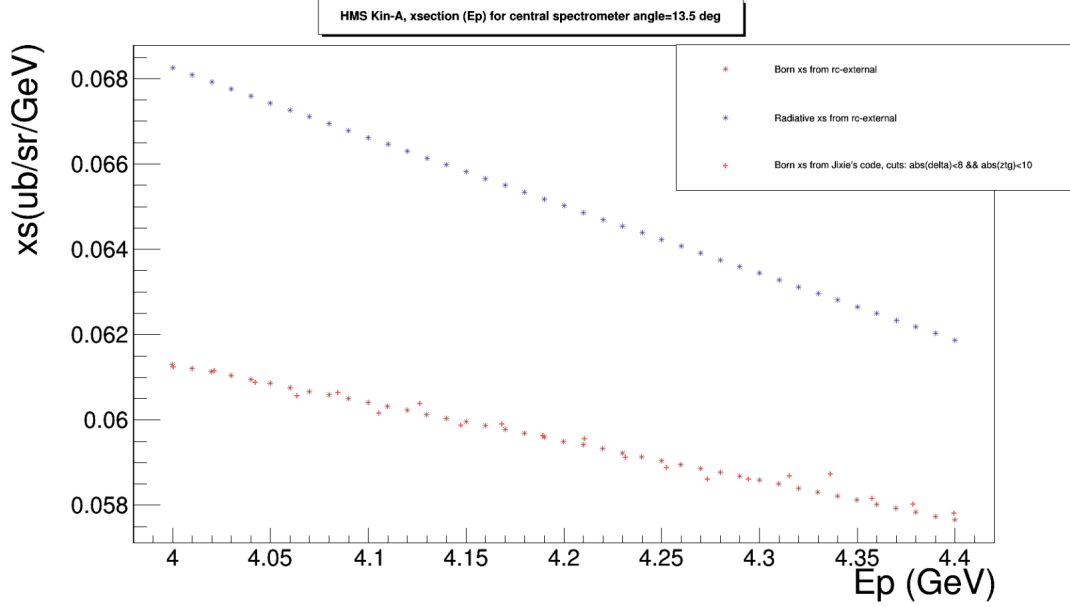


Figure 7.48: The Born and Radiative cross-section from F1F2IN21 model as a function of E' for fixed scattering angle, $\theta=13.5^\circ$.

for this kinematic setting. To determine the acceptance uncertainty, the forward radiative correction was applied to the simulated yield to compare it with data. The method of acceptance uncertainty estimation is described below.

- **Step 1:** The integral of the radiated z yield from simulation was scaled to match the data integral for specific z , δ , xp and yp cuts.
- **Step 2:** The percentage difference between the scaled simulation and data was determined by binning the data in x using the following formula.

$$P = \frac{(yield_{data} - yield_{simulation}) * 100}{yield_{simulation}} \quad (7.39)$$

- **Step 3:** The z , δ , xp , yp acceptance cuts were varied to get the scale factor and the P as a function of those cuts.
- **Step 4:** It was found that the variation of P was insignificant with different acceptance cuts. So only the variation of scale factor for different acceptance cuts contributed to the uncertainty due to spectrometer acceptance.

The Fig. 7.50 shows an example result from step 4 of acceptance uncertainty estimation. For the HMS Kin-A the scale factors were plotted as a function of z , δ , xp and yp cuts varying one cut at a time. The variation of scale factors with z , δ , xp and yp acceptance cuts were 3.0%, 1.0%, 1.6% and 2.7% respectively which resulted in an acceptance uncertainty of $\sim 4.45\%$ when added in quadrature.

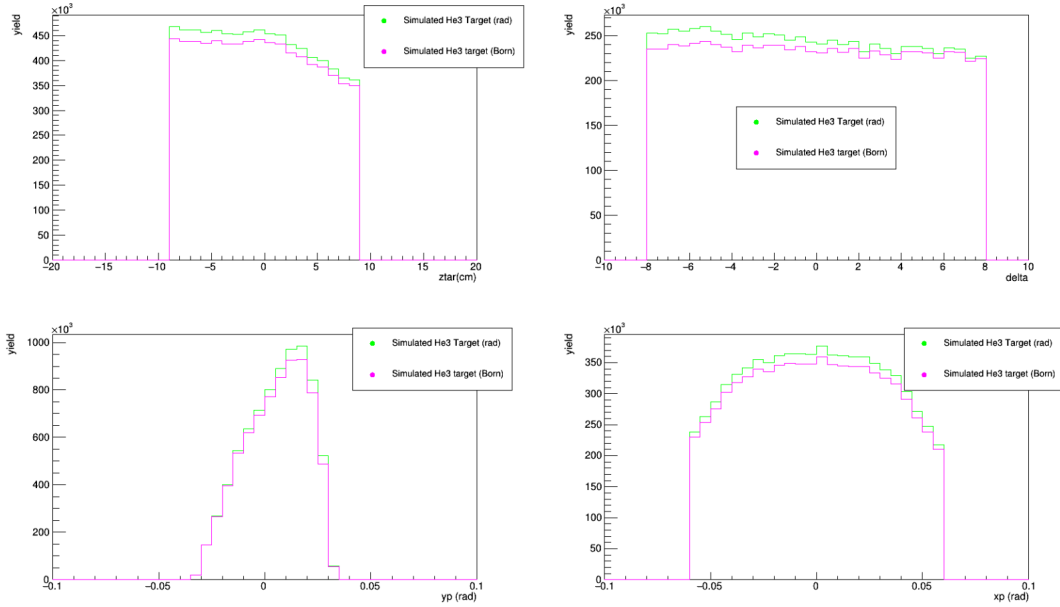


Figure 7.49: The Born and Radiative cross-section weighted yield for HMS Kin-A.

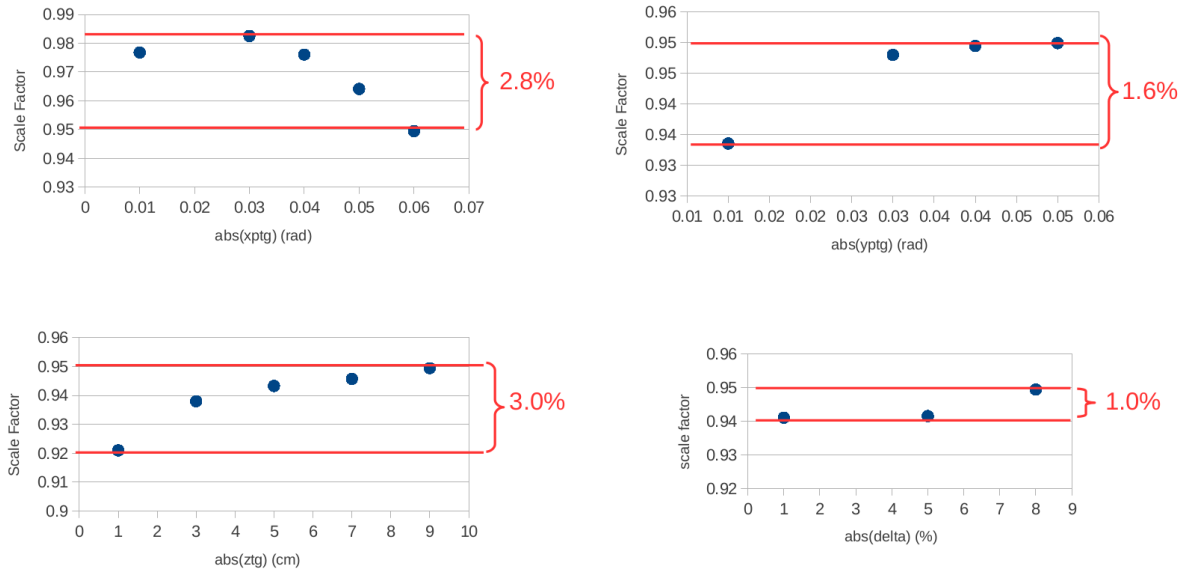


Figure 7.50: The acceptance uncertainty estimation from variation of scale factors with z , δ , xp and, yp acceptance cuts.

The systematic error in background correction originates from the measurement of nitrogen number density in the target cell. The maximum nitrogen dilution contribution in the measured radiative cross-section was $\sim 15\%$. The uncertainty in the nitrogen number density in the target cell was $\sim \pm 2\%$ which was propagated to the cross section. For the maximum nitrogen dilution contribution, this uncertainty was

$\sim \pm 0.3\%$ which was assigned as the background correction error for the cross-section extraction. The final systematic uncertainty in the Born cross-section was the error from radiative correction. The radiative correction uses the radiation lengths of different materials present in the electron path. The error in the thicknesses of those materials propagates in the cross-section. The model (F1F2IN21) used to estimate the correction also introduces some uncertainty. The radiative correction should be calculated varying the material thicknesses within their uncertainty and the spread of the final cross-section will be the estimate of the systematic uncertainty. Due to time constraint, the systematic radiative correction uncertainty study was not performed in this dissertation. A conservative uncertainty of $\sim \pm 4\%$ was assigned as the systematic uncertainty from radiative correction.

The total systematic error in the extracted Born cross-section was calculated by adding all aforementioned systematic errors in quadrature and a list of those systematic error contributions are summarized in the Table. 7.8.

Table 7.8: List of systematic uncertainty contributions in DIS cross-section extraction.

Quantity	Relative systematic error
Cut efficiencies	3%
Point-to-point errors from the calorimeter and Cherenkov efficiencies	0.02%
Beam Charge	1%
Target density	2%
Spectrometer Acceptance	4.5%
N ₂ dilution	0.3%
Radiative correction	4%

Chapter 8 Summary

The ultimate goal of experiment E12-06-121 is to explore the Q^2 evolution of neutron g_2 and d_2 which will be obtained after nuclear corrections to the ^3He structure functions. To extract the ^3He structure functions, the unpolarized cross-sections and double spin asymmetries need to be combined. In this work the unpolarized Born cross sections for deep inelastic scattering of electrons were extracted for a wide range of kinematic settings covering $0.21 < x < 0.63$ and $2.4 < Q^2 < 5.7 \text{ GeV}^2/c^2$. The extracted cross-sections were compared with the cross-sections from the most updated version of F_1F_2 parametrization (F1F2IN21). In the low x and Q^2 , the extracted cross-sections agree well with the model. In the higher x and Q^2 the deviation of model and data can be as large as 20%. The model needs to be updated including the extracted cross-section data from experiment E12-06-121. The systematic uncertainty in these cross-section results has a scope of improvement if a systematic study of radiative correction error is performed. These cross-sections will be combined with the double spin asymmetry analysis currently being done by Junhao Chen to extract the ^3He g_2 and d_2 . These new sets of results will benchmark the Lattice QCD prediction of d_2^n at $Q^2=5 \text{ GeV}^2/c^2$ and it will also provide a new precise dataset in the deep inelastic region to improve the current world data fits. I have contributed to this experiment in both hardware and software aspects including the installation of ^3He target system and optics in the hall, performing Moller polarimetry, precise measurement and analysis of ^3He polarization direction, and experimental data analysis. I have measured the unpolarized DIS cross-sections in the aforementioned kinematics for the first time and these cross-sections will be used in the extraction of neutron g_2 and d_2 to get the most precise values possible.

Appendix A: Compass Measurement Results

Table 1: The uncertainties in the magnetic field direction measurements for the d_2^n kinematic settings (March, 2020) with Helmholtz coil at 0° w.r.t. beamline

Kinematic settings	Polarization direction	Compass locations along z axis (cm)	Magnetic field direction (degrees)	$\pm \text{Error}_{\text{Survey}}$ (degrees)	$\pm \text{Error}_{\text{Mirror}}$ (degrees)	$\pm \text{Error}_{\text{Spotsize}}$ (degrees)	$\pm \text{Error}_{\text{Center}}$ (degrees)	$\pm \text{Error}_{\text{Total}}$ (degrees)
SHMS at 11° , 7.5 GeV/c	+X	11.965	88.487	0.012	0.065	0.006	0.01	0.067
		-0.14	88.613	0.012	0.065	0.006	0.01	0.067
		-12.017	88.467	0.012	0.065	0.006	0.01	0.067
	-X	11.965	268.809	0.012	0.041	0.006	0.01	0.044
		-0.14	268.702	0.012	0.041	0.006	0.01	0.044
		-12.017	268.883	0.012	0.041	0.006	0.01	0.044
	+Z	11.965	-0.245	0.036	0.041	0.006	0.01	0.056
		-0.14	0.256	0.034	0.041	0.006	0.01	0.055
		-12.017	0.218	0.032	0.041	0.006	0.01	0.054
	-Z	11.965	179.749	0.036	0.065	0.006	0.01	0.075
		-0.14	179.873	0.034	0.065	0.006	0.01	0.075
		-12.017	180.293	0.032	0.065	0.006	0.01	0.074
SHMS at 14.5° , 6.4 GeV/c	+X	11.965	88.543	0.012	0.065	0.006	0.01	0.067
		-0.14	88.647	0.012	0.065	0.006	0.01	0.067
		-12.017	88.47	0.012	0.065	0.006	0.01	0.067
	-X	11.965	269.347	0.012	0.041	0.006	0.01	0.044
		-0.14	268.786	0.012	0.041	0.006	0.01	0.044
		-12.017	268.884	0.012	0.041	0.006	0.01	0.044
	+Z	11.965	-0.493	0.036	0.041	0.006	0.01	0.056
		-0.14	-0.264	0.034	0.041	0.006	0.01	0.055
		-12.017	-0.152	0.032	0.041	0.006	0.01	0.054
	-Z	11.965	179.908	0.036	0.065	0.006	0.01	0.075
		-0.14	179.946	0.034	0.065	0.006	0.01	0.075
		-12.017	179.881	0.032	0.065	0.006	0.01	0.074

Table 2: The uncertainties in the magnetic field direction measurements (October, 2019) with Helmholtz coil at 45° w.r.t. beamline

(a) A_1^n kinematic settings

Kinematic settings	Polarization direction	Compass locations along z axis (cm)	Magnetic field direction (degrees)	\pm Error _{Survey} (degrees)	\pm Error _{Mirror} (degrees)	\pm Error _{Spotsize} (degrees)	\pm Error _{Center} (degrees)	\pm Error _{Total} (degrees)
SHMS at 12.5°, 7.5 GeV/c	+X	11.965	91.295	0.012	0.029	0.006	0.01	0.034
		0.135	91.194	0.012	0.029	0.006	0.01	0.034
		-12.028	91.551	0.012	0.029	0.006	0.01	0.034
	-X	11.965	268.959	0.012	0.029	0.006	0.01	0.034
		0.135	269.27	0.012	0.029	0.006	0.01	0.034
		-12.028	268.997	0.012	0.029	0.006	0.01	0.034
	+Z	11.965	0.62	0.025	0.029	0.006	0.01	0.04
		0.135	0.49	0.023	0.029	0.006	0.01	0.039
		-12.028	0.46	0.022	0.029	0.006	0.01	0.038
	-Z	11.965	180.03	0.025	0.029	0.006	0.01	0.04
		0.135	179.9	0.023	0.029	0.006	0.01	0.039
		-12.028	179.81	0.022	0.029	0.006	0.01	0.038
SHMS at 30°, 3.4 GeV/c	+X	11.965	90.309	0.012	0.029	0.006	0.01	0.034
		0.135	90.204	0.012	0.029	0.006	0.01	0.034
		-12.028	90.218	0.012	0.029	0.006	0.01	0.034
	-X	11.965	269.644	0.012	0.029	0.006	0.01	0.034
		0.135	269.931	0.012	0.029	0.006	0.01	0.034
		-12.028	269.873	0.012	0.029	0.006	0.01	0.034
	+Z	11.965	0.22	0.025	0.029	0.006	0.01	0.04
		0.135	0.17	0.023	0.029	0.006	0.01	0.039
		-12.028	0.19	0.022	0.029	0.006	0.01	0.038
	-Z	11.965	180.35	0.025	0.029	0.006	0.01	0.04
		0.135	180.14	0.023	0.029	0.006	0.01	0.039
		-12.028	180.04	0.022	0.029	0.006	0.01	0.038

(b) d_2^n kinematic setting

Kinematic settings	Polarization direction	Compass locations along z axis (cm)	Magnetic field direction (degrees)	\pm Error _{Survey} (degrees)	\pm Error _{Mirror} (degrees)	\pm Error _{Spotsize} (degrees)	\pm Error _{Center} (degrees)	\pm Error _{Total} (degrees)
SHMS at 18°, 5.6 GeV/c	+X	11.965	91.017	0.012	0.029	0.006	0.01	0.034
		0.135	90.805	0.012	0.029	0.006	0.01	0.034
		-12.028	90.972	0.012	0.029	0.006	0.01	0.034
	-X	11.965	269.355	0.012	0.029	0.006	0.01	0.034
		0.135	269.707	0.012	0.029	0.006	0.01	0.034
		-12.028	269.568	0.012	0.029	0.006	0.01	0.034
	+Z	11.965	0.46	0.025	0.029	0.006	0.01	0.04
		0.135	0.37	0.023	0.029	0.006	0.01	0.039
		-12.028	0.34	0.022	0.029	0.006	0.01	0.038
	-Z	11.965	180.19	0.025	0.029	0.006	0.01	0.04
		0.135	180.01	0.023	0.029	0.006	0.01	0.039
		-12.028	179.94	0.022	0.029	0.006	0.01	0.038

Table 3: The uncertainties in the magnetic field direction measurements for the d_2^n kinematic settings (September, 2020) with Helmholtz coil at 0° w.r.t. beamline

(a)

Kinematic settings	Polarization direction	Compass locations along z axis (cm)	Magnetic field direction (degrees)	$\pm \text{Error}_{\text{Survey}}$ (degrees)	$\pm \text{Error}_{\text{Mirror}}$ (degrees)	$\pm \text{Error}_{\text{Spotsize}}$ (degrees)	$\pm \text{Error}_{\text{Center}}$ (degrees)	$\pm \text{Error}_{\text{Total}}$ (degrees)
SHMS at $11^\circ, -7.5$ GeV/c	+X	11.957	88.98	0.018	0.064	0.006	0.01	0.067
		-0.3	89.16	0.018	0.064	0.006	0.01	0.067
		-12.022	88.93	0.018	0.064	0.006	0.01	0.067
	-X	11.957	269.26	0.018	0.08	0.006	0.01	0.083
		-0.3	268.92	0.018	0.08	0.006	0.01	0.083
		-12.022	269.05	0.018	0.08	0.006	0.01	0.083
	+Z	11.957	0.33	0.036	0.064	0.006	0.01	0.074
		-0.3	0.24	0.034	0.064	0.006	0.01	0.073
		-12.022	0.24	0.032	0.064	0.006	0.01	0.072
	-Z	11.957	180.31	0.036	0.08	0.006	0.01	0.088
		-0.3	179.67	0.034	0.08	0.006	0.01	0.088
		-12.022	179.61	0.032	0.08	0.006	0.01	0.087
SHMS at $14.5^\circ, -6.4$ GeV/c	+X	11.957	88.23	0.018	0.064	0.006	0.01	0.067
		-0.3	88.48	0.018	0.064	0.006	0.01	0.067
		-12.022	88.36	0.018	0.064	0.006	0.01	0.067
	-X	11.957	269.23	0.018	0.08	0.006	0.01	0.083
		-0.3	269.08	0.018	0.08	0.006	0.01	0.083
		-12.022	269.24	0.018	0.08	0.006	0.01	0.083
	+Z	11.957	-0.68	0.036	0.064	0.006	0.01	0.074
		-0.3	-0.61	0.034	0.064	0.006	0.01	0.073
		-12.022	0.19	0.032	0.064	0.006	0.01	0.072
	-Z	11.957	180.38	0.036	0.08	0.006	0.01	0.088
		-0.3	179.54	0.034	0.08	0.006	0.01	0.088
		-12.022	179.48	0.032	0.08	0.006	0.01	0.087

(b)

Kinematic settings	Polarization direction	Compass locations along z axis (cm)	Magnetic field direction (degrees)	$\pm \text{Error}_{\text{Survey}}$ (degrees)	$\pm \text{Error}_{\text{Mirror}}$ (degrees)	$\pm \text{Error}_{\text{Spotsize}}$ (degrees)	$\pm \text{Error}_{\text{Center}}$ (degrees)	$\pm \text{Error}_{\text{Total}}$ (degrees)
SHMS at $18^\circ, -5.6$ GeV/c	+X	11.957	88.18	0.018	0.064	0.006	0.01	0.067
		-0.3	88.37	0.018	0.064	0.006	0.01	0.067
		-12.022	89.25	0.018	0.064	0.006	0.01	0.067
	-X	11.957	269.44	0.018	0.08	0.006	0.01	0.083
		-0.3	269.31	0.018	0.08	0.006	0.01	0.083
		-12.022	270.64	0.018	0.08	0.006	0.01	0.083
	+Z	11.957	-0.65	0.036	0.064	0.006	0.01	0.074
		-0.3	0.08	0.034	0.064	0.006	0.01	0.073
		-12.022	0.06	0.032	0.064	0.006	0.01	0.072
	-Z	11.957	180.02	0.036	0.08	0.006	0.01	0.088
		-0.3	180.06	0.034	0.08	0.006	0.01	0.088
		-12.022	180.17	0.032	0.08	0.006	0.01	0.087
SHMS at $8.5^\circ, -2.12$ GeV/c, one pass	+Z	11.957	0.22	0.036	0.064	0.006	0.01	0.074
		-0.3	0.11	0.034	0.064	0.006	0.01	0.073
		-12.022	0.08	0.032	0.064	0.006	0.01	0.072
	-Z	11.957	180.11	0.036	0.08	0.006	0.01	0.088
		-0.3	179.55	0.034	0.08	0.006	0.01	0.088
		-12.022	180.03	0.032	0.08	0.006	0.01	0.087

Appendix B: F1F2IN09 and F1F2IN21 Models

The F1F2IN09 [95] and F1F2IN21 [94] models are phenomenological parametrization developed by fitting various Born cross-section world data. The F1F2IN09 model was developed by P. Bosted and V. Mamyan and it is written in Fortran script. This code calculates the F_1 and F_2 structure functions to extract Born cross-section using the following formula.

$$\frac{d^2\sigma}{d\Omega dE_p} = \frac{\alpha^2 \cos^2 \frac{\theta}{2}}{4E_s^2 \sin^4 \frac{\theta}{2}} \left[\frac{1}{\nu} F_2(W^2, Q^2) + 2 \tan^2 \frac{\theta}{2} F_1(W^2, Q^2) \right], \quad (8.1)$$

where α is the fine structure constant, ν is the electron energy that is transferred to the target, M_n is the mass of the nucleon, W is the invariant mass and, and Q^2 is the virtual photon momentum squared. However the F1F2IN09 model is only valid for $A > 2$, $0 < W < 3.5 \text{ GeV}$ and $0.2 < Q^2 < 5 \text{ GeV}^2/c^2$. The updated version of this model is F1F2IN21 where the $A > 2$ parametrization was developed by E. Cristy, T. Gautam and A. Bodek. This fit is good for all nuclei with $10 < A < 80$. This new model also included the proton cross section fit and a preliminary deuteron/neutron fit by M. E. Christy, N. Kalantarians, J. Either and W. Melnitchouk. This work is yet to be published. This fit is valid for the range $W^2 < 32 \text{ GeV}^2/c^2$ and $Q^2 < 32 \text{ GeV}^2/c^2$. A newer version of the F1F2IN21 is expected with fits from more nuclei data.

Appendix C: Inputs of the rc-externals Code

```

IF(INDEX(TARGET,'AIND2NPRODTOMMY').GT.0) THEN      ! target geometry for
                                                    ! pol 3He cell
ECIR=(0.87/2)*2.54-0.15                          ! endcap inner radius (cm)
ECOR=ECIR+0.0145                                  ! endcap outer radius (cm), Tommy downstream window thickness=0.0145 cm
TARGLEN=40.0                                       ! target length (cm)
c_1=1.38091E-5                                    !up win thickness change
c_2=0.110839                                       !up win thickness change
ENTEC=TARGLEN-ECIR                                ! entrance to end cap (cm)
TBAL=TBEAM                                         ! material bf the target
TBEFOR=T                                           ! distance traveled bf
                                                    ! vertex
tcm=(t*targlen/ttarg)+(targlen/2.0)-1.0          ! t in cm, Tommy shifted towards downstream (+z) by 1 cm
if(tcm.lt.0) tcm=0
if(tcm.gt.targlen) tcm=targlen

if((tcm+ECIR/tan(thr)).lt.ENTEC) then ! e goes through sidewall
  TAFTER=ECIR*ttarg/sin(thr)/targlen           ! gas target
  TAAL=TSPEC+TWALL/sin(thr)                   ! material of the target
  ! & side wall
else
  rho_tar=(sqrt(ECOR**2-((targlen-ECIR-tcm)*sin(thr))**2)
  > +(targlen-ECIR-tcm)*cos(thr))*sin(thr)!distance away tar center
  TAFTER=                                       ! e goes through end cap
  > (sqrt(ECIR**2-((targlen-ECIR-tcm)*sin(thr))**2)
  > +(targlen-ECIR-tcm)*cos(thr))*ttarg/targlen !gas target
  TAAL=TSPEC                                    ! material of the target
  > +(sqrt((ECOR+c_1*exp(rho_tar/c_2))**2
  > -((targlen-ECIR-tcm)*sin(thr))**2)
  > -sqrt(ECIR**2-((targlen-ECIR-tcm)*sin(thr))**2))
  > /7.04
endif
ENDIF

```

Figure 1: The target geometry update in rc-externals source code for polarized ^3He target.

```

Pol 3He target cell
AInd2n2020 (HMS)
-----1-----2-----3-----4-----5-----6-----7-----
iZ  (#)      2
iA  (#)      3

avgA (#)
avgM (GeV)

target type      AIND2NPRODTOMMY      : columns 21-27
thicknesses (rad. lengths):
  target         0.000890
  walls          0.021307
  pre-target     0.00363969
  post-target    0.00769421
nseg (even)     2

Pking: Ep/E > 1.0
ikk            15 elastic nucleon model
iout          2
idut          13 elastic d2 model: 0=old, 11,12,13,14=Ulmars(below
inel_model     4 inelastc 4=new; 0=ineft(Bodek);9,12=Stuart+F2Glob etc.
pauli_model    1 0= old stein model; 1=tsai model; 2 no suppression
Nuc Tail Method 1 0=No cos(theta_k) integration; 1= cos(th_k) integration
Nuc FormFac Mdl 1 0=Shell,Gauss, 1=Hicks for Si28 and O16

! INEL_MODEL inelastc h2 modl: 0=ineft(Bodek);9,12=Stuart+F2Glob
!                                     1=f2nmc(DIS),ineft(RES)
!
! **OR**
! INEL_MODEL =rrdd where rr is resonance model number and dd is DIS model
! It must be >=100
! DIS_MODEL= 1 ineft
!           2 f2nmc
!           3 f2nmc95
!           9 f2glob model 9
!          12 f2glob model 12
! RES_MODEL 1 ineft
!           2 H2Model
-----

```

Figure 2: The target input file in rc-externals code that specifies the thickness of all pre target and post target materials.

The following $E' - \theta$ grid was used to generate the radiative cross-section using F1F2IN21 parametrization.

	Kin Set	E (GeV)	E' min (GeV)	E' max (GeV)	dE' (GeV)	θ min (deg)	θ max (deg)	d θ (deg)
HMS								
	A	10.38	3.78	4.62	0.01	9.6	19.8	0.2
	B	10.38	3.78	4.62	0.01	12.1	22.3	0.2
	C	10.38	3.6	4.4	0.01	15.5	25.7	0.2
SHMS								
	X	10.38	6.375	9.375	0.01	7.8	18	0.2
	Y	10.38	5.44	8	0.01	10.5	20.7	0.2
	Z	10.38	4.76	7	0.01	13.5	23.7	0.2

Appendix D: Beam Current Monitors during Data Collection

The current output from the BCM1 and BCM2 are shown with time. BCM2 was significantly more stable than BCM1 in between the calibration runs. For this reason an uncertainty of $\pm 1\%$ was assigned to the total charge from the BCMS and the charge from the BCM2 was used to normalize the data yield.

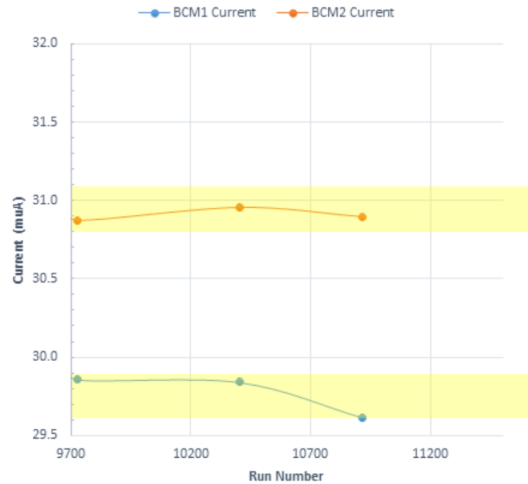


Figure 3: The BCM1 and BCM2 gain vs. calibration runs. The yellow bands correspond to $\pm 0.5\%$. This plot was generated by Dave Mack.

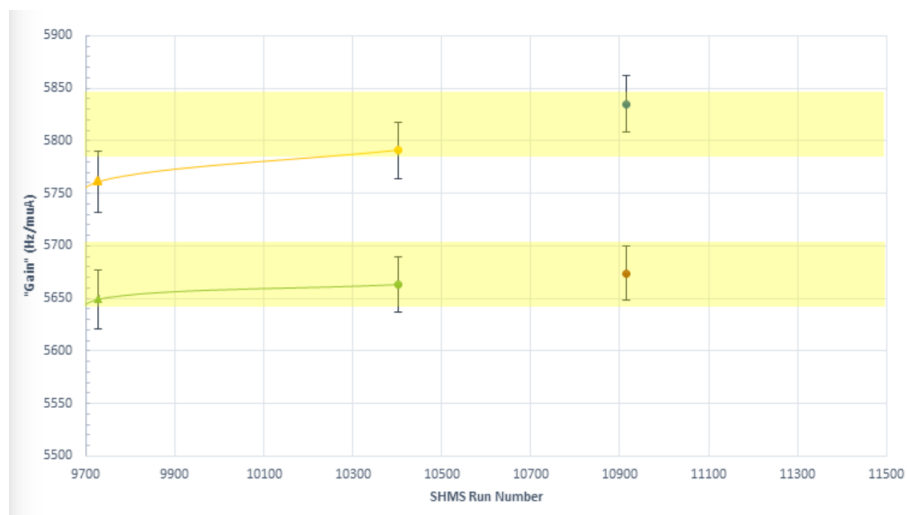


Figure 4: The beam currents with calibration runs taken during the experiment E12-06-121. The yellow bands correspond to $\pm 0.5\%$. This plot was generated by Dave Mack.

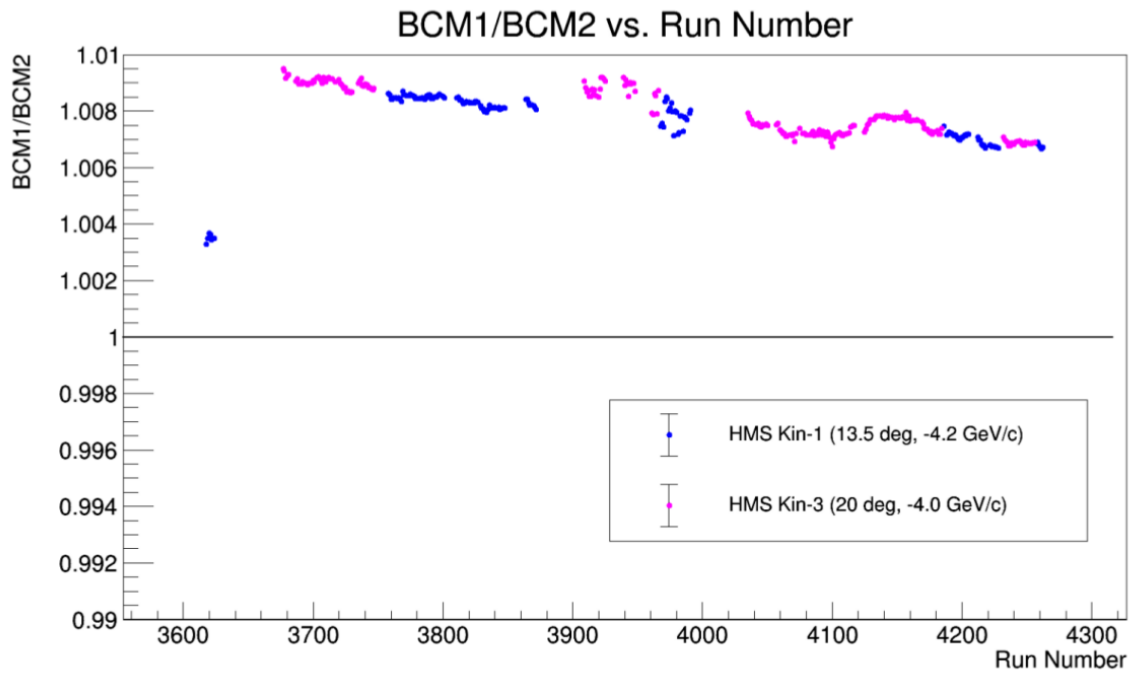


Figure 5: The ratio of BCM1 and BCM2 currents during the data collection period. The runs before 3660 were taken in March, 2020 before the COVID shut down. The ratio changed significantly after the experiment resumed in August, 2020

Appendix E: Tabulated Unpolarized Cross Sections

Table 4: Extracted radiative cross-section results binned in E' with the corresponding statistical and systematic errors for HMS ($\theta = 13.5^\circ$).

$E'(GeV)$	σ_{rad} (nb)	$\delta\sigma_{rad}^{stat}$ (nb)	$\delta\sigma_{rad}^{sys}$ (nb)
3.990	66.369	± 0.303	± 3.145
4.074	63.614	± 0.294	± 3.037
4.158	62.953	± 0.292	± 3.030
4.242	63.184	± 0.294	± 3.066
4.326	63.136	± 0.294	± 3.088
4.410	62.163	± 0.292	± 3.064

Table 5: Extracted radiative cross-section results binned in E' with the corresponding statistical and systematic errors for HMS ($\theta = 20.0^\circ$).

$E'(GeV)$	σ_{rad} (nb)	$\delta\sigma_{rad}^{stat}$ (nb)	$\delta\sigma_{rad}^{sys}$ (nb)
3.80	8.144	± 0.086	± 0.408
3.88	7.689	± 0.083	± 0.388
3.96	7.324	± 0.081	± 0.372
4.04	7.187	± 0.081	± 0.368
4.12	6.826	± 0.079	± 0.352
4.20	6.317	± 0.076	± 0.328

Table 6: Extracted Born cross-section results binned in E' with the corresponding statistical and systematic errors for HMS ($\theta = 13.5^\circ$).

$E'(GeV)$	σ_{Born} (nb)	$\delta\sigma_{Born}^{stat}$ (nb)	$\delta\sigma_{Born}^{sys}$ (nb)
3.990	59.518	± 0.277	± 4.323
4.074	57.481	± 0.270	± 4.182
4.158	57.345	± 0.269	± 4.172
4.242	58.016	± 0.273	± 4.221
4.326	58.435	± 0.276	± 4.251
4.410	57.977	± 0.276	± 4.218

Table 7: Extracted Born cross-section results binned in E' with the corresponding statistical and systematic errors for HMS ($\theta = 20.0^\circ$).

$E'(GeV)$	σ_{Born} (nb)	$\delta\sigma_{Born}^{stat}$ (nb)	$\delta\sigma_{Born}^{sys}$ (nb)
3.80	8.094	± 0.086	± 0.574
3.88	7.699	± 0.084	± 0.547
3.96	7.387	± 0.082	± 0.524
4.04	7.304	± 0.082	± 0.519
4.12	6.989	± 0.081	± 0.496
4.20	6.513	± 0.078	± 0.462

Table 8: Extracted radiative cross-section results binned in E' with the corresponding statistical and systematic errors for SHMS ($\theta = 11.0^\circ$).

$E'(GeV)$	σ_{rad} (nb)	$\delta\sigma_{rad}^{stat}$ (nb)	$\delta\sigma_{rad}^{sys}$ (nb)
6.84	135.501	± 0.444	± 8.015
6.99	118.980	± 0.400	± 7.131
7.14	104.844	± 0.364	± 6.368
7.29	90.661	± 0.327	± 5.588
7.44	77.442	± 0.293	± 4.842
7.60	64.292	± 0.263	± 4.093
7.75	52.461	± 0.227	± 3.427
7.91	41.966	± 0.197	± 2.749
8.06	32.347	± 0.171	± 2.262
8.21	24.336	± 0.142	± 1.162

Table 9: Extracted radiative cross-section results binned in E' with the corresponding statistical and systematic errors for SHMS ($\theta = 18.0^\circ$).

$E'(GeV)$	σ_{rad} (nb)	$\delta\sigma_{rad}^{stat}$ (nb)	$\delta\sigma_{rad}^{sys}$ (nb)
5.13	7.791	± 0.094	± 0.474
5.23	6.461	± 0.085	± 0.397
5.34	5.589	± 0.078	± 0.346
5.44	4.641	± 0.071	± 0.290
5.55	4.032	± 0.066	± 0.255
5.66	3.376	± 0.060	± 0.216
5.76	2.789	± 0.054	± 0.179
5.87	2.238	± 0.049	± 0.147
5.97	1.962	± 0.045	± 0.129
6.08	1.448	± 0.039	± 0.096
6.18	1.075	± 0.033	± 0.072

Table 10: Extracted Born cross-section results binned in E' with the corresponding statistical and systematic errors for SHMS ($\theta = 11.0^\circ$).

$E'(GeV)$	σ_{Born} (nb)	$\delta\sigma_{Born}^{stat}$ (nb)	$\delta\sigma_{Born}^{sys}$ (nb)
6.84	146.266	± 0.482	± 10.850
6.99	130.118	± 0.440	± 9.653
7.14	116.205	± 0.406	± 8.620
7.29	101.970	± 0.371	± 7.564
7.44	88.363	± 0.338	± 6.555
7.60	74.685	± 0.311	± 5.540
7.75	62.536	± 0.246	± 4.639
7.91	50.169	± 0.243	± 3.721
8.06	41.279	± 0.239	± 3.062
8.21	29.509	± 0.194	± 2.189

Table 11: Extracted Born cross-section results binned in E' with the corresponding statistical and systematic errors for SHMS ($\theta = 18.0^\circ$).

$E'(GeV)$	σ_{Born} (nb)	$\delta\sigma_{Born}^{stat}$ (nb)	$\delta\sigma_{Born}^{sys}$ (nb)
5.13	8.493	± 0.102	± 0.636
5.23	7.110	± 0.093	± 0.533
5.34	6.209	± 0.087	± 0.465
5.44	5.204	± 0.079	± 0.389
5.55	4.567	± 0.074	± 0.342
5.66	3.863	± 0.069	± 0.289
5.76	3.224	± 0.063	± 0.241
5.87	2.646	± 0.051	± 0.198
5.97	2.315	± 0.054	± 0.173
6.08	1.725	± 0.047	± 0.129
6.18	1.295	± 0.041	± 0.097

Bibliography

- [1] E. J. Moniz et al., Phys. Rev. Lett. 26, 445, 1971.
- [2] T. De Forest Jr., J.D. Walecka, “Electron scattering and nuclear structure” (Adv.Phys. 15, 1966), 1-109.
- [3] T. W. Donnelly, Nuclear Physics A 150, 393-416, 1970.
- [4] R.D. Woods and D.S. Saxon, Phys. Rev. 95, 577, 1954.
- [5] S. Klawansky, H.W. Kendall, A.K. Kerman, D. Isabelle, Phys. Rev. C7, 795-800, 1973.
- [6] Roger G. Newton, “Scattering Theory of Waves and Particles” (1982).
- [7] Yoshiyuki Kawazoe, Gyo Takeda and Hisao Matsuzaki, Progress of Theoretical Physics, Vol 54, No 5, 1975.
- [8] N. Svartholm, editor, “Elementary particle theory, relativistic groups and analyticity:proceedings” (Wiley, 1968).
- [9] S. Weinberg, Phys. Rev. Lett. 19, 1264-1266, 1967.
- [10] A. Thomas, W. Weise, “The Structure of the Nucleon” (Wiley-VCH, 2001).
- [11] A. Manohar, “ An Introduction To Spin Dependent Deep Inelastic Scattering”, 1992.
- [12] Zheng, Xiaochao, Ph.D., Massachusetts Institute of Technology, 2002.
- [13] C. G. Callon and D. J. Gross, Phys. Rev. Lett. 22, 156, 1969.
- [14] J. D. Bjorken and E. A. Paschos, Phys. Rev. 185, 1975, 1969.
- [15] Posik, Matthew, Ph.D., Temple University, 2014.
- [16] R. P. Feynman, Phys. Rev. Lett. 23, 1415, 1969.
- [17] Guy Bonneau, Scholarpedia, 4(9):8506, 2009.
- [18] E. Shuryak and A. Vainshtein, Nuc. Phys. B 201, 141, 1982.
- [19] R. L. Jaffe and X. Ji, Phys. Rev. D 43, 724, 1991.
- [20] B. W. Filippone and X. Ji, Adv. in Nucl. Phys. 26, 1, 2001.
- [21] S. Wandzura and F. Wilczek, Phys. Lett. B 72, 195, 1977.
- [22] X. Ji and P. Unrau, Phys. Lett. B 333, 228, 1994.

- [23] X. Ji Nucl. Phys. B402, 217, 1994.
- [24] S. A. Larin, T. van Ritbergen and J.A. Vermaseren, Phys. Lett. 404, 153, 1997;
S. A. Larin, Phys. Lett. B 334, 192, 1994.
- [25] F. E. Close and R. G. Roberts, Phys. Lett. B 336, 257, 1994.
- [26] Z. E. Meziani et al., Phys. Lett. B 613, 148, 2005.
- [27] M. Osipenko et al., Phys. Lett. B 609, 259, 2005.
- [28] A. V. Sidorov and C. Weiss, Phys. Rev. D 73, 074016, 2006.
- [29] A. Deur et al., Phys. Rev. Lett. 93, 212001, 2004.
- [30] M. Burkardt, Phys. Rev. D 88, 114502, 2013.
- [31] B. Ehrnsperger, A. Schfer, and L. Mankiewicz, Phys. Lett. B 323, 439, 1994.
- [32] M. Creutz. Quarks Gluons and Lattices. Cambridge Univ. Press, Cambridge, 1983.
- [33] I. Montvay and G. Münster, “Quantum Fields on a Lattice” (Cambridge Univ. Press, Cambridge, 1994).
- [34] H. J. Rothe. “Lattice Gauge Theories: An Intorduction” (World Scientific Lecture Notes in Physics- Vol.59, World Scientific, Singapore, 1997).
- [35] M. Gockeler et al., Phys. Rev. D63, 074506, 2001.
- [36] A. I. Vainshtein M .A Shifman and V. I. Zakharov. Nucl. Phys. B, 58-333, 1979.
- [37] E. Stein, Phys. Lett. B 343, 369, 1995.
- [38] B. Ehrnsperger, A Schfer, Phys. Rev. D 52, 2709, 1995.
- [39] I. Balitsky, V. Barun, A. Kolesnichenko, Phys. Lett. B 242, 245, 1990; B 318, 648, 1995.
- [40] H. Weigel, L. Gamberg, H. Reinhart, Phys. Rev. D55, 6910, 1997.
- [41] Dmitri Diakonov, “Chiral Quark-Soliton Model”, 1998.
- [42] P. Amaudruz et al., Phys. Rev. Lett. 66, 1991.
- [43] K. Abe et al., Phys. Rev. D 58, 1998.
- [44] K. Abe et al., Phys. Rev. Lett. 79, 1997.
- [45] P.L. Anthony et al., hep-exr994002, 1998.
- [46] B. Adeva et al., Phys. Rev. D 58, 1998.

- [47] M. Wakamatsu, Physics Letters B 487(1-2), 118124, 2000.
- [48] P. N. Bogoliubov. Ann. Inst. Henri Poincare, 8-163, 1967.
- [49] K. Johnson T. DeGrand, R. J. Jaffe and J. Kiskis. Phys. Rev. D, 12-2060, 1975.
- [50] K. Johnson A. Chodos, R. J. Jaffe and C. B. Thorne. Phys. Rev. D, 10-2599, 1974.
- [51] Jaffe, R. L.; Ji, Xiangdong, Physical Review D, 43(3), 724732, 1991.
- [52] K. Abe et al., Phys. Rev. Lett. 76, 587, 1996.
- [53] K. Abe et al., Phys. Lett. B 404, 377, 1997.
- [54] P. L. Anthony et al., Phys. Lett. B458, 529, 1999.
- [55] P. L. Anthony et al., Phys. Lett. B 553, 18, 2003.
- [56] M. Amarian et al., Phys. Rev. Lett. 89, 242301, 2002.
- [57] M. Amarian et al., Phys. Rev. Lett. 92, 022301, 2004.
- [58] P. Solvignon et al., Phys. Rev. Lett. 101, 182502, 2008.
- [59] K. Slifer et al., Phys. Rev. Lett. 105, 101601, 2010.
- [60] M. Posik et al., Phys. Rev. Lett. 113, 022002, 2014.
- [61] Flay et al., Phys. Rev. D.94, 052003, 2016.
- [62] Parno et al., Phys. Let. B 744, 309, 2015.
- [63] Armstrong et al., PRL 122, 022002, 2019.
- [64] S.A. Bogacz et al., Brookhaven National Laboratory, “A test of 5-pass energy recovery at CEBAF”, 2016.
- [65] A. Alley et al., Nucl. Inst. and Meth. in Phys. Res., A365, 1, 1995.
- [66] R. Prepost and T. Maruyama, Annual Review of Nuclear and Particle Science, 45, 41, 1995.
- [67] F. M. Gonzalez, “ Improved Neutron Lifetime Measurement with UCN τ ”, 2021.
- [68] Kramer, Kevin M., Ph.D., The College of William and Mary in Virginia, 2003.
- [69] S. Applet et al., Phys. Rev. A, 58, 1412, 1998.
- [70] H. Kopfermann. “Nuclear Moments” (Academic Press, New York, USA, 1959).
- [71] Joshua Abney, Ph.D., University of Kentucky, 2018.

- [72] K.Slifer, Ph.D., Temple University, 2004.
- [73] Earl Babcock, Ian Nelson, Steve Kadlecsek, Bastiaan Driehuys, L. W. Anderson, F. W. Hersman, and Thad G. Walker., Phys. Rev. Lett., 91, 123003, 2003.
- [74] W. C. Chen, T. R. Gentile, T. G. Walker, and E. Babcock., Phys. Rev. A, 75, 013416, 2007.
- [75] A. Ben-Amar Baranga, S. Appelt, M. V. Romalis, C. J. Erickson, A. R. Young, G. D. Cates, and W. Happer., Phys. Rev. Lett., 80, 1998.
- [76] Hall C Staff and Users, “2016 version: Jefferson Lab Hall C Standard Equipment Manual”, 2018.
- [77] Romalis, M. V. and Cates, G. D., Phys. Rev. A 58, 30043011, 1998.
- [78] Balling, L. C., Hanson, R. J. and Pipkin, F. M., Phys. Rev. 133, A607A626, 1964.
- [79] S Katugampola et al., physics.atom-ph., 2021.
- [80] J. Heefner and, W. Barry, “Beam Position Measurement in the CEBAF Recirculating Linacs by use of Pseudorandom Sequences.”, Technical report, CEBAF, PR-90-009, 1990.
- [81] Dave Mack and, Stephen A. Wood, “Hall C Expert Howto, BCM Calibration”.
- [82] Melanie Cardona, (private communication).
- [83] S. N. Santiesteban, L. Tracy, D. Flay, D. W. Higinbotham, D. Marchand, P. Vernin, A Saha, “Precise Beam Energy Determination for Hall A after the CEBAF 12 GeV Upgrade”, 2021.
- [84] Charles K. Sinclair, Jefferson Lab, “Electron Beam Polarimetry”.
- [85] M. Hauger et al., Nuclear Instruments and Methods in Physics Research A 462, 38239, 2000.
- [86] D. W. Higinbotham, arXiv:0901.4484v1[physics.acc-ph].
- [87] I. Niculescu, G. Niculescu, “E12-10-002 Charge Symmetric Background, A quick study”, 2019.
- [88] Carlos Yero, “Hall C 12 GeV Trigger Set-up”, 2019.
- [89] Mingyu Chen (private communication).
- [90] S. P. Malace, Ph.D., Hampton University, 2006.
- [91] L. Mo and Y. Tsai, Rev. Mod. Phys. 41, 205, 1969.
- [92] J. W. Lightbody and J. S. OConnell, Comp. in Phys. p. 57, 1988.

- [93] S. Stein et al., Phys. Rev. D 12, 1884, 1975.
- [94] E. Cristy et al., Hampton University, 2021 (unpublished).
- [95] P. Bosted and V. Mamyan, arXiv:1203.2262v2 [nucl-th], 2012.
- [96] Michael E. Peskin , Daniel V. Schroeder, “An Introduction to Quantum Field Theory”.
- [97] Thomas R. Hemmert, Barry R. Holstein, Joachim Kambor, Germar Knöchlein, Phys. Rev. 75.32, 1998.
- [98] F.E. Low, Phys. Rev. Lett. 96.1428, 1954.
- [99] M. Gell-Mann , M. L. Goldberger, Phys. Rev. Lett. 96.1433, 1954.
- [100] Susan Gardner, arXiv:astro-ph/0611684v3, 2007.
- [101] Krzysztof Rebilas, “Thomas Precession and the Bargmann-Michel-Telegdi Equation”, 2011.

Vita

NAME: MURCHHANA ROY

EDUCATION

- MS in Physics, University of Kentucky, Lexington, Kentucky, August 2019.
- MSc in Physics, Indian Institute of Technology, Madras, India, July 2016.
- BSc in Physics, St. Xaviers College, Kolkata, India, June 2014.

AFFILIATIONS

- GRADUATE USER, Jefferson Lab, Newport News, VA / August 2019-Present.
- GRADUATE RESEARCH ASSISTANT, University of Kentucky, Lexington, KY / May 2017-Present.
- GRADUATE TEACHING ASSISTANT, University of Kentucky, Lexington, KY / August 2016-May 2017.

HONORS AND AWARDS

- JSA Virtual Student Poster Competition winner, 1st Place, 2021.
- JSA Virtual Student Poster Competition winner, 2nd Place, 2020.
- University of Kentucky Max Steckler Fellowship Award, 2017.
- Parpati Chandumal Sahani Memorial Gold Medal Award, India, 2015.
- INSPIRE Scholarship Award, India, 2011-2015.

PUBLICATIONS

- J. Abney, M. Broering, M. Roy, W. Korsch, “Limits on Magnetically Induced Faraday Rotation from Polarized helium-3 Atoms, Phys. Rev. A 99, 2019 (023831).
- M. Roy et al., “Development and Construction of a Precision Compass (in preparation).
- M. Broering et al., “The Behavior of Charged Particles on Insulating Surfaces in Cryogenic Fluids within (Strong) Electric Fields (in preparation).